DEPARTMENT OF PHYSICS

TECHNISCHE UNIVERSITÄT MÜNCHEN

MAX-PLANCK-INSTITUT FÜR PHYSIK

WERNER-HEISENBERG-INSTITUT

PhD Thesis

Investigation of Hadronic Higgs Decays at CLIC at 350 GeV & Scintillator Studies for a Highly Granular Calorimeter

Marco Szalay

DEPARTMENT OF PHYSICS

TECHNISCHE UNIVERSITÄT MÜNCHEN

PhD Thesis

Investigation of Hadronic Higgs Decays at CLIC at 350 GeV & Scintillator Studies for a Highly Granular Calorimeter

Untersuchung von hadronischen Higgszerfällen mit CLIC bei 350 GeV & Szintillatorstudien für ein hochgranulares Kalorimeter

Author:	Marco Szalay
Supervisor:	Dr. Frank Simon
Advisor:	Hon.-Prof. Dr. Allen C. Caldwell
Submission Date:	March 23rd, 2017

I confirm that this phd thesis is my own work and I have documented all sources and material used.

München, March 23rd, 2017 Marco Szalay

Acknowledgments

First and foremost, I would like to express my sincere gratitude to my supervisor, Dr. Frank Simon, for the constant support, encouragement that he has always given me over the course of these years. Frank, I am sure you know you are a great boss, and I admire your dedication towards your students and your research.

I would also like to extend my thanks to my thesis advisor, Prof. Allen Caldwell, for his patience and his kindness in explaining things, no matter how elementary: I have always left your office feeling I had learned something.

A big thank you to Lucie Linssen and the CLIC group at CERN, and to Philipp Roloff in particular, not only for producing the simulations that were instrumental in the making of this thesis, but also for the constant feedback and suggestions that helped me immensely in my work.

To all my colleagues and friends in the *Future Detector* and *Belle* groups, working with you is a real pleasure and I am truly thankful for having had the luck to meet you all. I would like to thank especially Prof. Christian Kiesling for always finding the time to explain things to me: I am certain I have learned more Physics from you over the coffee breaks than in all my academic career. Also Christian Graf, who had the uneasy task of sharing an office space with me for the last year and helped me a lot with the proofreading of this work: thank you for enduring the chaos, I promise I will clean up my desk... next week.

Chris and Lars, I am very fortunate to have met you in my study carrier. You guys took me under your wing when I first got to the MPI and I am happy to be your friend. Martin, on top of that you deserve a special acknowledgment: if I have ever written a working line of code, I owe it to you.

A special thanks goes to Frank Steffen for organizing the MPP IMPRS, and the yearly Ringberg retreat so impeccably: I will keep the memories of those meetings forever.

To all the staff of the Max Planck Institute for Physics, and in particular to Ina Wacker and Corina Brunnlechner, for all the extra paperwork you had to put up with because

of me.

Special acknowledgements go also to the *Excellence cluster: Origin and Structure of the Universe*, for the funding that has made this thesis work possible.

To all my friends and family that are now scattered at the four corners of the Globe; we might see each other once a year, but we understand each other as if we never left.

To my parents, for having always pushed me to pursue my passions and for helping me become who I am today: to Mauro, for showing me how an oscilloscope works when I was three, and to Miki, for always making sure I did not electrocute myself on it.

And, finally, to Elisa. You know better than I do that I would be lost without you. Thanks for putting up with all my nonsense over the years, enduring the stressful weekdays and the even more stressful weekends for way longer than I probably deserve. For making me laugh when I am blue and for relieving all my stress with a smile. I am lucky to have you and I hope I will be able to be as supportive to you when you will need it as you have been with me for all this time.

Abstract

The energy frontier of accelerator-based physics has been dominated, for the best part of the last ten years, by the Large Hadron Collider (LHC). This remarkable accelerator has provided scientists with proton-proton collisions up to 13 TeV in energy, that led to exciting progress in the understanding of particle physics, culminating in the discovery of the Higgs boson in 2012. Despite its successes, the LHC carries an intrinsic limitation: since it collides composite particles, the initial conditions of each interaction cannot be completely determined. This limits the precision with which some observables can be measured. A new generation of colliders, designed for the acceleration of elementary electrons and positrons, is being developed to reach higher precision and to provide complementary discovery potential for new phenomena. The two most mature projects in this category are the Compact LInear Collider (CLIC) and the International Linear Collider (ILC).

One key component of the physics program at CLIC is the full exploration of the Higgs sector to understand the mass generation mechanism in detail. This experimental program includes the measurement of branching fractions of decays into various fermions and bosons, the coupling to the top quark and the self coupling.

This thesis evaluates the achievable accuracies of the measurement of the Higgs boson branching fractions to b and c quarks, as well as to gluons, for the CLIC_ILD detector using Monte Carlo generated samples with a Higgs mass of 126 GeV at a center-of-mass energy of 350 GeV. The Higgs production mechanisms under investigation are: ZH production ("Higgsstrahlung"), with the Z further decaying into neutrinos or quarks, and Vector Boson Fusion ("VBF"), in which two W bosons, radiated off a colliding electron-positron pair, combine to form a Higgs boson.

The jet reconstruction for the hadronic decays benefits from the high granularity of the calorimetric subdetectors and from particle flow algorithms that allow for unprecedented accuracies in the channels involving jets in the final state. Multivariate techniques are applied to determine the jet flavor, separating b, c and light jets, and to separate signal events from Standard Model physics background.

A multidimensional likelihood fit is then applied, in a toy Monte Carlo procedure, to simultaneously extract the uncertainties of the Higgs hadronic branching fractions, as well as their correlations. Possible sources of systematic uncertainties are investigated as well. This leads to precisions at the 1-2%, 14-26% and 6-10% levels, for decays into b-quarks, c-quarks and gluons respectively, the exact value for each depending on the particular Higgs production mechanism.

Complementary to the core analysis, the thesis also investigates a novel technique, that could potentially lower the costs and production time for the segmentation of scintillators for a highly granular calorimeter. This is based on an industrial process known as sub-surface laser engraving. After engraving, the response of the scintillator prototypes is analyzed by means of a position-sensitive beta ray scan and a silicon photomultiplayer (SiPM) readout, to study their light yield and the amount of intra-channel cross-talk.

Zusammenfassung

Physik auf Basis von Beschleunigern bei höchsten Energien wurde den größten Teil der letzten zehn Jahre vom Large Hadron Collider (LHC) dominiert. Dieser beeindruckende Beschleuniger hat Wissenschaftler mit Proton-Proton Kollisionen von bis zu 13 TeV versorgt, was zu spannendem Fortschritt in unserem Verständnis von Teilchenphysik führte und 2012 in der Entdeckung des Higgs-Bosons gipfelte. Trotz seines Erfolges, hat der LHC eine intrinsische Beschränkung: da am LHC zusammengesetzte Teilchen kollidieren, können die Anfangsbedingungen der einzelnen Kollision nicht genau bestimmt werden. Dies limitiert die Präzision mit der bestimmte Größen gemessen werden können. Um höhere Präzision zu erreichen und um einen komplementären Ansatz zur Entdeckung neuer Phänomene zu ermöglichen, wird eine neue Generation von Teilchenbeschleunigern, welche Elektronen und Positronen zur Kollision bringen, entwickelt. Die zwei auf diesem Gebiet am weitesten fortgeschrittenen Projekte sind der Compact LInear Collider (CLIC) und der International Linear Collider (ILC).

Ein Hauptbestandteil des Physik-Programms von CLIC ist die genau Vermessung des Higgs-Sektors um den Mechanismus zur Massenerzeugung im Standardmodell im Detail zu verstehen. Dieses experimentelle Programm beinhaltet die Messung von Verzweigungsverhältnissen von Zerfällen in verschiedene Fermionen und Bosonen, die Kopplung an das Top-Quark und die Selbstkopplung des Higgs-Teilchens.

Diese Arbeit untersucht die erreichbare Genauigkeit der Messung der Verzweigungsverhältnisse des Higgs-Bosonen-Zerfalls in b- und c-Quarks, sowie in Gluonen für den CLIC_ILD Detektor. Hierfür werden simulierte Datensätze mit einer Higgs Masse von 126 GeV und einer Schwerpunktsenergie von 350 GeV verwendet. Die untersuchten Higgs-Produktionsmechanismen sind: ZH-Produktion ("Higgsstrahlung"), wobei das Z in Neutrinos oder Quarks zerfällt, sowie Vektorbosonenfusion ("VBF"). Bei Letzterem entsteht das Higgs-Boson aus zwei W-Bosonen, welche von den kollidierenden Elektronen und Positronen abgestrahlt werden.

Die Jetrekonstruktion der hadronischen Zerfälle profitiert von der hohen Granularität des Kalorimeters und vom Particle-Flow-Konzept, welches zu noch nie dagewesenen Genauigkeiten in den Zerfallskanälen mit Jets im Endzustand führt. Um eine Unterscheidung zwischen b-Jets, c-Jets und leichten Jets zu treffen und um das Signal vom physikalischen Untergrund zu trennen, werden multivariate Techniken angewendet.

Mit Hilfe eines multidimensionalen Likelihood-Fits werden gleichzeitig die Unsicherheiten der Messung der hadronischen Verzweigungsverhältnisse des Higgs sowie ihre Korrelationen durch eine Toy-Monte-Carlo-Methode bestimmt. Außerdem werden mögliche Ursachen für systematische Unsicherheiten untersucht. Dies ergibt eine Präzision von 1-2%, 14-26% und 6-10% für Zerfälle in b-Quarks, c-Quarks und Gluonen. Die genauen Werte hängen vom jeweiligen Higgs-Produktionsprozess ab.

Ergänzend zur Hauptanalyse untersucht diese Arbeit außerdem eine neue Technik, die möglicherweise sowohl die Produktionszeit als auch die Produktionskosten für die Segmentierung von Szintillatoren für ein hoch granulares Kalorimeter reduzieren könnte. Diese Technik basiert auf einem Industrieprozess der als Laserinnengravur bekannt ist. Nach der Gravur wird das Verhalten der Szintillator Prototypen analysiert. Dies wird durch einen positionsabhängigen Betastrahlen-Scan mit einer Auslese durch Silizium Photomultiplier (SiPM) realisiert. Hiermit wird die Lichtausbeute, sowie die Höhe des optischen Übersprechens zwischen einzelnen Kanälen untersucht.

Contents

I. Introduction and Theory 1

Part I.

Introduction and Theory

1. Introduction

Of all the fundamental forces known to mankind, gravitation is certainly the one familiar to us for the longest time. The naive expectation that "object fall towards the ground" when dropped is as old as human history and there is neurological evidence that our brain evolved to embed a gravity model, adapted for the particular value of the gravitational constant of our planet [1]. Obviously the intuitive description of this interaction was at first very primitive, consisting only of empirical observations and lacking any kind of descriptive model; it will take the paradigm shift of the scientific method introduced by Galileo Galilei and the ingenuity of Sir Isaac Newton in the 17th century to come up with the first formal description of a theory of gravitation.

After gravity, the next forces to be discovered were electricity and magnetism, at about the same time. Minerals with magnetic properties and static electricity were probably known since ancient times, but the first exhaustive treatise on the subjects is from Thales of Miletus around 600 B.C. It was soon discovered that the Earth itself possesses an intrinsic magnetic field: approximately from the same era are rudimentary compasses, precursory of the modern navigation devices, both from the Mediterranean region as well as from the China of the Eastern Zhou dynasty. Again, it would take more than 20 centuries to get to the unification of the two phenomena and to the formalization of a comprehensive theory of electromagnetism with the works of great thinkers of the likes of Ampere, Volta, Savart, Faraday and, ultimately, Maxwell. Despite that, it is remarkable that, already with the limited scientific progress available to the presocratic Greeks, it was intuitively deducted that electricity and magnetism must be closely related to each other.

To mark the discovery of the next fundamental force of Nature, we have to fast forward to the beginning of the 20th century. It was the early stage of a golden age for physics, that marked the introduction of entire new research fields like quantum mechanics and particle physics, which eventually lead to the Standard Model of particle physics [2]. The agreement of this scientific theory of particles' interactions with experimental observations is still remarkably consistent, despite half a century of measurements and attempts to falsify it.

At the time, thanks to the contribution of many talented physicists, consistent theories for both electrodynamics and gravitation existed. Probably the most contributions to both fields came from Albert Einstein in his *annus mirabilis* (1905) when he contributed to science with four papers on different topics, each of them possibly worth the Nobel prize. The two most notable ones, namely "*Über einen die Erzeugung und Verwandlung des Lichtes betreffenden heuristischen Gesichtspunkt*" [3], that would later win him the Nobel prize in 1921, and "*Zur Elektrodynamik bewegter Körper*" [4], introduced the notion of photons being the quantized carriers of the electromagnetic force and redefined the near-the-speed-of-light equations of motion, respectively. The latter laid down the concept of non-absolute space-time dimensions that would be one the the founding pillars for his theory of general relativity ten years later.

Despite the big achievements in modeling the problems of classical physics, theoreticians were still falling short when trying to predict the outcome of several experimental results. For example, the continuum energy spectrum of the β^- decay products was very difficult to interpret using solely the existing theoretical frame and the already known particle interactions. The visible part of a β^- decay suggested the following mechanism: $n \to p^+ + e^-$. However, in order to be able to conserve total energy and momentum in this two-body decay configuration, the emission spectrum for the electron should have consisted of a single narrow energy line. Experimental evidence showed that this is not the case and the only way to reconcile data with theory maintaining a two-body decay configuration would have been to give up something as fundamental as the laws of motion for these microscopic systems. The solution to the discrepancy came in December 1930 from Wolfgang Pauli, whom, in a very famous letter [5] addressed to the Tübingen Gauverein meeting participants, postulated the existence of a non interacting neutral particle to allow a three-body decay configuration, preserving energy and momentum conservation, and explaining the continuum energy spectrum of the beta decay. He himself was very skeptical of this approach of introducing a new *ad hoc* particle, unsupported by direct experimental evidence, and this disbelief is clearly appreciable in the very informal tone of his writing style: he begins with "*Dear radioactive Ladies and Gentleman...*" and closes with "*Oh, it's better not to think about this at all, like new taxes.*" Despite his personal reluctance, the new particle, soon baptized with the name *neutrino*, was used in 1933 by Enrico Fermi in his explanation of the beta decay, were he introduced an additional force with zero range to couple to it [6]. Fermi's interaction was the forerunner of the weak interaction, the third of the fundamental forces of physics. This interaction was later unified with electromagnetism by Weinberg, Glashow and Salam, who won the Nobel prize for their electroweak theory [7] in 1979. The massive carriers of the weak charge that give this interaction its short-range behavior, namely the Z and W bosons, were directly produced and measured 4 years later in 1983 in the UA1 and UA2 experiments at the SPS accelerator at CERN [8, 9]. Around the same years strong indirect evidences of the existence of the *gluons*, mediators of a fourth force, were observed by the PLUTO collaboration at the DORIS and PETRA storage rings in Hamburg [10], complementing the pioneering research in *hadronic deep inelastic scattering* from SLAC [11] to unveil the latest of the fundamental forces known so far: the strong interaction. It took an additional five decades to directly observe all the pieces of the puzzle and complete the collection of particles described in the Standard Model. The final piece of this rather complex mosaic, the Higgs boson, was unveiled at CERN in 2012 [12, 13]. Its intimate connection to the electroweak force and its very peculiar and unique properties complete the theoretical framework of the Standard Model.

To complete this introductory journey in the realm of the fundamental forces of nature, it is remarkable that, out of the four known so far, the one that is proving to be the most resilient to any attempt of unification is the one that has been known for the longest time: gravity. Incidentally this is also the one whom force carriers have been experimentally observed, in the form of gravitational waves, for last [14].

In the next two chapters we will focus on the technological challenges that scientists face when building the instruments needed to conduct high-energy, high-statistics physics experiments, namely particle accelerators as a reliable source of particle interactions, and detectors, i.e. the devices in charge of measuring the underlying physics of these interactions as precisely as possible. In chapter 2 the accent will be put on linear electron-positron colliders, the most likely candidate among particle accelerators for the next generation of high-energy high-precision physics experiments. Chapter 3 will detail the various subdetector components needed in a modern multipurpose particle detector with an eye of regard towards particle flow reconstruction techniques and their stringent demands for the calorimetric subsytems.

After a brief recapitulation of the physics described by the Standard Model, chapter 4 will present a theoretical introduction to the Higgs mechanism and its role in completing the electroweak sector. In the last part of this chapter, we will explain the production and decay modes of the Higgs boson, focusing our attention on the processes accessible at the first energy stage of a possible future linear e^+e^- collider.

In the second part, we will discuss the core of this PhD thesis, with chapter 5 dedicated to explain some of the analysis techniques used in the Higgs to hadrons benchmark analysis performed in chapter 6. In chapter 7, we will show how the results from chapter 6 can be used as part of the inputs of a broader investigation of the full Higgs sector, contributing to the model-independent characterization of the Higgs couplings and total width. Chapter 8 will present a detector optimization analysis for the ILD hadronic calorimeter subdetector and, finally, chapter 9 will summarize the results of this PhD work.

2. The Next Generation of Linear Colliders

In this chapter we will show the feasible options for the next generation of high-energy physics accelerators and why it is widely agreed that a linear electron-positron collider should be the most viable path towards precision measurements and why there is a compelling case for such a machine to be a strong complement to the LHC [15] in increasing the chances of new physics discoveries. We will also introduce two different ongoing design efforts for linear e^+e^- colliders, namely the Compact LInear Collider (CLIC) [16] and the International Linear Collider (ILC) [17]. These are based on the implementation of very different acceleration techniques and we will discuss the technological compromises of both, as well as their impact on the physics outcome of their respective experiments.

2.1. Brief History of Accelerator Physics

At the turn of the 20th century, a new branch of experimental physics was arising. The discovery of several kinds of natural radiation (in the form of α, β, X and γ rays) provided scientists with a new set of tools to investigate nature at the microscopic scale. In fact it was soon realized that natural radioactivity was not only an interesting phenomenon to study on its own, but also that a narrow beam of radiation emanating from a point-like source made for a very effective instrument to examine the properties of matter.

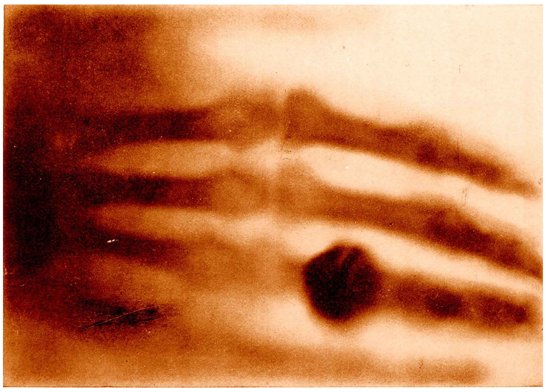

Figure 2.1.: The hand of Mrs. Röntgen: the first X-ray image, 1895 [18].

For example it took only two decades from the discovery of X-rays in Crookes tubes [19] discharges in 1875 to Röntgen's first X-ray radiography (figure 2.1) [18]. The first application of a beam of radioactive decays to investigate the subatomic scale dates back to 1909 when Wilhelm Geiger and Ernest Marsden, under the supervision of Ernest Rutherford, used the α particles from the $Bi^{214} \rightarrow Po^{214} \rightarrow Pb^{210}$ decay impinging on a thin gold-foil target [20] to test the Thomson atomic "plum pudding" model [21]. The results of the experiment were surprising: the deflection pattern of the α "projectile" was incompatible with the model proposed by Thomson:

the scattering angles were inhomogeneous and a small fraction of particles would bounce back (approximately one every 8000), not at all the almost unperturbed scenario with minimal deflections that would have been expected from "*...a number of negatively electrified corpuscles*[1] *enclosed in a sphere of uniform positive electrification...*" [21].

For the following two years, the group continued to prove their experimental results making slight variations of the experimental conditions such as the material under investigation and its thickness and, in 1911, Rutherford explained the data collected with his "planetary" model for the atom structure with a dense positively charged core, surrounded by a cloud of electrons [22]. This was probably the first major achievement of experimental particle physics and a driver for the development of the technology of particle beams.

There are in fact three main sources of ionizing particles:

- Naturally occurring and artificially created unstable isotopes: they can be extracted and purified from minerals or generated as byproducts of nuclear reactors and are, to these days, a reliable source of α, β and γ radiations. They have the advantage of being relatively cheap, transportable and, for α and γ decays, they provide extremely narrow peaks in the momentum spread of the particles emitted, but are limited in energy to at maximum a few MeV.

- Cosmic rays: mostly comprised of protons and photons, they can reach very high energies, but the flux decays exponentially with their energy and they tend to interact with the atmosphere resulting into a chain of secondary particles when reaching the detectors (see section 3.2.3). Moreover the large energy spread of the incoming particles energy and momentum is not ideal to probe with consistency the properties of subatomic structures and the vast majority of modern experiments involving cosmic rays are focused on the investigation of astronomical sources rather than fundamental mechanisms of physics (with some notable exceptions especially in the neutrino [23] and dark matter sectors [24].

- Artificial particle beams: charged particles can be accelerated and directed to a target using electromagnetic gradients. These devices have great advantages over natural source of radiation: they can produce stable beams of particles with high intensity and focus them precisely into the core of the detector system. Chaining several accelerators together allows to reach even higher beam energies and the projectile properties can be finely tuned for the physics under investigation. Moreover they are the only technology that can move away from fixed target experiments and investigate the interactions of two opposing beams. Their main disadvantages are the costs and technological challenges involved in building them, but the engineering advances of the beginning of the 20th century marked the tipping point for this technology to be more energetic, reliable and cost-effective than any natural source of radiation and, from the 1930s to present, the field of

---

[1] Thomson is referring to electrons here

particle physics is dominated by particle accelerators both when high energies as well as high intensities are required.

The first particle accelerators started to appear at the end of the 1920s [25], but the pace of technological achievements was restless: in 1928 Rolf Widerøe achieved to accelerate potassium ions to 50 keV using a 25 kV oscillator [26], the first linear accelerator (linac) ever created. In October of the same year Robert Van Der Graaf demonstrated a tabletop version of its homonym DC generator that could reach 100 kV; just two year later he was able to increase this threshold to 1.5 MV [27]. In the meantime Cockroft and Walton were perfecting their generator capable of 800 kV fields and in 1932 they achieved the task of spitting Lithium using 400 keV protons [28, 29]. It was soon clear that increasing the momentum of the projectile would have allowed to investigate shorter and shorter distances in the subatomic world and, conversely, push the boundaries of testability for the recent theoretical accomplishments of quantum mechanics. 1932 was also the year of birth of a new paradigm in particle accelerators: circular accelerators. Ernest Lawrence had the brilliant intuition to couple a magnetic field to the electric gradient to force the accelerated particles on a spiral trajectory, allowing them to pass through the accelerating electric field multiple times, thus achieving much higher energies: his 23 cm prototype cyclotron, built at University of California, Berkeley, could breach the 1 MeV barrier and a bigger, 69 cm version was put in operation in the same year, with energies in the order of 5 MeV [30, 31]. Both the linear and the circular technologies were improved further through the '30s reaching energies in excess of 100 MeV [32, 33], but all accelerators so far were accelerating light ions, protons at most.

The first electron accelerator, the betatron, was developed by Donald Kerst [34], and, in 1940, a 2.3 MeV machine was put to work. The remarkable property of the betatron is that, since trajectory is dictated by the magnetic field generated from the oscillating current in a coil, the electrons can be held on a closed circular path. Moreover, the electron momentum is bound to the radius of the trajectory as follows. The Lorenz force that the electron witnesses is:

$$F_L = q(\mathbf{v} \times \mathbf{B}) = q\omega r B \tag{2.1}$$

for perpendicular field **B** and velocity **v**. The centrifugal force on the electrons is:

$$F_C = \frac{mv^2}{r} = m\omega^2 r \tag{2.2}$$

and, reminding that $p = \gamma m_0 v$, at equilibrium we have that:

$$p = qBr = 0.3zBr \tag{2.3}$$

for the units p[GeV/c], B[T] and r[m]. So the beam of electron, at the so called cyclotron frequency

$$\omega_0 = \frac{qB}{\gamma m_0} \tag{2.4}$$

has a well defined momentum. On this respect, it is interesting to note that the cyclotron frequency depends on the particle momentum via the relativistic Lorenz factor γ, but this is very susceptible to the particle mass. For example, if we allow for a 1% deviation from the optimal ω_0, a proton can be accelerated to a kinetic energy of $\sim 10\,\mathrm{MeV}$, whereas an electron only reaches $\sim 5\,\mathrm{keV}$. This is the reason why cyclotrons, with their fixed magnetic field, are not suited for accelerating electrons. There is one additional key property of betatrons, namely *radial focusing*, a phenomenon experienced by particles in the beam that, due to fluctuations or initial conditions, have slightly different momenta and are not following the nominal trajectory. For radii larger (shorter) than the equilibrium, the Lorenz force F_L is greater (smaller) than the centrifugal force. This produces the radial focusing, i.e. a passive feedback mechanism that forces particles back to their nominal path. This results in big benefits in terms of efficiency, since the fraction of accelerated particles that don't contribute to the beam is minimized. More formally, we can introduce the magnetic field index n, defined by the following differential equation:

$$\frac{\partial B}{\partial r} = -n\frac{B_0}{r_0} \tag{2.5}$$

where B_0 and r_0 are the magnetic field and radius at the nominal trajectory. For n > 1, the field would exert a too-high horizontal correction, maintaining an ever increasing oscillatory disequilibrium or, in short, defocus. Similarly, if n < 0, the same would happen for the axial stability of the beam. The in-between situation of 0 < n < 1 is known as *weak focusing* and a careful design of the geometry of the magnet and the magnetic gradients can achieve this configuration. The oscillations around the stable orbit can be inferred by taking the first order expansion of the solution of equation 2.5, obtaining

$$\begin{aligned} \omega_z &= \omega_0\sqrt{n} \\ \omega_r &= \omega_0\sqrt{1-n} \end{aligned}$$

for the axial and radial components, respectively.

Before proceeding, it is useful to remind the three key parameters of particle accelerators:

Energy - As already mentioned, the capability of probing short distances grows with the available energy. In order to resolve the features of a nucleus for example, whose size is in the order of 10×10^{-10} m, the Coulomb potential of the electron cloud must be overcome, a task achievable with energies in the order of few eV. To break the interaction at the level of the atomic nucleus, four orders of magnitude smaller than an atom, the energies are in the MeV range. Deep inelastic scattering on nucleons like a proton, able to evidentiate its quark components at distances below 10^{-15} m, requires energies of the order of several GeV and above. It is no wonder then, that the technological race to achieve higher and higher energies in particle accelerators continued with an exponential growth over the decades. In this regard, particle beams have a big advantage over their natural counterparts: not only can a beam be used against a so-called fixed target, but two beams can be tuned to intersect each other from opposite directions, allowing for much greater energies in the center-of-mass reference frame. In fact, it is possible to use the relativistic laws of motion to calculate the energy gain of a two-beam collider versus a fixed target experiment. Let's assume the following two scenarios (where we use the widespread convention of *c = 1* and the reference frame of the four-vectors is the lab-frame):

Fixed target	Two-beams symmetric collision
$p_1^\mu = (E_1, \mathbf{p}_1)$	$p_1^\mu = (E_1, \mathbf{p}_1)$
$p_2^\mu = (E_2, 0)$	$p_2^\mu = (E_1, -\mathbf{p}_1)$

The Lorentz-invariant Mandelstam variable S is defined as follows:

$$S = (p_1^\mu + p_2^\mu)^2 = m_1^2 + m_2^2 + 2(p_1^\mu p_2^\mu)^2 \approx 2(p_1^\mu p_2^\mu)^2,$$

where the approximation accounts for the fact that the rest masses of the scattering particles can usually be neglected when compared to the high momentum generated in a particle accelerator. Therefore, the center of mass energy $\sqrt{S}$ will be:

Fixed target	**Two-beams symmetric collision**
$\sqrt{S} = \sqrt{2 \times E_1 m_2}$	$\sqrt{S} = \sqrt{2E_1E_1(1 - \beta_1\beta_2\cos\theta)} \approx 2E_1,$

where $\beta_{1,2}$ are the beta-functions, related to the transverse size of each beam. The approximation on the right hand side comes from the fact that, for relativistic particles, $\beta_{1,2}$ is close to 1 and the angle θ for colliding beams is 180 deg. It is apparent that, for reaching high energies, the two-beam setup linear energy growth is always at an advantage compared to the sublinear one of a fixed target experiment.

Luminosity - This is a measure of the number of particles collisions per unit area and unit time available in the particle beam. In a collider system, for beams structured in bunches of particles, the instantaneous luminosity is defined as follows:

$$\mathscr{L} = f\frac{N^2}{S}, \tag{2.6}$$

where f is the collision repetition rate, N is the number of particles in a bunch (the square represent all possible combinations of a particle of the bunch to interact with a particle of the crossing bunch) and S is the effective surface of the beam profile. In a simple gaussian profile beam scenario, S is:

$$S = 4\pi\sigma_x\sigma_y. \tag{2.7}$$

The instantaneous luminosity is a very useful parameter, especially in tandem with the cross-section σ of a physical process, a quantity defined in units of area that expresses the probability for that particular process to take place. Luminosity and cross-section are related, for a particular mechanism i, by the following equation:

$$\mathscr{L} = \frac{1}{\sigma_i}\frac{dR_i}{dt}. \tag{2.8}$$

Therefore R_i, the number of events expected for the process i, equals to:

$$R_i = \sigma_i \int \mathscr{L} dt. \tag{2.9}$$

The time integration of the instantaneous luminosity is often referred to as the integrated luminosity, and gives, in a single number, a pretty accurate overview of the physics potential of a collider experiment.

Emittance - This parameter gives a measure of the quality of a particle beam. It gives a quantitative overview of the spread in the phase space of the particles composing a beam, thus their momentum and position. Much like in the case of focusing, it is possible to separate the emittance into two components: longitudinal emittance and transverse emittance. The longitudinal component can be defined as follows [35]:

$$S = \frac{1}{\omega_{rf}}\pi\left(\frac{v}{c}\right)\Delta\phi^2\sqrt{\frac{eVE_s}{2\pi h|\eta|}}, \tag{2.10}$$

where $\Delta\phi$ is the phase oscillation of the beam around the optimal phase, E_S is the target energy that a particle on the ideal path would have, V is the amplitude of the potential in the accelerating cavity and η is the so called *slip factor*, a quantity that accounts for the particular geometry and design of the device under investigation. This gives an estimate of the energy spread of the particles in the beam.

And the transverse emittance:

$$\epsilon = \frac{6\pi\sigma^2 - D^2\left(\frac{dp}{p}\right)^2}{\beta} \tag{2.11}$$

where σ is the beam width and D and β are the values of the dispersion function and the beta function at the measurement point, respectively. Since the emittance depends on the particle momentum, higher energy beam will intrinsically have lower emittance values.

For this reason, it is sometimes useful to adopt the *normalized emittance*, which takes into account the relativistic corrections, allowing to compare different setups independently of their kinematics:

$$\epsilon^* = \epsilon\gamma\frac{v}{c}. \tag{2.12}$$

Finally, the instantaneous luminosity can be formulated in terms of emittance via the following expression:

$$\mathscr{L} = f\frac{N^2}{4\epsilon\beta^*}. \tag{2.13}$$

The advances in accelerator physics had a sudden halt during World War II, especially after the United States entered the conflict in 1941. Research in both Europe and North America had shifted abruptly to military applications in particular in the U.S. where the vast majority of talented theoretical and experimental particle physicists begun the development of the first atomic bomb: the Manhattan Project. One technology that was developed shortly before the war and was continuously developed through it due to its applications in radar systems was the klystron [36]: the first amplifier for radiofrequency (RF) signals capable of outputting high energies in the microwave domain.

Right at the end of the war, the renovated focus to fundamental research and the developments in RF technology allowed William Walkinshaw in Malvern, and independently William Webster Hansen and his team at Stanford, to build the first electron linear accelerators (linacs) in 1946 [37]. Simultaneously, on the circular accelerator side, ideas to overcome the limitations of the fixed magnetic field of the cyclotron started to develop. In particular, Vladimir Veksler in 1944 [38] and independently Edwin McMillan in 1945 [39] introduced the concept of phase stability and came to the conclusion that it was possible to decouple the forces responsible for increasing the beam momentum and keeping the particles on curved trajectories by separating the subsystem generating the bending magnetic field and the one imparting higher kinetic energy to the beam. This way it was possible to modulate the magnetic field to account for the decrease in cyclotron frequency dictated by the relativistic motion of particles (as in equation 2.4):

$$B'(t) = \gamma(t)B_0 \rightarrow \omega = \frac{qB'(t)}{\gamma(t)m_0} = \frac{qB_0}{m_0} = constant \tag{2.14}$$

This achievement was put into operation for the first time in 1945 at the 8 MeV electron synchrotron accelerator that McMillan, Goward and Barnes derived from a 4 MeV betatron [40]. Later on, in 1952, Sir Marcus Oliphant, whose idea for a synchrotron accelerator dates back to a memo written in 1943 that was classified due to the war, succeeded in building the Brookheaven's Cosmotron 2.3 GeV accelerator, the first proton synchrotron and the first multi-GeV accelerator ever created [41]. The crucial aspect of these machines, as the name suggests, is the remarkable time precision needed to synchronize the frequency swipes in the alternated current of the coils generating the magnetic field with the orbits of the ever-increasing relativistic particles in the electron beam. This precision was achievable solely thanks to the acquired mastery in RF cavities and technical ingenuity such as Oliphant's idea to cool the non-linear inductor of his synchrotron in a mercury bath (figure 2.2).

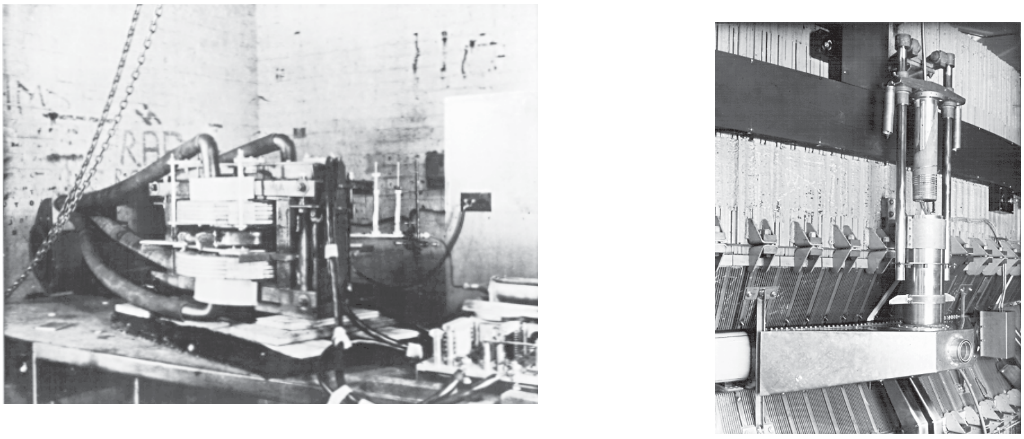

Figure 2.2.: On the left, The 4 MeV betatron converted to an 8 MeV synchrotron. On the right, Oliphant's non-linear inductor withdrawn from its mercury bath. Figures and caption from [42].

After the introduction of the concept of phase stability, another cornerstone of modern accelerator was discovered at BNL in 1952 by Ernest Courant, Stanley Livingston and Hartland Snyder: *strong focusing*[2] [44, 45]. Strong focusing is a technique to converge particle beams that, unlike weak focusing, relies on $|n|$ values much greater than one (see equation 2.5). This translates in practice into strong alternating magnetic fields orthogonal to each other and always perpendicular to the beam axis. Each field tends to focus the beam in one direction and defocus it in the perpendicular direction. Much like in optical lensing, the alternation of diverging and converging fields of similar magnitude leads to a net reduction of the beam emittance and oscillations. This allows, among other things, to have smaller magnets, smaller beam pipes and consequently more efficient and higher quality vacuum. For a comparison, the 10 GeV Synchrophasotron inaugurated in 1957 in Dubna near Moscow, one of the last machines to use the weak focusing technique, had beam pipes inner dimension of 55×110 cm^2 and a total magnet weight of 36000 tonnes [46]. Conversely the CERN alternating gradient Proton Synchrotron (PS), designed with the new focusing scheme, smashed that high energy record only two years later in 1959 [47], with a 24 GeV proton beam enclosed in a 7×14.5 cm^2 beam pipe and a total material budget for the magnet of only 3200 tonnes [48]. One year later, in 1960, scientists and engineers in Brookhaven finalized a 33 GeV strong focusing accelerator, the AGS [49]. The competition for the highest energy machine was heated and the pace at which progress was made was astounding. Each new accelerator was

---

[2] Another physicist, Nicholas Christofilos came to the same idea in 1949, but did not publish his results because of filing errors. [43]

opening the door to the investigation of ever new physical processes, often allowing for discoveries worth the Nobel prize. Up to this point all machines were designed for fixed-target experiments, but in 1961 a new quantum leap was about to take place: at the LFN laboratory in Frascati, Italy, the Austrian physicist Bruno Touschek proposed to inject positrons and electrons in the same storage ring in opposite directions to study their collisions. The first storage ring, Anello Di Accumulazione (ADA) [50], was just a feasibility prototype with 250 MeV of energy per beam, but it opened the doors to a paradigm shift in accelerators design, allowing for the center-of-mass energy to scale linearly with the energy of the colliding beams energy rather than with the square root as it had been until then. Later on in 1969, ADONE [51], a 1.5 GeV per beam collider intended for scientific research was installed at the same location. Unfortunately, the machine reference energy was just 3% shy of the J/ψ meson resonance, as it became apparent in 1974, when Samuel Ting's group at BNL and Burton Richter's team at the SPEAR collider in Stanford independently reported the discovery of the new meson [52, 53]. The Stanford facility had, in the meantime in 1968, confirmed the existence of an internal structure of protons and neutrons, using the deep inelastic scattering of electrons on nucleons, and proved the quark model that Gell-Mann and Zweig had proposed only few years before [54, 55]. In the same year Simon van der Meer invented the stochastic beam cooling [56], a technique to actively increase the emittance of a circular accelerator without loosing particles, allowing in particular for a very efficient cooling of antiproton beams improving their luminosity. This would prove to be a key component of the 540 GeV Sp$\bar{\text{p}}$S collider at CERN, that would lead to the discovery of the W and Z boson at the UA1 and UA2 experiments [8, 9].

On the linear accelerator side, in 1989 the SLC, the first electron-positron linear collider, started operations at SLAC again under Ritcher's supervision; it consisted of a 2 mile long linac stage to accelerate beams of both polarities into two storage rings that would serve several experiments. The possibility to serve highly polarized beams and the micro-sized beam spots at the interaction point allowed for high statistic precision measurements, e.g. in the Z boson parity violation sector [57].

The introduction of the cryogenic superconductive magnet technology allowed to step up the center-of-mass energy for proton machines. The first one to adopt this technology on a large scale was Tevatron, the 6.3 km ring at FNAL that breached for the first time the TeV energy barrier in 1983 [58]. In Europe, in the meantime, the projects for a new e^+e^- circular collider had begun: the Large Electron Positron collider (LEP) [59] spanned over a circumference of 27 km across the border between Switzerland and France at CERN. It started its physics program in 1989 with a center-of-mass energy of 91 GeV, around the Z boson resonance. It was further upgrade to reach energies of 209 GeV and run until 2000 with the hope to find the elusive Higgs boson. Unfortunately the energy was not quite enough to reach the ZH peak (see chapter 4). In 2000 the machine was shut down and dismantled to make room for the Large Hadron Collider (LHC) [15] a 14 TeV proton-proton and ions accelerator[3] that was completed in 2008 and is as of these

---

[3] because of a major accident in the ring superconductive magnets due to some faulty electrical joints, the

days the forerunner of accelerators with respect to the high energy frontier. In Juli 2012, the announcement that the last missing piece of the Standard Model puzzle, the Higgs boson, was discovered at the ATLAS [13, 60] and CMS [61, 62] experiments, marked the latest of a very long series of successes that almost a century of particle physics and accelerator technology made possible.

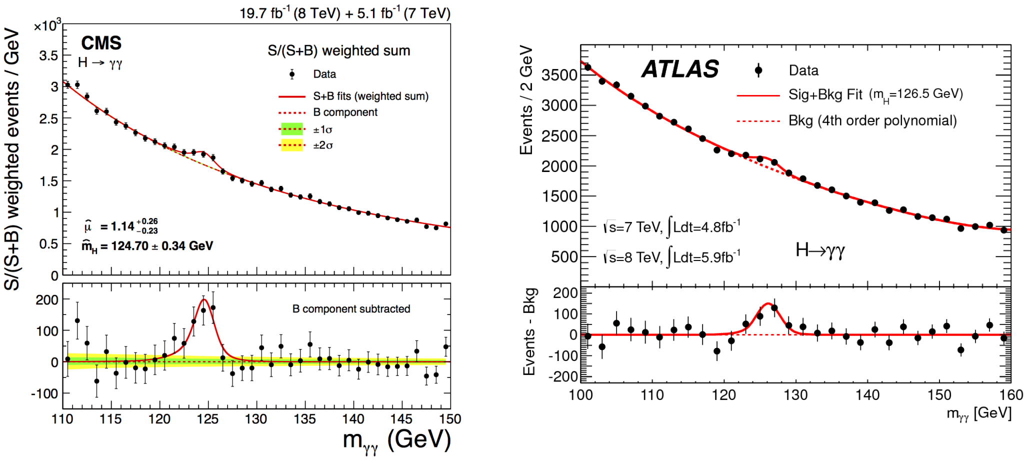

Figure 2.3.: The Higgs boson discovery in the diphoton channel at the CMS [62] and ATLAS experiments [13].

2.2. Hadrons vs Leptons

We have seen in the previous section that one of the main focuses in the advancement of accelerators technology was to achieve higher and higher center-of-mass energies to be able to push the frontiers of investigation of the theoretical models for particle physics. The attentive reader might have noticed that, for the vast majority of accelerators, one of two very different kind of *projectiles* was chosen: either hadrons, like protons and antiprotons, as in the PS, Tevatron and LHC, or leptons, like electrons and positrons, as in ADONE, SLC and LEP. Moreover, the energy achieved in hadron machines has always been consistently higher than the one obtained in lepton accelerators of the same generation, a trend still occurring nowadays. In fact, LEP, the 25 year old e^+e^- collider, still holding the center-of-mass energy record for this kind of accelerators, is one order of magnitude below its hadronic counterpart Tevatron, and even two orders of magnitude below the LHC. One might wonder why have lepton machines been developed for over seven decades despite the considerable energy penalty and why is it not possible to achieve the same performances for leptons as it is for hadrons. The explanation resides in the fact that hadron machines have three major drawbacks when it comes to physics experiments, whereas leptons pose a substantial technological disadvantage that limits

---

accelerator was soon shut down after commissioning for a 2 year maintenance program, after which it resumed operations at 7, 8 and finally 13 TeV.

the effectiveness of most accelerator designs. In this section we will go through the positives and negatives of both.

Let's start with a reminder of the interactions of a charged particle in a magnetic field. Lorenz law (2.1) tells us that a charged particle in a magnetic field that is not parallel to its velocity vector, witnesses a force and, therefore, an acceleration. To conserve the total momentum, the electromagnetic field needs to *recoil*. This recoil takes place in the form of emission of photons, i.e. synchrotron radiation, from the charged particle on the force/velocity vector plane perpendicular to the magnetic field. It is possible to compute the total power output of these photons using the Larmor equation, here computed in the laboratory frame for relativistic electrons and a magnetic field perpendicular to their motion vector [35]:

$$P = \frac{e^2 a^2 \gamma^4}{6\pi\epsilon_0 c^3} = \frac{e^2 c \gamma^4}{6\pi\epsilon_0 \rho^2} = \frac{e^4 B^2 E^2}{6\pi\epsilon_0 m_0^4 c^5} \tag{2.15}$$

where the acceleration a has been replaced with the centripetal acceleration c^2/ρ of a relativistic electron. It is apparent that the power dissipated grows quadratically with the magnetic field B and the beam energy E, but depends on the inverse fourth power of the particle's rest mass m_0. It takes 1836 electron masses ($\approx 511\,\mathrm{keV}$), to match the rest mass of a proton ($\approx 938\,\mathrm{MeV}$). This means that, maintaining all other parameters unchanged, the power dissipation for electrons in a bending magnet will be 13 orders of magnitude higher than that for protons. Since in circular machines particles get accelerated over tens of revolutions in the RF cavities, the energies achieved at LEP are at the limit where any additional power pumped into the beam would be dissipated by synchrotron radiation. The alternatives are to build accelerators with larger radii or move to more massive leptons. There are two known leptons more massive than the electron: τ and μ leptons. Tauons are unusable due to their extremely short half-life of only $2.9 \times 10^{-13}\,\mathrm{s}$. Muons, with a rest mass of 105.7 MeV and a mean lifetime of $\approx 2\,\mu\mathrm{s}$, seem more technically feasible and a lot of research [63] and effort [64] has been put into investigating a circular muon collider, but the technology is not quite there yet. Circular machines larger than the LHC are under study [65, 66], but there are costs and technological limitations to the achievable size of such colliders and none of the proposed solutions would be able to fill the existing gap with proton accelerators. The only practicable solution to accelerate electrons and positrons is to get rid of the synchrotron radiation altogether, and thus focus on linear colliders. In the next section we will discuss two designs currently under investigation for this option.

Let's now have a look at the limitations of experiments carried out with hadron machines, and why lepton machines are, from the experimental research point of view, much nicer to work with. As already pointed out in the previous section, protons, and hadrons in general, are not fundamental particles as leptons are. They are bound states of even smaller constituents of matter: valence and sea quarks, and gluons [55]. Since at the energy regimes reached by modern hadron-collider experiments all physical processes take place between fundamental particles, when two hadrons are collided together the actual interaction takes place at the so called parton level. At this scale, a combination of valence quarks and gluons from the two hadrons, usually one for each side, is responsible for the complex final state observed by the experimental setups studying the collisions. This has several fundamental implications: first, the exact composition of the initial state of an event is known only at a statistical level, with several possible configurations concurring to create the same signature in the detectors. Second, the momentum distribution of the hadron constituents is not well defined and anyway much lower than the total momentum of the hadron. This means that:

- the kinematics of the initial state can’t be defined, at least along the beam axis, giving one less degree of freedom to constrain the experimental results and disallowing the possibility to perform threshold scans of resonances of interest;
- the interaction takes place at only a fraction of the nominal beam energy, on average $\approx 1/6$ of the total energy for valence quarks interactions and much less for interactions involving gluons;
- since the kinematics of the two interacting partons are not equal, there is a big chance for the collision reference frame and the laboratory reference frame to differ, giving the event a relativistic boost along the beam direction. This has to be accounted for not only when analyzing the data, but also in designing the geometrical acceptance of the detectors, that need to cover the regions of high pseudorapidity, i.e. the forward regions very close to the beam pipe, much more precisely than at a lepton collider;
- the partonic fractions that constitute composite particles but do not participate to the interaction of interest, still produce very visible signatures in the experimental setup, usually referred to as *underlying events*, that need to be accounted for and filtered out when analyzing the data sample.

For all these reasons, lepton colliders still maintain an important role in particle physics and the two kinds of accelerators are usually considered to be complementary: high energy hadron machines such as the LHC swipe the energy frontier looking for direct observations for new particles and new physics in a region of the phase space not accessible otherwise, while lepton machines can be used for higher precision measurements of the particles quantum numbers, some of them not accessible at all with composite projectile.

2.3. The ILC and CLIC Concepts

In the previous section, the case was made for pushing the boundaries in lepton colliders beyond what was achieved at LEP. It was also pointed out that, due to synchrotron radiation, the limits for circular e^+e^- accelerators are not far away from what LEP provided. For these reasons, the most credible designs for the next generation of colliders, and the only capable of reaching the TeV center-of-mass frontier with leptons, are linear colliders.

Two projects are at an advanced level of study: the International Linear Collider (ILC) [67] and the Compact LInear Collider (CLIC) [68], with center-of-mass energies up to 1 and 3 TeV, respectively.

The design for such colliders consists of four fundamental components, each of which is crucial for the achievement of the stringent specifications necessary for the next generation of high energy physics experiments.

Positron source: contrary to a circular accelerator, in a linear collider each particle bunch crosses the interaction point only once. Therefore, to maintain the high luminosity requirements, it is necessary to have a steady source of electrons and positrons. Electrons are relatively simple to obtain: by exploiting the photoelectric effect, they can be extracted from a cathode using a high intensity beam of light. By using a polarized light source, such as a laser beam, the electrons' polarization can be selected as well. Positrons, on the other hand, are more difficult to obtain in high quantities. Natural β^+ emitters are simply too weak to produce the high-intensity stream of particles needed. For this reason, a completely different approach is used: the electron beam is accelerated to an optimal threshold and pointed at a thin layer of absorbing material. This initiate a so-called *electromagnetic shower*, a phenomenon that will be explained in more detail in section 3.2.2. For the purpose of this explanation it is sufficient to say that such process produces a cascade of particles, including positrons. These can be steered by means of intense electromagnetic fields, and collected into a beam that is not yet ready for collisions, given their relatively high momentum spread.

Damping rings: the purpose of damping rings is to minimize the momentum and energy spread (and thus, the emittance) of a particle beam. This is achieved by constraining the particle beam onto a circular path where, by successive emission of synchrotron radiation and re-acceleration in radiofrequency cavities, it is forced on a path that dampens the transversal and longitudinal oscillations. This phenomenon, sometimes referred to as *cooling*, harmonizes four-momenta of the particles in the beam and is of particular importance for the positrons' beam, given the high variance in momentum with which they are produced in the positron source.

Main Linacs: these are the primary sources of acceleration for the e^+e^- beams and consist of a progression of carefully aligned and synchronized RF cavities that accelerate the beams from a few hundred MeV all the way up to half of the center-of-mass energy. Since length is the limiting factor of all modern high energy physics accelerator, the highest energy achievable is directly proportional to the acceleration gradient obtainable in the RF cavities. As we will see in the next paragraphs, this is also one of the main points in which the ILC and CLIC design differ the most.

Final Focus: after being accelerated for many kilometers, the two colliding beams need to be pointed at each other, so that they cross precisely at the interaction point. This is achieved by a set of magnetic lenses, placed after the main linacs, that steer the beams accurately to the interaction region. To further increase the luminosity, the beams' lateral dimensions are shrunk to a nanometric scale. This imposes an additional challenge to the mechanical tolerances of such magnet multipoles.

Before we can summarize the state of development of both accelerators, along with their peculiarities, it is convenient to conclude this overview of the most prominent design features with one of the main technological distinction between the ILC and CLIC colliders, i.e. the choice of normal-conductive versus superconductive RF cavities for the main linac, and to briefly point out the effects and compromises that this has on the quality of the beams delivered to the interaction point.

The need to reach, at the latest energy stage of CLIC, a center-of-mass energy that is three times greater than that of ILC, while keeping the total length of such machines comparable, is bound to higher accelerating gradients. These in turn require the higher frequencies to operate with an acceptable mean time between breakdown arc discharges in the cavity. The high frequencies, coupled to the sheer power density required to drive the main beam at CLIC produce quite intense magnetic fields on the surface of the RF cavities. This places a strict constrain on the possibility to implement superconductive cavities. In fact there is a critical threshold for the magnetic field of a superconductor of the first kind that goes as follows:

$$H_C(T) \sim H_C(0)\left(1 - \frac{T^2}{T_C^2}\right) \tag{2.16}$$

where T is the temperature $H_C(0)$ and T_C are the critical threshold at 0 K (quantity that depends on the material) and the critical temperature, above which the superconductor becomes normally conductive again, respectively. While the technology of superconductive materials improves, with new alloys and, possibly in the future, surface coatings to minimize the surface resistance of superconductors [69], there is at the moment no material that suits the CLIC requirements, thus making the normal-conductive option the only choice. This has quite an impact on the design of many other accelerator parameters: the low, but still appreciable resistance of the cavities implies that their conversion efficiency is quite low, with the injected energy rapidly dissipated by ohmic losses. For this reason, the length of each microwaves pulse must be minimized, to avoid wasting too much energy and to keep the cooling manageable.

Short pulses directly translates in short time windows available to accelerate bunches in the main beam; this means that, to maintain a high luminosity, the bunch spacing must be shortened, to fit more bunches in one pulse. This is the reason why the bunch spacing at CLIC is a mere 500 ps apart, three orders of magnitude below that of ILC, which, as we will see in the next chapter, poses a great challenge for the detector triggers and readout systems.

2.3.1. ILC

ILC is an e^+e^- collider proposed to be hosted in the Kitakami Mountains in Japan across the prefectures of Miyagi and Iwate. For what concerns the maturity of the feasibility studies, the R&D phase for the accelerator is, for the large part, concluded with a technical design report published in 2013 [17]. As introduced in the previous section, the acceleration technology is based on cryogenic superconductive RF generators for the main linacs, a well-established and well-tested choice that is capable of producing, by means of klystrons microwave generators, gradients in excess of 30 MV/m.

The particular design chosen for the ILC, namely the 1.3 GHz *"L-band"* superconducting niobium nine-cell cavities, has been already produced in volumes for another accelerator: the free-electron laser facility (FLASH) at DESY [72]. To maximize the physics output of such an endeavor as well as distributing the construction costs over a longer period of time, a staged design was chosen for the implementation of ILC. At present, the machine reference staging scenario (H-20 [73]), is the following: in the first construction stage, the target is to achieve the nominal center-of-mass energy of 500 GeV. Such a machine would have the option to be operated at *"low-energy"* scenarios with center-of-mass energies between 250 and 350 GeV, for precision measurements in the Higgs sector and also to perform a top mass threshold scan. Successively, in a second stage, the collider could be upgraded with longer linacs and additional RF cavities capable of higher gradients, in order to reach a 1 TeV center-of-mass energy in the interaction point. To accommodate the linac, the beam optics and the dumping rings, such a machine would necessitate of a tunnel of 30 to 50 km, the actual length depending on the energy stage. Since, unlike circular colliders, a linear collider can't reuse particle bunches multiple times, the strategy to keep an high instantaneous luminosity in excess of 10^{34} cm^{-2} s^{-1} resides in the exceptionally small beam profile at the interaction point: depending on the center-of-mass energy, the horizontal beam size would span between 335 and 729 nm, whereas the vertical size would be between 2.7 and 7.7 nm [67]. Table 2.1 summarizes the key parameters of the several stages of the accelerator.

Finally it is interesting to note that the bunch crossing rate is not homogeneously distributed in time, but has a structure: the repetition rate of the main linacs varies from 5 to 10 Hz. This rate is mostly limited by the damping time, i.e. the time the beams take

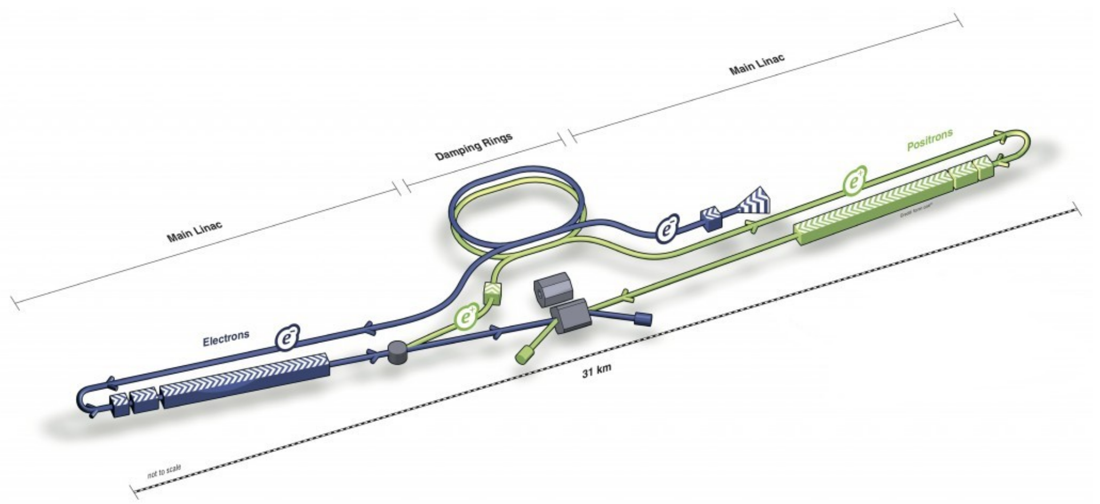

Figure 2.4.: Schematic view of the International Linear Collider design. Figure from [70].

Figure 2.5.: 9-cell superconductive niobium 1.3 GHz radiofrequency cavities for the DESY FLASH linac. The same technology and design is proposed for the ILC main linacs. Figure from [71]

Center-of-mass energy	GeV	250-350	500	1000(B)
Collision rate	Hz	10	5	4
Number of bunches		1312	2625	2450
Bunch separation	ns	554	336	336
Linac Average Gradient	MV/m	31.5	31.5	39.2
Estimated AC power	MW	129	204	300
Luminosity	$\times 10^{34}/\mathrm{cm}^{-2}\mathrm{s}^{-1}$	31.5	31.5	38-39
Horizontal Beam Size	nm	729	474	335
Vertical Beam Size	nm	7.7	5.9	2.7

Table 2.1.: Recapitulation of the principal parameters' settings for the ILC for various center-of-mass energy configurations [67].

to reach the desired emittance in the damping rings. Therefore, every 100 to 200 ms, a train of few thousands packets is injected within a 1-2 ms time frame (this quantity is constrained by the quality factor of the cavities and power consumption considerations) with an even spacing of a few hundred ns among packets. This peculiar configuration implies that the duty cycle of such a collider is a fraction of a percent. By carefully designing the readout electronics to power cycle very fast, this time structure can be exploited: the readout is switched on shortly before the colliding bunch-trains reach the *interaction point* and switched back to a lower energy state immediately after the bunch-trains pass. This setup allows to improve dramatically the power efficiency of the readout electronics, which in terms leads to much milder requirements on the readout cooling loops, a feature particularly useful when designing the innermost components of a detector whose accuracy, as we will see in the next chapter, is very susceptible to the total material budget used.

2.3.2. CLIC

The *Compact LInear Collider* (CLIC) [16] is a linear e^+e^- collider concept, proposed to be built at CERN for the *post-LHC* particle physics era. In this section we will give an overview on its key properties and some of the novelty technological advancements that would make this accelerator unique.

Starting from the acceleration scheme, the CLIC concept adopts a design that has no precedents. To generate the alternating electric gradient inside their acceleration cavities, almost all modern particle colliders utilize microwaves produced by the Klystron devices introduced in section 2.1.

To do so, modern state-of-the-art Klystrons, capable of producing microwaves in the GHz band and with radiative outputs in the order of tens of MW, are being developed and tested. As we have seen in the previous sections, though, the normal-conductivity nature of the CLIC RF cavities require very short pulses to overcome the ohmic losses, at which point the Klystron technology is past its optimal operation regime, resulting in a significant efficiency drop. For this reason, the RF cavities developed for CLIC operate with a completely different approach. The system is based on a two-beam scheme with a *low-energy, high-intensity* driver beam, operating at an energy of 2.38 GeV and a current of 100 A, driven through a *power extraction and transfer structure (PETS)*, whose job is to convert the beam energy into microwaves and guide those to the RF cavities of the main linac beam.

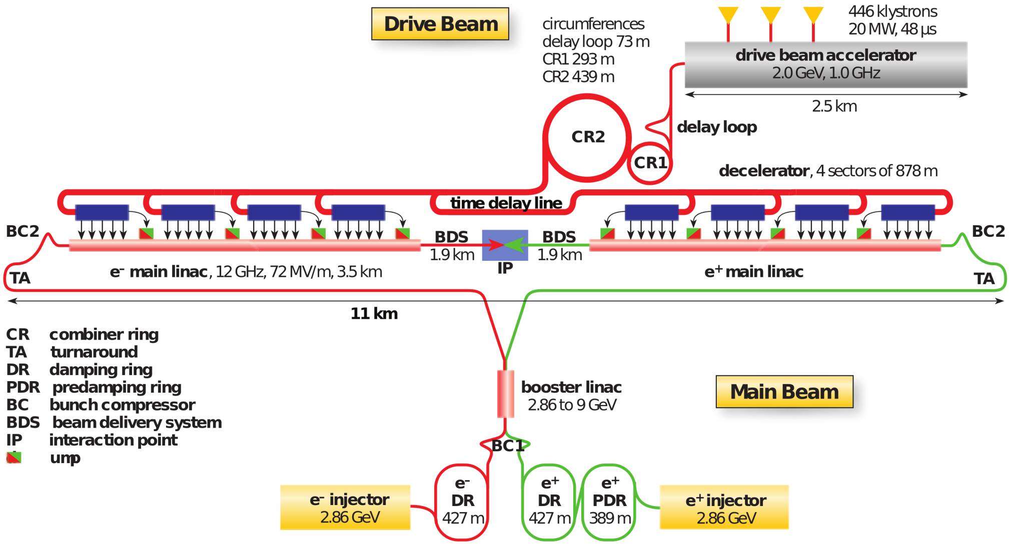

Figure 2.6.: Schematic view of the Compact Linear Collider (CLIC) injection and acceleration scheme. A low-energy, high-intensity driver beam is used to produce the RF microwaves to accelerate the main beam with gradients up to 100 MV/m. Figure from [74].

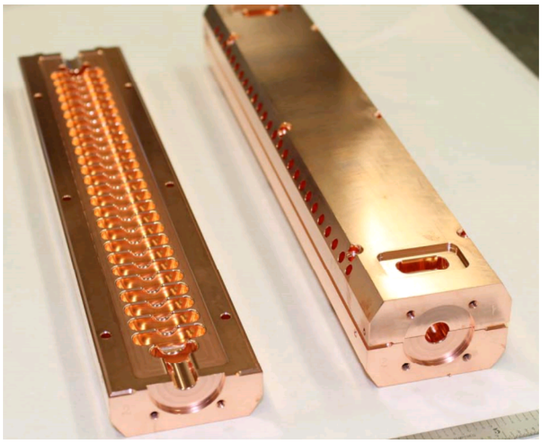

Figure 2.7.: Copper X-band RF cavity prototypes for CLIC [75]. This is one of the several design under investigation by the CLIC/CTF3 group for the main linac accelerator. Figure from [74].

This is the *low-intensity, high-energy* primary beam, that witnesses accelerating gradients in the order of 70 to 100 MV/m (depending on the energy stage and costs and efficiency optimizations) in the 12 GHz *X-band* non-superconductive copper RF cavities. Given the novelty of such acceleration technique, R&D on the cavities and operations is ongoing at the CTF3 facility at CERN [76]. The aim is to find the optimal cavity design that maximizes the production yield with the necessary operational requirements, both in terms of high accelerating gradients, as well as in the high mean time between arc discharges in such cavities, events that quickly deteriorates the beam quality and the life expectancy of the linac modules. Moreover, since all the RF cavities receive the sinusoidal microwaves from a single driver beam, and given the relatively short longitudinal window to properly inject in phase the electrons and positrons from the main beams into a chain of consecutive accelerating cavities, an additional test setup, namely the *Two-beam Test-stand (TBTS)* [77], has been devised to investigate all the parts involved into the creation of the accelerating gradient, from the reliability of the driver beam to the quality of the main beam.

The status of such studies is at quite an advanced state, but the time schedule for building a complete collider with this technology is definitely longer than that of an accelerator like ILC. It will certainly take a few more years to optimize the prototypes and then to transfer the necessary knowledge from a short-batch prototype production line to a large-scale industry endeavor[4].

Now that this novel acceleration scheme has been introduced, it is interesting to mention a few foreseen figures of merit for a particle collider like CLIC. Similarly to ILC, CLIC is also planned to be built in stages. At first, a *low-energy* center-of-mass energy stage of 350 to 420 GeV (depending on the particular design choice and different compromises on its physics reach [78]) would be operated for roughly half a decade (not including the commissioning period) to collect a total integrated luminosity of 500 fb^{-1}. Coincidentally, the main analysis of this thesis work, presented in chapter 6, is based on simulated events from this low-energy stage scenario. Successively the accelerator would undergo two additional center-of-mass energy stage upgrades: 1.5 and 3 TeV,

---

[4] The current estimate for the full CLIC design is to have over 20000 two-beam linac modules, for a total of almost 80000 PETS components.

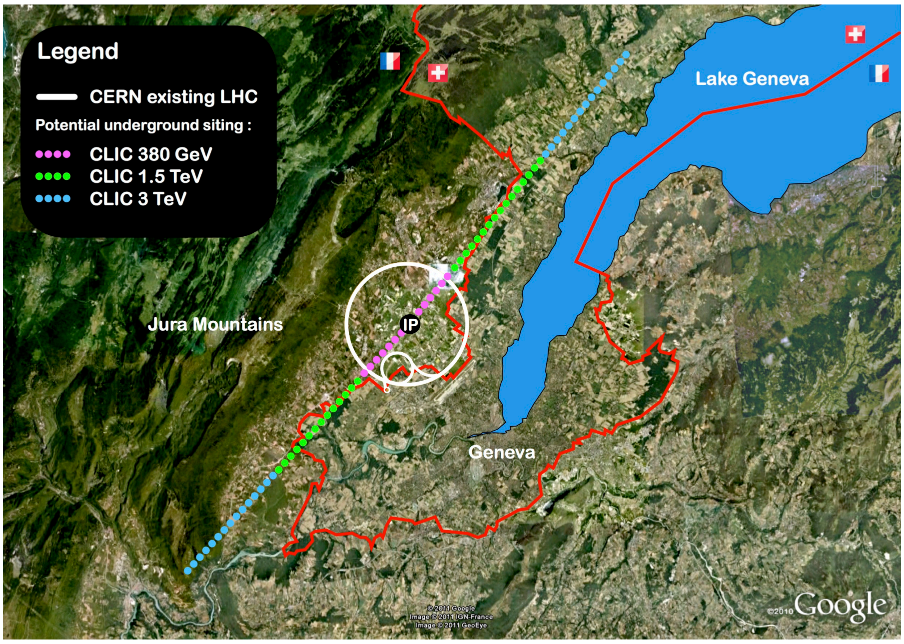

Figure 2.8.: Schematic representation of the CLIC site and its multi-energy staging at CERN. Figure from [74].

operated for a total integrated luminosity of 1.5 and 2.0 ab^{-1}, respectively. For each of the stages, an electron polarization of up to 80% is foreseen. Table 2.2 reviews the main parameters for each stage of the collider. From the table, two sets of parameters are

Center-of-mass energy	GeV	350 - 420[5]	1500	3000
Collision rate	Hz	50	50	50
Number of bunches		352	312	312
Bunch separation	ps	500	500	500
Linac Average Gradient	MV/m	72	72-100	72-100
Estimated AC power	(MW)	252	364	589
Luminosity	$\times 10^{34}\mathrm{cm}^{-2}\mathrm{s}^{-1}$)	1.5	3.7	5.9
Horizontal Beam Size	nm	150	60	40
Vertical Beam Size	nm	3	1.5	1

Table 2.2.: Summary of the main figures of merit for the three CLIC center-of-mass energies staged construction plans [79].

particularly challenging either from the accelerator or from the detector perspectives: (a) the beam spot size at the interaction point and (b) the sub-ns bunch crossing rate. The former is necessary to maintain the instantaneous luminosity of this machine to high values, but requires an extraordinary set of beam optics that will span a length of

---

[5] for the rest of this column, the values will refer to the 380 GeV option

almost 3 km [80] around the interaction point with active-feedback quadrupoles with spatial jittering in the order of few tenths of a nanometer [81]. The latter quantity, i.e. a collision rate of 2 GHz, is intrinsic to the beam acceleration scheme adopted and can prove to be particularly challenging for the detector readout systems.

The very high center-of-mass energy achievable by this lepton collider, coupled to its high luminosity, makes such a machine the perfect complement for the studies conducted at the LHC.

3. Detector Concepts for Future Colliders

In chapter 2 we have seen what the prospects are for the next generation of particle accelerators. In this chapter we will expose the parameters to keep in consideration when planning for a multi-purpose particle detector using the current state-of-the-art technological advancements. After reviewing what are the challenges and the demands for detectors at the frontier of precision measurements in high-energy physics and after a brief reminder of the main interactions of particles and matter, we will focus on the implementation choices in the design of the CLIC detector, as a real-life example of detector R&D effort. The particular combination of high energy and high bunch crossing rate for this accelerator, already covered in section 2.3.2, makes for an ideal case scenario to introduce the complications facing the designers and showcase some of the technological solutions proposed.

3.1. Detector Requirements for the Next Generation of Experiments

Modern particle physics experiments investigate very rare and complex final states, that require equally elaborate instrumentation to perform the task. On one side there are specialized experiments, where the focus and main effort is spent on analyzing very particular and well defined research niches. The level of specialization and intricacy of their detectors is often astonishing, but, because of their very nature, they are unfit to cover broad portions of the phase space and obviously work at their best only for a limited amount of final state configurations. Detectors of this kind are, for example, ALICE [82] and LHCb [83] at CERN, the first having as primary focus the study of heavy ion collisions, whereas the latter investigating CP violation in the B meson sector. Although their achievements are remarkable, this section targets a different set of experiments: general purpose detectors that try to balance their strengths over the many different measurements of a broader physics program. This sometimes results in design compromises that specialized detectors do not need to implement. Nevertheless, the current generation of multi-purpose detectors, ATLAS [60] and CMS [61], whose design started almost 25 years ago, have proven to have many strengths and have already achieved impressive discoveries, like the direct observation of the Higgs boson. General purpose detectors need to excel at multiple assignments and be capable to cover a broad set of tasks, in order to study as many aspects of the known models as possible, as well as be ready to investigate new complex final states that might arise from new physics. There are, in particular, some measurements emerging from current state-of-the-art experiments, that would greatly benefit our understanding of the mechanisms of the Standard Model and, possibly, give a hint of the direction to take when looking for new physics that need to be taken in consideration when planning for a new detector. Those are, for example, precision measurements of the top quark sector and the investigation of the Higgs boson properties.

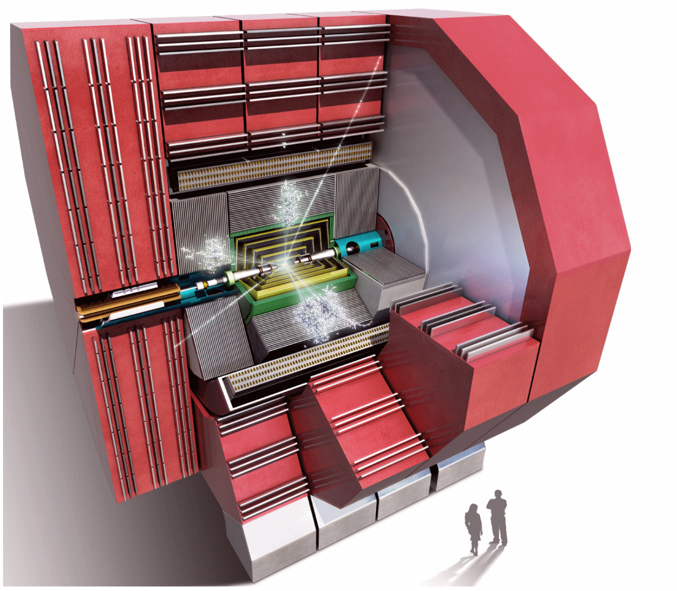

Figure 3.1.: A schematic representation of the CLIC-ILD detector concept. Figure from [80].

Multipurpose detectors for a two-beam symmetric collider do share an overall similar design scheme, although the particular implementations vary enormously. First, in order to have a full picture of an event final state configuration, they need to cover as much as possible the full 4π solid angle. This is achieved by using a cylindrical geometry around the interaction point. Figure 3.1 shows a schematic depiction of a detector concept for the CLIC accelerator, but the overall shape, and in particular the onion-like layered structure, can be applied to most modern general purpose detectors.

From the innermost layer to the outermost ones it is possible to find, enclosed in a magnetic field, a *vertexing* and a *tracking* detector, used to reconstruct particles momenta, followed by a set of *calorimeters*, to reconstruct the particles energy. Each of these subdetectors will be explained in more detail in sections 3.3 and 3.4. After a cryogenic vessel, that contains the superconductive coil that produces the magnetic field, the return yokes of such magnet are instrumented with muon chambers designated to the identification and characterization of muons from the interaction point.

For the next generation of lepton colliders, several multipurpose detectors have been proposed. For the ILC, the most notable ones are ILD and SID. Their main design concepts have also been borrowed by the CLIC collaboration [84] and adapted to fit the higher center-of-mass energies achievable there, as well as the different machine-induced backgrounds. These are, for example, the higher beamstrahlung introduced by the stronger final focusing and the demanding time-stamping capabilities required to disentangle events from different particle bunches at the higher collision frequency.

In the following subsections, the accuracy and resolution requirements for the main subdetectors will be introduced by presenting a few notable examples of the performances necessary to resolve key physics processes, while the rest of the chapter will focus on the technologies investigated to achieve such specifications. While the essential requisites will not depend on the particular choice for the detectors' technologies, a particular emphasis will be put on the ILD-based detector concept for CLIC (figure 3.1), since the simulations performed for the main analysis of this thesis work are based on this detector.

3.1.1. Lepton Reconstruction

Measuring the properties of leptons in an event final state is of particular interest: since very few background processes produce them, especially in the high p_T region, they can be used for precision physics measurements as well as for calibration purposes. An example of the latter is the leptonic decay of the Z boson, for which the rest mass is known to a 6-digit precision from LEP data [85], that can be used as a *"standard candle"* to calibrate the energy response of the detector. Since leptons are charged particles, they ionize matter when passing through it (as we will see in detail in section 3.2). This means that they leave a trail in the tracker, that can measure their momentum.

How precisely such momentum can be reconstructed largely affects the physics investigations achievable with such detector. A clear example of this is given by the study of Higgs leptonic decays. Albeit very rare, these decays can provide a very

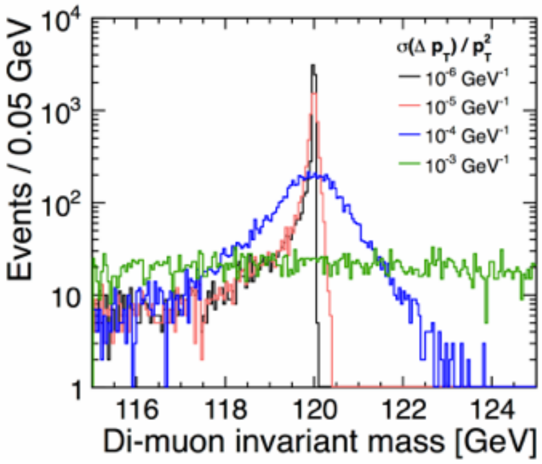

Figure 3.2.: $H \to \mu^+\mu^-$ invariant mass reconstruction as a function of the tracker momentum resolution. From this study it is apparent that a resolution of at least 10^{-5} GeV^{-1} is necessary [80].

useful tool to directly measure any possible deviation in its coupling to leptons from the Standard Model predictions. Figure 3.2 shows the invariant mass distribution of a Higgs boson, reconstructed from the momenta of the two daughter muons. From the simulations of various tracker momentum resolutions it appears that, to be able to obtain the high signal-to-background separation needed to investigate this process proficiently, it is necessary to aim at a target resolution of a few tens parts per million.

3.1.2. Hadronic Jet Energy Reconstruction

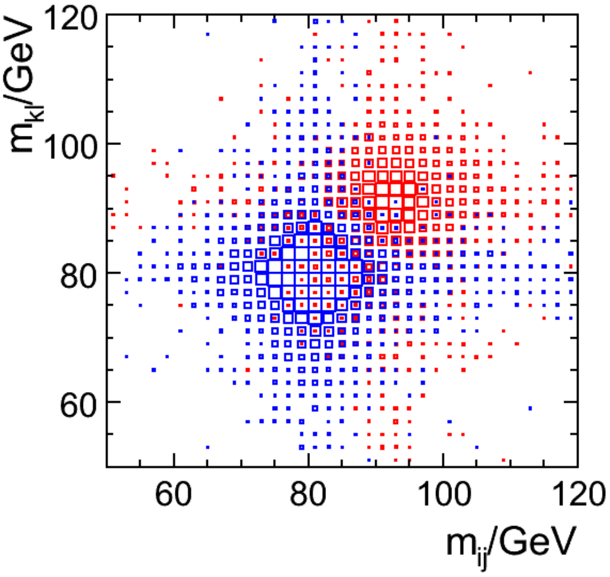

Figure 3.3.: Separation of WW and ZZ hadronic final states by reconstructing the dijet invariant mass of the daughter jets at CLIC. The Monte Carlo generated events, blue for WW and red for ZZ events, can be separated quite precisely thanks to the narrow uncertainties of the two distributions. Figure from [86].

One of the biggest limiting factors in modern physics detectors is the energy resolution achievable for hadronic final states, i.e. states with quarks and gluons that quickly hadronize into composite particles, mesons and baryons, that fly through and interact with the detectors subsystems. We will see in sections 3.2 and 3.4 how the complex and stochastic nature of hadronic interactions, combined with the physical constrains in the size of a calorimetric subdetector, makes very difficult to produce systems with resolutions that are better than $\frac{40-60\%}{\sqrt{E}}$ single particle resolution. As a meter of comparison, CMS and ATLAS stochastic terms for their hadronic calorimeters single particle resolutions are of the order of $\frac{90-110\%}{\sqrt{E}}$ and $\frac{50\%}{\sqrt{E}}$, respectively [87].

Moreover, because of the added complexity of quarks' and gluons' hadronizations, it happens very seldomly that they generate a single hadron, which in turn flies towards the detector. Much more likely is the scenario in which a narrow *spray* of up to a few dozen particles is confined in a small cone around the momentum vector of the originating quark or gluon. Such spray of particles is referred to as *particle jet* and it is crucial to reconstruct the energy of such jet in its entirety to be able to infer information regarding the parent quark or gluon. Being a composition of many particles, the resolution, the uncertainty achievable for the energy of a particle jet, is even worse than that of a single particle.

One of the goals for the next generation of particle detectors is the ability to disentangle W and Z bosons hadronic decays by reconstructing the di-jet system invariant mass. This requires a jet energy resolution on the order of $\approx 3.5\%$ for 100 GeV jets, much better than the $\geq 10\%$ achievable today for a comparable energy regime.

Figure 3.3 shows a Monte Carlo simulation of the reconstruction capabilities for this foreseen energy resolution. To achieve this resolution a novel technique involving more demanding offline data analysis has been developed: Particle Flow Algorithms [88]. In section 3.5 we will dive into some detailed explanation of these methods, for now it is sufficient to mention that the procedure requires calorimetric subdetectors with remarkable spatial resolution, and therefore a high number of readout channels, to produce the best results.

3.1.3. Flavor Tagging

One of the key components of this thesis work is the determination of the achievable precision obtainable when measuring the various branching fractions of the Higgs boson into hadronic final states, namely $b\bar{b}$, $c\bar{c}$ and *gluon* pairs, which altogether account for almost 70% of all Higgs decays [89]. In chapter 4, we will describe the theoretical background for these values, and in chapter 6, we will illustrate the analysis implemented to evaluate them. As we will see, one of the steps at the core of the analysis, and the only possibility to discern the various Higgs hadronic decay modes, relies on the ability to differentiate the slight variations in the jets observables that are characteristics of the particular hadron involved. For example, the Higgs can decay into b quarks that form B mesons, with a half-life of the order of $1.5 - 1.6 \times 10^{-12}$ s, depending on their charge. Because of the Lorenz boost given by the high kinetic energy, this half-life translates into mean flight distances of the order of several hundreds of µm in the detector, that lead to the formation of so-called secondary vertices. Charm quarks behave similarly, but the mesons they produce, mostly J/ψ and D mesons, have much shorter half-lives and therefore shorter mean flight distances. While the J/ψ half-life of only 7.2×10^{-21} s gives no hopes when searching for a displaced vertex, the D mesons $0.4 - 1.0 \times 10^{-12}$ s makes the identification of c quarks vertices possible, although complicated.

It is therefore crucial to have a very good pointing resolution to be able to distinguish if a given track originated from the primary interaction point or from one of the secondary vertices. For this purpose, the innermost layers of a detector, demanded for this task, are labeled as vertex subdetector. We will see in the next section the implementation details of one of such systems, namely the CLIC vertex detector that, with its impact parameter resolution of

$$R\phi \approx 5 \oplus 15(p[\text{GeV}]sin^{3/2}\theta)[\mu\text{m}]$$

and a rather sophisticated multivariate analysis, will allow to reconstruct heavy-flavored decays with a remarkably high efficiency [90].

3.2. Passage of Particles Through Matter

Before we dig into a real-life example of the detector subsystems planned for the CLIC accelerator, it is useful to give a short reminder of the primary interactions of the various particle types with matter, to make the rationale behind design choices of subdetector components more clear.

The vast variety of fundamental and composite particles that can be produced at the interaction point can be divided into a relatively small number of categories, to account for their main interactions when traveling through matter, for example that of a particle detector. The first division that can be made is between charged and neutral particles: the former can produce signals by releasing energy in several forms, for example ionization effects. Neutral particles, on the other hand, produce a detectable signal only through more complex interactions: hadronic interactions in high density materials for neutral (but also charged) mesons and baryons, and e^+e^- *pair-production* in the case of photons. On top of that, relativistic electrons and positrons lose a significant fraction of their energy in high-Z materials via a phenomenon called *Bremsstrahlung* that creates additional photons that can undergo further pair production. For this reason, although their interactions with matter are very different, it is interesting to study photons and electrons mechanisms together.

Finally, muons interact with matter in a special way. Despite being unstable particles, their rather long half-life of $\sim 2.2\,\mu\text{s}$ allow them to travel significant distances before decaying. Moreover, being substantially heavier than electrons, their Bremsstrahlung losses are negligible. Both characteristics allow them to travel through thick layers of matter for long distances with very little, but still detectable, energy losses generated, for the most part, via ionization processes.

In the next four paragraphs, we will overview in more detail all these interactions.

3.2.1. Charged Particles

All charged particles, when passing through matter, can interact electromagnetically both with the electrons, and the charged nucleus of the material they are traversing. When interacting with the outer shell electrons of the atoms of the material — by far the most probable interaction — the average energy loss by ionization is well described by

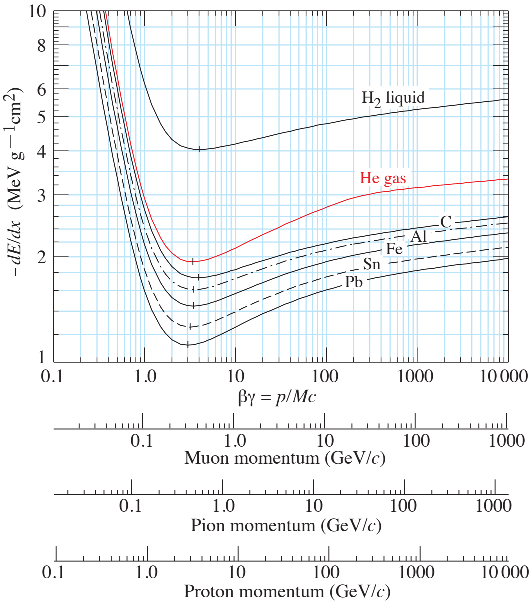

Figure 3.4.: Ionization energy losses for charged particles passing through various materials as a function of their momentum. Figure from [91].

the Bethe-Bloch formula:

$$-\left\langle \frac{dE}{dx} \right\rangle = 4\pi \frac{N_A Z\rho}{A} r_e^2 m_e c^2 \frac{z^2}{\beta^2} \left[ln \left(\frac{2m_e c^2 \beta^2 \gamma^2}{I} \right) - \beta^2 - \frac{\delta(\gamma)}{2} \right] \tag{3.1}$$

where N_A is the Avogadro's number, I is the absorber average potential, $\delta(\gamma)$ a density factor that mitigates the logarithmic increase in energy loss for high values of the incoming particle Lorentz factor, and ρ, A and Z the density, mass number and atomic number of the traversed material, respectively. Figure 3.4 quantifies these energy losses for several materials, showing the characteristic dip in energy loss for values around $\beta\gamma = 3$ GeV/c that represent the regime of so-called *minimum ionizing particles*.

3.2.2. Electrons & Photons

As mentioned in this chapter's introduction, electrons and photons, while witnessing very different physics processes when interacting with matter, are intimately connected to each other. In fact, on one hand, photons above the energy threshold of 1.022 MeV, i.e. twice an electron rest mass, can produce e^+e^- pairs, on the other hand, relativistic electrons and positrons do lose most of their energy via the emission of photons. These processes can develop into a cascade of particles, usually referred to as an electromagnetic shower, that terminates when the energy of the single particles in the shower is too low to further produce additional particles.

More in detail, in vacuum, photons can constantly fluctuate into pairs of virtual electrons and positrons that have to quickly recombine into a photon to avoid violating the conservation of the total momentum. When the photon, however, travels close to a charged object, such as an atom nucleus, enough to be able to "feel" its electromagnetic field, if a virtual e^+e^- pair is produced, the total momentum can be conserved by transferring part of it to the nucleus, that can recoil to compensate for the momentum difference. Not being in violation of any other fundamental rule of quantum mechanics, the electron and positron are free to *pop into existence*, each carrying almost exactly half of the total photon energy, while the originating photon is lost forever. This is the reason why high energetic photons can travel for millions of light-years in the vacuum of outer space, but quickly produce electromagnetic cascades once they have reached the Earth's atmosphere.

Electrons (and positrons), on the other hand, can interact with the electromagnetic field of the material they are traversing. From Maxwell equations, any acceleration of a charged particle is accompanied by the emission of electromagnetic wave, i.e. a photon. The semi-empirical Bethe-Heitler equation describes rather precisely the energy losses from Bremsstrahlung as a function of the absorber's atomic number and the impinging particle's energy:

$$-\left\langle \frac{dE}{dx} \right\rangle \simeq \frac{4N_A Z^2 \alpha^3 (\hbar c)^2}{m_e^2 c^4} E \ln\left(\frac{183}{\sqrt[3]{Z}}\right) \tag{3.2}$$

where N_A is the Avogadro number and α is the fine-structure constant ($\approx 1/137$).

To quickly compare the stopping power for electrons and positrons in various materials, it is convenient to introduce a quantity called *radiation length (X_0)*. This represents the total length an electron or a positron has to travel, on average, in a certain material before losing $1 - \frac{1}{e}$ of its initial energy. It is interesting to note that, with QED calculations, it is possible to prove that this quantity is intimately related to the mean free path of a photon (above the 1.022 MeV threshold) in the same material. This is in fact equal to $\frac{9}{7}X_0$.

3.2.3. Hadrons

Hadronic interactions with matter are a very complex subject, since this term comprehends several profoundly different processes involving composite particles. In general, an incoming meson or baryon, interacts via strong processes with the nucleons in the material, producing a plethora of secondary fragments that develop a particle shower, mostly but not exclusively consisting of pions. The shower constituents can behave in different ways:

- **π^0 mesons** decay almost exclusively into two photons, originating electromagnetic subshowers with the mechanisms explained in the previous subsection.

- **$\pi^\pm$ and other mesons, and baryons** can further interact with additional nuclei, developing the hadronic shower.

- **nuclear fragments**, mostly generated by spallation or fission in the material, can produce hard X-ray photons, neutrons, α particles and other light nuclei.

- **neutrons** mainly from meta-stable isotopes evaporation or fission, can travel for long distances in the material before depositing their energy. Sometimes, they cover enough distance to escape the volume of the detector altogether, resulting in a deficit in the reconstruction of the total shower energy.

- **X-ray and γ photons** from nuclear de-excitation can be generated by some longer-lived meta-stable excited nuclei up to seconds after their excitation.

All these processes combined are very difficult to precisely predict and simulate, and are also showing large stochastic fluctuations between events with similar initial conditions. All these circumstances contribute to a much less precise reconstruction of hadronic showers in comparison to the electromagnetic ones. As a general rule, approximately 30% of an hadronic shower energy is converted in electromagnetic sub-showers, 60% is converted in successive hadronic fragments and 10% transforms in neutral hadrons, that might escape the sensitive detector area undetected [92]. It is however sufficient for an extra neutral pion to be produced at the first iteration to substantially increase the electromagnetic energy fraction and render a precise assessment of the energy of the incoming hadron a very hard task. Similarly to the radiation length X_0 of their electromagnetic counterparts, also hadronic interactions have a characteristic *nuclear interaction length (λ_n)* that accounts for the mean distance a particle has to travel in a given material before carrying only ≈ 0.368 times the initial energy.

3.2.4. Muons

Muons are very interesting particles for high energy physics experiments. Although they are not stable, their rather long mean lifetime of $\sim 2.2\,\mu\text{s}$, coupled with the Lorenz boost generated by their relativistic speed, allows them to easily cover the distance from the interaction point to the edges of the detector. Moreover, given their high rest mass and the fact that, in equation 3.2 a square mass term is present in the denominator, their radiative energy losses, at least in the energy ranges typical for a high-energy physics collider experiment, are practically negligible. This means that the only energy loss comes from ionization processes, such as those described by equation 3.1. Figure 3.5 summarizes the behavior of muons through matter over a wide range of energies, much wider than what is expected even at the highest center-of-mass energies of a possible CLIC stage 3. Those properties, combined, give muons the unique ability to pass through all subdetector systems, regardless of the material budget used, while still being detected in almost all components. This leads to an identification efficiency of nearly 100% and a very good momentum reconstruction.

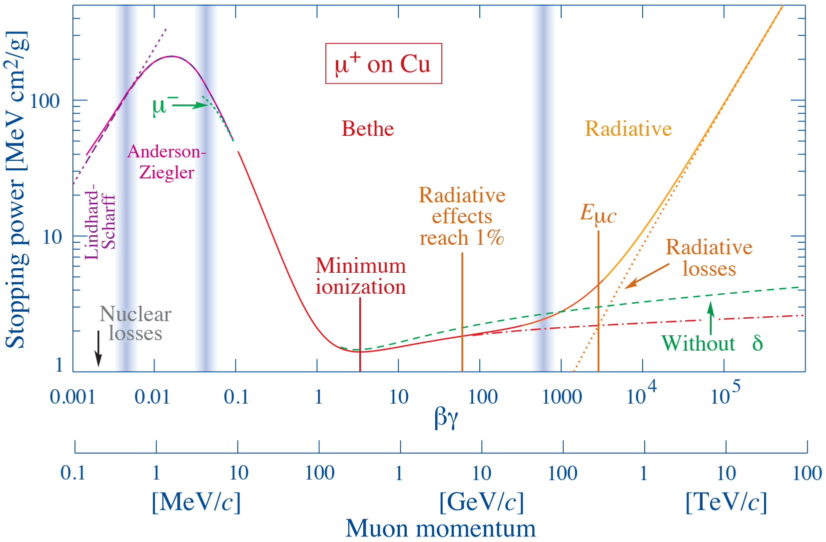

Figure 3.5.: Energy losses for muons in copper as a function of their momentum [91]. The typical energies for muons produced at a future e^+e^- collider, range from a few ten MeV to a couple of hundred GeV.

3.3. Vertexing and Tracking

The vertex detector is the innermost instrument of every modern collider experiment. It sits only millimeters away from the interaction point, around a section of the beam pipe that is usually thinned down to a smaller radius compared to the rest of the accelerator. This is crucial because, as the name suggest, the vertex detector's duty is to reconstruct the exact location of the interaction point and that of the eventual secondary vertices. The resolution for these measurements rapidly decreases with the distance, since the uncertainties in the pointing capabilities of these detectors are more impacting when measuring the small angles that result from looking at the interaction region from far away. Over time, the technological implementations for this subsystem have varied greatly, from gaseous detectors to bubble chambers. In the last 20 years, however, vertex detectors have almost exclusively been built with silicon devices. These usually work as follows: lithographic techniques are

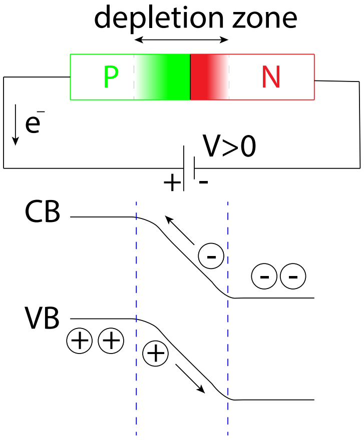

Figure 3.6.: Schematic representation of the depletion region created in a pn junction, when a voltage in reverse bias is applied.

used to imprint a pattern on a silicon substrate and create pn-junctions using doping materials. The junctions are then subject to an external electric field that forces a reverse bias on them. This leads to the p-type component to be at a lower voltage than the n-type part (Figure 3.6). This electric bias generates a region at the interface of the junction, that is emptied of charge carriers, called depletion zone. In the absence of additional stimuli this operates like an insulator. When an ionizing particle traverses the depletion zone though, the free charges it produces are collected by the field and drift to the faces of the silicon producing a measurable electric signal. If the pattern imprinted is a grid of pixels or short strips, it is possible to deduce the position of the hit on the silicon wafer. By keeping track of the hits recorded on several layers, stacked perpendicularly to the direction of flight of the ionizing particles coming from the interaction region, it is possible to reconstruct the particles trajectories. To do so it is crucial, especially in an environment like CLIC, to have a remarkable time-stamp resolution, so that all the pixel modules that form the vertex detector are synchronized to an accuracy much higher than the 500 ps interval between bunch crosses. This is to ensure that there is no confusion between hits of uncorrelated events and to help suppress some of the beam-induced backgrounds.

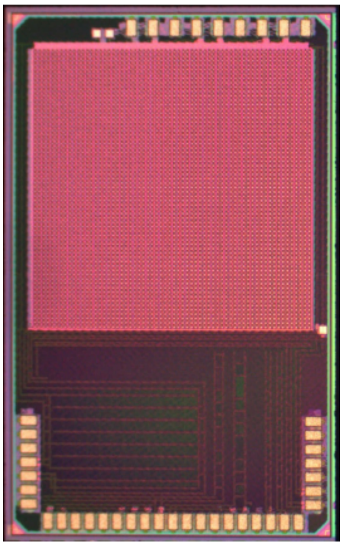

Figure 3.7.: *CLICpix* 64x64 pixel matrix prototype chip with 25 µm pixel pitch. The bottom area contains the electronics necessary for I/O and timing [93].

Usually these detectors have a pixel pitch of the order of 20 to 50 µm and a vertex spatial resolution of few microns. The CLICpix chips under development for the CLIC vertex detector [94], for example, have a pixel pitch of 25 µm and a single point resolution of 3 µm (Figure 3.7). Ideally, one would stack as many layers as possible to obtain more points from which to reconstruct the particles trajectory, but there is one main drawback in this scenario. When traversing the vertex detector, the particles information collected is only a small fraction of that needed to completely characterize their properties. For this reason, this measurement needs to be non-destructive and to perturb the state of the particle as little as feasible. This way it is possible for successive layers of detectors to perform additional measurements to obtain the full four-momentum information of all the elements composing the event final state (Figure 3.8). Since, as we have seen in the previous section, the amount of material that a particle has to traverse directly impacts the probability for the particle to be absorbed or significantly deflected, the so-called material budget of these layers must be kept to a minimum. This is also the reason for the pixel pitch: it is

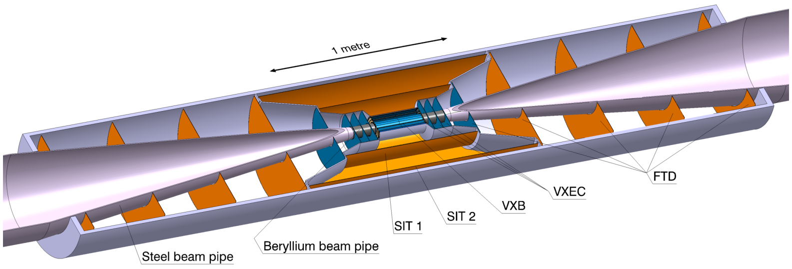

Figure 3.8.: Schematic representation of the CLIC ILD vertex and tracker silicon detectors. Multiple layers are arranged in a cylindrical symmetry to cover as much as possible the full 4π solid angle around the interaction point [95].

a compromise between the achievable spatial resolution and the available bandwidth for the readout system.

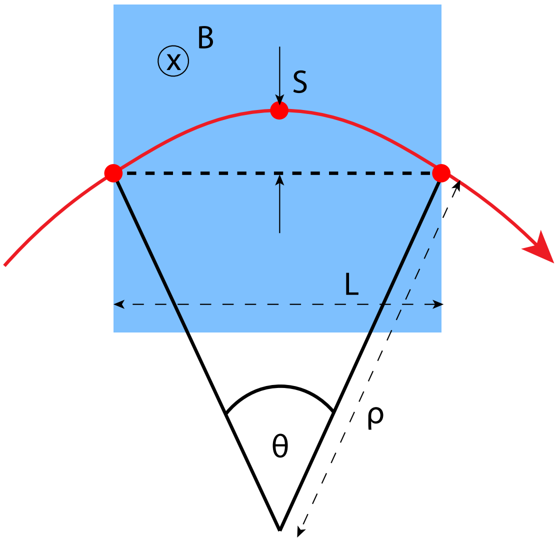

Figure 3.9.: Momentum reconstruction for a charged particle in a magnetic field, flying on an arc trajectory, in red. The particle momentum can be reconstructed from the track curvature and the intensity of the magnetic field.

In fact, higher bandwidths do require more readout lines and more complex electronics for the in-situ signal processing and compression. Both requirements have the drawback to increase the material budget for the subdetector, the former with more copper lines and cables, while the latter, increasing the power requirements of the readout electronics, compels for additional bulkier cooling systems. For the vertex detector at CLIC, the aim is to keep the material budget parameter below 1% X_0 (see section 3.2.2).

The next subsystem, the tracking detector, sits right after the vertexer to reconstruct the momentum of charged particles. For this measurement it is crucial that this region is subject to a strong magnetic field, usually of the order of few Tesla, capable of curving the trajectory of the charged particles. When the tracker is able to record at least three points for a particle trajectory, it is possible to reconstruct the track curvature κ, using the arc *sagitta*, as we can see in Figure 3.9.

For small angles we have:

$$\frac{L}{2\rho} = sin\left(\frac{\theta}{2}\right) \approx \frac{\theta}{2} \tag{3.3}$$

and

$$s = \rho \left(1 - cos\left(\frac{\theta}{2}\right)\right). \tag{3.4}$$

Reminding equation 2.3, the relation between the sagitta s, the intensity of the transverse magnetic field B and the particle momentum p, is:

$$s \approx \rho\frac{\theta^2}{8} = \frac{0.3}{8}\frac{BL^2}{p} \tag{3.5}$$

and, therefore, the momentum is:

$$p \approx \frac{0.3}{8}\frac{BL^2}{s} \tag{3.6}$$

Similarly to the case of vertex detectors, trackers as well need to minimize their material budget. These detectors have been produced over the decades with a large variety of technologies optimized for costs, engineering advancements and the particular environment they had to face. Notable examples are the ALICE gaseous time projection chamber (TPC) [96] and the several wire chambers built in the past for OPAL, BaBar and Belle [97–99]. Silicon experienced a steep decrease in cost due to the high demand from the semiconductor industry and the consequent development of larger wafers with better yields. As a consequence, for the CLIC detector concept, it was possible to opt for the increased resolution of silicon detectors in the tracker as well. This setup was pioneered by the CMS collaboration, the first large experiment to equip an all-silicon main tracker [100]. The tracker at CLIC will be arranged, in the barrel region, in 4-5 cylindrical layers with a material budget of $1 - 2\%$ X_0 each and an estimated resolution of $\approx 7\,\mu\text{m}$ [101].

3.4. Calorimetry

Calorimeters are a key component of modern particle detectors. They aim at measuring the energy of particles and particle jets, converting a fraction of it into a measurable signal. To do so, high density materials, in which particles tend to interact frequently and have limited travel-range, are used as stopping media. Because of its very nature, this is a destructive technique, that means that the particles, whose energy is measured in a calorimeter, are lost in the process and no further analysis can be performed. For this reason, this subdetector is located after the non-destructive vertexing and tracking measurement layers. Calorimeters can be split into two main technological categories, based on their implementation, as well as two physical categories, based on the particles they are optimized for. In the continuation of this section we will overview these categorizations.

3.4.1. Homogeneous vs Sampling Calorimeters

From a technological point of view, we can make the distinction between *homogeneous* and *sampling* calorimeters (Figure 3.10).

- **Homogeneous calorimeters:** are build with a material that is not only high in density, but also acts as the *active medium*. In other words, it converts part of the kinetic energy of the impinging particle into an easier to measure quantity such as a light pulse.

- **Sampling calorimeters:** the material delegated to stop particles, referred to as the *absorber*, and the active material are separated in stacked layers so that, for each, the best material choice for the particular task can be made. In sampling calorimeters, usually, the absorber consist of layers of high-density metal alloys, such as steels, lead or tungsten. All of these materials have short radiation and nuclear interaction lengths (see section 3.2), but lack the ability to convert any of the energy they receive from the particle into a useful measurable impulse. The active material in the sandwich, on the other hand, has much less stringent density requirements, making the choice options much more diverse and vast. For example, a detector based on *liquid argon* for the active layer is a perfectly good option in sampling calorimeters (that is, in fact, used in the ATLAS ECAL [102]), but due to the low density, and consequently high χ_0 and λ_0, would never make for a practical homogeneous calorimeter. In fact this would need to extend over impractical distances to compete with the stopping power of a sampling calorimeter.

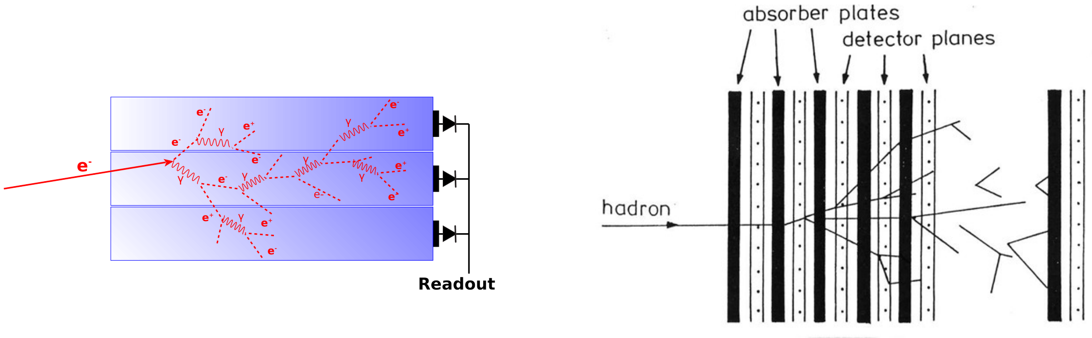

Figure 3.10.: Schematic representation the typical geometries of a homogeneous (on the left) and a sampling (on the right) calorimeters.

Both categories of calorimeters have their strengths and weaknesses. Because of the stochastic nature of the interactions of particles and matter, sampling calorimeters suffer from the fact that the fraction of energy deposited in the active layer and that dispersed in the absorber have a wide variance. Homogeneous calorimeters do not have this problem since the signal can be generated in any point of the detectors, making them much more robust to fluctuations and therefore, usually, more precise. Sampling detectors, however, have a major advantage when it comes to dimensions: the sandwich structure allows for denser absorbers and, therefore, shorter detectors for the same particle energy compared to homogeneous calorimeters. This is crucial to prevent another source of uncertainties: *leakage*, which is the phenomenon that occurs when the particle under investigation is not completely stopped inside the calorimeter, resulting in an underestimated assessment of its energy. This happens mainly for two reasons: (a) the energy of the particle is too high for the calorimeter design, and the shower that it creates, whose longitudinal extension is in first approximation proportional to its energy, continues past the thickness of the calorimeter, or (b), since the interaction of a particle with matter is a stochastic process, it can sometimes happen that the particle traverses a long distance with minimal interaction before starting the shower, which, for this reason, is able to stretch past the end of the calorimeter. Finally, homogeneous calorimeters are well suited for measuring hadronic showers for causes that will be clarified in the next section.

3.4.2. Electromagnetic and Hadronic Calorimeters

Has we have seen in section 3.2, there are two kinds of particle showers associated with the passage of particles through matter: electromagnetic showers, initiated by photons, electrons and positrons, and hadronic showers, generated by charged pions, protons and all other mesons and baryons. This introduces another major dichotomy in calorimeters: electromagnetic calorimeters, usually referred to as *ECALs*, which are optimized for the first type of interactions, and hadronic calorimeters, or in short *HCAL*, optimized for the second. When discussing the interactions between particles and matter, we have also shown that the length scales, at which these two types of interactions take place, can be very different to one another and can be summarized by the two parameters X_0 and λ_0 for electromagnetic and hadronic processes, respectively. Since, for most materials, X_0 is sensibly shorter than λ_0, an electromagnetic calorimeter must be placed in front of an hadronic one. There is another major difference between hadronic and electromagnetic showers (as pointed out in section 3.2) that reflects in the way a calorimeter is build: the e.m. subshowers from π_0 decays. Since the energy fraction of these components has a very large variance, to be able to generate the same response for showers of the same energy, it is essential that the response of a hadronic calorimeter to the electromagnetic and hadronic subcomponents is as similar as possible. The ratio between these two components, usually referred to as e/π, can be partially controlled by the *sampling fraction*, i.e. the proportion between the thickness of the absorber and active layers of a sampling calorimeter. This is the reason why every hadronic calorimeter implemented so far is of this kind.

3.4.3. Uncertainties in Calorimeters

The variance in the energy measurement of a calorimeter can be parametrized by three components, as follows:

$$\frac{\sigma E}{E} = \frac{a}{\sqrt{E}} \oplus \frac{b}{E} \oplus c, \tag{3.7}$$

The first term, proportional to $\frac{1}{\sqrt{E}}$ is the *stochastic term* and depends on the physical development of the particle shower in the calorimeter. Usually homogeneous electromagnetic calorimeters perform much better, compared to sampling ones, on this component, since the fluctuations in the energy deposited in the active material are smaller. The second term is the *noise term* and depends on the noise contributions from the signal conversion and readout electronics chain. This is inversely proportional to the measured energy. Finally the *constant term* includes all those contributions whose amplitude is not correlated with the measured energy at all. These are, for example, spatial inhomogeneities in the detector geometry or miscalibrations that translate in non uniform responses of the calorimetric system.

In sampling calorimeters, the stochastic term is by far the dominant one, with values for the parameter a that can span, for hadronic calorimeters for example, from 40 to above 100%. This rather high uncertainties are generated, in large part, from the fluctuations in the e.m. fraction of a shower, as we have seen in section 3.2.3. There have been several different approaches to decrease this quantity, mostly by trying to equalize the detector response to hadrons with that of the electromagnetic subshowers. As we have pointed out in the previous section, the e/π detector response must be as close as possible to unity, so that the response of the calorimeter to the hadronic and e.m. fractions coincides. To achieve this value, several strategies have been implemented over time, such as: (a) *hardware compensation* and (b) *software compensation*. The former consists either in the choice of absorbing materials that undergo fission (e.g. depleted uranium), to naturally enhance the signal generated by the hadronic components, or in the careful selection of the best absorbers and active layers' thicknesses, in order to suppress part of the e.m. response and optimize the sampling fraction. These expedients have been implemented in the 1992 ZEUS HCAL [103, 104], the only high-energy sampling hadron calorimeter to achieve a stochastic term of $\frac{35\%}{\sqrt{E}}$ [105].

Software compensation, on the other hand, relies on calorimeter segmentation to be able to weight each energy deposition as a function of the neighboring energy density. Since e.m. showers are denser than their hadronic counterparts, it is possible to partially recover the e/π compensation by adapting to the local topology of the shower.

Both techniques have some drawbacks: in the hardware compensation case, the use of hazardous materials such as depleted uranium, makes it very difficult to build the detectors, while the software compensation case can recover from the energy fluctuations only to a certain degree.

In the next section, we will have a look at a novel approach for jet energy measurements that can enhance the results obtained so far.

3.5. High Granularity and Particle Flow

As we have seen in the previous sections, when dealing with particles ranging in energy from a few GeV up to several hundreds GeV, the uncertainty with which such energy can be measured in a hadronic calorimeter is, even with state-of-the-art detectors, decent at most, and by far worse than any other quantity measured in a high-energy physics experiment. This comes partially from technological limitations and size constrains, but is also intrinsically nested in the stochastic fluctuations that occur, event by event, in the distribution of hadronic and electromagnetic interactions in the cascade that generates from the particle under consideration.

This limitation is particularly disadvantageous when measuring the energy of particle jets, since the fluctuations from each particle in the jet can add up to further worsen the calorimeter's response. This, in turn, hinders the measurement of the properties of quarks and gluons in the final state of an event, as these elementary particles can only be investigated indirectly through the jets of particles that they create.

To overcome these limitations, there is one property of particle detectors that we need to keep in consideration: for most particles, the calorimeters are not the only source of measure for the energy. It is indeed possible to infer a particle energy from its momentum and rest mass, so if some sort of particle identification is in place, it is possible to calculate the energy of charged fragments from the momentum measurement performed with the tracking detector. This form of energy measurement is much more precise at low energies compared to calorimeters, and reaches a plateau for momenta around several hundred GeV/c, the exact number for such limit depending on the particular tracker and calorimeter implementations. This means that, for the kinematics of most final states, and particle jets in particular, at the present accelerator energy frontier, the best energy estimation could potentially be carried out by subdetectors components other than the calorimeters. The limitation that prevented most experiments to do so until now is the fact that there is a non-negligible component in particle jets that cannot be measured in any other way than with the calorimeters, namely photons and neutral hadrons. Previous measurements of jet fragmentation at LEP [106] have shown that, on average, these two components carry 27% and 10% of the total energy of a jet respectively, but do fluctuate greatly on an event-to-event basis. The ideal solution would be to use each subdetector for the energy fraction of a jet that it can measure best, i.e. charged particles in the tracker, photons in the ECAL and neutral hadrons in the HCAL. To do so, and since the particles in a jet usually have a narrow angular spread, it is necessary to segment the calorimeters not only longitudinally, but also transversally to the particles' direction, in order to be able to disentangle the energy deposition of each individual component of a jet and match the depositions of charged hadrons with trajectories in the tracker. This results in a fine detector segmentation and a dramatic increase in the number of readout channels, compared to the current generation of experiments. On the technological side, the computing power and miniaturization needed to achieve this task is only recently become feasible: the few millions readout channels that are under study for the next generation of particle detectors would, until not long ago, only be taken in consideration for vertex detectors. To be able to reconstruct the increased complexity in the signature of a particle jet, and match each energy component to the proper tracklet, a novel set of algorithms had to be implemented, referred to as *Particle Flow* techniques.

These work as follows: first, hit clusters in the calorimeters are merged together using several pattern recognition techniques to form energy clusters that are likely to have been produced by a single particle or particles jet. Then, the list of tracks from charged particles in the tracker is traversed,in search for particles whose direction and energy is compatible with hit clusters in the calorimeters. If such match is found, the hits are removed from the calorimeter and the energy for those particles is measured from the tracker information [1]. Once this is done, the only hit clusters remaining come from neutral hadrons and photons. These get their energy measured exclusively in the calorimeters, but since they account for a small fraction of the overall energy, even if their energy is measured with a lower accuracy, the overall energy measurement is still remarkably better than a calorimeter-only approach. One of the software tools capable of performing such complicated analysis is the PandoraPFA package, developed at the University of Cambridge with an eye of regard for future lepton collider experiments [107]. This is also the tool that has been used to reconstruct the simulated events for the main analysis of this thesis work, as presented in chapter 6.

---

[1] At this point some particle identification information can be extracted by the topology of the matched hit cluster in the calorimeter. For example, for a particle to be identified as an electron, its calorimeter hits must be confined in the ECAL

4. The Physics of the Higgs Boson

This chapter introduces the theoretical framework that, for the last fifty years, has been able to describe almost every outcome of experiments in particle physics, namely the *Standard Model of Particle Physics*, and the latest addendum in the observation of its constituents: the Higgs boson. After a short description of the Standard Model, we will justify the necessity of a Higgs-like mechanism, and the *quantum field theory* mathematical procedure to include it into the existing framework, first in the simplified case of an abelian interaction, and then in the more complex case of the non-abelian electroweak model. After that, the main Higgs production and decay mechanisms will be reviewed.

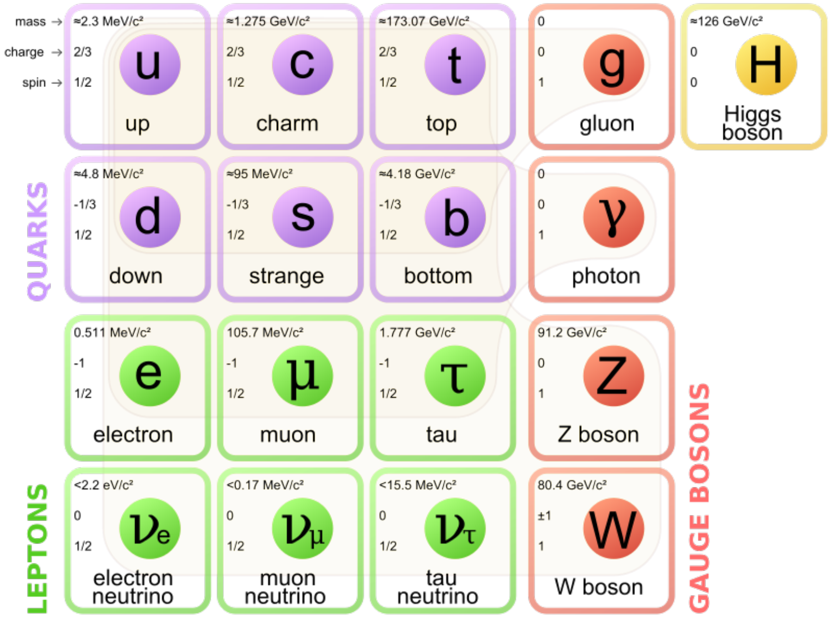

Figure 4.1.: The *"periodic table"* of fundamental particles forming the Standard Model of particle physics. [108]

4.1. The Standard Model of Particle Physics

The modern picture of the theory of fundamental particle interactions comprises 17 building blocks divided as follows: 12 fermions — six leptons and six quarks — (and their antiparticles), and five bosons, four being the force carriers for the electromagnetic, weak and strong forces, and the Higgs boson, whose utility will be explained in section 4.2. By definition, fermions carry half-integer spin (which, for quarks and leptons is always 1/2) and follow Fermi-Dirac statistics, while bosons have integer spin and follow Bose-Einstein statistics. Moreover, from phenomenology, the total number of fermions is a conserved quantity while the total number of bosons is not.

Among fermions, the terms quarks and leptons describe which interactions these particles undergo: all of them witness the electroweak force (and therefore couple to $W^{\pm}$ and Z bosons), but only quarks carry a *color* quantum number necessary to interact via the strong force through the exchange of gluons. Additionally, the electric charge quantum number is a quantity proportional to the coupling strength of charged particles to photons. This is non-zero for all quarks, the three heavy leptons e, μ and τ, and the $W^{\pm}$ bosons. All these particles have by now been experimentally detected. The landscape was quite different in the '50s and '60s, where only a handful of these 17 elementary particles had been observed. On the other hand, the number of subatomic particles discovered was already quite sizable, with new baryons and mesons being added each time a new particle accelerator went online (see chapter 2). Moreover, repetitions in the quantum numbers of such particles lead Gell-Mann to the arrangements of these particles into a structure of octets and decuplets [109], hinting at a deeper level of fundamental constituents that eventually culminated in the quark model. Figure 4.2 shows the arrangements of these particles in relation to their quantum numbers.

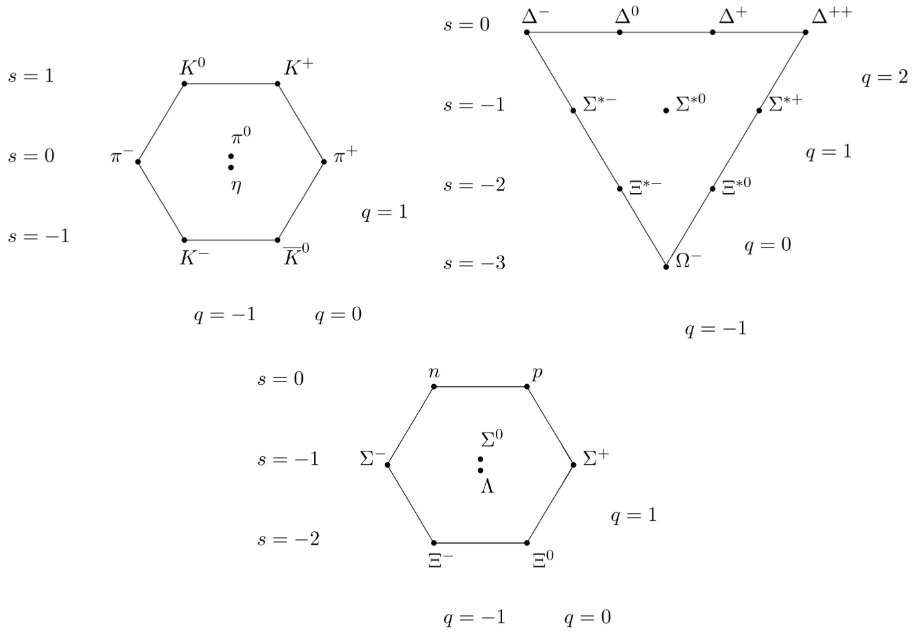

Figure 4.2.: Gell-Mann multiplets representation of the mesonic and baryonic sector. [108, 109]

The conserved quantities of this rather complex phenomenological scenario can be related to the continuous symmetries of the action in a field theory using Noether's theorem [110]. In particular, it is possible to extend the gauge theory of an abelian U(1) group to non-abelian groups using a SU(N) Lie group. This idea was pursued in the '50s by Yang and Mills [111], trying to extend the formalism of QED to the quark sector. The drawback of such a method was that, by construction, the Lagrangian would necessitate a massless boson, giving the interaction unlimited range, in clear contrast with experimental evidence. Less than a decade after that, Goldstone [112] and Nambu [113] introduced the concept of *spontaneous symmetry breaking* to allow for a massive boson in the theory (we will see how this mechanism works in the next section). Successively, with the work of Glashow, Weinberg and Salam on the electroweak sector [7], and Zweig and Gell-Mann [55] on the quark side, it was possible to define the complete gauge group for the Standard Model as:

$$SU(3) \times SU(2) \times U(1), \tag{4.1}$$

where the SU(3) component describes the strong interactions and the $SU(2) \times U(1)$ the electroweak interactions. In the rest of this section we will introduce the formalism of these quantum field theories. For the electroweak sector, the generators of the conserved gauge symmetries are three operators for the *weak isospin*:

$$W^k = \frac{1}{2}\sigma^k, \tag{4.2}$$

with

$$\sigma^1 = \begin{pmatrix} 0 & 1 \\ 1 & 0 \end{pmatrix}, \sigma^2 = \begin{pmatrix} 0 & -i \\ i & 0 \end{pmatrix}, \sigma^3 = \begin{pmatrix} 1 & 0 \\ 0 & -1 \end{pmatrix}, \tag{4.3}$$

being the Pauli matrices and one weak hypercharge operator for the $U(1)_Y$ group, usually referred to as Y, that is proportional to the identity operator $\mathbb{1}$. The electric charge is a conserved quantity and, in this representation, it is defined by the Gell-Mann-Nishijima formula [114]:

$$Q \equiv W^3 + \frac{1}{2}Y. \tag{4.4}$$

This set of operators acts on all left-handed electroweak doublets:

$$\begin{pmatrix} e^- \\ \nu_e \end{pmatrix}_L \begin{pmatrix} u \\ d \end{pmatrix}_L \begin{pmatrix} \mu^- \\ \nu_\mu \end{pmatrix}_L \begin{pmatrix} c \\ s \end{pmatrix}_L \begin{pmatrix} \tau \\ \nu\tau \end{pmatrix}_L \begin{pmatrix} t \\ b \end{pmatrix}_L \tag{4.5}$$

leaving the right-handed singlets unaffected. The four generators W^1, W^2, W^3, Y can be observed, although not directly, as the bosons of the electroweak force. The physical observables are linear combinations of them, as follows:

$$\begin{aligned} W^{\pm} &= \frac{1}{\sqrt{2}}(W^1 \mp iW^2) \\ Z^0 &= -Y\sin(\theta_w) + W^3\cos(\theta_w) \\ A &= W^3\sin(\theta_w) + Y\cos(\theta_w) \end{aligned} \tag{4.6}$$

these are the three heavy bosons W^+, W^- and Z^0, and the photon. θ_w is the *Weinberg* or *weak mixing* angle, experimentally measured to be ≈ 0.23.

A similar approach can be used for the QCD part of the model. From the clusterings in figure 4.2, it was possible to deduce that they are the representation that follows from a SU(3) Lie group. In this case the conserved quantities of this gauge symmetry group are three charge states. Since their compositions follow an algebra almost identical to that of the composition of primary colors, these charge states are usually referred to as *"color charges"*, and can be either *blue, red* or *green*. In an analogy to the composition of light in which the combination of all three colors, as well as of a color/anti-color pair, is defined to be *"colorless"* or *"white"*, so is the composition of the color charges of quarks. Phenomenologically, only such colorless states are observable, either in the form of mesons (color-anticolor pairs) or baryons (*rgb* triplets). Higher composed states such as tetra-quarks and penta-quarks are theoretically allowed, but not yet unambiguously detected.

The eight generators of this field are the gluons, defined in terms of their color charge as follows:

$$\begin{aligned} &\frac{1}{\sqrt{2}}\left(r\bar{b} + b\bar{r}\right) \quad , \quad \frac{-i}{\sqrt{2}}\left(r\bar{b} - b\bar{r}\right) \\ &\frac{1}{\sqrt{2}}\left(r\bar{g} + g\bar{r}\right) \quad , \quad \frac{-i}{\sqrt{2}}\left(r\bar{g} - g\bar{r}\right) \\ &\frac{1}{\sqrt{2}}\left(b\bar{g} + g\bar{b}\right) \quad , \quad \frac{-i}{\sqrt{2}}\left(b\bar{g} - g\bar{b}\right) \\ &\frac{1}{\sqrt{2}}\left(r\bar{r} - b\bar{b}\right) \quad , \quad \frac{-i}{\sqrt{6}}\left(r\bar{r} + b\bar{b} - 2g\bar{g}\right) . \end{aligned}$$

These massless bosons mediate the strong force in what is known as the QCD field theory. In this case, the short-range behavior of the force is not defined by the mass of the gauge bosons, but rather by a phenomenon called *color confinement*, for which only colorless objects are allowed to exist as free particles, limiting the effective range of such a force to the ≈fm scale.

Because of the non-abelian nature of the SU(3) group, self-interaction of gluons are allowed, as long as the vertex of a triple coupling does not connect three gluons with identical color charge. In general, in non-abelian groups, the self-coupling of the group generators is allowed, as long as it is not the self-coupling of a single generator. For a similar reason, in the Standard Model, a ZZZ boson vertex is not allowed.

4.2. The BEH Field Mechanism

In the previous section, we have seen how to construct the electroweak interaction starting from a Yang-Mills gauge field theory. In this representation, however, there is a notable property missing: as the theory is described, the gauge bosons are massless, a condition that does not reflect the experimental evidence, given that the weak force acts at short ranges only. Introducing a mass term to the bosons of a non-abelian SU(2) field theory is rather tedious, so in this section we will use the homologous calculation for the abelian U(1) electromagnetic field case as a "warm-up". In doing so we will follow a path similar to that described in [115, 116].

We start from the electromagnetic potential field:

$$A_\mu = \left(\phi, \vec{A}\right) \tag{4.7}$$

and the four-derivative:

$$\partial_\mu = \left(\frac{1}{c}\frac{\partial}{\partial t}, \vec{\nabla}\right) \tag{4.8}$$

from which it is possible to define the e.m. tensor:

$$F_{\mu\nu} = \begin{pmatrix} 0 & \frac{E_x}{c} & \frac{E_y}{c} & \frac{E_z}{c} \\ -\frac{E_x}{c} & 0 & -B_z & B_y \\ -\frac{E_y}{c} & B_z & 0 & -B_x \\ -\frac{E_z}{c} & -B_y & B_x & 0 \end{pmatrix} = \partial_\mu A_\nu - \partial_\nu A \mu \tag{4.9}$$

and, from this, using Einstein summation for the indices, the e.m. field term of the Lagrangian:

$$\mathscr{L}_{EM} = -\frac{1}{2}Tr(F^2) = -\frac{1}{4}F_{\mu\nu}F^{\mu\nu}. \tag{4.10}$$

We are building a U(1) gauge invariant theory, this means that the Lagrangian must be conserved for arbitrary infinitesimal modifications of the potential field:

$$A_\mu \to A'_\mu = A_\mu - \partial_\mu \eta(x), \forall \eta, x. \tag{4.11}$$

The e.m. tensor then looks as follow:

$$\begin{aligned} F'_{\mu\nu} &= \partial_\mu A'_\nu - \partial_\nu A' \mu \\ &= \partial_\mu \left(A_\nu - \partial_\nu \eta(x)\right) - \partial_\nu \left(A_\mu - \partial_\mu \eta(x)\right) \\ &= \partial_\mu A_\nu - \partial_\nu A_\mu - \partial_\mu \partial_\nu \eta(x) + \partial_\nu \partial_\mu \eta(x) \\ &= \partial_\mu A_\nu - \partial_\nu A_\mu = F_{\mu\nu} \end{aligned}$$

since, from Schwarz theorem, the second mixed derivatives are the same and cancel out. This also proves that the e.m. Lagrangian is conserved. We can see that adding a mass term to it would break the local gauge, in fact:

$$\mathscr{L}_{EM} = -\frac{1}{4}F_{\mu\nu}F^{\mu\nu} + \frac{1}{2}m^2 A_\mu A^\mu \tag{4.12}$$

under the gauge transformation of equation 4.11 would lead to:

$$\begin{aligned} \mathscr{L}_{EM} =& -\frac{1}{4}F_{\mu\nu}F^{\mu\nu} + \frac{1}{2}m^2 \left(A_\mu - \partial_\mu \eta(x)\right)\left(A^\mu - \partial^\mu \eta(x)\right) \\ =& -\frac{1}{4}F_{\mu\nu}F^{\mu\nu} + \frac{1}{2}m^2 \left(A_\mu A^\mu + \partial_\mu \eta(x) \partial^\mu \eta(x) - A_\mu \partial^\mu \eta(x) - (\partial_\mu \eta(x)) A^\mu\right) \end{aligned}, \tag{4.13}$$

where, clearly, the last two terms would not cancel out, making the Lagrangian a non-conserved quantity. This is the gauge field theory justification for a massless photon. Before introducing a mechanism to give mass to the e.m. boson, let's have a look at another component of the Lagrangian: the free-particle Lagrangian for a spinor. This is, in bra-ket notation:

$$\mathscr{L}_{Free} = \langle \psi | \, i\gamma^\mu \partial_\mu - m \, | \psi \rangle \tag{4.14}$$

It is easy to prove that this is invariant for a global phase transformation

$$\psi(x_\mu) \rightarrow \psi'(x_\mu) = e^{i\alpha}\psi(x_\mu), \tag{4.15}$$

since it results in:

$$\mathscr{L}_{Free} = \left\langle \psi' \right| i\gamma^\mu \partial_\mu - m \left| \psi' \right\rangle = e^{-i\alpha} \left\langle \psi \right| (i\gamma^\mu \partial_\mu - m) e^{i\alpha} \left| \psi \right\rangle \tag{4.16}$$

and since $e^{i\alpha}$ is just a constant, it can be extracted from the operator, combined with its complex conjugate $e^{-i\alpha}$ and canceled out. But again, we want the Lagrangian to be invariant under local gauge transformations, i.e.:

$$\psi(x_\mu) \rightarrow \psi'(x_\mu) = e^{i\alpha(x_\mu)}\psi(x_\mu) \tag{4.17}$$

and we can see that, unlike before, the extra term cannot easily be extracted from the ∂_μ operator. In fact:

$$\partial_\mu \psi(x_\mu) \rightarrow \partial_\mu \psi'(x_\mu) = e^{i\alpha(x_\mu} \left[\partial_\mu \psi(x_\mu) + i(\partial_\mu \alpha(x_\mu))\psi(x_\mu)\right], \tag{4.18}$$

where the last term violates the local phase invariance. To recover it, we can slightly modify our definition of the four-derivative, opting for a covariant derivative, that, in the general SU(N) case, is:

$$\partial_\mu \rightarrow D_\mu \equiv \mathbb{I}\partial_\mu + igT^a A^a_\mu, \tag{4.19}$$

where g is the coupling strength and T^a the generators of the gauge group. In the particular case of the U(1) e.m. group, this is:

$$\partial_\mu \to D_\mu \equiv \partial_\mu - ieA_\mu, \tag{4.20}$$

where the coupling strength is given by the quantum of the electric charge, and the potential A_μ transforms as:

$$A_\mu \to A'_\mu = A_\mu - \frac{1}{e}\partial_\mu \alpha(x), \tag{4.21}$$

a choice for the e.m. field potential perfectly compatible with the gauge transformation shown in 4.11. We are now ready to write the full Lagrangian for a spinor in an e.m. field:

$$\mathscr{L} = -\frac{1}{4}F_{\mu\nu}F^{\mu\nu} + D_\mu\phi D^\mu\phi + V(\phi), \tag{4.22}$$

where the first term accounts for the e.m. field, the second term for its interaction with a fermion and $V(\phi) = m^2|\phi|^2 + \lambda\left(|\phi|^2\right)^2$ can be proven to be the most general renormalizable potential available for a U(1) gauge trasformation.

It is interesting to take a closer look at such potential. Ignoring the scenario in which $\lambda < 0$, not interesting because there would be no lower bound of the potential for $|\phi| \to \infty$ and, therefore, no ground state allowed, it is possible to distinguish two different scenarios: (a) $m^2 > 0$ and (b) $m^2 < 0$. Figure 4.3 shows the shape of the potential for both cases. When $m^2 > 0$, the gauge symmetry is conserved and theory reverts to the standard QED scenario of a charged scalar field ϕ with mass m and a massless boson. $m^2 < 0$ presents a more interesting scenario in which the lowest energy state shifts from $\phi = 0$ to:

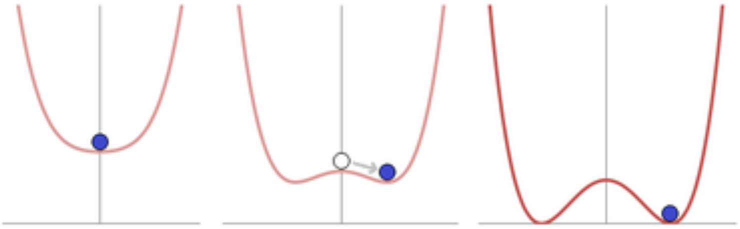

Figure 4.3.: Spontaneous symmetry breaking in the Higgs mechanism [108].

$$\langle\phi\rangle = \sqrt{-\frac{m^2}{2\lambda}} \equiv \frac{v}{\sqrt{2}}. \tag{4.23}$$

This quantity is usually referred to as the *vacuum expectation value (VEV)* of the scalar field. When the VEV is not at $\phi = 0$, the system evolves along the potential until such condition is fulfilled, in a mechanism known as *spontaneous symmetry breaking* of the global U(1) symmetry.

It is customary to rewrite the complex scalar field ϕ as a function of two real fields χ

and h for which $\langle\chi\rangle = \langle h\rangle = 0$, with the following relation:

$$\phi \equiv e^{i\frac{\chi}{\sqrt{2}\langle\phi\rangle}}\left(\langle\phi\rangle + \frac{h}{\sqrt{2}}\right). \tag{4.24}$$

With this, the total e.m. Lagrangian can be rewritten as:

$$\begin{aligned}\mathscr{L} = & -\frac{1}{4}F_{\mu\nu}F^{\mu\nu} + \frac{1}{2}\left(\sqrt{2}e\langle\phi\rangle\right)^2 A_\mu A^\mu + \frac{1}{2}\left(2m^2h^2\right) + \frac{1}{2}\partial_\mu h\partial^\mu h + \frac{1}{2}\partial_\mu\chi\partial^\mu\chi \\ & - \left(\sqrt{2}e\langle\phi\rangle\right) A_\mu\partial^\mu\chi + O(h,\chi\ S.I.),\end{aligned}$$

which represents a system with a massive photon of mass $\left(e\sqrt{2}\langle\phi\rangle\right)$, and where $O(h,\chi\ S.I.)$ represents higher order self-interactions of the h and χ fields, that can be neglected. In addition to that, the scalar field h has a mass-squared term $M_h^2 = -2m^2$, and the other scalar field χ has no mass and is often referred to as a Goldstone or Nambu boson. In return it shows up in the terms $-\left(e\sqrt{2}\langle\phi\rangle\right)A_\mu\partial^\mu\chi + \frac{1}{2}\partial_\mu\chi\partial^\mu\chi$, and its dependence can be removed from the Lagrangian by the choice of the *unitary gauge*, i.e. choosing A_μ such that:

$$A_\mu \to A'_\mu = A_\mu - \frac{1}{e\sqrt{2}\langle\phi\rangle}\partial_\mu\chi \tag{4.25}$$

thus completing the so-called *Higgs mechanism* in the U(1) case.

We can now apply the same mathematical construct to the non-abelian $SU(2)_L xU(1)_Y$ electroweak scenario.

In this case we start with a Lagrangian that looks like the following:

$$\mathscr{L} = -\frac{1}{4}W^i_{\mu\nu}W^{i\mu\nu} - \frac{1}{4}Y_{\mu\nu}Y^{\mu\nu} + \langle\psi|\, i\gamma_\mu D^\mu\, |\psi\rangle\,, \tag{4.26}$$

where the weak hypercharge tensor has the same form as the e.m. tensor in 4.9 and the weak isospin tensors have the form:

$$W^i_{\mu\nu} = \partial_\mu W^i_\nu - \partial_\nu W^i_\mu + g\epsilon^{ijk}W^j_\mu W^k_\nu, \tag{4.27}$$

where ϵ^{ijk} is the Levi-Civita symbol and accounts for the non-abelian component of the symmetry group and can be seen as the self-interactions of the gauge field bosons.

Reminding the general form of the covariant derivative from 4.19, and substituting for SU(2)xU(1), we obtain:

$$D_\mu = \mathbb{I}\partial_\mu + igW^j_\mu\sigma^j - \frac{ig'}{2}Y_\mu, \tag{4.28}$$

where W^j_μ and Y_μ are the generators of the weak isospin and hypercharge and σ^j the corresponding Pauli matrices.

In this case, since, by construction, the electroweak theory couples to left-handed SU(2) doublets, to be able to interact with the electroweak bosons the complex scalar field must be a doublet as well:

$$\Phi = \begin{pmatrix} \phi_1 \\ \phi_2 \end{pmatrix} = \begin{pmatrix} \phi_+ \\ \phi_0 \end{pmatrix} \tag{4.29}$$

with the furthermost labels hinting to the charge quantum number of the fields $\phi_{1,2}$. Again, similarly to the U(1) abelian case, the minimal renormalizable potential is:

$$V(\Phi) = m^2\Phi^\dagger\Phi + \lambda\left(\Phi^\dagger\Phi\right)^2. \tag{4.30}$$

It follows from the abelian case that, if $\lambda > 0$, $m^2 < 0$, then $\langle\Phi\rangle \neq 0$, and the VEV doublet is generally chosen to be:

$$\langle\Phi\rangle \equiv \frac{1}{\sqrt{2}}\begin{pmatrix} 0 \\ v \end{pmatrix} \tag{4.31}$$

whose quantum numbers are $Q\langle\Phi\rangle = 0$ and $\mathrm{Y}\langle\Phi\rangle = 1$.

We can now look at the interaction of such field with the electroweak gauge bosons $W^\pm$ and Z^0. The scalar field contributes to the total Lagrangian in a similar way to the U(1) case of equation 4.22, as follows:

$$\mathscr{L} = (D^\mu\Phi)^\dagger(D_\mu\Phi) - V(\Phi). \tag{4.32}$$

Keeping in mind that the covariant derivative, expressed in equation 4.28, depends on the weak isospin generators, and using the VEV from equation 4.31, we can extract the bosons masses as a function of the kinetic term of the Higgs scalar field from the following equation:

$$\frac{1}{2}(0, v)\left(\frac{1}{2}g\sigma\cdot W_\mu + \frac{1}{2}g'B_\mu\right)^2\begin{pmatrix} 0 \\ v \end{pmatrix}, \tag{4.33}$$

where the observable bosons are, similarly to what was done in equation 4.6, a combination of the generators:

$$\begin{aligned} W^\pm_\mu &= \frac{1}{\sqrt{2}}(W^1_\mu \mp iW^2_\mu) \\ Z^\mu &=- \frac{g'B_\mu + gW^3_\mu}{\sqrt{g^2+g'^2}} \\ A^\mu &= \frac{g'B_\mu + gW^3_\mu}{\sqrt{g^2+g'^2}} \end{aligned} \tag{4.34}$$

and, from these:

$$\begin{aligned} M_W^2 &= \frac{1}{4} g^2 v^2 \\ M_Z^2 &= \frac{1}{4} \left(g^2 + g'^2\right) v^2 \\ M_A &= 0 \end{aligned} \tag{4.35}$$

Finally, it is interesting to note that, since the photon e.m. coupling is the charge e, the Higgs couplings g and g' constrain the electroweak angle θ_W:

$$\begin{aligned} e = &\quad g \sin\left(\theta_W\right) \\ e = &\quad g' \cos\left(\theta_W\right). \end{aligned} \tag{4.36}$$

Similarly to the bosons case, for fermions the mass can be extracted from the coupling to the Higgs scalar field as well and even in this case the couplings are proportional to the fermion masses.

4.3. Higgs Production Channels

As we have seen in the previous section, the Higgs boson direct coupling is proportional to the mass of a particle and, for this reason, it is produced mainly by the interaction of heavy quarks and bosons, either directly or via virtual loops. The dominant production mechanisms for the Higgs boson depends greatly on the species of particles used as projectile and on the energy at their disposal. At a proton-proton machine, such as the LHC, the main production mechanism is an indirect one, namely gluon-gluon fusion, as schematized in figure 4.4. The interaction goes as follows: since gluons are massless, they cannot couple to the Higgs boson directly; so two gluons, radiated from the two incoming protons, interact via the loop-exchange of a heavy virtual quark (usually a top quark), that, given its mass, serves as a link to connect the massless gluons to the Higgs boson. It is interesting to note that such process, despite being of higher order in QFT, is so strong that it surpasses tree-level processes such as $q\bar{q} \to ZH$.

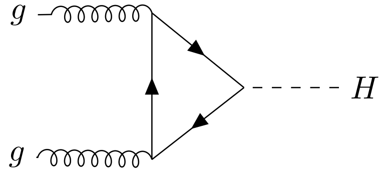

Figure 4.4.: Feynman diagram of the main Higgs production mechanisms at LHC: the gluon-gluon top-loop fusion process. Despite being a higher order loop process, it is favored, by the Higgs-to-top quark coupling strength, over other simpler tree-level processes.

Compared to the gluon-gluon fusion process of a proton-proton accelerator, in e^+e^- colliders the production mechanisms are very different. Since the rest mass of an electron is only 511 keV, although the direct e^+e^- annihilation into a Higgs boson is permitted by the Standard Model, it is a very unlikely possibility.

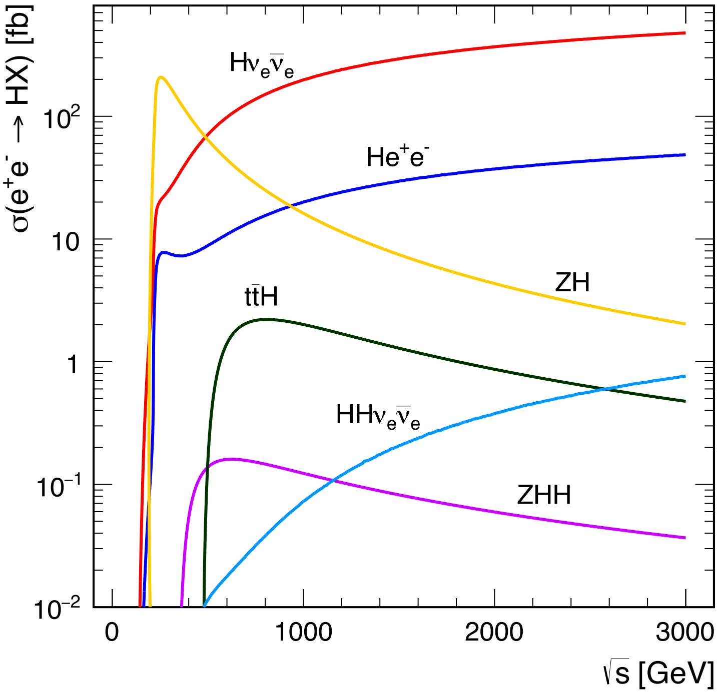

Figure 4.5.: Higgs boson production cross section as a function of the e^+e^- center-of-mass energy [117].

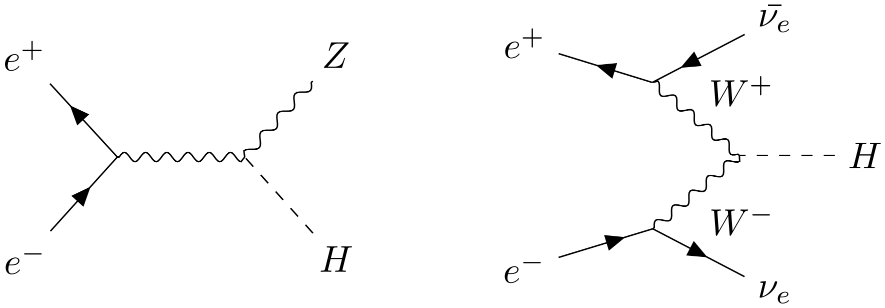

Figure 4.6.: Main Higgs production mechanisms at a 250-400 GeV center-of-mass energy e^+e^- collider. On the left side, an off-shell Z boson radiates a Higgs boson in a process known as *Higgs Strahlung* whereas on the right side, two W bosons emitted by the incoming electron-positron undergo a *Vector Boson Fusion* into an Higgs boson.

Figure 4.5 shows the Higgs boson production cross section at an e^+e^- collider, as a function of the center-of-mass energy. At the lower energies that would constitute the first stage of a machine like CLIC or ILC, namely 250-400 GeV, the main production mechanisms are *Higgs Strahlung* from an off-shell Z boson or *Vector Boson Fusion (VBF)*, mostly from W bosons, two processes whose Feynman diagrams are depicted in figure 4.6.

It is interesting to note that the Higgs Strahlung is an *s-channel* event and this reflects immediately on the shape of its cross-section vs center-of-mass energy slope: a resonant peak is present at 250 GeV, i.e. slightly above the threshold of the combined rest mass energies of the Z and H bosons (to account for *initial state radiation* and final-state kinematics), after which the cross section rapidly decreases, following an inverse square root trend. On the other hand, VBF is a *t-channel* mechanism, therefore its cross section increases logarithmically with energy. At 350 GeV, the center-of-mass energy under study in this thesis, the cross section for Higgs Strahlung is still approximately six times higher than that of VBF. The only overlapping final-state signature between the two, however, comes from the $Z \to \nu\bar{\nu}$ decays. This decay channel accounts only for approximately 20% of the total Z boson decays [118], thus giving almost exactly the same cross section as the vector boson fusion process at this energy. This is the reason why it is possible to study both production mechanisms at once only at the energies foreseen for the low energy stage of an e^+e^- linear collider, allowing to cancel out several systematic uncertainties when comparing the two production mechanisms.

4.3.1. Higgs Cross-Section Measurements via Z Recoil Mass

A precision measurement of the visible decays of the Z boson is crucial, because it allows to perform a model-independent measurement of the Higgs boson absolute cross-section and couplings, when produced with the Higgs-Strahlung mechanism, introduced in the previous section, using the recoil mass technique. For Z leptonic decays, the procedure goes as follows: first, events with a lepton-antilepton pair in the final state, whose invariant mass matches the Z boson mass, are isolated. Given this very clean signature, the selection efficiency for this step is almost completely independent with respect to the additional components of the final state configuration.

Now that the Z boson candidates have been identified, it is interesting to overview the kinematics of the Higgs-Strahlung mechanism. As we have seen in the previous section, the Higgs-Strahlung process results in a two-body final state: the Z and the Higgs bosons.

In order to be able to conserve the total momentum, we have that, in the laboratory reference frame [119]:

$$P_Z = P_H = \frac{\sqrt{(s - (M_H - M_Z)^2) \times (s - (M_H + M_Z)^2)}}{2\sqrt{s}} \tag{4.37}$$

where $\sqrt{s}$ is the center-of-mass energy and, since:

$$M_Z^2 = E_Z^2 - \mathbf{P}_Z^2 \tag{4.38}$$

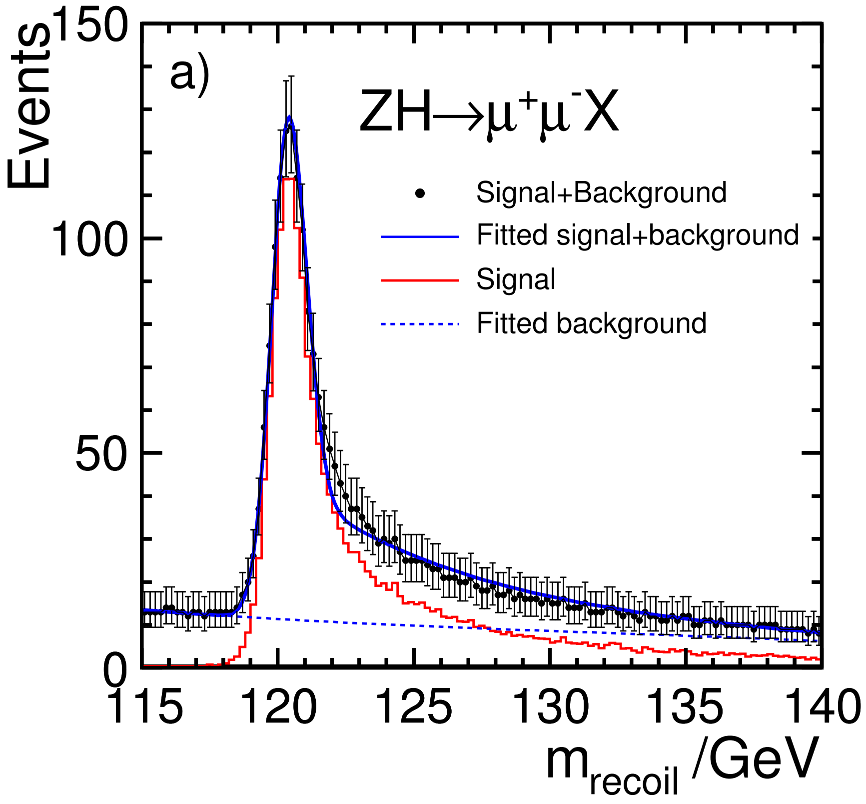

Figure 4.7.: Simulated result of a Higgs boson recoil mass measurement for $Z \rightarrow \mu^+\mu^-$ events at ILC [121].

is known from the reconstruction of the lepton pair, we can substitute it in equation 4.37 and solve for M_H as follows:

$$M_H^2 = M_{recoil}^2 = s + M_Z^2 - 2E_Z\sqrt{s}. \tag{4.39}$$

It is important to note at this point that, in equation 4.39, the *recoil mass*, relies solely on the measurement of the center-of-mass energy and the Z boson; not only no model is assumed for the decay modes of the recoiling object, but in principle these decays products do not even need to be measured at all. This implies that the uncertainties in this measurement technique only depend on the achievable precision in the measurements of the beam parameters and the dilepton (being it an e^+e^- or a $\mu^+\mu^-$ pair) energy. Moreover, since the measurement is agnostic to the rest of the final state, even potential *invisible* Higgs decays are accounted for and show up in the recoil mass measurement [120]. This is what makes the recoil mass measurement fully model-independent.

Since the two visible leptons are charged particles, they leave a track in the detector that can be used to reconstruct their momentum and, ultimately, their energy. It has been shown [122] that, with a tracking subdetector capable of achieving a resolution in the order of $\frac{\sigma P_T}{P_T} \approx 2 \times 10^{-5}$ GeV^{-1}, the mass measurement uncertainties at a 250 GeV ILC option, with 250 fb^{-1} of integrated luminosity, are below 50 MeV for both the $Z \to e^+e^-$ or a $Z \to \mu^+\mu^-$ options.

A similar measurement can be performed also for the hadronic final states of the Z boson. In this case, the inherent increase in difficulty originated by the measurement of complex particle jets in the final state, rather than isolated leptons, is compensated by the sheer number of events in this channel: in fact, while leptonic Z decays account for only 10% of all decays, the hadronic decay modes dominate the scene with almost 70% of the total [118]. The difference in branching ratios makes the recoil mass measurement more precise for the hadronic Z boson decays than for the leptonic ones [120].

This result is also at the core of the measurement of one more quantity of interest: the total cross section for Higgs-Strahlung events. This is a key parameter as it serves as a normalization factor for many successive Higgs decay studies. The uncertainty in Monte Carlo simulations, for the ILC 250 GeV, 250 fb^{-1} option and Z leptonic decays, has been estimated to be 2.5% [121] whereas, in a 350 GeV, 500 fb^{-1} CLIC scenario with $Z \to q\bar{q}$ decays, the statistical error is at the 1.8% level [120].

4.4. Higgs Decay Channels

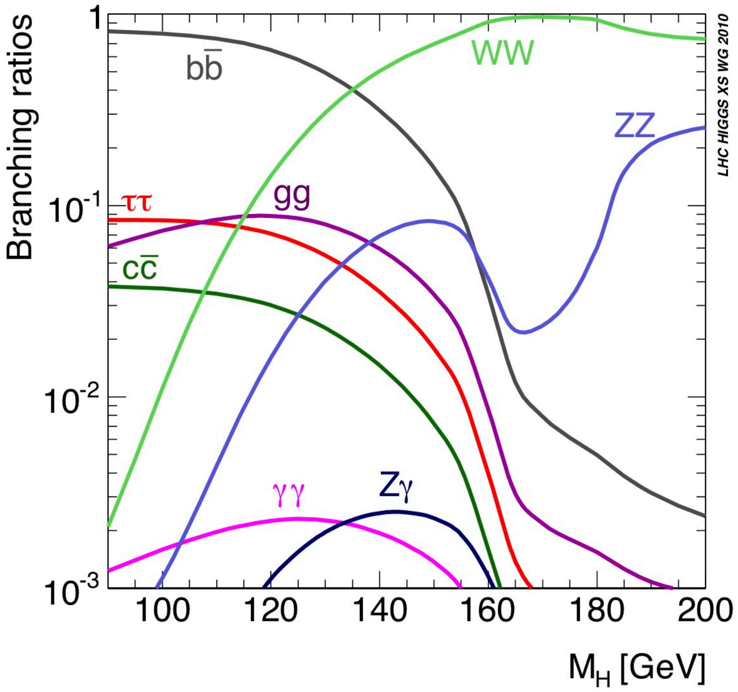

Figure 4.8.: Higgs boson branching ratios as a function of its invariant mass [123].

The discovery of the Higgs boson in 2012 at LHC delivered to the particle physics community not only a new particle and the last missing block in the Standard Model framework, but also a measurement of its mass that puts this scalar particle in one of the most interesting regions of the phase space, as far as its decay products are concerned. Figure 4.8 shows the computed branching ratios of a Standard Model Higgs as a function of its rest mass. It is immediately apparent that the region around the 125 GeV mass measurement that we have today is the richest in possible decay channels for the Higgs. Similarly to its production, also the decays of the Higgs boson reflect its fundamental characteristic of coupling to mass. Taking into consideration the Higgs rest mass and the energy conservation principle, it is clear that the decay probability of the Higgs boson to some particles, whose coupling to the Higgs would be highly favored by their mass, is suppressed to a negligible amount by the mass difference between the Higgs and the particles into consideration. This is the case for $H \rightarrow t\bar{t}$, where the energy in the Higgs reference frame is simply not enough to produce a top-antitop pair. Despite this fact, the Htt vertex is still present when considering higher order loops, and it is the main contributor to the $H \rightarrow gg$ decay, that generates two gluons from a virtual top triangle, much like the LHC Higgs production mechanism presented in figure 4.4, only with the time arrow reversed. It is, once again, only because of the large coupling constant to the massive top quarks that this decay channel can compete in strength to lower order diagrams, such as $H \rightarrow \tau\bar{\tau}$. For similar kinematic restrictions, also $H \rightarrow W^+W^-$ and $H \rightarrow ZZ$ can only be achieved when at least one of the outgoing bosons is highly off-shell, and this is the reason why the otherwise large fractions of events in these channels are comparable to less massive decay products at 125 GeV

Table 4.1 summarizes the Standard Model branching fractions for a 126 GeV Higgs, the invariant mass chosen for all the CLICdp collaboration simulations involving the Higgs boson, including those used further on in this thesis work.

Process	Branching Fraction
$H \rightarrow b\bar{b}$	56.1%
$H \rightarrow \tau^+\tau^-$	6.2%
$H \rightarrow \mu^+\mu^-$	0.021%
$H \rightarrow c\bar{c}$	2.83%
$H \rightarrow s\bar{s}$	0.024%
$H \rightarrow gg$	8.48%
$H \rightarrow \gamma\gamma$	0.23%
$H \rightarrow Z\gamma$	0.16%
$H \rightarrow W^+W^-$	23.1%
$H \rightarrow ZZ$	2.89%

Table 4.1.: 126 GeV Standard Model Higgs branching fractions [89].

Part II.

Analysis and Measurements

5. Machine Learning and Multivariate Analysis

In this chapter we will get acquainted with some of the most powerful tools of modern computer science, that have proven to be a game changer in many fields of research, including experimental particle physics: machine learning and multivariate analysis. Although all of these methods are rather agnostic when it comes to the particular field or class of problems they are applied to, the accent will be put, where possible, to the aspects peculiar to the challenges encountered during the realization of this thesis work. In this respect, this chapter is by no means a complete compendium of machine learning, but a partial and biased overview of the tools that have proven useful in extracting signal events from the large Standard Model background, thus maximizing the significance and resolving power of the data set under consideration.

5.1. Machine Learning Algorithms

Machine learning is the branch of computer science that specializes on solving classification and regression problems without explicitly encoding a step-by-step solution for each possible configuration of the given parameter space. Much like the approach of a human being to a problem, machine learning diverges considerably from the classic *if ... else* list of statements, typical of many canonical data processing algorithms, in which a programmer would have to foresee all possible input scenarios and program the computer to cope with each of them in a deterministic way. The approach is rather to present a set of examples to the multivariate algorithm and to allow it to make small (and often random) modifications to the importance the system gives to each input variable in its internal set of feedback loops. The process continues until the machine *learns* the tasks, i.e. until the changes in the *weights* of the algorithm, when presented with a fresh set of example, give the desired result in an acceptable fraction of trials. In sections 5.3 and 5.4 we will have a look at two very powerful machine learning algorithms that have been actively used to generate the results of this thesis. Thanks to the ever increasing processing power that modern CPUs provide, this class of algorithms is seeing a dramatic spread in their use in every field of human endeavors, including science. Their flexibility and robustness allow to tackle several classes of problems, in particular in the field of multivariate analysis.

Multivariate analysis refers to the study of multivariate statistics problems, i.e. statistical occurrences in which the effects of multiple variables, often correlated to one another, are investigated simultaneously. For this class of events, machine learning algorithms provide a very powerful tool-set, especially when increasing the dimensionality of a problem, a condition that would require an exponential increment in the amount of time and work programmers would need to put in defining the solution, if they were to hard-code the outcome for every possible subset of the input phase-space.

5.2. Classifiers

In this context, a *classifier* is a member of a particular subclass of machine learning algorithms, namely the one that encompasses the all methods whose task is to partition a given input ensemble in two (or more) groups, each of them carrying some distinct peculiar property. Contrary to classical classifiers, one based on machine learning does not need to be explicitly taught the features of interest, but rather presented with a statistically significant and representative sample of events from each of the classes of relevance (called supervised learning). The machine learning algorithm task is to find the optimal set of hyper-cuts in the parameters hyper-space that maximize the separation between what is considered signal and background for that given choice of test statistics.

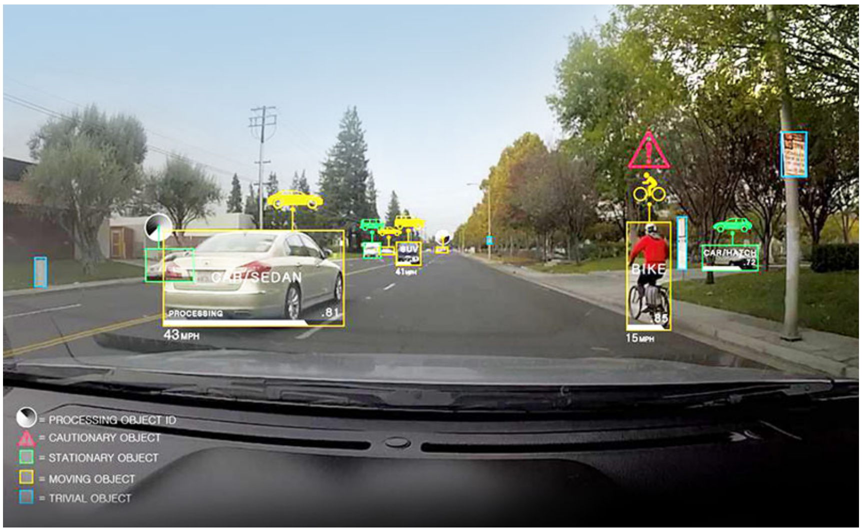

Figure 5.1.: A machine learning classifier detects road obstacles in real time for a self-driving car [124].

These algorithms are seeing an ever increasing spread in their usage in most fields of science as well as in everyday life, from medical diagnostics, to object-recognition in self-driving cars (as in figure 5.1), from stock-market predictive models to data mining.

5.3. Multi Layer Perceptron

Artificial neural networks, based on the modelization of biological networks of neuron cells, are among the most commonly used machine learning algorithms.

In biology, neurons are specialized cells that mediate electrical and chemical signals. The cell shape is unique, with many branches that loosely resemble the roots of a plant. These are divided in two kinds: (a) the shorter, denser ones, called dendrites, and (b) a single longer filament called axon. The dendrites can be seen as the *inputs* of this atomic processing unit, while the axon acts as the *output*. In animals, neurons are not isolated: they rather form complex webs of interconnections, called synapses, between each other's dendrites and axons. Each neuron's behavior is quite simple: each dendrite can react to a signal coming from any connected axon, and generates an electric signal that is transmitted to the neuron core. The neuron's axon remains inactive until enough dendrites are activated simultaneously. When a certain threshold is reached, the neuron *″fires″* an electric stimulus to the axon that propagates this information to the next set of dendrites connected to it. A peculiarity of the network is that new interconnections form constantly, but only those along the paths that produce electrical signals more often are long lived, while the synapses with little activity among each other, quickly regress, dynamically altering the weight that each synapse carries when processing the electrical signal. The remarkable property of this setup is that, from a rather simple starting recipe, given time and external stimuli, a complex system arises, capable of remarkable signal processing and intuition: the brain. The governing laws of this system can be described, in first approximation, with a very simple set of rules. Mathematicians, computer scientists and biologists have dedicated many decades on the development of models to reproduce such behavior in an artificially generated system, trying to replicate the brain's signal processing capabilities. Unfortunately, while the building bricks are easy to model, the sheer number of modeled neurons and interconnections,

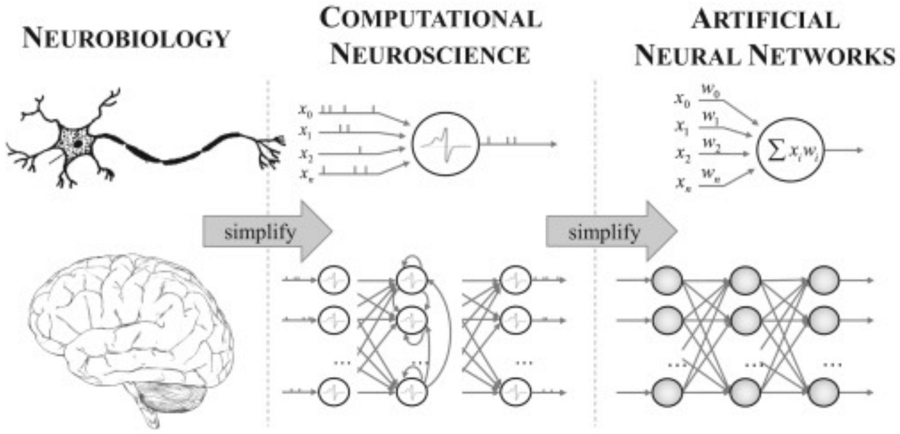

Figure 5.2.: "From biology to neuroscience to AI, the abstraction of neurons in machine learning computer science." Figure and caption from [125].

and their extremely complex topology filled with loops and positive feed-backs, is not. In fact, until quite recently, there were not CPUs with enough processing power to perform simulations that could compete with human skills in a reasonable amount of time. In the last decade, however, the exponential growth of operations per second that a microprocessor can complete, and a massive push toward parallel architectures, even in consumer products, have solved many of these limitations.

The mathematical model of a neuron usually looks like a weighted linear combination of its many inputs that is then fed through a steep non-linear function such as an error-function or a sigmoid function. The single output value from this computation is then propagated further to the next set of neurons. The weights can be then adjusted, using one of many methods developed so far, until the total output of the network mimics the desired classification properties.

Multi-layer perceptrons are a particular implementation of neural networks in which part of the complexity of the topology can be simplified by organizing the neurons in ordered layers, in which the outputs of a layer can only connect to the inputs of the next layer, much like in the bottom right corner of figure 5.2. This configuration allows for code implementations that are intrinsically more parallelizable and, because of its one-way signal flow, enables the use of the so called back-propagation method to update the neurons' weights [126].

This consists in the comparison, for a given input signal, of the output of the neural network to the expected result. A so-called *cost function* can then estimate the error associated to each neuron in the output layer. The procedure can be repeated, for each neuron in the network, to compute the error of its direct predecessors all the way back to the input layer, hence the name back-propagation. The error estimation for each neuron can then be used in an optimization procedure to tweak the weights of each neuron and find the minimum of the loss function.

5.4. Boosted Decision Trees

Decision trees are simple yet very powerful tools in the domain of machine learning. Although their implementation relies on many parameters that can be fine tuned to achieve the best results (which will be discussed later in this and the following section), the general algorithm concept for classifiers based on a decision tree works as follows:

- In preparation to the classifier's training stage, a set of example events, for which the characterization in signal and background is known *a priori*, is randomly split into two sub-groups. These events can be either real data from previous experiments, or, as in the case of this analysis, Monte Carlo generated. The first collection of events will be used for the decision tree training procedure, whereas the second, statistically independent from the first, will be used to test the signal-to-background separation power of the generated classifier, before applying it to the unsorted sample of events that needs classification.

- To create the first decision tree, the training sample parameter space is scanned in discrete steps in search of the best user-defined input variable and variable value that maximizes the following *cost function*:

  $$S = \frac{\Sigma_s w_s}{\Sigma_s w_s + \Sigma_b w_b}, \tag{5.1}$$

  where s and b refer to the index of signal and background events, respectively, and w refers to a weighting factor that for the first tree is set to 1. This binary cut can be seen as an hyper-plane that splits the parameters hyperspace into two regions, one of which has the highest signal-to-background ratio achievable with a single cut.

- Once this hyper-plane is found, the sample is *branched* into two parts, usually referred to as *leaf nodes*, and the process is recursively applied to each node until some stopping criterion, usually a threshold value for S or a minimum number of events in a node, has been reached. This creates a cascade of nodes and binary branching options that resemble a tree-shape, as can be seen in figure 5.3.

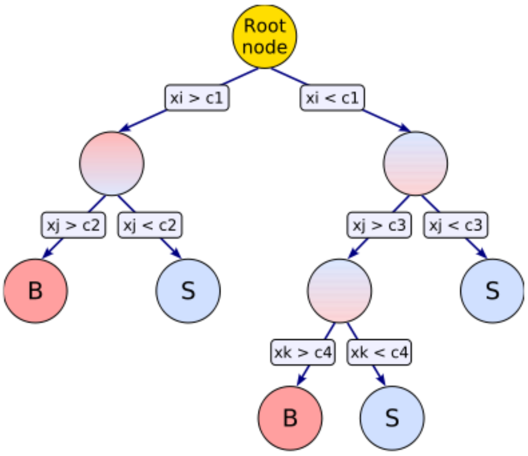

Figure 5.3.: Diagrammatic sketch of a decision tree structure. Figure from [127].

So far we have produced a single tree in a fashion that is not very different from a classical cut-flow analysis. It is apparent that there is a trade-off between the accuracy achievable by adding steps, and therefore increasing the *depth* of the tree, and the risk of *overtraining*, i.e. specializing the cuts to a degree that starts to pick up the statistical fluctuations of the training sample, focusing on these artifacts to give an artificially inflated signal-to-background ratio. This is why keeping a pristine statistical independent sample is crucial to validate the classifier performance without the hinder of artifacts. As a result, the depth is generally kept to a minimum and this generates, for a single decision tree, a so-called *weak learner*, that is a modelization of our data sample whose separating power is not much higher than a simple random sample. If we where to generate additional trees following exactly the aforementioned deterministic recipe, nothing would change and we would end up with a multitude of decision trees, all looking precisely the same.

This is where the concept of boosting comes in: when training the second tree, the weights in equation 5.1 are modified, event by event, in order to give a higher impact to the signal and background event that have been misclassified by the first decision tree and, conversely a lower relevance to those that have been sorted properly.

Generating sequentially several hundred trees allows to create a *forest* of weak learners, each specialized in some feature of the parameter phase-space, that can individually express a *yes/no* vote on the classification of an unknown event. The sum of all votes can be easily normalized and converted to a rational number that expresses the probability for that event to be part of the signal sample. Again, the risk of overspecializing the classifier on the particular training set is mitigated by the validation realized with the testing sample.

5.5. TMVA - The MultiVariate Analysis Toolkit

The algorithms described in the previous sections give an implementation-agnostic general overview of two machine learning methods. In this section we will discuss the analysis library used in this thesis work, namely TMVA [127]. This is a multivariate analysis software toolkit specifically designed to work in tandem with the ROOT analysis toolkit developed at CERN. It implements many machine learning algorithms, including several kinds of neural networks, boosted decision trees (BDTs), support vector machines and Fisher discriminants among others.

As we will see in the next chapter, the events' selection method, designed for the main analysis of this thesis, makes a large use of the TMVA BDT method. For this reason it is useful to introduce the parameters that this library exposes to the user, whose values have been optimized for the best performances in the given task.

NTrees: the number of target trees that populate the forest. Typically smaller values result in a faster, but less accurate classification.

nCuts: the number of sampling points in each dimension of the input phase space used to find optimum signal-to-background cuts. Finer resolutions can help resolve discontinuous input parameters, especially when the number of trees under training is not too large, but the performance hit scales very fast with the dimensionality of the input phase space.

MaxDepth: the maximum distance of a node from the root node. This parameter affects how specialized a tree can become, but it exposes the algorithm to potential overtraining, especially when the *minimum node size* is allowed to be too small.

MinNodeSize: the minimum fraction of the total training sample required by the algorithm to further work on a node. This parameter, together with the previous one, is quite important to assess how weak a single tree learner might be. The trade-offs are in terms of speed and potential overtraining issues.

BoostType: the type of boosting adopted to update the trees' weights. AdaBoost, a.k.a. *adaptive boosting* [128] is the most widespread algorithm for BDTs, and, being the strategy used in the course of this thesis, it is worth investigating in a little more detail.

In the previous section we have already introduced the concept of boosting, so let's have a more formal look at the actual algorithm used to achieve it. As we have seen before, the duty of a boosting algorithm is to update a set of weights $W(0), W(1)...W(m)$, one for each example presented as input. This input consists, for each example, of the vector of input parameters $\mathbf{x}_i$ and a value $y_i \in \{-1, +1\}$ that characterizes the event as signal or background. For T iterations (in our case trees) the boost algorithm has to provide an estimation of: $W_{t+1}(i)$ as a function of $W_t(i)$ and the distance between the *weak hypothesis* $h_t(\mathbf{x}_i)$ and the actual set of known results y_i. This distance can be formulated as a function of $W_t(i)$ as:

$$\epsilon_t = \sum_{i:h_t(\mathbf{x}_i)\neq y_i} W_t(i). \tag{5.2}$$

This is where adaptive boosting takes place: the suggested update for the weights is chosen according to:

$$D_{t+1}(i) = \frac{D_t(i)}{Z_t} \times \begin{cases} e^{-\alpha_t} & if\ h_t(\mathbf{x}_i) = y_i \\ e^{\alpha_t} & if\ h_t(\mathbf{x}_i) \neq y_i \end{cases} \tag{5.3}$$

where Z_t accounts for the overall normalization and α_t is defined as:

$$\alpha_t = \frac{1}{2} ln \left(\frac{1-\epsilon_t}{\epsilon_t}. \right) \tag{5.4}$$

AdaBoostBeta: The Adaptive boosting algorithm just shown, can be further tuned by applying the following transformation:

$$\alpha_t \rightarrow \alpha_t^{\beta}, \tag{5.5}$$

where the β term can be used to force a sub-linear learning rate, in order to avoid abrupt and discontinuous changes in the weights among trees that could potentially make the results more noisy.

6. Higgs Analysis

In this chapter we will discuss the main component of this thesis: the achievable resolution in the measurement of the Higgs boson branching fractions to hadronic final states in a scenario where the center-of-mass energy for CLIC stage 1 is 350 GeV. This is a particularly interesting analysis because, as we have seen in chapter 4, for a Higgs boson in the 126 GeV mass region, the hadronic final states account for almost 70% of all possible Higgs boson decays, and this fraction can be further split into its subcomponents $H \to b\bar{b}$, $H \to c\bar{c}$ and $H \to gg$ with total branching fractions of 56.1%, 2.83% and 8.48%, respectively [129].

Moreover, the relatively low center-of-mass energy gives simultaneous access to the two main production mechanisms, Higgs-strahlung and VBF, of the Higgs boson at an e^+e^- collider. This results in the ability to measure even more processes at the same time, possibly cancelling out some of the correlated systematic uncertainties.

The analysis can be conceptually divided into three main components:

- In the first step, a representative sample of events is produced, using Monte Carlo techniques, to simulate the integrated luminosity of several years of continuous data taking, using the CLIC accelerator luminosity spectrum estimates and the CLIC_ILD [68] detector concept for the event reconstruction. At this stage Particle Flow is applied, after which the reconstructed particle candidates are further clustered into jets. Flavor tagging is applied as well and a set of observables, useful for the successive analysis steps, are calculated and stored with the event.

- Step two consists of training a set of multivariate classifiers with a subset of the observables extracted in step one. These machine learning techniques are then used to label and reject background events in the full simulated set, thus maximizing the signal significance. Since the events under investigation can be produced with different interactions, the signature for the relevant final states is not unique and, for this reason, the signal extraction is performed separately on each final state of interest.

- Finally, from the selected events, a set of multidimensional templates are created, using variables that maximize the separating power between the Higgs decay channels under study. The templates are then fitted with a maximum likelihood procedure to a set of data-like samples generated with a toy Monte Carlo method. As we will see, extracting the uncertainties for different branching fractions simultaneously allows to infer their correlations, a feature that would otherwise not be accessible and would require the interdependence between different final states to be treated separately as systematic uncertainties.

In the following sections we will explain in detail each step of the analysis, as well as the statistical and software tools used to obtain the final results.

6.1. Event Simulation

When simulating particle physics events using Monte Carlo techniques, the first step is to calculate the matrix elements of each scattering process to precisely evaluate its cross-section and the kinematics of the final state. To do so, for all Higgs-related analyses, the CLICdp group has decided to utilize *WHIZARD* version 1.95 [130], a scriptable event generator capable of computing matrix elements at the tree-level precision. This approach has the advantage, over other widely-used event generators that utilize fixed tables of processes, of not being limited in the number of particles at the scattering level, thus allowing to compute the amplitudes of rich multi-particle final states. Additionally, having been developed with an eye of regard for lepton colliders, WHIZARD allows for a very detailed description of the beam properties (energy spread, crossing angle, beamstrahlung, ISR, polarization) [131] an example of which can be found in figure 6.1.

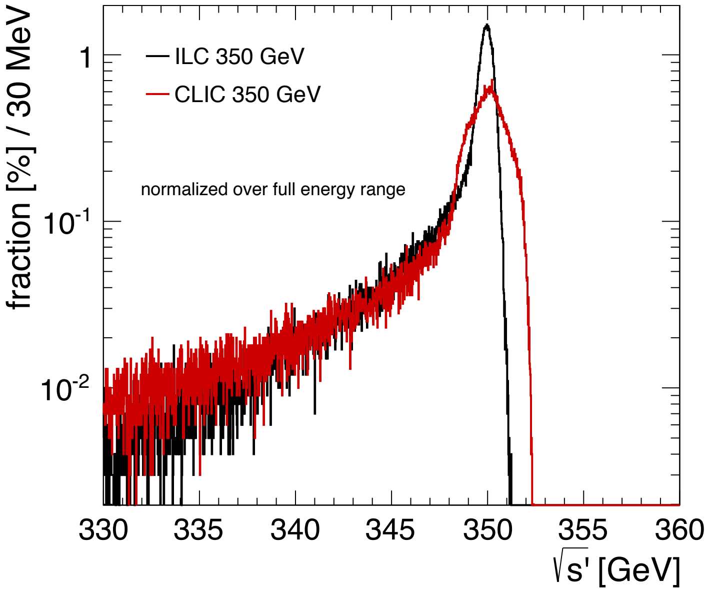

Figure 6.1.: The beam energy spectrum for CLIC and ILC at a nominal center-of-mass energy of 350 GeV [132].

For all simulations regarding the Higgs boson, it was agreed to use a Higgs mass $H_M = 126\,\text{GeV}$ and couplings according to the *Handbook of LHC Higgs Cross Sections* [129] from the LHC Higgs Cross Section Working Group. To produce the Standard

Model background samples and avoid double counting events among several processes, the Higgs mass was set to 12 TeV for these sets of events.

Final states that are only accessible at the loop-level, such as $H \to gg$, are not directly available in WHIZARD; for this reason and to ensure the uniformity of results over different decay channels, all Higgs boson decays, as well as the hadronization and fragmentation of every parton generated, were processed with *PYTHIA* version 6.4 [133].

Process	σ[fb]	Number of Expected Events	Number of Simulated Events
$e^+e^- \to Hq\bar{q}; H \to b\bar{b}$	52.3	26163	256637
$e^+e^- \to Hq\bar{q}; H \to c\bar{c}$	2.62	1308	120820
$e^+e^- \to Hq\bar{q}; H \to gg$	7.94	3971	132189
$e^+e^- \to H\nu\bar{\nu}; H \to b\bar{b}$	28.86	14431	226262
$e^+e^- \to H\nu\bar{\nu}; H \to c\bar{c}$	1.44	722	113720
$e^+e^- \to H\nu\bar{\nu}; H \to gg$	4.38	2190	127290
$e^+e^- \to Hq\bar{q}; H \to other$	30.5	15250	165501
$e^+e^- \to H\nu\bar{\nu}; H \to other$	17.8	8900	145500
$e^+e^- \to q\bar{q}\nu\bar{\nu}$	324.6	162300	259979
$e^+e^- \to q\bar{q}l\nu$	5914	2957000	1376242
$e^+e^- \to q\bar{q}ll$	1704	852000	457583
$e^+e^- \to q\bar{q}q\bar{q}$	5527.3	2763650	1381232
$e^+e^- \to q\bar{q}(u,d,s,c,b)$ $M(q,q) > 50\,\text{GeV}$	24405.4	12202700	7406897

Table 6.1.: List of simulated signal and background processes, their cross section and expected number of events for an integrated luminosity of 500 fb^{-1} and a center-of-mass energy of 350 GeV at CLIC.

Table 6.1 summarizes the signal and background final states that have been used for this analysis, as well as their cross-section, and the simulated number of events with the number of events expected for a nominal integrated luminosity of 500 fb^{-1}. The choice of background samples to include has been made with the following consideration:

- The $q\bar{q}q\bar{q}$ backgrounds mainly come from the processes depicted in figure 6.2, mainly $e^+e^- \to W^+W^- \to q\bar{q}q\bar{q}$ and $e^+e^- \to ZZ \to q\bar{q}q\bar{q}$ that share a kinematic signature very similar to that of $e^+e^- \to HZ \to q\bar{q}q\bar{q}$ and are the dominant backgrounds for that channel.

- The $q\bar{q}\nu\bar{\nu}$ events, from ZZ states where one of the bosons decays into two neutrinos, as well as from vector boson fusion events where the $W^\pm$ bosons merge into a Z boson that further decays hadronically, are the main background for $H\nu\bar{\nu}, H \to q\bar{q}$ final states.

- The $q\bar{q}l\nu$ and $q\bar{q}ll$ backgrounds can also potentially contribute to the contamination of $H\nu\bar{\nu}, H \rightarrow q\bar{q}$ in those cases where the leptons in the final state have not been properly identified and reconstructed by the detector systems.

- The $e^+e^- \rightarrow q\bar{q}$ background is in principle very different compared to all the signal final states since its signature consists of two jets and no missing energy. Despite this, it is still one of the most significative backgrounds. To understand why this is the case, it must be noted that this is an *s-channel* process; at the relatively low center-of-mass energy of this analysis, the sheer number of events of this kind is almost three orders of magnitude higher even compared with the most abundant of the signal processes under investigation. For this reason, a relatively small fraction of false positive events is still very large in absolute terms.

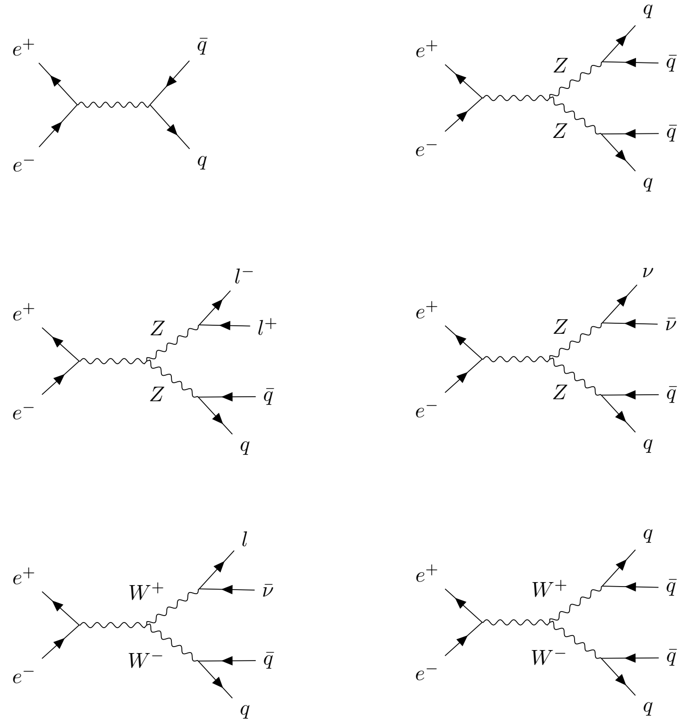

Figure 6.2.: Feynman diagram representation of the dominant background mechanisms at an e^+e^- collider at 350 GeV, when searching for two-jets plus missing energy, as well as four-jets events.

For a realistic description of the physics at the interaction region, the beam recoil for the nominal cross beam angle of 20 mrad was parametrized and taken into account in the simulation. Combined with the accurate simulation of the *initial state radiation (ISR)* emitted by the beams, it induced some of the ISR-generated photons to scatter into the particle detectors, especially in the forward regions. These ISR photons, that would otherwise not have been detected because of their collinearity with the beams, need to be taken into account when analyzing the properties of the event kinematics since they lower the energy at disposal for any further physics process to take place.

Once the task of simulating the interaction process has been carried out by the event generator, a full-detector simulation was performed on the outgoing fragments to model the interplay between the final state daughter particles and the particle detectors. For this an ad-hoc modified version of *GEANT4* [134], the *GEometry ANd Tracking* simulation toolkit, called *MOKKA* [135], specifically designed for the simulation of detectors at future linear colliders, was used.

The detector prototype in use was CLIC_ILD [136] and Mokka utilised the QGSP_BERT physics list [137], to describe hadronic interactions in the detector material.

The calibration, digitization and the initial tracklet and cluster reconstruction steps were performed by dedicated plugin processors in the MARLIN framework [138]. The processed events have been then handled to PandoraPFA [107]: a particle flow (see section 3.5) analysis framework, responsible for the reconstruction of the four-vectors and IDs of PFOs, i.e. particle candidates. The algorithms at the core of Pandora are based on multiple layers of pattern recognition and clusterization algorithms, to precisely separate particle candidates in an event.

The collection of events processed thus far, was stored at the CERN computer *GRID*, awaiting further processing.

6.2. Event Preprocessing

Once a representative sample of events has been properly simulated and, for each event, raw detectors hits have been processed into particle-like objects, it is possible to implement a higher-level physics analysis to disentangle signal event candidates from the Standard Model background. At this point we have to consider that the final states for the signals we are after consist of two main signatures: four particle jets for $H \to q\bar{q}, Z \to q\bar{q}$ events and two jets plus missing energy for $H\nu\bar{\nu}, H \to q\bar{q}$ events. These are diametrically opposite to each other and, therefore the choice was made to split the selection procedure into two independent event processing pipelines, each of which taking care of one of the signal final state signatures, resulting in two dedicated multivariate event-classifier, as shown in figure 6.3.

For each event, the procedure goes as follows: first the *initial state radiation (ISR)* photons are isolated and removed from the event particle collection. In order to do so, a cut on the photon reconstructed energy is applied: if this is above 15 GeV the photon is tagged as ISR. The threshold for this cut was obtained by comparing the energy distributions of all the reconstructed photons in two distinct set of events: simulated with and without beam-recoil, respectively. When the beam-recoil is turned off, all eventual ISR photons are produced collinear to the beam, and thus do not interact with the detector. In other terms, all reconstructed photon candidates in these events are guaranteed to be *final state radiation (FSR)*. By contrast, when the beam recoil is taken into consideration, ISR photons can be deflected enough to hit the detector and be,

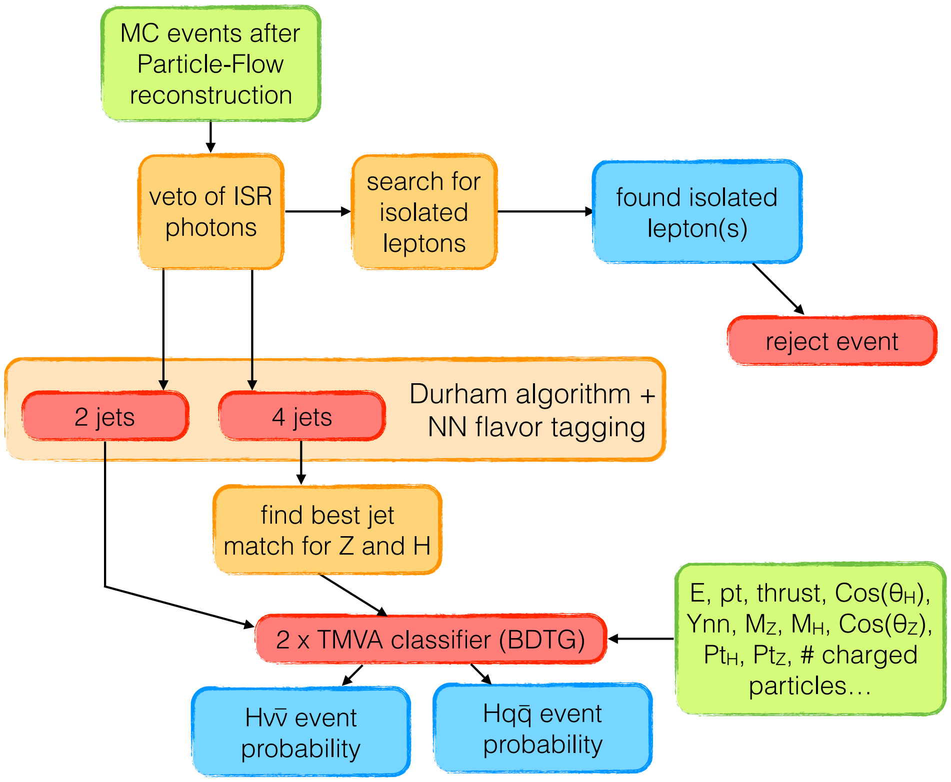

Figure 6.3.: Diagram representing the analysis strategy for the processing and classification of events into signal and background candidates.

therefore, reconstructed. By comparing the energy distribution of the photons in these two scenarios, it is possible to optimize the energy cut that gives the best separation, allowing to reject ISR, while keeping FSR photons.

After that, an *isolated lepton finder* can be used to separate high energetic leptons, produced in reactions associated with Standard Model background processes, from leptons originated in semi-leptonic meson decays inside a particle jet. The former are in fact characterized by a relatively low particle density around them, when compared to those that are produced inside a jet. The selection criterion adopted to separate the two categories of leptons in this case was to consider a lepton *isolated* if it had an energy of at least $E_l > 10\,\mathrm{GeV}$ and if the sum of the energy of all particles within a cone of 20 around its trajectory was smaller than 20 GeV. When such isolated leptons were identified, the event was immediately rejected.

Before we continue the description of the signal extraction procedures, it is useful to introduce the jet clustering algorithm that have been used on the reconstructed particle collections of all events. In the following section we will introduce the *lcfiplus* [139] library that has been used, not only for its efficiency in reconstructing and finding particle jets, but also for the capability of tagging the flavor of a jet, i.e. classifying those jets by the flavor of the quark (or gluon) responsible for initiating the jet.

6.3. Jet Clustering and Flavor Tagging

6.3.1. Particle Jets

To introduce the concepts that govern jet clustering algorithms [140], it is important to define the meaning of *particle jets* in this context. Because of color confinement, (anti)quarks and gluons in the final state can exists, in isolation, only for too-short-to-measure periods of time, of the order of less than 10^{-27} s, before undergoing hadronization. This process consists in generating pairs or multiplets of partons from the vacuum, and to bind them to each other, until all the generated fragments are color neutral. This results in a *spray* of hadrons that, collectively, retain most information about the energy and momentum of the generating (anti)quark or gluon and allows for treating the high-energy perturbative and low-energy unperturbative QCD components of an event separately [141]. Despite the intrinsic limitations, both conceptual (there is no unambiguous progression from one QCD regime to the other), as well as practical (smearing effects introduced by color reconnection and detector effects), this allows to reduce an event final-state into a much simpler configuration, consisting of, as far as (anti)quarks and gluons are concerned, a handful of particle jets, each correlated to one of the final-state partons. Such jets of particles are usually produced in a narrow cone along the parton's initial momentum vector.

Since we are interested in the properties of these initial quarks and gluons (and their parent particles), it is quite useful to have a strategy to *sum-up* the energies and momenta of all the secondary particles, produced in the hadronization step, that ultimately are the visible particles that can be observed in our detectors. This process is usually referred to as *jet clustering*. Since it is not possible to uniquely identify which detected particles belong to a particular (anti)quark or gluon (particles jet cones from different partons or from unrelated background events could be partially overlapping), the implementation of an algorithmic definition for a jet is somewhat arbitrary and heavily depends on simulations to tune its parameters. For this reason, there are several strategies to implement a jet clustering algorithm for particle physics. Some of them, based on *sequential clustering* methods, work better in clean environments such as lepton colliders. Others, like *cone-type* algorithms, have been widely used at hadron colliders in the past, but are potentially *infrared* and *collinear* unsafe. These are the undesirable properties of producing different outcomes if either (a) soft particles are emitted from the jet, or (b) one particle is factorized in two collinear components.

For the rest of this section, we will focus on two jet clustering algorithms belonging to the first class, the *JADE* [142] algorithm, and its derivation, the *DURHAM* algorithm, that is ultimately used in the lcfiplus library.

6.3.2. The JADE and Durham Algorithms

The main contribution to physics of JADE [143] (JApan, Deutschland, England) experiment at the PETRA [144] accelerator of DESY, Germany, was the co-discovery of the gluon from three jets final-state events.

To achieve this remarkable milestone, the collaboration developed a jet clustering algorithm, based on a binary joining scheme, that could handle multiple jets more efficiently than than a generalized n-jets definition of thrust.

The iterative process of this algorithm works as follows:

- The algorithm is presented with a list of particles of the event. Each of them is treated as the seed of a cluster containing only a single particle.
- A distance $d_{i,j}(\mathbf{p_i}, \mathbf{p_j})$ between clusters with four-momenta $\mathbf{p_i}$ and $\mathbf{p_j}$ is defined as such:
$$d^2_{i,j} \equiv 2\, E_i E_j \left(1 - \cos\theta_{i,j}\right) \tag{6.1}$$
where $\theta_{i,j}$ is the opening angle between the two clusters and E_i, E_j their energies. It is worth noting that this distance is not Lorentz-invariant. Therefore when the four-momenta are expressed in the laboratory rest frame, information on ISR can be used to correct for the relativistic boosting.
- $d_{i,j}$ is computed for every pair of clusters *i,j* and the pair that minimizes it is merged into a single cluster *k* by simple addition of the four-momenta.
- The process is iterated until the distances between each pair of clusters is greater than a given threshold value d_{cut} or the target number of clusters has been reached.

Sometime the dimensionless quantity $y_{i,J} = \frac{d_{i,j}}{Q^2}$, with Q being the total visible energy in the event, is preferred since it can cancel out some detector-related uncertainties from the distance computation.

As all sequential clustering algorithms, such an algorithm is infrared and collinear safe. In both cases, by construction, the algorithm will simply merge up the additional particles and recover the same final cluster configuration.

The Durham algorithm is an extension of the JADE algorithm and works exactly in the same way, except for the definition of cluster distance that becomes:

$$d^2_{i,j} \equiv 2\, min(E_i^2, E_j^2) \left(1 - \cos\theta_{i,j}\right) \tag{6.2}$$

This transverse energy dependence has the advantage, over the the JADE definition, to be less dependent of higher-order perturbative corrections [145].

6.3.3. Flavor Tagging

The ability to effectively separate the quark flavor of the Higgs decays, and, in particular, of *b* and *c* quarks, is one of the points of strength of the detector's system developed for CLIC. As we have previously seen in section 3.1.3, thanks to the high accuracy of the vertex detector, it is possible to precisely reconstruct the displacements of secondary vertices. This information, can be complemented with several other observables of interest, such as the number of electrons and muons that can be traced back to a given vertex, the distribution of the d0 and z0 impact parameters for all the helical track candidates matched to a specific vertex, their energy, and more, to distinguish between the various quark species. The lcfiplus package offers an interface to a neural-network-based multi-variate classifier, that can be used for such purpose, for which a complete set of input variables is available in at [146]. Since we are planning to use such classifier to catalog simulated Higgs boson decays, if we were to use simulated Higgs decays for the training of the neural network as well, there would be no protection against systematic errors introduced by the events' simulation procedure, potentially compromising the quality of the classification. To avoid such scenario, the network has been trained on a sample of Z hadronic decays. In particular, the Feynman diagram for the process under consideration is depicted in figure 6.4.

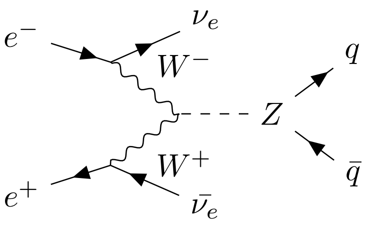

Figure 6.4.: Feynman diagram of the vector-boson-fusion production of Z bosons. The further decay of the Z boson to $b\bar{b}$, $c\bar{c}$ or light quark pairs is then used as training sample for the flavor tagging classifier of the lcfiplus package.

This has the advantage of presenting a kinematic similar to that expected for the simulated signal events, while minimizing the risks of biasing the tagging efficiency.

After the training phase, the classification can be applied to a test statistics, to estimate the flavor tagging efficiency of such method. Figure 6.5 summarizes the results of such test for both the *beauty* and the *charm* classifications, in terms of the efficiency of the signal sample as a function of the efficiency of the backgrounds.

From this it is possible to see that, while the *b-tagging* outperforms, as expected, the *charm* classifier, the latter still produces acceptable results.

Combining the two information for each particle jets it is possible to separate b-jets from c-jets from light-jets. Considering that the couplings of the Higgs boson to u, d and s quarks is negligible, and that $H \to \tau^+\tau^-$ events can be suppressed by means of a careful events selection strategy (that will be introduced in the next section), the two classifiers can be used to deduce candidates of Higgs-to-gluons decays as well.

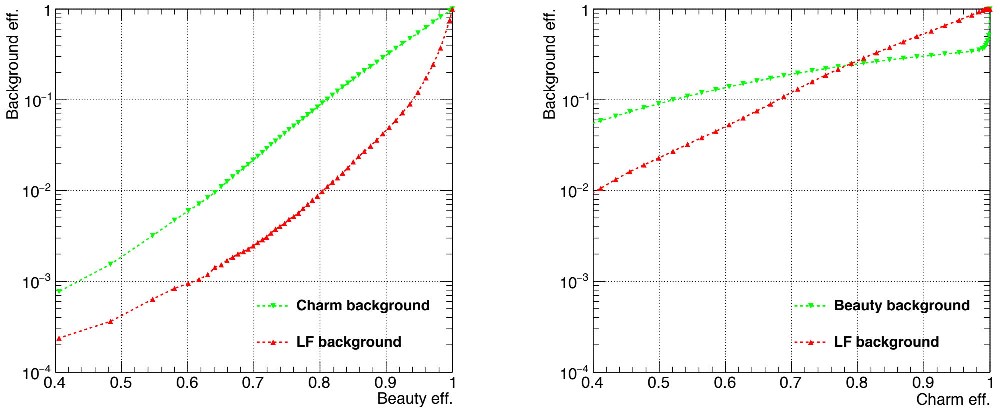

Figure 6.5.: Performance of the lcfiplus flavor tagging classifier for b-tagging (on the left) and c-tagging (on the right). The graphs show the efficiency of the classifiers to the signal species (on the linear X axis) versus that of the backgrounds (on the logarithmic Y axis). The background species are: charm and light quarks for the b-classifier, beauty and light quarks for the c-classifier.

6.4. Event Selection

Now that we are familiar with the concept of jet clustering and its implementation in *lcfiplus*, we can go back to the two scenarios depicted at the end of section 6.2, namely the 2-jets plus missing mass and the 4-jets signatures that are characteristic of our signal events. To search for instances of the former, we force the Durham algorithm to cluster each event into a 2-jet topology, whereas for the latter we do the same, but forcing a 4-jets topology.

Clearly, for events that are indeed constituted by an Higgs boson decaying hadronically and two neutrinos in the final state, the two jets must come from the daughter particles of the Higgs boson. For this reason the four-vectors of the 2-jets topology are summed together to obtain the four-vector of the potential Higgs-boson candidate. From this several interesting observables can be deducted, for example its invariant mass, that will prove to be one of the quantities with the highest separating power between signal and background events.

In the 4-jets scenario, that accounts for ZH events where both bosons have decayed hadronically, there is still a confusion about which jet belongs to which boson. To disambiguate the situation and find the best match for the Z and Higgs boson jets, a simple χ^2 minimization procedure is set, and the jets are assigned as follows:

$$\chi^2 = \frac{(M_{ij} - M_H)}{\sigma_H^2} + \frac{(M_{kl} - M_Z)}{\sigma_Z^2} \tag{6.3}$$

For the set of indices *i,j,k,l* that minimize this equation, where M_{ij} and M_{kl} are the invariant masses of the jet pairs candidates for the Higgs and the Z boson respectively, M_H and M_Z are the rest masses of the two bosons and σ_H^2 and σ_Z^2 are the widths of the invariant mass distributions, estimated to be at the 3.8 GeV level. Again, from the reconstructed Higgs and Z bosons candidates, several observables can be calculated to be later used for separating signal and background events.

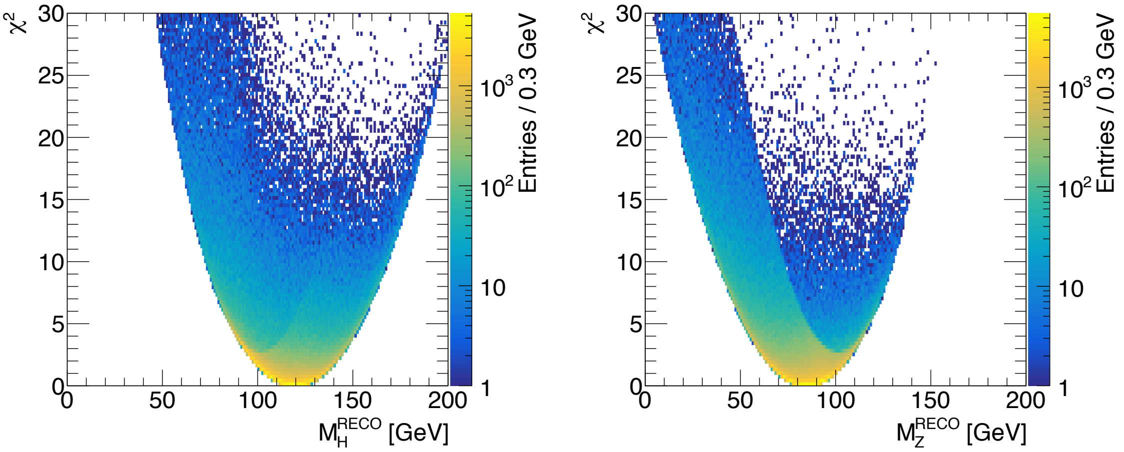

Figure 6.6.: χ^2 distribution as a function of the invariant mass of the jet pair candidates of the Higgs boson (left) and Z boson (right).

At this point of the analysis, for each event, we have a rich set of more than 100 observables, coming from two different reconstruction strategies, that can be used to extract the signal events from SM background.

A complete list of the observables that ended up being relevant in the selection procedure adopted here, can be found in appendix A, but we will investigate some of less obvious ones in the following paragraphs.

Thrust

This observable is defined, for a final state consisting of *M* particles, as follows:

$$T = max_{\hat{n}} \frac{\sum_{i=1}^{M} |\mathbf{p}_i \cdot \hat{n}|}{\sum_{i=1}^{M} |\mathbf{p}_i|} \tag{6.4}$$

where $\mathbf{p_i}$ is the momentum vector of the *i*-th particle and $\hat{n}$, usually referred to as the *thrust axis*, is the versor that maximizes the value of T.

The maximum value for this dimensionless quantity can be reached when, for each particle, the thrust axis direction coincides with that of the particle's momentum, i.e. $T = 1$. This configuration is only possible when all particles' momenta are focused in two narrow back-to-back cones, resulting in an event characteristics pencil-like shape. The opposite situation, i.e. that of a spherically symmetric event, results in a thrust value of 0.5.

The thrust distributions for the various signal and background processes, can be found in figure 6.7.

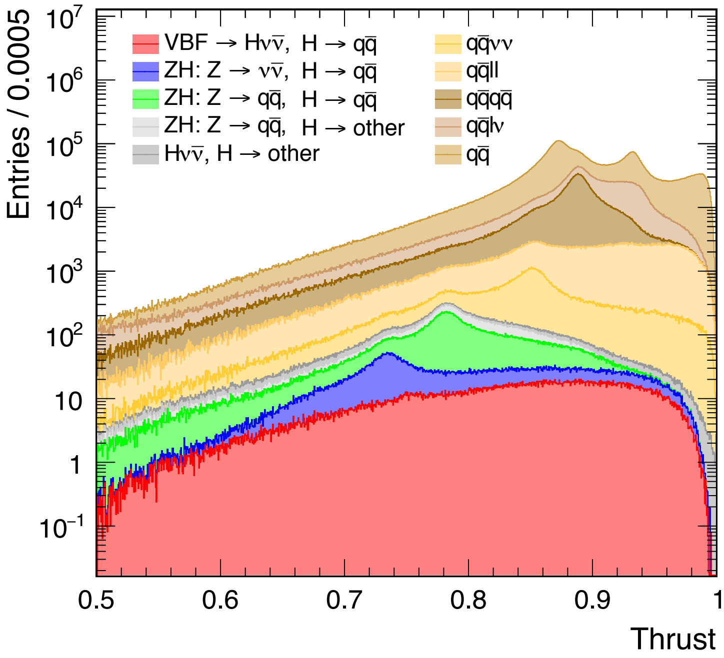

Figure 6.7.: Thrust distribution for different signal and background Monte Carlo samples, normalized by the number of expected event at $\int \mathscr{L} = 500\,\text{fb}^{-1}$.

This observable is a measure of the overall *jets-like* shape of an event. In doing so, it provides a good tool to discern a few background configurations that tend to be more focused along the direction of the beams, thus producing thrust values on average higher than those of some of the signal configurations.

Sphericity

This quantity, complementary to thrust, can also give an insight into the event topology. The definition of sphericity for N particles $\mathbf{p_n}$ is the following [147]:

$$S^{i,j} \equiv \frac{\sum_{n=1}^{N} p_n^i p_n^j}{\sum_{n=1}^{N} p_n^2} \tag{6.5}$$

with i, j being two of the three axial components x, y or z.

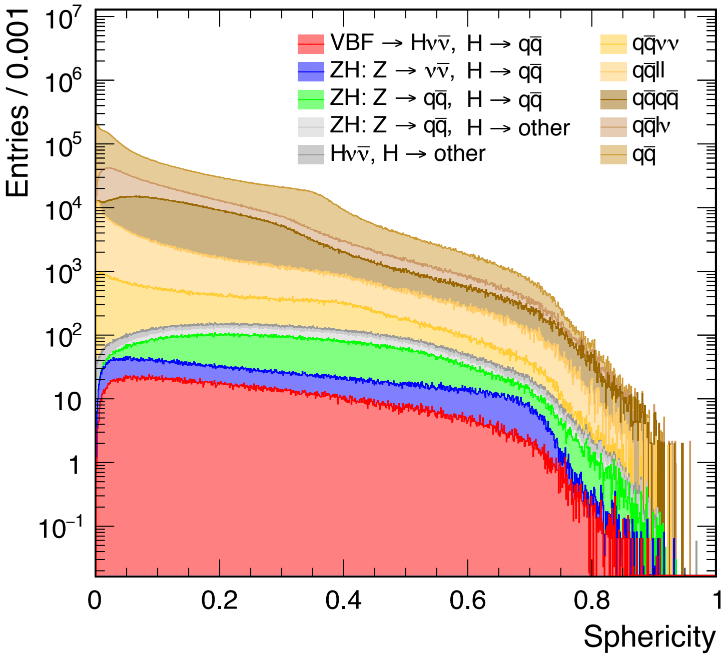

Figure 6.8.: Sphericity distribution for different signal and background Monte Carlo samples, normalized by the number of expected event at $\int \mathscr{L} = 500\,\text{fb}^{-1}$.

This is an eigenvector problem with three eigenvalues $\lambda_1 \geq \lambda_2 \geq \lambda_3$. The sphericity is defined in terms of these three values as follows:

$$S \equiv \frac{3}{2}\left(\lambda_2 + \lambda_3\right) \tag{6.6}$$

Unfortunately this definition is not collinear safe, i.e. it is not invariant if one of the vectors $\mathbf{p_k}$ is split into two shorter vector with the same direction. For this reason it is possible to use a slightly modified version as follows:

$$S^{i,j} \equiv \frac{\sum\limits_{n=1}^{N} \frac{p_n^i p_n^j}{||\mathbf{p_n}||}}{\sum\limits_{n=1}^{N} ||\mathbf{p_n}||} \tag{6.7}$$

That is sometimes referred to as the *linearized* sphericity.

Oblatness

Since we have already introduced thrust and the thrust axis, it is useful to define, two more measures related to it. The *thrust major axis* is the axis that maximizes *thrust major*,

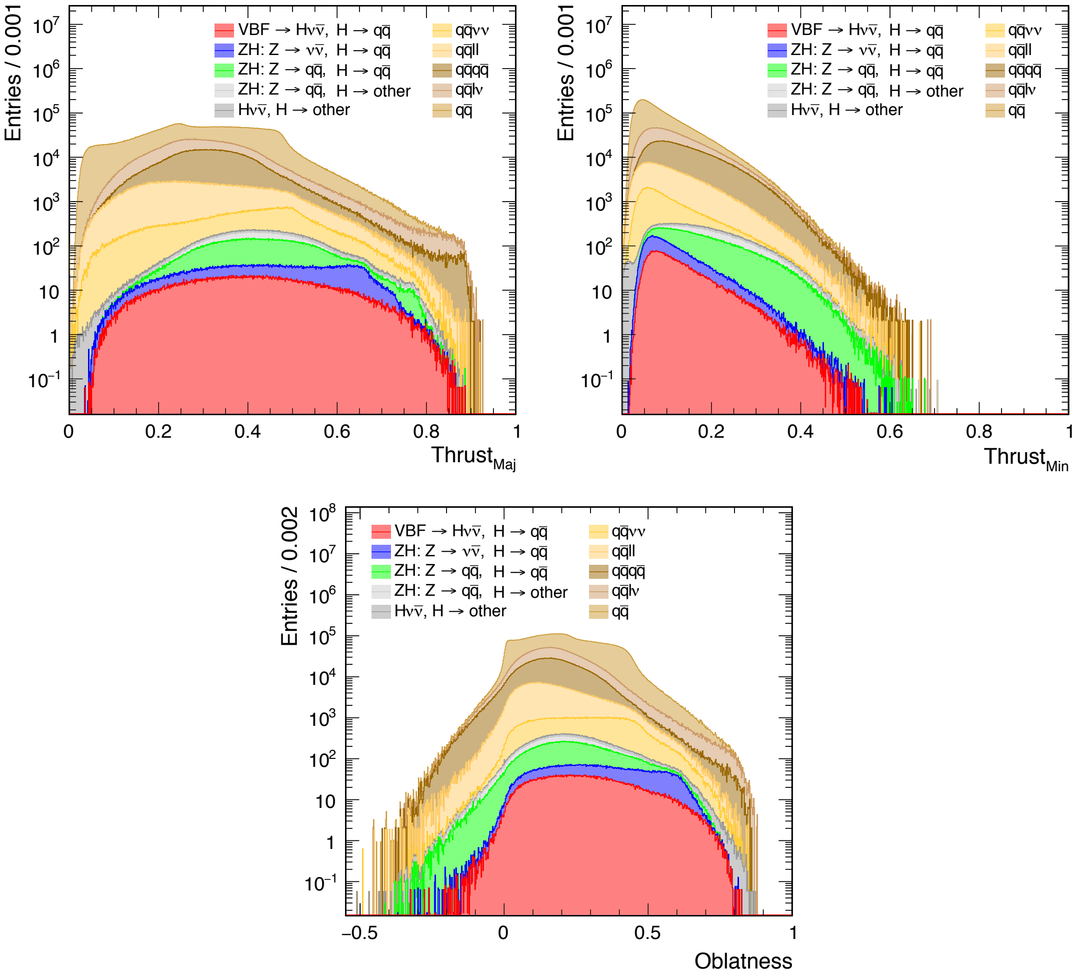

Figure 6.9.: Distribution of thrust major, thrust minor and oblatness for different signal and background Monte Carlo samples, normalized by the number of expected event at $\int \mathscr{L} = 500\,\mathrm{fb}^{-1}$.

while being also perpendicular to the thrust axis, i.e. $\hat{n}'$ such that:

$$Thrust_{Maj} = max_{\hat{n}',\hat{n}\cdot\hat{n}'=0} \frac{\sum_{i=1}^{M} |\mathbf{p}_i \cdot \hat{n}'|}{\sum_{i=1}^{M} |\mathbf{p}_i|} \tag{6.8}$$

The *minor axis* is the perpendicular to the thrust and thrust major axes and the corresponding quantity is:

$$Thrust_{min} = \frac{\sum_{i=1}^{M} |\mathbf{p}_i \cdot \hat{n}'|}{\sum_{i=1}^{M} |\mathbf{p}_i|}, \text{with } \hat{n}'' \cdot \hat{n'} = \hat{n}'' \cdot \hat{n} = 0 \tag{6.9}$$

Oblatness is defined as $Thrust_{Maj} - Thrust_{min}$ and can help characterize 3 and 4 jets events.

Spin

Spin is the intrinsic quantum number that accounts for a particle angular momentum. It presents itself in nature as an integer multiple of a base quantity, usually taken by convention to be $\frac{1}{2}$. As we have seen in chapter 4, particles with integer and half-integer spin behave according to very different statistics and conservation rules.

Spin is of particular interest for the study of the Higgs boson since this is the only elementary particle observed so far that is predicted to be a *scalar*, i.e. its intrinsic spin is 0. This gives us a powerful discriminating tool to extract potential Higgs candidates in sea of background events, especially when trying to filter out false positive Z bosons events. Although we cannot measure spin directly for these bosons, their the decay products carry an angular dependence to this quantity. In particular, there is a strong correlation between the direction of the particle under investigation and the angle, measured in the particle's rest frame, at which the decay products are produced.

For this reason, we can use the distribution of the apertures of the angles between the reconstructed 4-momenta of Higgs boson candidates and those of one of their decay products as an observable from which the spin can be inferred. Since the Higgs always undergoes a two-body decay, it is irrelevant which of the two daughter 4-momenta is chosen: being a back-to-back process in the reference frame of the Higgs boson, both carry the same information.

The procedure to determine such angle goes as follow:

- Let $\mathbf{d_1}$ and $\mathbf{d_2}$ be the 4-vectors of the daughter particles or jets of the Higgs boson candidate, the latter having 4-vector $\mathbf{H} \equiv \mathbf{d_1} + \mathbf{d_2}$
- Calculate the Lorentz boost of $\mathbf{H}$
- Calculate $\mathbf{d_1^H}$ the 4-vector of $\mathbf{d_1}$ in the reference frame of the boosted $\mathbf{H}$
- Calculate the cosine of the angle θ between $\mathbf{d_1^H}$ and $\mathbf{H}$, divided by their norm:

$$\cos\theta = \frac{\mathbf{d_1^H} \cdot \mathbf{H}}{||\mathbf{d_1^H}||\;||\mathbf{H}||} \tag{6.10}$$

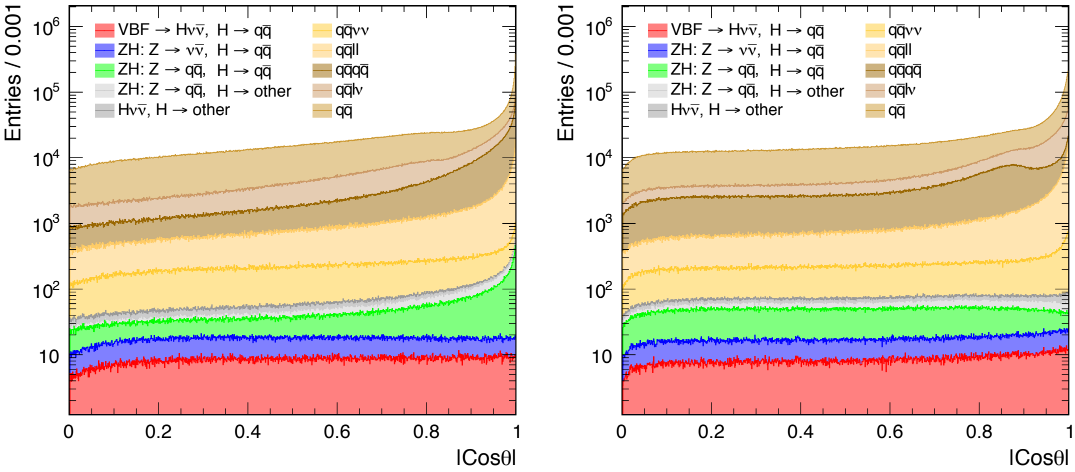

Figure 6.10.: Angular distribution of a decay product of the Higgs boson candidate, compared to the direction of the reconstructed Higgs, for 2 and 4 jets reconstructed event on the left and the right hand side respectively. The distributions are shown for different signal and background Monte Carlo samples, normalized by the number of expected event at $\int \mathscr{L} = 500\,\mathrm{fb}^{-1}$.

As we can see in figure 6.10, the distribution for such a variable for Higgs boson final state events is flat, while it peaks towards one for background events. This can help in the analysis to reject a large fraction of the two and four quarks background contamination.

Jet Topology In the previous section, we have already discussed the dimensionless quantity $y_{i,j} = \frac{d_{i,j}}{Q^2}$ that characterizes a distance between clustered jets. Instead of setting a threshold value for such distance or a target number of jets in the final state, it is possible to let the clustering algorithm keep combining jets together until there is only one jet left encompassing all the particles in the final state. In doing so, if one keeps track of the distance $y_{n,n-1}$ of the jets combined together in each step, it is possible to construct a set of observables that carry information about the topology of the event. Indeed when the number of jets clustered is still higher than the true number of jets in the final state, the distance to merge two jets will be smaller than that necessary to merge actual final state jets. Looking at the succession of values y_{56}, y_{45}, y_{34}, y_{23}, it is usually possible to find a *phase change* between relatively small values, to relatively large values, once the actual number of jets in the final state event is reached. Since these distances can span over several order of magnitude it is customary to represent them with their inverse logarithmic value, as is the case in figure 6.11, where an overview of the distributions of these threshold values, for the final state of several signal and background samples, is presented.

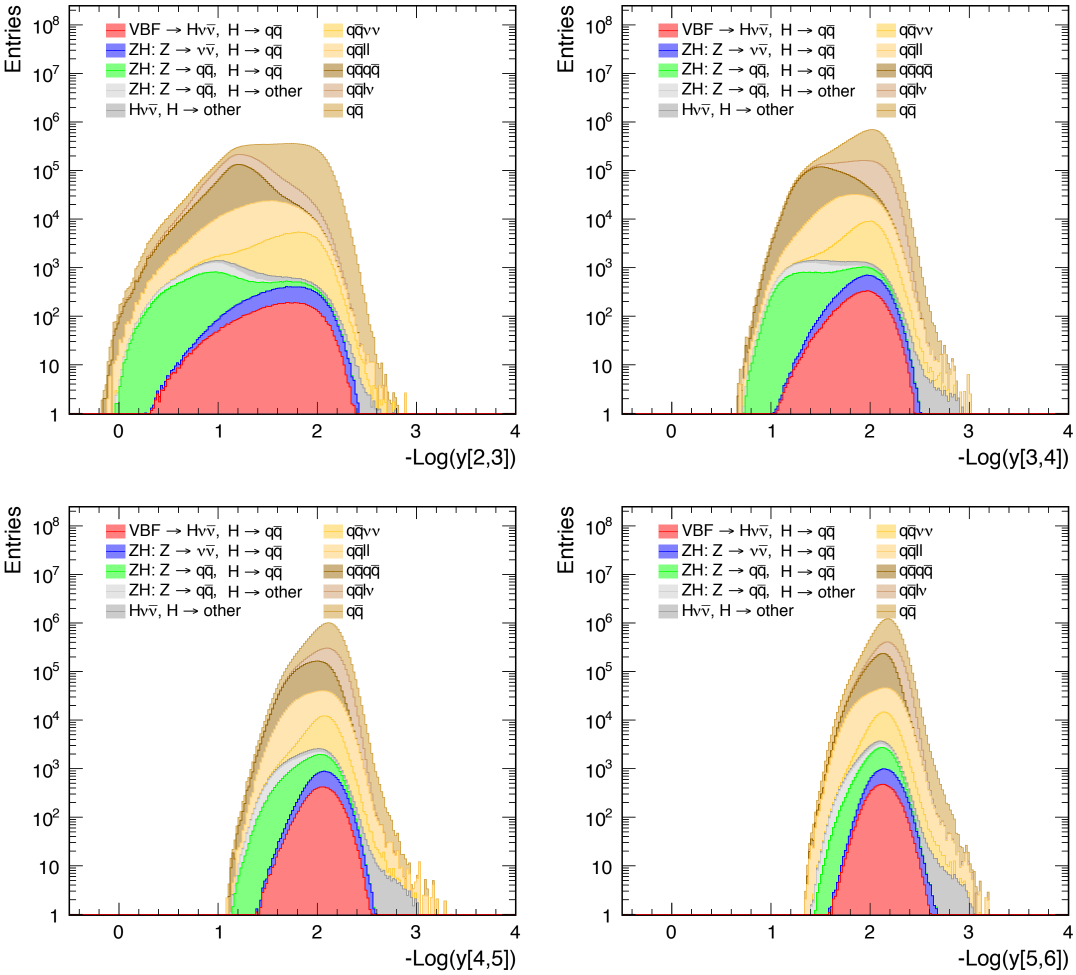

Figure 6.11.: Distributions of the logarithm of the topology-related quantities $y[n, n+1]$ for different signal and background Monte Carlo samples, normalized by the number of expected event at $\int \mathscr{L} = 500\,\text{fb}^{-1}$.

6.4.1. Background rejection

Given the large number of observables, a cut-flow based background rejection system would be impractical to establish and would provide little guarantees of giving the best significance for signal events. For these reasons and since, as we have seen in table 6.1, the difference in number of events for some of the signal channels compared to the SM background can be as high as five orders of magnitude and require a very efficient set of filters, the decision was made to use a *multivariate analysis technique*. In particular, the final implementation consisted of two independent classifiers, based on *boosted decision trees (BDT)* algorithms (see chapter 5), that were trained and used to sort $H\nu\nu, H \to q\bar{q}$ and $Hq\bar{q}, H \to q\bar{q}$ event candidates.

For each of the classifiers the training procedure was conducted as follows:

- A representative sample of Monte Carlo generated events was randomly selected among signal and background ensembles. Since the number of events generated for each process was not normalized by the integrated luminosity, a weighting factor was applied to the BDT training for each event to account for the proper SM cross-sections in order to give the BDT a realistic description of the distribution of each signal and background feature.

- Since we are only interested in Higgs hadronic decays, all other Higgs decay channels were treated as background for the training. This has proven to be particularly useful to reject $qqqq$ background events, whose features could otherwise have been mistaken for $H \to W^+W^- \to qqqq$ and $H \to ZZ \to qqqq$ processes.

- To avoid biasing the selection of Higgs hadronic decays to preferentially pick one possible decay channel among others, no flavor tagging information of the Higgs jets candidates was used to train the BDT. Despite this, since not all the observables in use are uncorrelated with respect to the flavor tagging information, an artificial additional weighting factor was introduced to up-weight signal processes with a smaller branching fraction, i.e. $H \to gg$ and $H \to c\bar{c}$, to make sure the BDT would not focus on features peculiar to the $H \to b\bar{b}$ final state.

- The number of input variables would be too large to handle in a real physics experiment, given the large number of systematics that would need to be taken care of. For this reason, an iterative method, similar to what was utilized in [148], was introduced to reduce the MVA parameter space. This is based on the following structure:
    1. The training procedure is performed using the given set of variables.
    2. The efficiency of the classifier is evaluated on the test event sample that, in a procedure that simultaneously allows to evaluate the separation power of each variable.
    3. The list of variables is sorted, in decreasing order of separation power, in a ranked list.
    4. If the impact of the lowest ranked variable to the classification is below the 1% level, the variable is removed from the set of observables under consideration.
    5. After the removal of the lowest ranked variable, procedure loops back to point 1.

The stopping criterion is then clear: as soon as each of the observables contributes to the total classification efficiency by more than 1%, the BDT optimization terminates. The complete list of all the observables that remain after this optimization is summarized in appendix A.

This leads to two classifiers, whose output distributions, divided by signals and backgrounds species, are shown in figure 6.12.

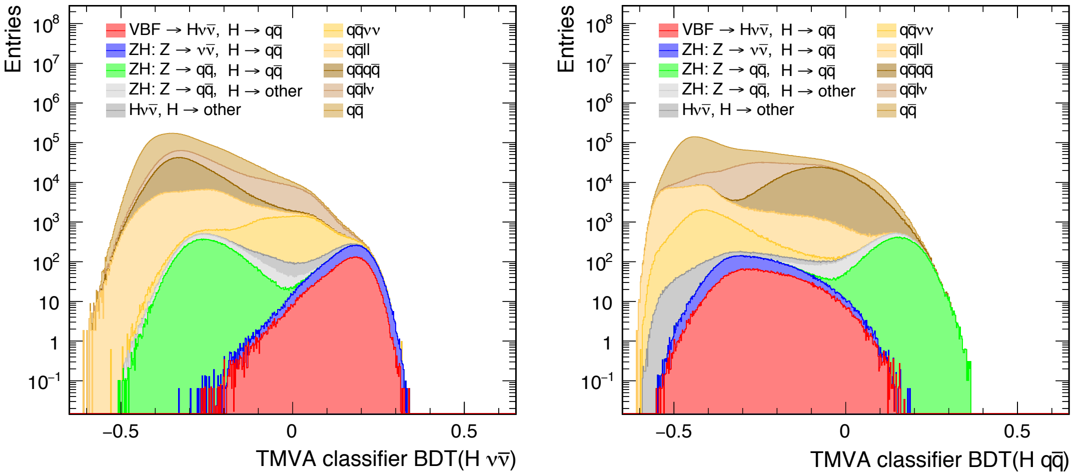

Figure 6.12.: Classifier response to signal and background events for a BDT trained on $H\nu\bar{\nu}, H \to hadrons$ final states (left) and one trained on $Hq\bar{q}, H \to hadrons$ final states (right), normalized by cross section.

By scanning the classifier outputs, it is possible to find the value for the cut that maximizes the combined signal significance, i.e.:

$$Significance = \frac{S_C}{\sqrt{S_C + B_C}} \tag{6.11}$$

where S_C and B_C are the number of signal and background events respectively, that passes the filter for a certain cut value C.

In this case, for both classifiers, a cut value of 0.16 was chosen, and the efficiency of the resulting cuts has been summarized in table 6.2.

6.5. Template Fit

Now that we have a selected sample of signal events with minimal background contamination, it is necessary to further analyze the event structure to separate the various hadronic decays of the Higgs boson candidates. For this we can use the flavor tagging information extracted by the jet clustering algorithm, as explained in section 6.3. Since both jets generated by the Higgs boson candidate have been flavor tagged with a b-likeliness and a c-likeliness, it is useful to introduce, for each tag, a combined likelihood value that represent the joint probability for the Higgs boson to have decayed in a $b\bar{b}$, $c\bar{c}$

Process	σ/fb	ϵ_{BDT}, classified as $H\nu\bar{\nu}$	ϵ_{BDT}, classified as $Hq\bar{q}$	N_{BDT}, classified as $H\nu\bar{\nu}$	N_{BDT}, classified as $q\bar{q}$
$e^+e^- \to Hq\bar{q}; H \to b\bar{b}$	52.3	0 %	42.3 %	0	11100
$e^+e^- \to Hq\bar{q}; H \to c\bar{c}$	2.64	0 %	32.8 %	0	434
$e^+e^- \to Hq\bar{q}; H \to gg$	7.92	0 %	37.4 %	0	1480
$e^+e^- \to H\nu\bar{\nu}; H \to b\bar{b}$	28.9	55.0 %	0 %	8000	0
$e^+e^- \to H\nu\bar{\nu}; H \to c\bar{c}$	1.46	51.0 %	0 %	372	0
$e^+e^- \to H\nu\bar{\nu}; H \to gg$	4.37	58.0 %	0 %	1270	0
$e^+e^- \to H\nu\bar{\nu}; H \to other$	17.8	6.1 %	0 %	513	0
$e^+e^- \to Hq\bar{q}; H \to other$	30.5	12.6 %	0.12 %	20	1920
$e^+e^- \to q\bar{q}\nu\bar{\nu}$	325	1.3 %	0 %	2110	0
$e^+e^- \to q\bar{q}l\nu$	5910	0.07 %	0.002 %	2090	60
$e^+e^- \to q\bar{q}ll$	1700	0.012 %	0.01 %	104	89
$e^+e^- \to q\bar{q}q\bar{q}$	5530	0.01 %	0.36 %	30	9990
$e^+e^- \to q\bar{q}(u,d,s,c,b)$ $M(q,\bar{q}) > 50\,\mathrm{GeV}$	24405.4	0.01 %	0.093 %	1230	11400

Table 6.2.: Summary of the expected numbers of events for the different signal and background final states passing the multivariate classifications into $Hq\bar{q}$ and $H\nu\bar{\nu}$, for an integrated luminosity of 500 fb^{-1} and a center-of-mass energy of 350 GeV for unpolarised beams.

or gg pair. To do so, we define the combined b- and c- likelihoods as follows:

$$b\bar{b}_{likelihood} = \frac{B_{jet1} \times B_{jet2}}{B_{jet1} \times B_{jet2} + \left(1 - B_{jet1}\right) \times \left(1 - B_{jet2}\right)} \tag{6.12}$$

$$c\bar{c}_{likelihood} = \frac{C_{jet1} \times C_{jet2}}{C_{jet1} \times C_{jet2} + \left(1 - C_{jet1}\right) \times \left(1 - C_{jet2}\right)} \tag{6.13}$$

where B and C refers to the value given by the lcfiplus flavor tagging algorithm (see section 6.3) to the jet indexed in the subscript.

Given the scarce number of entries for some of the signal channels, as well as the challenges involved in the *c-jets* identification that we have seen in section 6.3.3, a simple *cut and count* analysis would not lead to optimal results. To use all the information available from the flavor tagging distribution, a better approach is to perform a template fit that utilizes the entire domain of the flavor tag space.

The general rule to perform such fit, in a scenario where experimental data are available, proceeds as follows:

- From each Monte-Carlo-generated signal and background sample a multi-dimensional histogram, whose axes represent the variables with the highest separating power among samples, is constructed. Each of these histograms, usually referred to as *templates*, is normalized to the integrated luminosity collected by the experiment.

- From the experimental data sample, for which obviously the ratio between the various signal channels and the backgrounds is unknown, the corresponding histogram is generated.
- To find which fraction of the data corresponds to which of the simulated processes, a likelihood maximization strategy is used, that is finding the set of weights w_k that maximize the quantity:

  $$\mathscr{L} = \prod_{x_1, x_2 ... x_i} \frac{\left(\sum_k w_k \times T_k\right)^n e^{-\left(\sum_k w_k \times T_k\right)}}{n!} \tag{6.14}$$

  where T_k and n are the values of the k-th template and the data sample respectively for the bin with coordinates $x_1, x_2 ... x_i$. We assume Poisson-distributed fluctuations in each bin.

One might wonder why the fit is performed on templates consisting of binned distributions, rather than on smooth analytic functions, describing the underlying physics of the distributions of interest. The problem with that sits in the observables at disposal to perform the fit in the first place. As we have seen previously, the flavor tagging information is generated as the output of a neural network classifier, an entity that, by its very nature, is impossible to represent with a simple analytic function. The use of a binned fit, compared to an unbinned one, has the advantage to be completely agnostic of the shape of the templates, that can therefore be constructed with complex variables as those in equations 6.12 and 6.13.

The fit procedure depicted so far assumes to already have performed a real measurement and to have collected experimental data. In our case, the experiments are far from being ready and the only samples available are simulated events. Before explaining the details of the technical implementation of the binned likelihood fit for this analysis it is therefore crucial to show how the *data-like* samples have been produced.

Data Template and Toy MC Models

In an ideal world, we would have access to an infinite amount of computing power, that would in turn translate to an infinitely large set of simulated events to sample from. This would produce not only perfectly smooth templates that can be fitted without errors, but also an endless amount of statistically independent event samples that can serve as data mock-ups to validate the accuracy of the fit. Unfortunately, simulating full-detector-reconstructed events is a challenging task even for modern state-of-the-art computing facilities and it is impossible to generate enough statistics to have acceptable results with statistically independent templates and data sets. For this reason the *data-templates* have been generated as follows: all the templates have been stacked into a single histogram containing the entire simulated events statistic. Every time a data sample is required, random numbers are generated according to this histogram's distribution.

These numbers are used to fill the new data set and the procedure continues until the target integrated luminosity is reached. To account for the error in the templates derived from their limited simulated statistics, it is optionally possible to introduce an additional Poissonian fluctuation, bin-by-bin, to such templates prior to the generation of a new data set. The width of this fluctuation is proportional to the actual number of simulated events that contribute to the particular bin into consideration.

On one hand, this method allows to utilize the entire simulated statistics at its fullest, while accounting for the natural variations introduced by non-smooth templates of limited statistics.

On the other hand, though, since the fit is performed between data sets and templates whose entries are correlated, extra care needs to be put into it to avoid biasing the results. Section 6.6.1 will be dedicated to a detailed explanation of this issue.

While, for a real-data scenario, the data sample is unique and limited only by the integrated luminosity provided by the experiment, in a simulated benchmark it is possible to generate an endless number of data-like samples from the template distributions. Although they share a common origin in the templates used to create them, which makes their statistical significance less good than that of fully independent samples, they can still help to gain some insights on the quality of the fit itself. It is in fact possible to perform the fit procedure thousands of times, each time with a freshly-generated data-like set.

This technique is known as *Toy Monte Carlo* and is based on the simulation and fit of $\mathcal{N}$ experiments so that, for each, the set of weights w_k, i.e. the scaling factors of each fit's template, can be extracted. For each weight, it is possible to build another distribution that depicts the dispersion of that weight parameter around the average fit value over the N iterations of the fit. This spectrum can, in turn, be fitted with a Gaussian distribution, in which the variance defines the uncertainty on that parameter, and the mean can be compared to the known expected value, to give an estimate on the stability and convergence of the fit.

Extracting the Uncertainties

Now that we are familiar with the concepts of template fits and toy MC introduced in the previous two sections, we can have a look at the practical implementation of the fit for this analysis. As stated before, events are classified into two possible final states of interest: a 4-jets final state and a 2-jets plus neutrinos final state.

These result in two different sets of templates, one for each of the branches of the analysis. For the 4-jets final states, the parameters used for the templates are the $b\bar{b}-$ and $c\bar{c}$-likelihoods defined in equations 6.12 and 6.13. This generates a total of 5

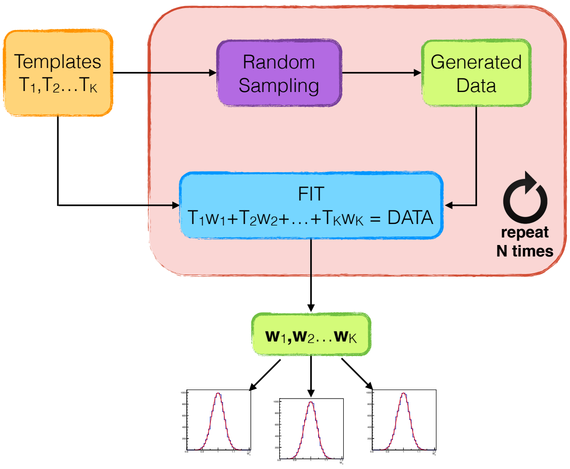

Figure 6.13.: Schematic representation of the Toy Monte Carlo procedure. A set of templates is random-sampled to create a data-like distribution. The templates are fitted against the generated data to extract their scaling fractions w_k. The procedure is repeated $\mathcal{N}$ times. The distributions of each fitted weights is further fitted with a Gaussian distribution to estimate the fit uncertainty on that parameter.

two-dimensional templates for the following processes:

$$
\begin{aligned}
e^+e^- &\to ZH : Z \to q\bar{q}, H \to b\bar{b} \\
e^+e^- &\to ZH : Z \to q\bar{q}, H \to c\bar{c} \\
e^+e^- &\to ZH : Z \to q\bar{q}, H \to gg \\
e^+e^- &\to ZH : Z \to q\bar{q}, H \to other \\
e^+e^- &\to SMbackground
\end{aligned}
$$

where the upper three mechanisms represent the signal templates of interest, and the last two, namely the other possible decays of the Higgs boson and the Standard Model background, are the two sets of backgrounds that survived the selection criteria. Figure 6.14 shows the distributions for this templates, normalized to $500\,\mathrm{fb}^{-1}$.

A similar approach can be used for the 2-jets plus missing mass event candidates, with one notable exception: as we have seen in chapter 4, in this case the production mechanism of the Higgs boson is not unique. At these center-of-mass energies, two different processes are involved, sharing an almost equal amount of events each, namely vector boson fusion and Higgs-Strahlung where the Z boson decays into two neutrinos. Although the particles in the two final states, the Higgs and two neutrinos, are the same, these two Feynman diagrams can still be disentangled from one another thanks to the kinematics of the event: in fact the Higgs-Strahlung events present a boost, coming from the momentum of the intermediate Z propagator, that is not present in the VBF events. For this reason, a quantity such as the event transverse momentum (that in the

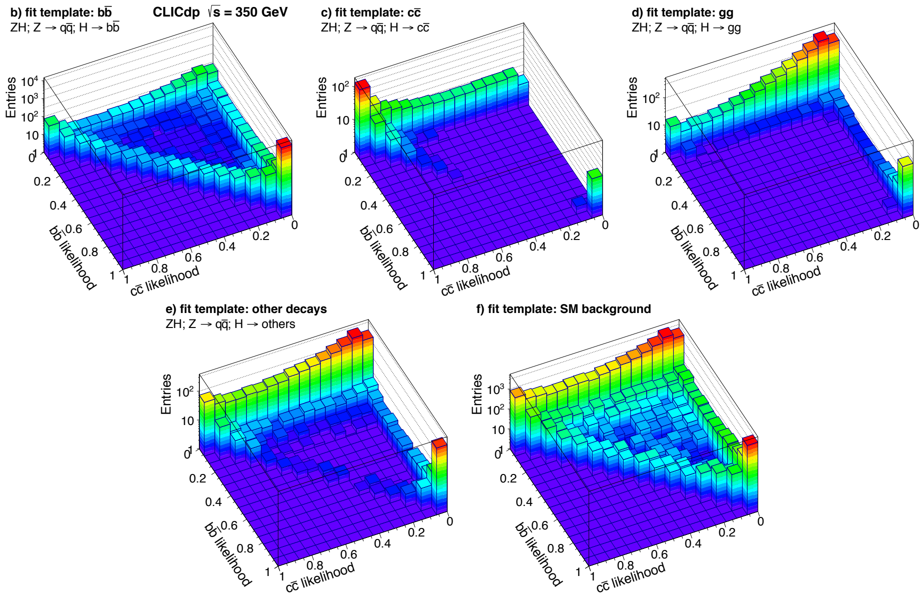

Figure 6.14.: Templates for events reconstructed as 4-jets final states for: (a) $ZH : Z \to Z \to q\bar{q}, H \to b\bar{b}$, (b) $Z \to q\bar{q}, H \to c\bar{c}$, (c) $Z \to q\bar{q}, H \to gg$, (d) $Z \to q\bar{q}, H \to other$ and (e) $SMbackground$. The x- and y-axis depict the $b\bar{b}-$ and $c\bar{c}-$likelihoods respectively, two quantities defined in 6.12 and 6.13. The z axis is logarithmic [117].

case of 2-jets final states is equivalent to the transverse momentum of the Higgs-boson candidate) is a very good observable to split the contribution of both.

To achieve this it is necessary to make a small digression on the way $H\nu\bar{\nu}$ events are produced: the event generator used for this analysis, i.e. WHIZARD, does not allow to create pure samples of $H\nu\bar{\nu}$ coming exclusively from one of the two production mechanisms. This is because in reality the diagrams of the two processes interfere with each other and it would be theoretically inaccurate to produce a sample from only one of the two diagrams. For the same reason, no direct information can be retrieved from the Monte Carlo-truth information either to split the events. The best approximation available then is to scan through the collection of Monte Carlo particles, looking for the two final state neutrinos. The invariant mass of the neutrino pair is shown in figure 6.15.

It is immediately clear from the peak around 90 GeV that this comes from events in which a Z boson has decayed into two neutrinos, i.e. Higgs-Strahlung events, whereas the rest of the distribution comes from VBF events. If we define a mass window around the peak of ±5 GeV we can separate, with a relatively high degree of precision, the two contributions on a per-event basis. This allows us to generate separated templates for Higgs-Strahlung and VBF processes, so that the template fit can asses the fraction of each in the event sample. To do so, for this branch of the analysis, an additional dimension, for a total of 3, is added to the templates and to the fit, since the $b\bar{b}-$ and $c\bar{c}$-likelihood space used so far is insensitive to this difference. This is the Higgs-candidate transverse

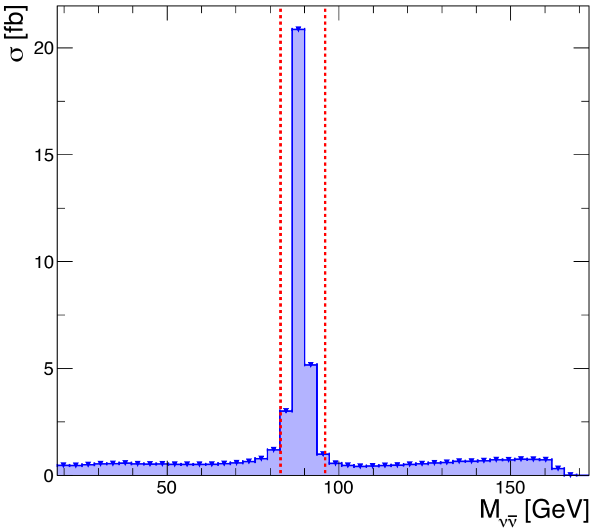

Figure 6.15.: Invariant mass of the Monte Carlo generated neutrino pair in $H\nu\bar{\nu}$ events. The peak around the Z boson mass, inside the red dashed lines, represents events that have been created via Higgs-Strahlung, with the Z decaying into neutrinos, while the almost flat remaining regions consist of vector-boson-fusion events candidates.

momentum. Figure 6.16 shows such distribution for ZH and VBF events, with $H \to b\bar{b}$, as well as for SM background events that survived the MVA classification.

The projections of these 3D-templates to the 2D $b\bar{b}$- and $c\bar{c}-$ likelihood space, are deferred to appendix B. At this point we have two different sets of templates from the two branches of the analysis that can be fitted separately, thus allowing for two sets of almost independent measurements of the same quantities. But this strategy is not optimal for two reasons: (a) the separate measurements of the uncertainties of the Higgs hadronic branching fractions would then need to be merged with a non-trivial error propagation given by their small, albeit non-zero, correlation and (b) the resulting correlation matrices for the two fits would not be easy to fit together. For these reasons the choice was to perform a simultaneous fit of both set of templates in a likelihood maximization procedure. This consists in the maximization of the quantity defined in equation 6.14, in order to find the optimal set of weights w_k that would fit the templates and data-like distributions best. For this task, the MINUIT [149] minimization library was chosen. This is a very powerful and reliable tool to find the minima of a multi-dimensional function even in high-dimensional phase-spaces. In our case a total of six free parameters were used: one for each Higgs hadronic decay times the two possible Higgs production mechanisms. The additional weights associated to the two background channels have been fixed prior to the fit assuming that their contribution can be obtained from the outcome of other related analyses (a study on the systematic impact of their uncertainties will be presented in the next section).

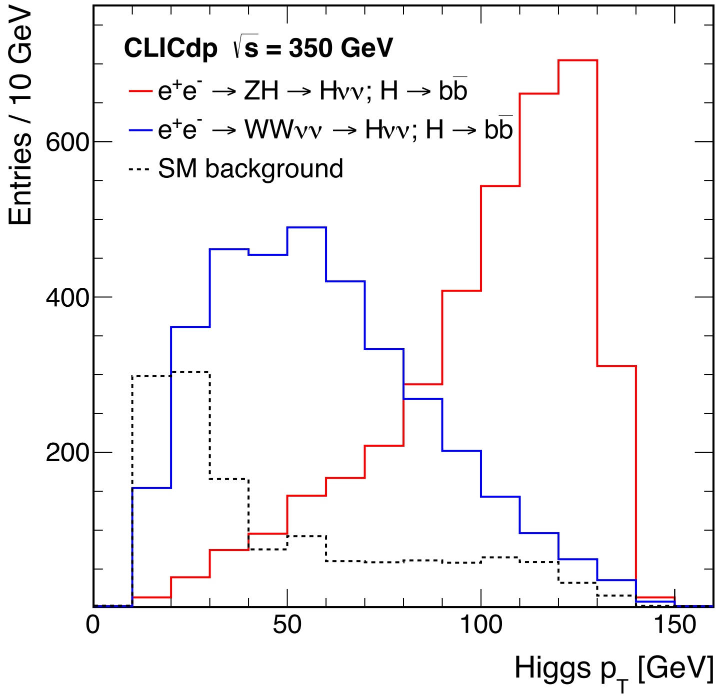

Figure 6.16.: Higgs candidate P_T distribution for $e^+e^- \to ZH : Z \to \nu\bar{\nu}, H \to b\bar{b}$ (red) and $e^+e^- \to W^+W^- \to H\nu\bar{\nu} : H \to b\bar{b}$ events (blue). The dotted black line represents the SM background that passed the classification criteria [117].

For the three hadronic decays associated with Higgs-Strahlung production, both the 2D-templates from the 4-jet classification, as well as the 3D-templates from the 2-jets plus neutrinos classifications were simultaneously fit, whereas the VBF channels could rely solely on the 3D-templates. A toy Monte Carlo procedure was set in place, where 10000 data-like samples were produced and fitted to obtain the best set of weights, whose distributions, shown in figure 6.17, represent the expected uncertainties for each of the channels under investigation. Table 6.3 summarizes these quantities as resulting from a Gaussian fit of the distributions.

Decay	Statistical uncertainty	
	Higgs-Strahlung	W^+W^--fusion
$H \to b\bar{b}$	0.86 %	1.9 %
$H \to c\bar{c}$	14.4 %	25.8 %
$H \to gg$	6.1 %	10.2 %

Table 6.3.: Summary of statistical uncertainties for events with a $H \to b\bar{b}$, $H \to c\bar{c}$ or $H \to gg$ decay, where the Higgs boson is produced by Higgsstrahlung or WW-fusion, at a center-of-mass energy of 350 GeV.

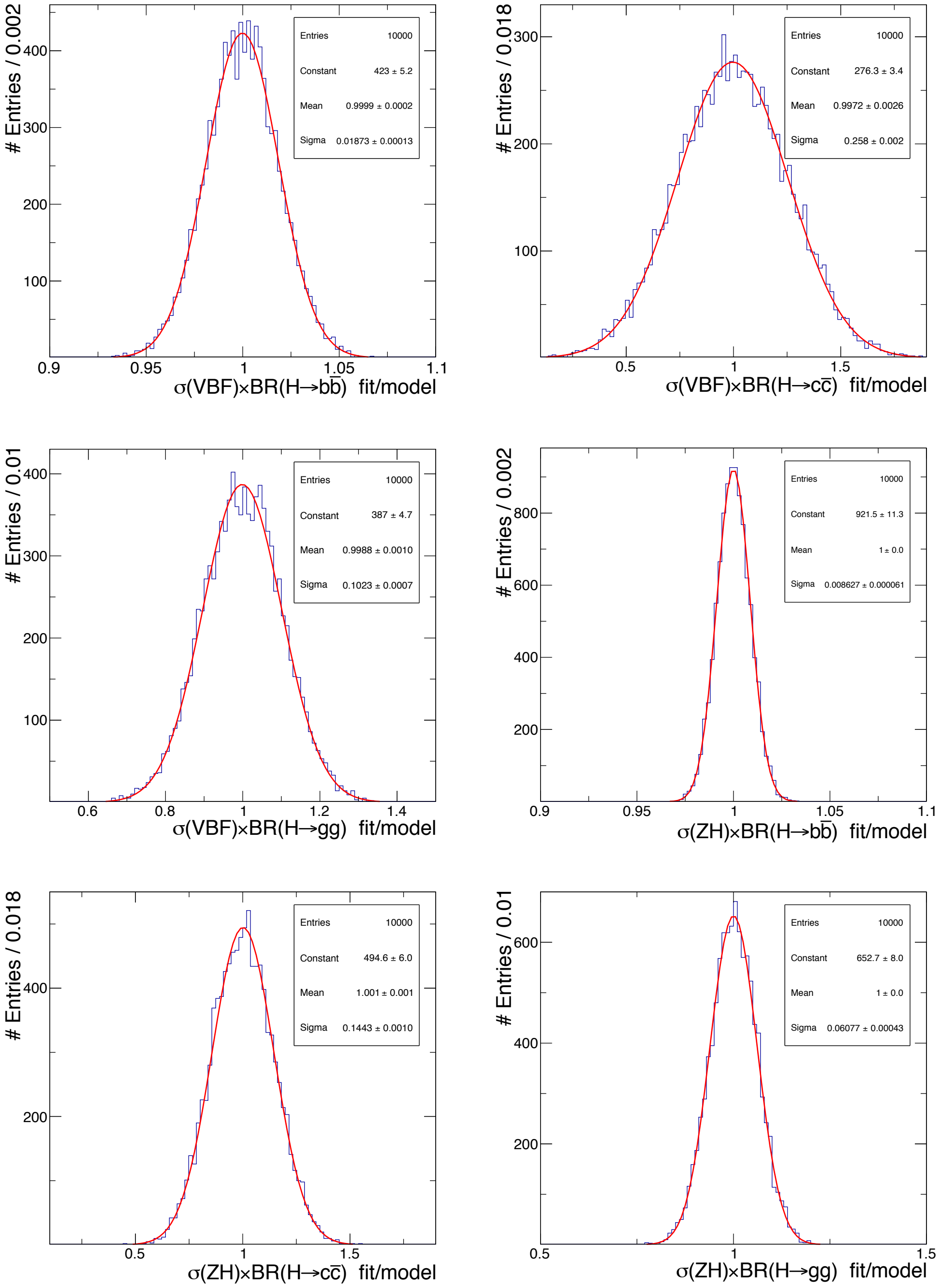

Figure 6.17.: Distribution of the toy MC fit results for the six $\sigma \times BR$ Higgs hadronic signal channels. On the X-axis of each figure is the ratio between the fitted value of the observable and the SM value. The width of each distribution serves as estimation of the uncertainty achievable at CLIC with 350 GeV and an integrated luminosity of 500 fb^{-1} for the various measurements.

	$\sigma(ZH)\times BR(H\to c\bar{c})$	$\sigma(ZH)\times BR(H\to gg)$	$\sigma(VBF)\times BR(H\to b\bar{b})$	$\sigma(VBF)\times BR(H\to c\bar{c})$	$\sigma(VBF)\times BR(H\to gg)$
$\sigma(ZH)\times BR(H\to b\bar{b})$	-0.0802	-0.0863	-0.244	0.0245	0.0285
$\sigma(ZH)\times BR(H\to c\bar{c})$		-0.202	0.0215	-0.311	0.0690
$\sigma(ZH)\times BR(H\to gg)$			0.0215	0.0592	-0.323
$\sigma(VBF)\times BR(H\to b\bar{b})$				-0.072	-0.040
$\sigma(VBF)\times BR(H\to c\bar{c})$					-0.203

Table 6.4.: Matrix of the correlations between the observables associated with the hadronic decays of the Higgs boson, for a center-of-mass energy of 350 GeV. The correlation are extracted from the simultaneous toy Monte Carlo fit procedure used to determine each observable estimated resolution.

Table 6.4 shows a feature unique to this method of simultaneously extracting the uncertainties of all channels, i.e. the matrix of the correlation strengths of all the signal channel measurement uncertainties. In the next chapter we will see how this matrix of correlations can ameliorate the uncertainties associated to the Higgs couplings. In the mean time, though, we must carefully analyze other possible sources of errors of this study.

6.6. Additional Sources of Uncertainty

In the fit results presented in the previous section, no source of systematic uncertainty has been taken into account, in particular the templates generating both the data and the fit have been used as if they had an infinite degree of precision. This is, in first approximation, possible only provided that the statistics generated is large enough to accurately describe the signal and background parameter space. This has to take into account the fact that, for some of the background channels, the suppression can be as high as five orders of magnitude (see table 6.2). It must also account for the exponential growth of the number of bins in the multidimensional space used for the adopted binned likelihood fit. This growth can quickly result in a level of granularity that is incompatible with the simulated statistics and lead to statistical artifacts that can drive the fit to non-physical conclusions.

This section is dedicated to the introduction of some of such uncertainties and to the discussion of the strategies that have been adopted to minimize their impact.

6.6.1. Limited Statistics

Ideally, when performing simulations of a real-world experiment using Monte Carlo events, we would like to have a perfect representation of the underlying physics. Given the limited knowledge embedded in our models, this is not possible. More than that, even if we had a perfect modelization, since generating a Monte Carlo event requires some computing time, a set of Monte Carlo generated templates would only asymptotically describe nature in the limit of an infinite amount of events. In our case, given the complexity of a full detector simulation, the production of each event, even on state-of-the-art CPUs, takes up to a few minutes, depending on the amount of particles that need to be tracked in the final state. For the creation of the samples used in this analysis, the CERN GRID computing [150] infrastructure was used, consisting of thousands of computing nodes scattered around the world. Even with this massive computational power at disposal, generating samples of hundreds of thousands of events is a task that requires weeks, and the production of the over 15 million events included in this analysis has been processed over several months of intensive use of the CLICdp collaboration GRID CPU quota. To justify the need of such a massive number of simulated events, it is useful to introduce a scaled-down example, to show the impact of limited statistics in a binned fit procedure.

To do so, in this section, we will perform an illustrative analysis on a simpler one-dimensional scenario, as follows:

1. First we will define two elementary 1D-functions that will serve as the equivalent of the underlying error-free physical distributions of signal and background for an arbitrary observable X. These consist of a Gaussian distribution with $\mu = 3$ and $\sigma = 1$ for the signal, and an exponential distribution $e^{-\lambda x}$ for the background, with $\lambda = 1$.

2. From these distributions, we will random-sample three data sets, each with a factor 10 more statistics than the previous one. The normalization coefficients of the target number of signal and background events in the three data sets will then be $S_{MODEL} = 12.5, 125, 1250$ and $B_{MODEL} = 1000, 10000, 100000$. For the continuation of this example, these three scenarios will be referred to as having integrated luminosities $\int \mathscr{L} = 1, 10, 100$, respectively. The rather high amount of background events, compared to the number of signal events in this example has been selected to showcase a background-dominated scenario, similar to the situation present for the low-entries signal channels of the Higgs analysis of the previous section.

3. The three simulated data sets will be stored in three separate histograms with ten bins each. For each of them, we will perform simple fits to extract the normalization coefficient of the signal distribution, using both the χ^2 and the *Likelihood* methods. In each fit, the normalization coefficient will be fixed, making the signal normalization coefficient the only free parameter of the fit. For this first fit scenario, to perform the fits we will use as templates the functional forms introduced in point one.

4. After the first set of fits, we will focus on the data set with the highest integrated luminosity, and rebin its histogram to obtain three identical samples, stored in either 10, 100 or 1000 bins.

5. Performing the χ^2 and *Likelihood* fits again, for each binning configuration (still using the 1D-functions of point one as templates), we will show the limitations of the χ^2 minimization method, when dealing with scarcely populated bins.

6. After showing the impact of binning for the data points, we will introduce an additional layer of complexity to the problem: we will substitute the smooth 1-dimensional error-free functional representations of our signal and background distributions with a binned version of them. To generate the templates, we will use three different amounts of simulated MC statistics, equivalent respectively to *scaling factors* of 0.1, 1 and 10 times the target integrated luminosity. For each scaling factor, we will, as previously, consider three binning configurations (10, 100 or 1000 bins).

7. Using data samples that are statistically independent from the binned templates, we will perform a toy Monte Carlo study of the impact of binning and scaling factors, when performing a binned-templates likelihood fit. In particular we will show how a limited Monte Carlo statistics for the template generation, coupled to a high number of bins, results in a biased fit that converges to nonphysical outcomes, driven by statistical artifacts in the templates.

8. After that, we will show that the same toy Monte Carlo procedure, performed on data sets generated by random-sampling the binned templates, still can produce inaccurate results. In fact the fit converges to unrealistically small uncertainties when the binning is too fine or the MC statistics to generate the templates is too low, with the additional pitfall that the statistical dependence of the data from the templates hides, in the results, almost all the signs of this bias.

9. Finally, to counteract situations like the one in the previous point, we will introduce a procedure to estimate this systematic bias by means of an additional smearing of the templates. This procedure will be applied to the full Higgs analysis, to evaluate the contribution of this systematic error to the total uncertainty.

Let's start with the introduction of the one-dimensional signal and background distributions of our example, shown in figure 6.18.

For the purpose of our example, we can regard these distributions as the error-free "true" representations of nature. From them it is possible to quickly generate a virtually infinite number of samples, making it possible for us to show the impact of binning and statistics on the fit outcome. Sampling from these distributions is, in our scaled-down example, the equivalent of performing a full-detector Monte Carlo simulation and extracting from it some particular parameter X. To simplify the explanation even further, we assume that, for our analysis, all the parameters of the model are known with infinite

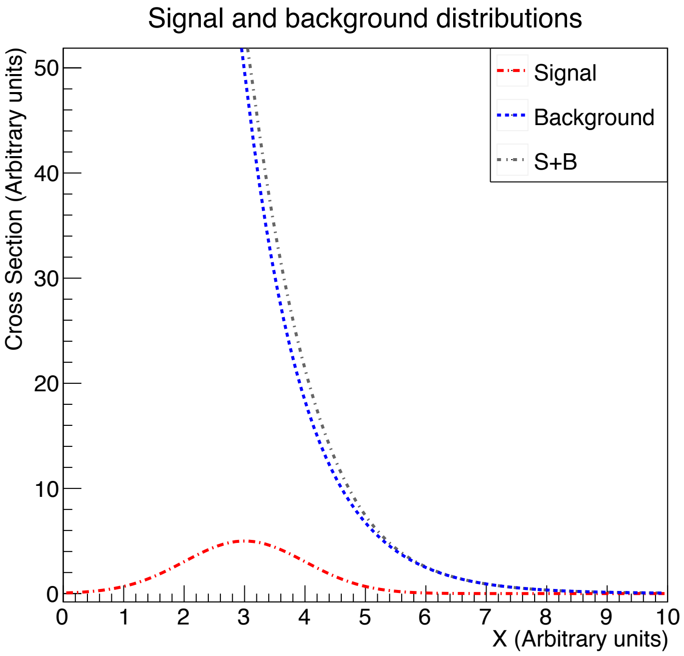

Figure 6.18.: Signal and background "true" distributions for the 1-dimensional binned fit example.

precision, apart for the normalization coefficient S of the signal distribution. So the problem becomes finding, for a given integrated luminosity and a fixed background, the coefficient S for our signal distribution, i.e. the number of signal events. We can begin by having a look at the impact of data sets with different values of integrated luminosity to the fit uncertainty of the parameter of interest.

Figure 6.19 shows, on a logarithmic vertical scale, the signal and background distributions, as well as a random-sampled data set, for each of the three integrated luminosities scenarios: 1, 10 and 100 times the reference distributions from figure 6.18. Clearly, since we have a functional form of the signal and background distributions, the best possible fit results can be achieved by using these as the fitting functions on our data samples.

Table 6.5 shows the fit estimate for the signal normalization coefficient, as a ratio between the fitted result S_{FIT} and the expected value S_{MODEL}, for the χ^2 and the *Likelihood* methods for the different integrated luminosities scenarios. Each of the entries in the table is the result of a single fit performed on one occurrence of the data sets. It is, therefore, normal for the mean value of the fit to not be exactly equal to one. Moreover, to better compare the results of the two fit methods, for each integrated luminosity scenario, the same data set was used to perform both the χ^2 and the *Likelihood* fits.

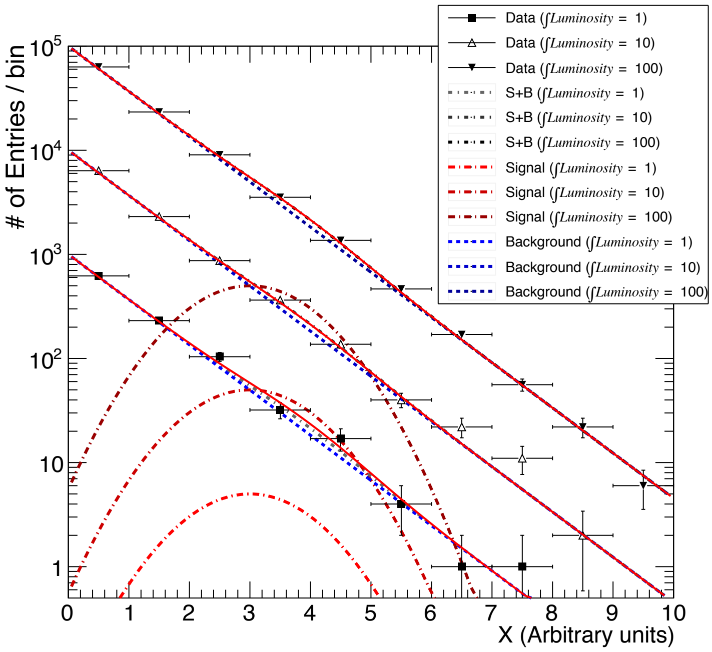

Figure 6.19.: Signal and background distributions, and data histograms for three integrated luminosities scenarios ($\int \mathscr{L} = 1, 10, 100$).

$\int \mathscr{L}$	$\frac{S_{FIT}}{S_{MODEL}}, \chi^2$	$\frac{S_{FIT}}{S_{MODEL}}$, *Likelihood*
1	1.40 ± 1.06	1.47 ± 1.03
10	1.34 ± 0.33	1.35 ± 0.33
100	0.97 ± 0.10	0.97 ± 0.10

Table 6.5.: χ^2 and *Likelihood* fit results for the estimation of the number of signal events in the data sample, as a function of the total integrated luminosity ($\int \mathscr{L} = 1, 10, 100$). The result is presented as a ratio between the fit outcome and the expected value from the model from which the data set was created.

We can see that, as expected, the uncertainty on the fit result decreases proportionally to the square root of the integrated luminosity, or, equivalently to the square root of the number of entries in the data set. In all cases the fit outcome is compatible, at the 1σ level, with the number of signal events described by the model.

Let's now take the data set that we created for the scenario with the highest integrated luminosity ($\int \mathscr{L} = 100$) and have a look at what happens when we vary the number of bins in which we split our data sample. Figure 6.20 shows the fit results for three cases, each having one order of magnitude more bins than the previous one. For easier comparison of the fits results, the data set used to generate these histograms is the same in all cases. Similarly to the previous fit, we can compile a table of the fit results:

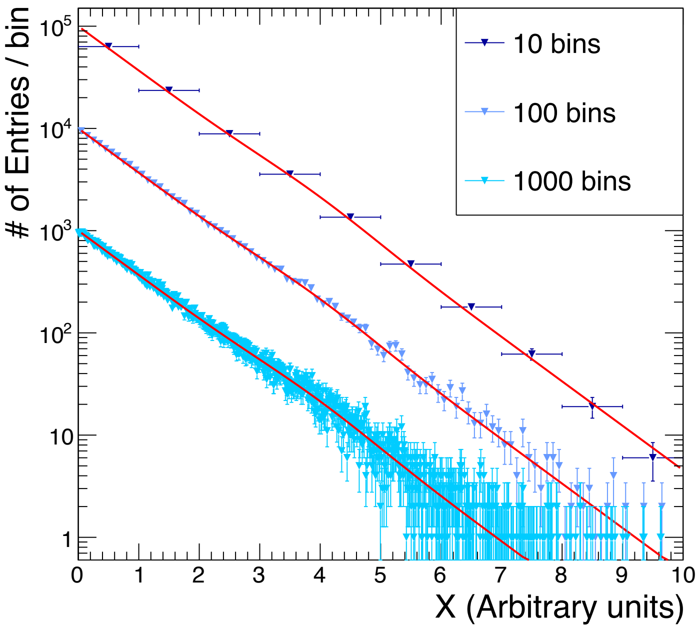

Figure 6.20.: Fit of a data sample with $\int \mathscr{L} = 100$ as a function of binning (10, 100, 1000 bins). The *"factor-ten"* steps in the vertical axis are a direct consequence of the different binning of the three histograms.

№ of bins	$\frac{S_{FIT}}{S_{MODEL}}, \chi^2$	$\frac{S_{FIT}}{S_{MODEL}}, Likelihood$
10	0.97 ± 0.10	0.97 ± 0.10
100	0.92 ± 0.10	0.97 ± 0.10
1000	0.55 ± 0.10	0.97 ± 0.10

Table 6.6.: χ^2 and Likelihood fits results for $\int \mathscr{L} = 100$ with 10, 100 or 1000 bins. The results are expressed as ratios between the fitted number of signal events and the one expected from the underlying model. When the binning is very granular, the number of entries per bin drops considerably. In this case the uncertainty of the number of entries in each bin can no longer be approximated with a Normal distribution, leading to the failure of the χ^2 minimization fitting procedure.

Since the data histogram is the same, the result of the last row of table 6.5 and those of the first row of table 6.6 are identical. It is worth noting that, even in this very simple scenario, when the binning is too fine, the χ^2 method fails to address the problem correctly. This is because this method holds only when the uncertainties on the data entries can be properly approximated to Normal distributions, i.e. in the limit of a high number of events in each bin. The typical symptom of such erroneous behavior is an incorrect central value for the fit (while the uncertainty on the parameter is usually represented correctly). Such basic behavior is unfortunately often overlook when fitting data sets with a low number of entries. In this example, it is apparent from the χ^2 fit results, that the more empty or near-empty bins are present in the data sample, the more this "runaway" effect occurs. In fact, for the finest binning configuration, the mean value of the fit differs by more than 4σ from the expected value. In contrast, the *Likelihood* fit results are unaffected.

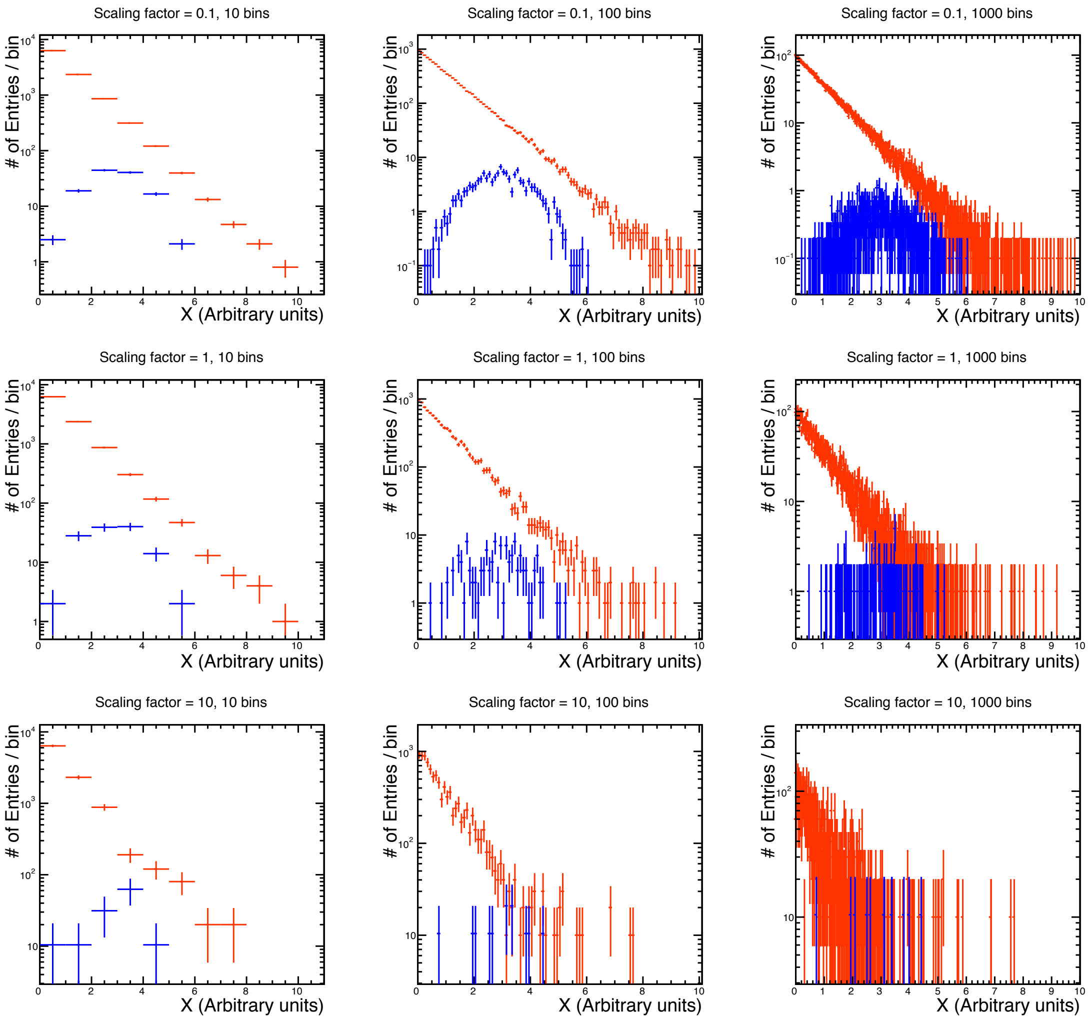

Figure 6.21.: Binned templates generated with decreasing MC statistics (top to bottom, respectively 10, 1 and 0.1 times the target luminosity), and increasing number of bins (left to right, 10, 100 and 1000 bins, respectively). All templates are scaled to match the same integrated luminosity.

Now that we have covered the scenarios where there is a functional form for the underlying signal and background distributions, let's have a look at the case in which such description is not available, but the distributions are only accessible as a set of binned template histograms.

To make it possible to cross-check the quality of the fit outcomes, we will generate such binned templates from the original distributions in figure 6.18, but for all practical purposes, when computing the fits, we will pretend that this link does not exist.

In figure 6.21 we can see examples of such binned templates, generated simulating three MC statistics differing by one order of magnitude each, but scaled to the same integrated luminosity, and three choices of binning.

If we now take a data sample, statistically independent from the templates, similar to what we would obtain in a real experiment (and we can do that from the underlying functional distributions), we can perform a *Likelihood* fit and get, for each of the nine templates' configurations in figure 6.21, a value depicting the best approximation for the number of signal entries S_{FIT}. Since we are working with simulated data, we can produce an arbitrary large set of independent data samples, and for each extract the fitted value of the signal normalization coefficients in a toy MC method similar to that performed in Higgs analysis introduced in the previous section.

The fit results of such a procedure are presented in figure 6.22 and summarized in table 6.7. In this case, each fit outcome consists of two values. These are the mean μ and the variance σ associated with the Gaussian fit of the output distribution for the parameter S_{FIT}/S_{MODEL} of the toy MC procedure.

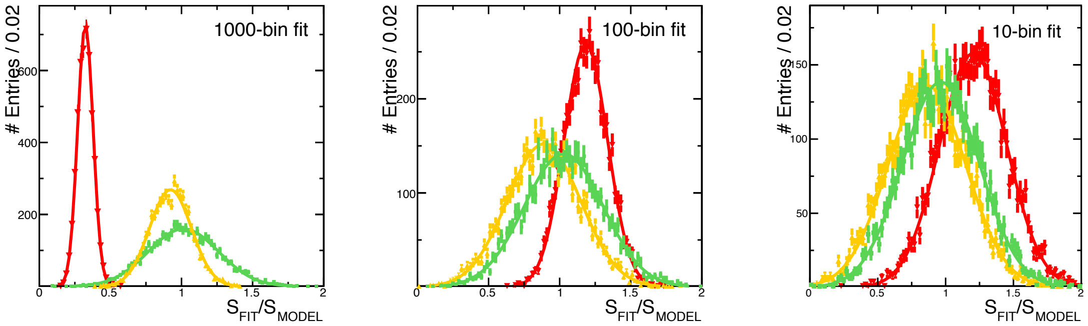

Figure 6.22.: Results of a toy Monte Carlo binned *Likelihood* fit, performed using binned templates generated with different MC statistics and normalized to the same integrated luminosity The green distribution refers to the results from templates generated with MC statistics 10 times higher than the target integrated luminosity (scaling factor = 0.1). Similarly, the orange distributions come from templates with a scaling factor of 1, and the red distributions from templates with a scaling factor of 10 . We consider three different binning configurations (10, 100 or 1000 bins). The data samples created for the 10000 iteration of the toy MC procedure are statistically independent from the templates and are generated from the functional forms of signal and background. For the high-bins, high-scaling factor scenario, the fit converges to nonphysical results.

	Scaling factor		
№ of bins	10	1	0.1
10	$\mu = 1.20, \sigma = 0.25$	$\mu = 0.86, \sigma = 0.29$	$\mu = 0.97, \sigma = 0.28$
100	$\mu = 1.18, \sigma = 0.15$	$\mu = 0.89, \sigma = 0.26$	$\mu = 1.03, \sigma = 0.28$
1000	$\mu = 0.32, \sigma = 0.05$	$\mu = 0.92, \sigma = 0.15$	$\mu = 1.01, \sigma = 0.25$

Table 6.7.: Mean and variance of Gaussian fits performed on the output distributions of the the toy MC procedure. This is performed, by applying a *Likelihood* fit with binned templates, on statistically independent data histograms, for different binning scenarios. When the statistic to generate the templates is low(high), a high(low) scaling factor must be used. The use of data sets that are statistically independent from the templates, shows the limits of the fit: when the templates' scaling factor is too high and the binning is too granular, the fit converges to nonphysical results.

We can see that, when the simulated MC statistics used to create the templates is high (i.e. the scaling factor is low and deviations in the binned templates from the underlying physics are negligible), the fit gives good results regardless of the binning. Similarly, a coarser binning leads to fit results well within a 1σ range around the simulated value. The problem arises in the configurations of relatively scarce MC statistics for the template generation, coupled to fine binning: in this case the uncertainty on the templates cannot be neglected, since, as it is obvious from the fit results, such templates do not convey a representative description of the underlying physics anymore. In this situation the fit is driven by an artificial separation of the signal and background entries: the templates are so sparsely populated that many bins contain only one signal or one background entry. These binning artifacts lead the fit to converge to nonphysical results.

As long as the data sets used are statistically independent from the templates, the quality of the fit can still be monitored by looking at the average deviation of the fit central value with respect to the expected one, i.e. the mean μ that we have used so far. The situation complicates when the data sets are sampled from the binned templates and are, thus, statistically correlated to them. The final goal of this one-dimensional example is to point out the dangers of performing the complete toy MC fit procedure in this manner, i.e. without any knowledge of the analytical description of the signal and background distribution from which to create statistical independent data sets (as is the case in the Higgs analysis in this thesis). As we can see in table 6.8, the fit still produces, in the limits of fine binning and low MC statistics to generate the templates, unrealistically good estimations of the uncertainties σ. Because of the correlation of the data sets and the templates, this time, the central value μ cannot be used to check that the fit is unbiased.

To account for this bias in the toy MC fit, a possible solution is to take into consideration the errors associated with each bin of the templates. To do so, for each iteration of

	Scaling factor		
№ of bins	10	1	0.1
10	$\mu = 1.00, \sigma = 0.27$	$\mu = 1.00, \sigma = 0.28$	$\mu = 1.01, \sigma = 0.27$
100	$\mu = 1.00, \sigma = 0.18$	$\mu = 1.00, \sigma = 0.26$	$\mu = 0.99, \sigma = 0.29$
1000	$\mu = 1.00, \sigma = 0.11$	$\mu = 1.00, \sigma = 0.16$	$\mu = 1.00, \sigma = 0.25$

Table 6.8.: Mean and variance of Gaussian fits performed on the output distributions of the the toy MC procedure. This is performed, by applying a *Likelihood* fit with binned templates, for different binning scenarios. The data histograms, created for each iteration of the toy MC fit, are generated by randomly sampling from the binned templates, thus making each data set statistically dependent from the templates. Because of this dependence, the central value μ cannot be used to estimate the fit bias anymore. To colors in the table, referring to the fit accuracy, can only be assigned from prior knowledge of the best resolution achievable in this particular problem.

the toy MC, an additional step must be added right after the generation of a data set from the binned templates. Once a data set is created by sampling the binned templates up to the desired integrated luminosity, to perform the toy MC fit each template is temporarily replaced. The replacement consists of a new binned distribution, randomly sampled from the original template. The number of entries sampled to fill such new distribution can be varied by a scaling factor λ, to reproduce different amounts of simulated statistics for the generation of the templates. This way, in the *Likelihood* fit procedure of each toy MC step, the temporary templates and the data set are not as strongly correlated as before, and fit central value μ can be used again to estimate the systematic bias for a particular λ (i.e. for a particular amount of MC statistics at disposal to generate the binned templates).

For this reason, the fit introduced in the previous section, where we extracted the uncertainties associated to the hadronic decays of the Higgs boson, has been performed again, randomly fluctuating the binned templates before applying the likelihood fit, assuming three scenarios that differ in the amount of Monte Carlo events produced for generating the templates: 0.1, 1 and 10 times the target integrated luminosity of $500\,\text{fb}^{-1}$. The results of such a procedure are summarized in table 6.9.

Recalling the values of table 6.1, we can see that for all of the signal channel, we simulated statistics for the Higgs analysis is one to two orders of magnitude above the target integrated luminosity. The amount of simulated background events is a factor 2 to 5 higher than the target luminosity for the $q\bar{q}\nu\bar{\nu}$ and $q\bar{q}l\nu$ backgrounds. Despite the number of simulated events for the $q\bar{q}ll$ background template needs to be up-scaled by a factor 2, this channel does not constitute a problem for the analysis, since the rejection efficiency on it is so good that only a handful of events pass the cut. The potential sources of errors are the $q\bar{q}$ and the $q\bar{q}q\bar{q}$ background channels, since their scaling factors

	Scaling Factor λ	2	1.33	1	0.5	0.1
$Higgs - Strahlung$	$H \to b\bar{b}$	0.88%	0.55%	0.42%	0.2%	0.11%
	$H \to c\bar{c}$	17.9%	14.1%	11.6%	7.1%	0.72%
	$H \to gg$	3.1%	2.2%	2.0%	0.9%	0.4%
W^+W^- fusion	$H \to b\bar{b}$	7.3%	5.3%	4.6%	2.5%	0.18%
	$H \to c\bar{c}$	29.3%	26.1%	22%	14.6%	2.9%
	$H \to gg$	11.8%	9.2%	8.7%	5.4%	1.1%

Table 6.9.: Estimation of the systematic bias in the determination of the $\sigma \times BR$ uncertainties for Higgs hadronic decays in a binned-template *Likelihood* fit, as a function of the amount of MC statistics at disposal to produce the templates. The amount of MC statistics is expressed in terms of its scaling factor to achieve the target integrated luminosity (the lower the scaling factor, the higher the amount of MC statistics available to generate a template).

λ are 1.6 and 2, respectively. Fortunately, their total energy signature, close to the full center-of-mass energy of 350 GeV allows to separate them quite effectively from the $H\nu\bar{\nu}$ final states originated by both VBF and $ZH, Z \to \nu\bar{\nu}$. For this reason despite, their rather high scaling factors, they don't affect the VBF measurements. The main sources of concern are the $ZH, H \to b\bar{b}$ and $ZH, H \to c\bar{c}$ measurements since the systematic error associated with a template scaling factor of 2 is, in the worst-case-scenario where all templates have such rather poor scaling, at the same level as their statistical uncertainty. Clearly the actual situation is much better than that, since for the signal templates, the available statistics is almost two orders of magnitude higher. For this reason, we can estimate that the actual impact of the limited statistics in the background channel, is closer to the scenario involving a scaling factor of 1. Moreover, thanks to the remarkable b-tagging efficiency of the CLIC_ILD detector, the parameter space in the templates occupied by $ZH, Z \to \nu\bar{\nu}, H \to b\bar{b}$ is rather clean, as we have shown previously in figure 6.16. This accounts for a considerable portion of the $ZH, H \to b\bar{b}$ measurement, a condition that lowers the systematic error on this channel even further.

This leaves us with one problematic channel, namely $ZH, H \to c\bar{c}$. Given the low number of signal events for this process (in the order 1300 events in total at 500 fb^{-1}) and the lower efficiency of the c-tagging, the fit cannot recover completely from the background templates with low statistics. Using the systematic error value of 11.6% corresponding to a scaling factor of 1, as a compromise between the low MC statistics at disposal to generate the main background $q\bar{q}q\bar{q}$ and the virtually error-free template for the signal channel, we estimate total uncertainty of:

$$\Delta(\sigma(ZH) \times BR(H \to c\bar{c}) = 14.4\%(stat) \oplus 11.6\%(syst) = 18.49\% \tag{6.15}$$

It is worth noting that, despite the systematic errors described here are the ones with potentially the highest impact to the analysis, they are fortunately also the easiest eliminate. In fact, since they originate from the limited MC events simulated statistics, they can be lowered, potentially at the expenses of the statistical uncertainties, by adding more simulated events to the analysis. In this respect, the exponential growth of computing power comes to help: in a few years it will be possible to simulate a factor 10, or even 100 more MC statistic, in an acceptable time scale, thus rendering the error on the binned templates negligible.

6.6.2. Standard Model Background and Other Higgs Decays

In this section we investigate the additional potential sources of errors connected to the uncertainties in the templates used as background, namely the one related to the non hadronic Higgs decays and that associated with Standard Model backgrounds events that have outlasted the classification cuts presented in section 6.4.1. The CLICdp collaboration estimates, for 500 fb^{-1} of integrated luminosity, a 5% absolute uncertainty from the analyses associated with the non hadronic decays of the Higgs and a 0.1% systematic error on the absolute normalization of the Standard Model background [117]. To measure the impact of such uncertainties on our fit results, we can perform the toy MC fit again, fixing the background templates according to these fluctuations and look for deviations of the fit mean values. Table 6.10 summarizes these results.

		$H \to other$	
		$+5\,\%$	$-5\,\%$
$Higgs - Strahlung$	$H \to b\bar{b}$	$-0.03\,\% \pm 0.02\,\%$	$0.01\,\% \pm 0.00\,\%$
	$H \to c\bar{c}$	$0.9\,\% \pm 0.5\,\%$	$3.7\,\% \pm 0.5\,\%$
	$H \to gg$	$-0.3\,\% \pm 0.2\,\%$	$2.6\,\% \pm 0.2\,\%$
W^+W^- fusion	$H \to b\bar{b}$	$0.0\,\% \pm 0.0\,\%$	$0.0\,\% \pm 0.0\,\%$
	$H \to c\bar{c}$	$-1.51\,\% \pm 0.86\,\%$	$0.3\,\% \pm 0.8\,\%$
	$H \to gg$	$-0.8\,\% \pm 0.25\,\%$	$0.6\,\% \pm 0.3\,\%$

		SM background	
		$+1$ ‰	-1 ‰
$Higgs - Strahlung$	$H \to b\bar{b}$	$-0.06\,\% \pm 0.03\,\%$	$-0.02\,\% \pm 0.03\,\%$
	$H \to c\bar{c}$	$-0.01\,\% \pm 0.47\,\%$	$1.4\,\% \pm 0.5\,\%$
	$H \to gg$	$-0.64\,\% \pm 0.19\,\%$	$0.3\,\% \pm 0.2\,\%$
W^+W^- fusion	$H \to b\bar{b}$	$0.0\,\% \pm 0.0\,\%$	$0.0\,\% \pm 0.0\,\%$
	$H \to c\bar{c}$	$-0.63\,\% \pm 0.86\,\%$	$1.2\,\% \pm 0.9\,\%$
	$H \to gg$	$-0.14\,\% \pm 0.33\,\%$	$-0.18\,\% \pm 0.32\,\%$

Table 6.10.: Fit results for ±5 % and ±1 ‰ absolute deviations of the $H \to$ other decays and SM background templates, respectively.

We can see that the measurements that are affected the most are $\sigma(ZH) \times BR(H \rightarrow c\bar{c}$, $\sigma(VBF) \times BR(H \rightarrow c\bar{c}$ and $\sigma(ZH) \times BR(H \rightarrow gg$.

To put these results in perspective, it is useful to recall the statistical uncertainties of these channels reported in table 6.3. The total uncertainty then becomes:

$$\Delta(\sigma(ZH) \times BR(H \rightarrow c\bar{c})) = 14.4\%(stat)^{+3.7\%}_{-0.0\%}(oth^{\dagger}, stat)^{+0.3\%}_{-0.64\%}(SM, sys)$$
$$\Delta(\sigma(VBF) \times BR(H \rightarrow c\bar{c})) = 25.8\%(stat)^{+0.3\%}_{-1.5\%}(oth^{\dagger}, stat)^{+1.2\%}_{-0.6\%}(SM, sys)$$
$$\Delta(\sigma(ZH) \times BR(H \rightarrow gg)) = 6.1\%(stat)^{+2.6\%}_{-0.3\%}(oth^{\dagger}, stat)^{+0.0\%}_{-1.4\%}(SM, sys)$$

where the terms with a "†" represent the additional statistical uncertainty associated with the channels corresponding to the non hadronic decays of the Higgs. The only channel affected by any noticeable amount is $\sigma(ZH) \times BR(H \rightarrow gg)$, where the additional uncertainties account for a 10% relative increase, compared to the purely statistical one.

6.7. Signal Channel Efficiencies

Now that we have seen the impact of systematic shifts in the background templates, it is interesting to study the effect of systematic uncertainties on the selection efficiencies of our signal channels. We can estimate [117] a systematic error in the $H \rightarrow b\bar{b}$ channel of ±0.25 %. For the less numerous $H \rightarrow c\bar{c}$ and $H \rightarrow gg$, a more conservative error of ±1 % has been estimated. To assess the consequences of these uncertainties on the fit results, the fit procedure was performed once more for each of the six systematic shifts. Table 6.11, summarizes the outcome of the toy Monte Carlo likelihood fit.

We can see that the uncertainties are negligible almost everywhere, since, even in the channels that show the highest absolute deviations of $\approx 1.0 - 1.3\%$, the statistical error is such that these additional systematics can be be neglected.

The only channel that shows an appreciable increase of the total uncertainty is $\sigma(ZH) \times BR(H \rightarrow b\bar{b})$: given its sub-percent statistical resolution, even a shift of only 0.3% can be detected. The total uncertainty on this channel then becomes:

$$\Delta(\sigma(ZH) \times BR(H \rightarrow b\bar{b})) = 0.86\%(stat) \oplus^{+0.3\%}_{-0.25\%} (syst),$$

that translates to a total resolution of 0.91%.

6.8. Effects of Beam Polarization and Center-of-Mass Energy

As with many other measurements in physics, the crucial factors in determining the achievable accuracy for the presented analysis is the relative abundance of signal events versus background events, i.e. the significance of the data sample. Since signal and background events derive from different physical processes, it is possible to variate the

		$\sigma \times BR(H \to b\bar{b})$	
		+0.25 %	−0.25 %
Higgs − Strahlung	$H \to b\bar{b}$	−0.25 % ± 0.01 %	0.3 % ± 0.0 %
	$H \to c\bar{c}$	0.01 % ± 0.01 %	0.1 % ± 0.1 %
	$H \to gg$	0.0 % ± 0.0 %	0.0 % ± 0.0 %
W^+W^- fusion	$H \to b\bar{b}$	−0.26 % ± 0.02 %	0.2 % ± 0.0 %
	$H \to c\bar{c}$	−0.29 % ± 0.26 %	−0.28 % ± 0.26 %
	$H \to gg$	−0.12 % ± 0.10 %	−0.12 % ± 0.10 %

		$\sigma \times BR(H \to c\bar{c})$	
		+1 %	−1 %
Higgs − Strahlung	$H \to b\bar{b}$	0.0 % ± 0.0 %	−0.02 % ± 0.01 %
	$H \to c\bar{c}$	−0.89 % ± 0.15 %	1.3 % ± 0.2 %
	$H \to gg$	0.0 % ± 0.0 %	−0.12 % ± 0.06 %
W^+W^- fusion	$H \to b\bar{b}$	−0.01 % ± 0.02 %	0.0 % ± 0.0 %
	$H \to c\bar{c}$	−1.39 % ± 0.26 %	0.7 % ± 0.3 %
	$H \to gg$	−0.12 % ± 0.1 %	0.1 % ± 0.1 %

		$\sigma \times BR(H \to gg)$	
		+1 %	−1 %
Higgs − Strahlung	$H \to b\bar{b}$	0.0 % ± 0.0 %	0.0 % ± 0.0 %
	$H \to c\bar{c}$	0.1 % ± 0.1 %	0.1 % ± 0.1 %
	$H \to gg$	−0.97 % ± 0.06 %	1.0 % ± 0.0 %
W^+W^- fusion	$H \to b\bar{b}$	−0.02 % ± 0.02 %	−0.01 % ± 0.02 %
	$H \to c\bar{c}$	−0.28 % ± 0.26 %	−0.28 % ± 0.26 %
	$H \to gg$	−1.12 % ± 0.1 %	0.9 % ± 0.1 %

Table 6.11.: Fit results for ±0.25 %, ±1 % and ±1 % on the absolute deviations of the $H \to b\bar{b}, c\bar{c}$ and gg signal channels.

initial conditions of an interaction to enhance or reduce the fraction of the events of interest. In a particle collider there are two main tools available to achieve this task: (a) the variation of an event center-of-mass energy and (b) the polarization conditions of the incoming beams. An increase of the former rewards *t-channel* processes while penalizing *S-channel* ones. The latter, on the other hand, influences weak couplings, thus allowing to modulate processes involving Z and W bosons.

As we have seen in chapter 2, there are several energy options for the first stage of the CLIC collider as well as the possibility to polarize the electron beam to ±80 %. It would be useful to asses the impact of these various accelerators setups to the uncertainties on the Higgs hadronic decays investigated in this analysis. Unfortunately, as we have mentioned in the previous sections, the amount of time necessary to produce a significant sample of full-detector simulation Monte Carlo events is too long to examine all these combinations thoroughly. For this reason it was decided to scale the signal and background templates obtained from the 350 GeV unpolarized analysis to match the cross-sections expected for other beam configurations and to perform the fit with these parameters as well.

Of course this procedure is by no means an adequate substitute for a full-detector simulation, in particular because a different center-of-mass energy and polarization states can vary the kinematic and the angular distribution of some of the events, thus possibly impacting the event selection efficiencies and the shape of the aforementioned templates. But it is nevertheless a hint of the direction in which the results might pull, given different beam configurations.

In this section we will take into consideration five possible alternative scenarios for the operation of CLIC stage 1:

- 380 GeV center-of-mass energy with unpolarized beams.
- 350 GeV with an electron beam polarization of +80 % and −80 %, as per the CLIC baseline design.
- 350 GeV with an electron beam polarization of ±80 %, and a positron beam polarization of ∓30 %, that is not part of the CLIC baseline, but can be interesting to compare these results with those of ILC.

Before we continue it is useful to remind the definition of a polarized beam. Electrons, positrons and fermions in general can exist in two distinct *elicity* states [151]: (a) *right-handed*, when the spin is parallel to the the particle momentum, and (b) *left-handed*, when the spin and momentum vectors are antiparallel. The beam polarization is expressed as:

$$\mathscr{P} \equiv \frac{N_{RH} - N_{LH}}{N_{RH} + N_{LH}} \tag{6.16}$$

where N_{RH} and N_{LH} are the numbers of right-handed and left-handed particles in the beam respectively.

From this we can see that, if 50% of the particles are right-handed and 50% are left-handed, the beam is unpolarized ($\mathscr{P} = 0$). A polarization of 80%, typically achievable for an electron beam, implies that 90% of the particles are right-handed.

To compute the cross sections of several signal and background processes as a function of the beams energies and polarization, WHIZARD 1.95 was used once again, with realistic beam spectra and ISR contributions. The integration was run, typically over a couple of million of generated events, until the relative error on the cross-section converged below the percent level.

Table 6.12 summarizes the calculated cross-sections as a ratio to the unpolarized 350 GeV center-of-mass scenario.

Energy Polarization (%) e^+e^-	380 GeV unpolarized	350 GeV -80/0	 +80/0	 -80/+30	 +80/-30
$e^+e^- \to ZH, Z \to q\bar{q}$	0.853	1.177	0.823	1.483	0.997
$e^+e^- \to ZH, Z \to \nu\bar{\nu}$	0.854	1.176	0.824	1.484	1.000
$e^+e^- \to W^+W^-\nu\bar{\nu} \to H\nu\bar{\nu}$	1.311	1.799	0.201	2.336	0.139
$e^+e^- \to q\bar{q}\nu\bar{\nu}$	1.000	1.467	0.533	1.882	0.598
$e^+e^- \to q\bar{q}l\nu$	0.941	1.762	0.238	2.273	0.175
$e^+e^- \to q\bar{q}ll$	1.019	1.044	0.954	1.090	0.960
$e^+e^- \to q\bar{q}q\bar{q}$	0.914	1.755	0.245	2.279	0.201
$e^+e^- \to q\bar{q}(u,d,s,c,b)$ $M(q,\bar{q}) > 50\,\text{GeV}$	0.845	1.235	0.765	1.563	0.912

Table 6.12.: Normalization factor for the cross section of various physics processes as a function of center-of-mass energy and beam polarization, adjusted to the 350 GeV scenario with unpolarized beams. The results are extracted with WHIZARD 1.95.

These values can be used, column by column, to reiterate the fit to extract the uncertainties for the Higgs hadronic decays for the five different beam setups. The result of such fits are summarized in table 6.13.

Energy Polarization (%) e^-e^+		380 GeV unpolarized	350 GeV -80/0	 +80/0	 -80/+30	 +80/-30
$Higgs - Strahlung$	$H \to b\bar{b}$	0.94%	0.84%	0.83%	0.75%	0.74%
	$H \to c\bar{c}$	16.0%	14.4%	13.2%	12.8%	11.1%
	$H \to gg$	6.8%	6.1%	5.5%	5.5%	4.9%
W^+W^- fusion	$H \to b\bar{b}$	1.5%	1.6%	6.1%	1.1%	10.0%
	$H \to c\bar{c}$	19.6%	18.0%	87.4%	15.6%	176%
	$H \to gg$	7.8%	7.0%	32%	6.1%	49%

Table 6.13.: $\sigma \times BR$ fit uncertainties in the determination of Higgs hadronic decays, for different center-of mass energies and beam polarization scenarios. The fit is performed by rescaling each signal and background template from the unpolarized-beams 350 GeV scenario with the scaling factor in table 6.12.

From the table we can observe that, for a center-of-mass energy of 380 GeV, there is, as expected, a penalty on the measurements that depend on *s-channel* Higgsstrahlung production process. This is similar for all channels and corresponds to a relative increase of $\approx 10\%$ on the statistical uncertainty. On the contrary, the VBF channels are enhanced. The average relative gain in these channels is higher than the losses in the ZH channels because the main backgrounds $e^+e^- \to q\bar{q}$ and $e^+e^- \to q\bar{q}q\bar{q}$ are suppressed as well by

15% and 10%, respectively.

The situation varies a lot more when polarization is introduced. In fact, the coupling of the W and Z boson is greatly affected by the beam polarization, to the point that, when the electron(positron) beam consists only of right(left)-handed particles, the the VBF process is suppressed completely. Realistic beam polarization scenarios are not quite that extreme, but can still suppress VBF by 80 to 86% in the +80/0 and +80/-30 e^+e^- polarization configurations.

Overall, it seems like the -80/+30 configuration is the best choice giving, on average, the lowest statistical uncertainties on all the observables.

In reviewing these uncertainties, it must not be forgotten that the actual results of a full-detector simulation of various center-of-mass energies and beam polarization configurations, can potentially lead to outcomes than those presented in this section. In fact, the simple rescaling of the templates adopted here cannot account for the differences in the distributions of the final state kinematics that arise from the various beam configurations.

The results in table 6.13 must be therefore be taken only as indications of the overall trend in the uncertainties.

7. Global Fit of Higgs Couplings

After having seen what is the expected resolution achievable at the first energy stage of the CLIC accelerator for Higgs hadronic decays, it is useful to give an overview of how these measurements can be further utilized and how they fit in the broader picture of a full Higgs-sector investigation at such a linear collider.

The full potential of CLIC in the Higgs-sector has been studied in a large number of independent analyses, that have been recently summarized in an overview paper [117].

In this chapter we will introduce the strategy adopted in the CLICdp collaboration to combine the information from these Higgs-related analyses, as it is performed in the aforementioned publication. In particular the focus will be on the low-energy stage of CLIC, where the uncertainties, extracted in this thesis work, play a major role in determining the expected achievable resolution for the Higgs couplings to fermions and bosons. In particular we will see how the rather unique feature of this analysis, i.e. the correlation matrix obtained by the simultaneous extraction of several Higgs branchings, as well as different production mechanisms, from a concurrent fit procedure, have been used by members of the collaboration to improve these global results even further.

7.1. Model Independent Fit

When performing multiple measurements of the characteristics of a particle such as the Higgs boson, it is of great interest to correlate all these data points and to compare them against the available theoretical model. Combining the output generated by multiple observables allows in many cases to over-constrain the model, thus validating, or rejecting, its predictions with a degree of confidence that is much higher than what could be achieved by any single measurement alone.

In the particular case of a Standard Model-like Higgs boson, the notable quantities to extract are the magnitude of its couplings to other fermions and bosons, and its total width Γ_H.

Most of the measurements performed (with the notable exception of the evaluation of the $e^+e^- \to ZH$ total cross-section, introduced in section 4.3.1) probe the cross-section times branching ratio, i.e. $\sigma \times BR$, for a given Higgs production and decay mechanism.

If we define the coupling of the Higgs boson to a particle-antiparticle pair of a given species X as g_{Hxx} and we adopt a zero-width approximation for the Higgs boson, we can define:

$$C_i \equiv \frac{g^2_{Hxx} g^2_{Hyy}}{\Gamma_H} \tag{7.1}$$

as the measurement for a particular $\sigma \times BR$ observable.

From this, one can generate a χ^2 entry as follows:

$$\chi_i^2 = \frac{\frac{C_i}{C_{i,SM}} - 1}{\sigma_i^2} \tag{7.2}$$

where $C_{i,SM}$ is the Standard Model prediction for that observable and σ_i^2 the statistical uncertainty estimated for that channel.

The total χ^2 distribution is then simply defined as the sum over all the partial components χ_i^2:

$$\chi^2 \equiv \Sigma_i \chi_i^2$$

Using the σ_i evaluations, and, where available, the inter-measurement correlations, assuming that the measurement C_i converge to the Standard Model predictions, a χ^2 minimization procedure can be used to find the best estimation of their global uncertainty. If the assumptions on the model are kept to a minimum, the fit can be considered model-independent. So far, the only postulate we embedded in the fit is the zero-width Higgs boson approximation, which seems to be a reasonable hypothesis considering that experimental evidences suggest that the ratio between the Higgs mass its width exceeds five orders of magnitude [152].

If we account for all the measurements of couplings, foreseen in the Higgs sector at the low energy stage of CLIC, we obtain a total of ten observables. Their statistical uncertainties, assuming that all of them are in agreement with the Standard Model, are summarized in table 7.1.

Observable	Measurement	Statistical Uncertainty
$\sigma(ZH), Z \to l^+l^-$	g_{HZZ}^2	3.8%
$\sigma(ZH), Z \to q\bar{q}$	g_{HZZ}^2	1.8%
$\sigma(ZH) \times BR(H \to b\bar{b})$	$g_{HZZ}^2 g_{Hb\bar{b}}^2/\Gamma_H$	0.86%
$\sigma(ZH) \times BR(H \to c\bar{c})$	$g_{HZZ}^2 g_{Hc\bar{c}}^2/\Gamma_H$	14%
$\sigma(ZH) \times BR(H \to gg)$	$g_{HZZ}^2 g_{Hgg}^{*2}/\Gamma_H$	6.1%
$\sigma(ZH) \times BR(H \to \tau^+\tau^-)$	$g_{HZZ}^2 g_{H\tau\tau}^2/\Gamma_H$	6.2%
$\sigma(ZH) \times BR(H \to W^+W^-)$	$g_{HZZ}^2 g_{HWW}^2/\Gamma_H$	5.1%
$\sigma(VBF) \times BR(H \to b\bar{b})$	$g_{HWW}^2 g_{Hb\bar{b}}^2/\Gamma_H$	1.9%
$\sigma(VBF) \times BR(H \to c\bar{c})$	$g_{HWW}^2 g_{Hc\bar{c}}^2/\Gamma_H$	26%
$\sigma(VBF) \times BR(H \to gg)$	$g_{HWW}^2 g_{Hgg}^{*2}/\Gamma_H$	10%

Table 7.1.: Statistical uncertainties for the Higgs-related measurements, performed with $500\,\text{fb}^{-1}$ of integrated luminosity at CLIC at 350 GeV. The couplings with a marked with a "$*$" are effective couplings [152].

It is worth mentioning that this thesis produced six out of ten of these measurements. With these values, the χ^2 minimization can be performed on a seven-parameter space, whose results are summarized in table 7.2.

Parameter	g_{HZZ}	g_{HWW}	$g_{Hb\bar{b}}$	$g_{Hc\bar{c}}$	g^{*}_{Hgg}	$g_{H\tau\tau}$	Γ_H
Uncertainty	0.8%	1.4%	3.0%	6.2%	3.7%	4.3%	6.7%

Table 7.2.: Relative uncertainties on the Higgs couplings and total width, extracted from a model-independent global fit of the 350 GeV CLIC stage [153]. The parameter marked with a "$*$" refers to an effective coupling.

While most of these uncertainties can be further improved by the measurements performed at higher CLIC energy stages, it is important to stress that observables involving the Higgs-Strahlung production mechanism are accessible only at the relatively low center-of-mass energy of the first CLIC stage. In fact this production, being a S-channel process, quickly fades out with the increase of an event's center-of-mass energy. This makes these low energy measurements particularly useful, since, without them, it would be impossible to produce a model-independent global fit. For example, it is interesting to have a look in particular at the minimal set of observables necessary to infer the Higgs boson total width Γ_H. Since the theoretical prediction for this quantity is to be smaller than 5 MeV, its direct measurement is beyond the experimental reach.

Consulting the list of Higgs-related measurements in table 7.1, we can focus our attention on four in particular:

- **M$_1$**: $\sigma(ZH)$, sensitive to g^2_{HZZ}
- **M$_2$**: $\sigma(ZH) \times BR(H \to W^+W^-)$, sensitive to $\frac{g^2_{HZZ} g^2_{HWW}}{\Gamma_H}$
- **M$_3$**: $\sigma(VBF) \times BR(H \to b\bar{b})$, sensitive to $\frac{g^2_{HWW} g^2_{Hb\bar{b}}}{\Gamma_H}$
- **M$_4$**: $\sigma(ZH) \times BR(H \to b\bar{b})$, sensitive to $\frac{g^2_{HZZ} g^2_{Hb\bar{b}}}{\Gamma_H}$

From the first and second, we have that:

$$\Gamma_H = \frac{g^2_{HZZ} g^2_{HWW}}{M_2} = \frac{M_1}{M_2} g^2_{HWW}, \tag{7.3}$$

while from the third and fourth measurement (that are a direct result of the analysis performed in the previous chapter), we can obtain:

$$\frac{M_3}{M_4} = \frac{g^2_{HWW} \cancel{g^2_{Hb\bar{b}}}}{\cancel{\Gamma_H}} \frac{\cancel{\Gamma_H}}{g^2_{HZZ} \cancel{g^2_{Hb\bar{b}}}} \to g^2_{HWW} = \frac{M_1 M_3}{M_4}, \tag{7.4}$$

and, therefore:

$$\Gamma_H = \frac{M_1^2 M_3}{M_2 M_4}. \tag{7.5}$$

The ability to extract the Higgs width this way, serves as an additional motivation to the CLIC low-energy stage.

8. ILD Calorimeter Optimization

In this chapter we will discuss the second topic of this thesis, i.e. the investigation of a novel technique to segment scintillator-based detectors for a possible cost-effective implementation of a highly granular hadronic calorimeter for future detectors at a linear collider. In section 3.4 we have already introduced the need for highly segmented calorimetric subdetectors, to be able to profit from the use of particle-flow algorithms thanks to the highly granular spatial information available.

The CALICE [154] collaboration is a research and development group focused on the design of such a detector for calorimetry in high energy physics.

In the next sections we will briefly discuss the technologies, materials and geometries, investigated by the collaboration, for one of the choices available for the ILD [155] HCAL, namely the *Analog hadronic calorimeter (AHCAL)* option. This is based on a plastic scintillator active medium coupled to *Silicon Photomultipliers* (SiPM) [156].

After that we will introduce the *subsurface laser engraving* technique (SSLE) [157], a technology to create features inside optically transparent materials, widely used in industrial applications and, therefore, quite cost-effective and reliable.

Finally we will present some of the prototypes, developed with this technique, aimed at optically separating the readout channels in a plastic scintillator, and the subsequent signal cross-talk measurements performed.

8.1. The ILD AHCAL design

The CALICE (*CAlorimeter for LInear Collider Experiment*) collaboration is an R&D group focused on the design and implementation of hardware and software solutions for highly granular electromagnetic and hadronic calorimeters. For the hadronic component of a detector for ILD, several designs are under investigation. One consists of steel absorbers interspersed with plastic scintillators coupled to SiPMs and a 8-bit analog readout (AHCAL). There is, also, a secondary option, made with the same steel absorbers geometry, in which the absorber plates are alternated to *glass resistive plate chamber* (GRPC) [158] active layers with a semi-digital (SDHCAL) [159] readout. For each of the designs a 1 m^3 instrumented prototype has been instrumented and tested with particle beams at DESY, CERN and FNAL [160, 161]. Tungsten has been also investigated as a possible candidate for the absorbing material [162].

In the continuation of this chapter, we will focus our attention on the analog solution. It is worth mentioning that this study is of equal interest for the calorimetric subdetector proposed for CLIC; we are using here the concrete ILC/ILD implementation since, at the time this study was performed, the CLIC detector was undergoing design changes in an optimization effort.

Before discussing the technological implementation of an analog calorimeter for ILC, it is interesting to briefly point out the foreseen geometry of such a subdetector.

The main mechanical structure of the calorimeter design consists of a cylinder with a barrel, divided into two independent rings, and two endcaps. Figure 8.1 shows a schematic representation of such geometry.

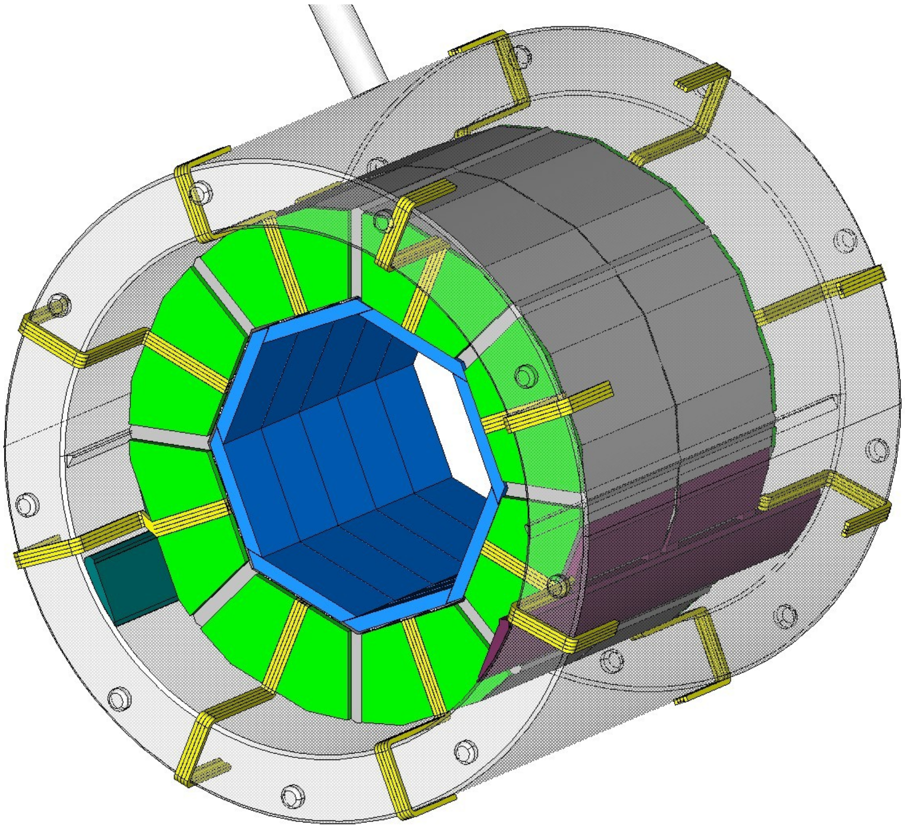

Figure 8.1.: ILC AHCAL barrel geometry. Highlighted in green are the eight stave that compose one ring of the calorimeter barrel [163].

Each calorimeter barrel ring is further subdivided into eight units called *staves*, each of them further divisible into two half-sectors. Figure 8.2 shows a detailed design of such component.

Each half-sector consists of 48 layers of steel absorber, active material and readout. The lateral dimension of each layer varies, to accommodate for the increasing detector cross-section, but, radially, they all share a 19 mm thick absorbing layer, interleaved with 6.5 mm thick active layers. The latter can be further subdivided into 3 mm of scintillating plastic tiles, 2 mm for the readout electronics, 0.5 mm of reflective foil around the tiles and 1 mm of steel for the support structure. Laterally each active layer

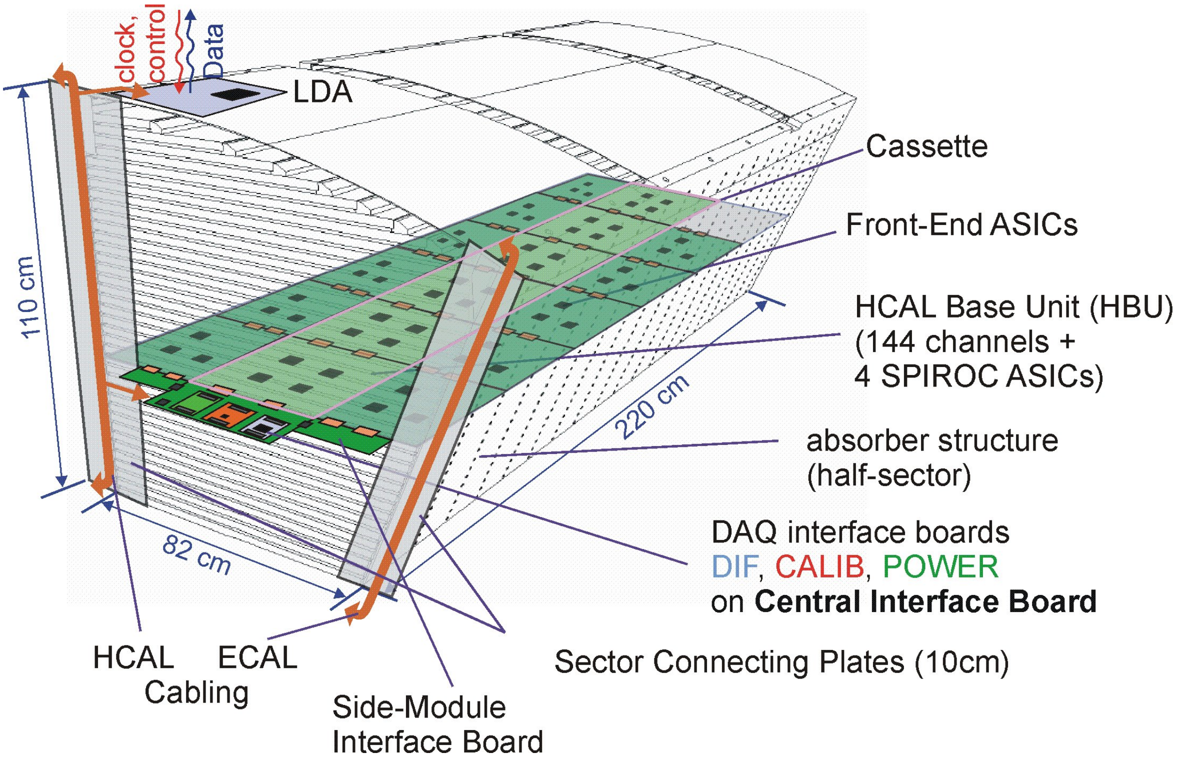

Figure 8.2.: AHCAL half-sector structure. [164]

is subdivided into up to three rows, depending on the particular layer dimensions, each of them consisting of six HCAL base units (HBU). These are the elementary readout units whose output can be cascaded into the detector readout bus system. Each HBU accounts for four ASICs capable of driving an 8-bit resolution ADC on 144 readout channel, each consisting of a scintillating tile with lateral dimensions of $30 \times 30\,\text{mm}^2$. In total each half-sector accounts for almost 150000 readout channels, with the full hadronic calorimeter barrel and endcaps totaling a little under 10 million channels.

In the next section we will discuss in detail the technology underlying this readout design.

8.1.1. Active Layer and Readout Technology

As already discussed in section 3.4, the active layers of a calorimeter convert a portion of the energy deposited by a flying-through particle into a visible signal. One possible way to achieve this task is to rely on the property of some materials to *scintillate*, that is producing photons in a well defined portion of the e.m. spectrum as a consequence of atomic or molecular de-excitations. The excited states are caused by the high-energy particles, and their byproducts created in the absorbing layers, passing through the scintillating medium. In the case of the ILC AHCAL design, the scintillation is generated in a layer of tiles made of plastic, to which an organic scintillator dopant has been added before polymerization.

The exact choices in the type of plastic and dopant are still a matter of optimization, but several have been tested so far, including: polystyrene (PS), polyethylene-naphthalate (PEN) and various proprietary amalgamate from Bicron [165], mainly based on polyvinyltoluene (PVT), such as BC-408 and BC-420. These materials vary in their cost, light output, attenuation length, pulse length and other significant parameters, but they all share a relatively similar peak emission wavelength in the *blue* to *soft-UV* spectrum (typically $380\,\mathrm{nm} - 420\,\mathrm{nm}$).

Silicon Photomultipliers

This wavelength range is optimal for the coupling of such plastic scintillators with a class of photon-sensitive devices called *silicon photomultipliers (SiPM)*. These solid-state detectors are an evolution of the photodiode design and consist of a matrix of miniaturized avalanche photodiodes (APD) lithographed on a shared silicon substrate (see figures 8.3 and 8.4) and operated in Geiger mode. To each photodiode cell a negative bias voltage is applied, depleting a region of semiconductor around the pn-junction. When a photon impinges on the device surface, it can penetrate the substrate for a few micron, eventually being absorbed by one of the atoms of the bulk. If the photon energy is above a certain threshold, enough energy is transferred to an electron to promote it from the valence band into the conduction band, creating a series of electron-hole pairs in the junction.

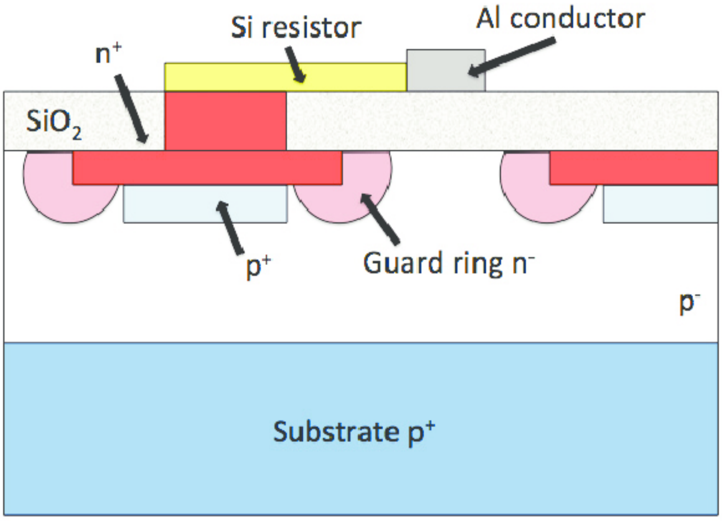

Figure 8.3.: SiPM microcell schematic view. [166]

Because of the high gradient electric field in the depletion region, such electron-hole pairs start drifting into opposite directions toward the anode and cathode respectively. Since the device is operated in Geiger mode, the drifting electrons gain enough kinetic

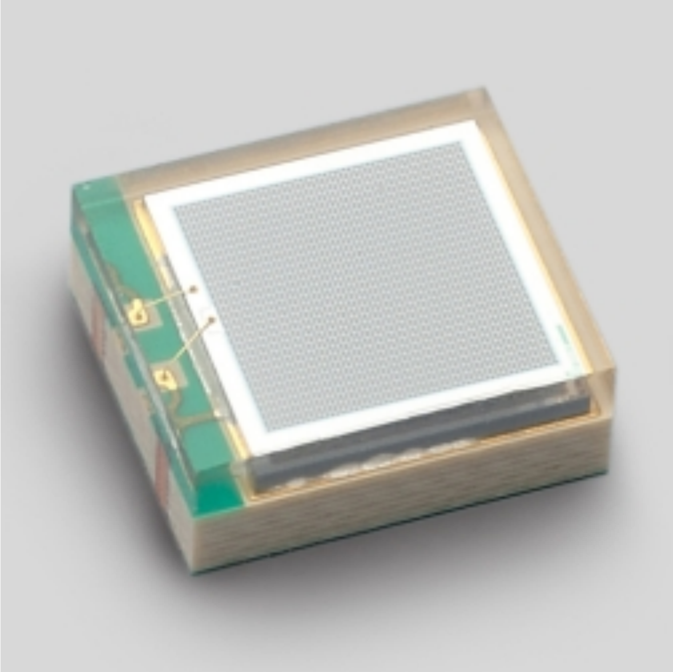

Figure 8.4.: Hamamatsu S13600 series SiPM, a surface-mounted $3 \times 3\,\mathrm{mm}^2$ active area device with a microcell pitch of $25\,\mu\mathrm{m}$. [167]

energy to be able to displace additional electrons, that, in term, start drifting and exciting more electrons, ultimately producing an avalanche. This signal amplification is at the core of the very high gain of a SiPM, usually in the order of $100\,\mathrm{dB} - 120\,\mathrm{dB}$. That is a gain factor of $10^5 - 10^6$ or four to five orders of magnitude above that of a conventional proportional avalanche photodiode. Unlike an APD though, the avalanche in a SiPM cell can self-sustain, and, once initiated, the cell would behave as a closed switch, allowing all the current generated by the bias-voltage power supply to flow through it, saturating the output signal line of the SiPM. To overcome this drawback, the biasing voltage is delivered to each cell via a *quenching resistor* in the order of $0.1\,\mathrm{M\Omega} - 1\,\mathrm{M\Omega}$. A scanning electron microscope image of such resistor can be seen in figure 8.5. The purpose of this resistor is to limit the current provided by the power supply to the SiPM cell, forcing a voltage drop on the diode junction, once the current becomes significant. This lowers the V_{bias} voltage below the Geiger threshold forcing the avalanche to stop and gives the cell a dead time of several nanoseconds (the actual time gap depending on the value of the quenching resistor and the capacitance of the SiPM cell, with a time constant $\tau \sim RC$) before the nominal V_{bias} is reestablished.

Although the signal for each microcell is binary (either avalanche or no avalanche), the output of a single SiPM is the superposition of the signal generated by the entire microcell matrix, which can consist of hundreds or thousands of photodiodes. For this reason such signal is usually regarded as analog, with the signal amplitude directly proportional to the number of photons simultaneously hitting the active area of the

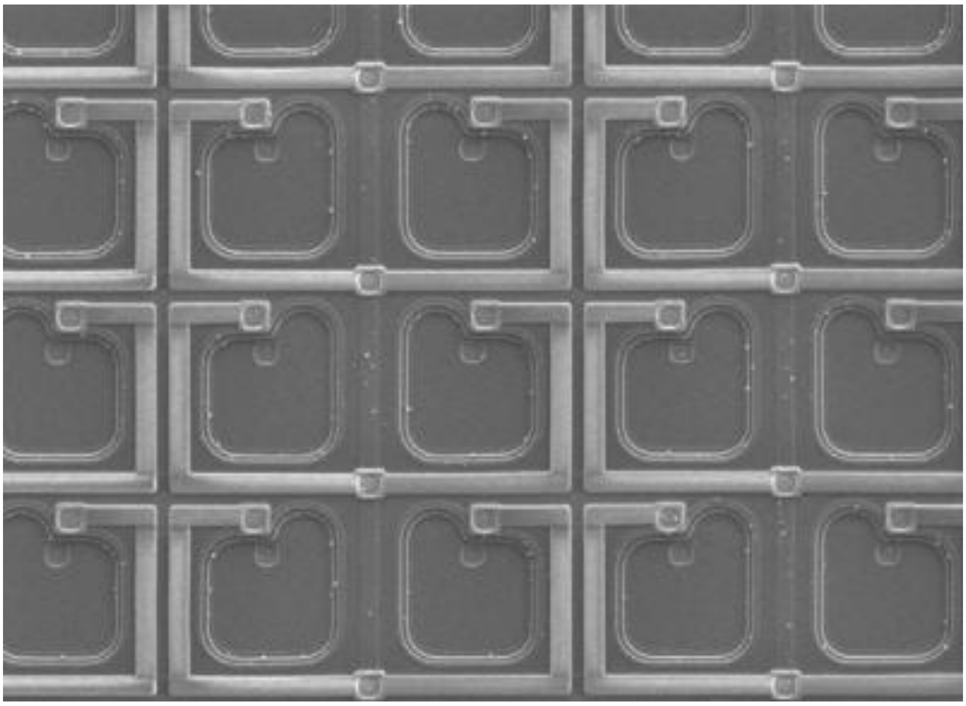

Figure 8.5.: Scanning electron microscope magnification of an array of SiPM microcells, including the V_{bias} rails and quenching resistors. [168]

SiPM.

The advantages of this photon-sensitive devices over conventional APD or even photomultiplier tubes are: high gain, compact dimensions, relatively low bias voltages (in the order of 30-80 V), insensitivity to magnetic fields and, also, high quantum efficiency in the blue-violet light spectrum, as can be seen in figure 8.6 for a S13600 series SiPM from Hamamatsu [167], a device used later on in this thesis work.

This latter property is of particular interest, when such devices are coupled with scintillators that, as explained earlier on in this section, emit mainly in the $380\,\text{nm} - 420\,\text{nm}$ range. In fact, the high efficiency in that spectral region allows to directly couple such SiPMs to the scintillator, without having to implement an intermediate wavelength-shifting mechanism, very common in the current and previous generations of scintillator-based detectors. This allows to skip several manufacturing steps, thus improving the per-channel production rate and cost, both desirable features when dealing with a channel count in the order of a few million.

For the AHCAL design, several SiPM geometries and manufacturers have been investigated. The one that, at the moment, is being used for most of the prototypes is a surface-mounted SiPM from Hamamatsu, with an active area of $1.3 \times 1.3\,\text{mm}^2$ and a microcell pitch of $25\,\mu\text{m}$, directly mounted on the HBU PCB with a grid spacing of 30 mm. For this configuration, a special geometry for the scintillating tiles was developed as well and is introduced in the next section.

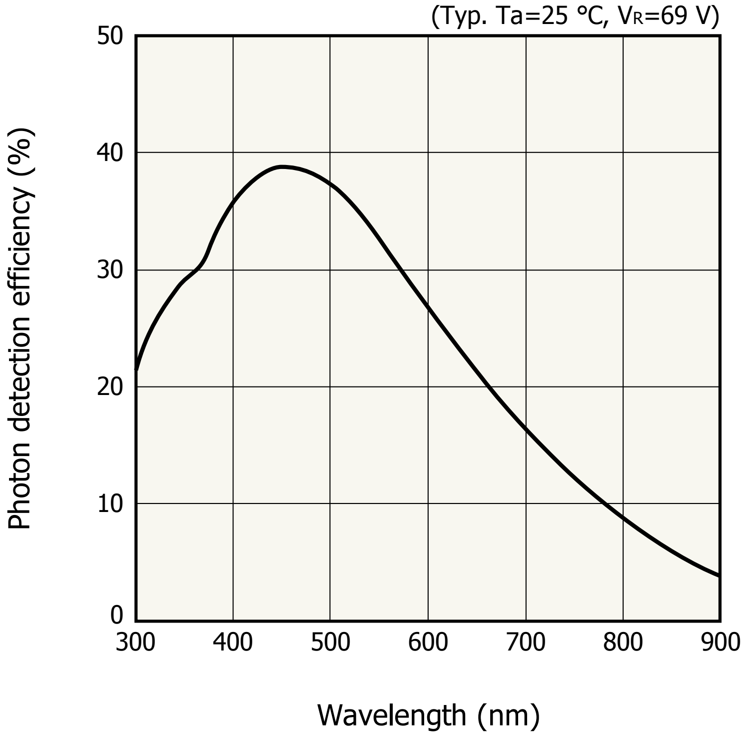

Figure 8.6.: Hamamatsu S13600 series quantum efficiency as a function of the wavelength of the incident light. The measurement has been performed at $T = 25\,^{\circ}\mathrm{C}$ and a $V_{bias} = 69\,\mathrm{V}$ [167].

Scintillating Tiles

Now that we have seen what are the characteristics and location of the photon-sensitive devices in an AHCAL active layer, as well as the options under investigation for the scintillators' material, it is useful to have a more detailed look at the geometry of the scintillating tiles.

Since the SiPMs are SMD mounted on the HBU PCB, the tiles need to couple to them on the square bottom side [169]. To accommodate the thickness of the SiPM packaging protruding from the electronic board, as well as to direct most of the photons produced in the tile towards the SiPM active area, a spherical dimple is milled into each tiles bottom face. Figure 8.7 summarizes the schematic drawing of such geometry.

The tile is then semi-automatically wrapped in a highly reflective, laser-cut, aluminium-based foil that further enhance the number of collected photons, as well as lowering the cross-talk with neighboring tiles to a sub-percent level [170].

Figure 8.8 shows one of such tiles, made of Bicron BC-408 scintillating material prior to wrapping and under an intense UV light illumination. Since this material has a peak emission at $\lambda = 425\,\mathrm{nm}$, part of the emitted light in the UV spectrum is not detected by the camera sensor.

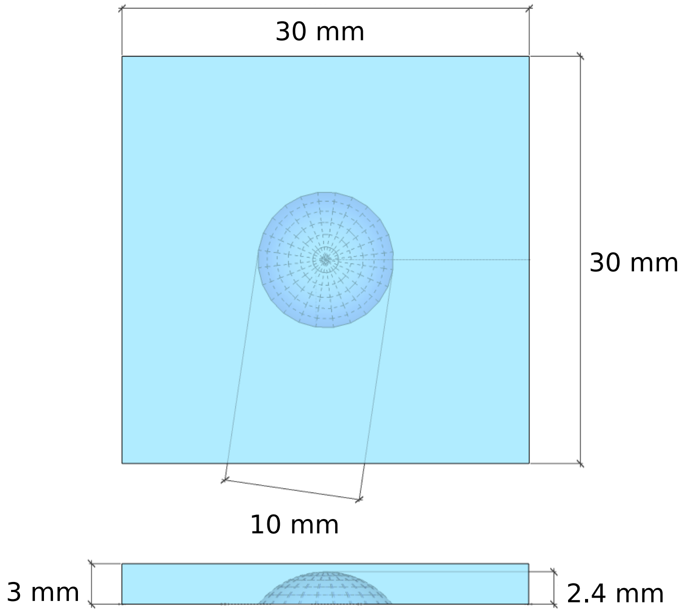

Figure 8.7.: Schematic drawing of the geometry of a typical AHCAL scintillating tile. In the tile's center, a spherical dimple to accomodate the SiPM is present. The shape of such dimple has been optimized to focus the light on the photon-sensor active area, as well as uniform the response of the tile to incoming ionizing particles.

Although this tile design provides an excellent uniformity and light yield, while minimizing the intra-channel cross-talk, making it a particularly suitable candidate from the physics point of view, from a detector construction perspective it has several disadvantages: (a) the foil wrapping at present needs human intervention, increasing the production time and cost per channel and (b) since each channel consists of a separate tile, the mechanical rigidity of the layer of scintillating plastic is rather poor and prone to misalignment with the underlying SiPM mounted on the PCB.

For these reasons several groups [171] [172] are investigating a *megatile* solution: that is a single $36 \times 36\,\mathrm{cm}^2$ plastic tile, spanning the entire 144 readout channels of an HBU, in which the optical separation is achieved by grooving thin trenches with a 30 mm spacing and filling them with an opaque coating. All these options benefit both the mechanical stability, as well as the construction time of a readout layer when compared to foil wrapping, but still require several time-consuming production steps and introduce weak points in the layer structure.

For this thesis work, a different approach has been investigated, based on a laser engraving process that will be discussed in the next section.

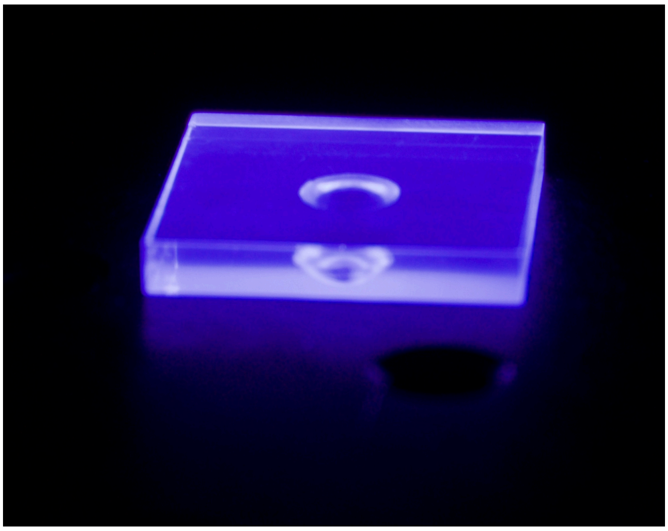

Figure 8.8.: BC-408 AHCAL tile before wrapping in reflective material. The picture is taken under an intense UV light source to enhance the scintillation output.

8.2. Sub-Surface Laser Engraving

Sub-surface laser engraving (SSLE) is an industrial process by which three-dimensional patterns can be embedded in a optically transparent material by mean of a high energy pulsed laser beam. The technique consists in focusing a short, intense laser beam inside a transparent medium, producing a sudden thermal shock around the focus point. The typical pulse width, of the order of microseconds, is much shorter than the time it would take the material to distribute the pulse energy over a large volume. This means that the entire laser pulse energy remains concentrated in a sphere with a radius of few microns. The energy density is so high that the material is quickly turned into plasma, generating a shock-wave that creates a small vacuum pocket in the bulk. Once the energy pulse is interrupted, the dislocated material quickly solidifies without being able to fully refill the generated gap. This leaves a very localized region of stress in the material that encompasses a small empty bubble. This process was discovered in the late 1960's with the advent of a novel technique to generate pulsed lasers called *Q-switching*. In the beginning, the glass optics, necessary to steer and focus the laser beam to the desired target, would crack and fail under the heavy energy load. For this reason a new materials science branch was developed, with the sole purpose of studying laser-induced defects in glass optics. Over time the understanding of laser-induced damages in transparent material was understood to a degree at which defects could be carefully placed on purpose and with high accuracy in optically transparent media. In 1991, Dr. R. Clement, a physics professor at the University of Swansea, UK, filled and obtained a patent, explaining the sub-surface engraving technique in detail [173]. Since then, the process has become relatively inexpensive, to the point that it is used nowadays to produce all sorts of promotional items, including those of physics experiments such as in figure 8.9.

Subsurface laser engraving has been used lately in the automotive industry and anti-counterfeit industry as well, thanks to its ability to produce markings that can not be tampered with. The aspect most interesting for the purpose of this study though, is the recent interest that the medical imaging devices industry has shown for this technique. Thanks to its precision and reliability, it is possible to produce optically segmented arrays from monolithic inorganic crystals [175, 176].

The idea arose to use the same process as a mean of segmenting the organic plastic scintillators used in the AHCAL prototypes, to produce optically separated tile-like channels from a larger material sheet, thus leaving the mechanical rigidity of the layer almost unaffected, while keeping the per-channel production cost at a minimum.

The first obstacle to overcome was to find a company specialized in sub-surface laser engraving that would agree to work small prototype batches on custom material, and that would be able to provide a reasonable time-cycle for the prototyping iterations. In fact, although it is relatively easy to obtain customized gadgets using such technique, most of the manufacturers production is almost completely outsourced to Asia. There are very few companies who offer this service in Europe that actually have the necessary machinery in-house and even less that accept to work on non-standard materials. Fortunately one of this company, Grüner Laser Products GmbH [177], located in Munich, has accepted to work on plastic scintillators provided by us. The ability to have direct contact with the company technical department has accelerated immensely the prototyping iteration time, making the testing of several materials and laser parameter configurations possible.

The next sections will report the results of these experimentation, after introducing the setup built to benchmark these iterations and its outcome.

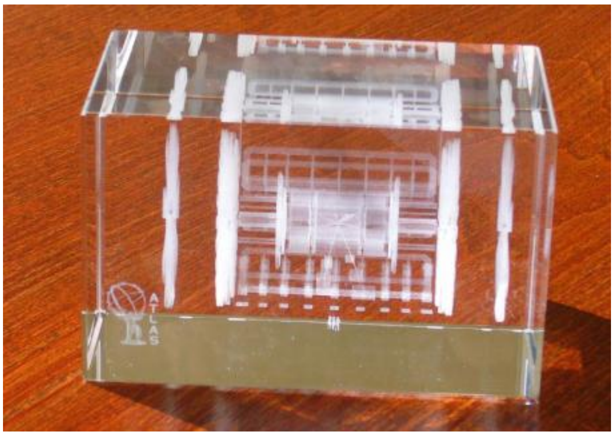

Figure 8.9.: 3D sub-surface laser-engraved model of the ATLAS particle detector [174].

8.3. Tiles Characterization

8.3.1. Scanning Setup

Since the ultimate goal of a scintillator-based readout is to convert the energy of flying-through ionizing particles into a measurable signal, to compare the capabilities of different plastic and SiPM configurations, it is necessary to test them under realistic conditions. One possibility would be to use the natural occurring minimum-ionizing muons, produced in the interactions of cosmic rays with the Earth atmosphere, as probes to characterize the response of the scintillating tiles under investigation. Unfortunately the limited flux of such muons per unit of surface, coupled to the modest size of an AHCAL readout tile, would result in prohibitively long integration windows. To be able to speed up the process, it is necessary to turn to a reliable source of ionizing particles, namely a radioactive source. For this a setup, already adopted in the past for the characterization of AHCAL active layer material and geometry candidates, has been used. This infrastructure for scintillating tiles tests has been developed at the Max Planck Institute for Physics, operated as part of the AIDA-2020 E.U. project [178]. It consist of a ^{90}Sr source as the provider of β^- radiation with an activity of 15 MBq. The source is mounted on a two-axis translation stage, coupled to a trigger detector cube, as shown in figure 8.10 and 8.11. In between the source and the trigger cube, the tile of interest, coupled to a readout SiPM, can be inserted. Since the SiPM are sensitive to the visible light spectrum, the entire setup is enclosed in a light-tight dark-box to minimize the noise level of such devices. Thanks to the motorized stage, it is then possible to move the source and trigger device over the surface of the tile under investigation, collecting a position-sensitive map of the response of the tile and SiPM bundle to ionizing penetrating electrons. This gives an overview of the light yield of the tile and the spatial uniformity of the bundle under investigation. Moreover, if multiple tiles and SiPMs are placed adjacent to each other, by moving the radioactive probe over the tiles' gap, it is possible to characterize the inter-channel cross-talk between tiles. The spatial limitations of such setup derive from the β^- collimator. At the energy emission spectrum of ^{90}Sr, the relatively large aperture of the collimator in which the source is encased results in an emission angle of a few degrees, that in terms limits the scanning stepping granularity at the millimeter level.

8.3.2. Readout Design

As mentioned earlier on in this chapter, SiPMs require a bias voltage to operate. Moreover, despite the high gain of such devices, the signal amplitude is generally not significative enough to be directly fed into an oscilloscope input. For these reasons, a readout board was designed and produced by the electronic workshop of the Max Planck Institute for Physics. The board provides the necessary reverse bias voltage to the SiPM, via an external power supply. An additional 5 V input line is present to feed an Infineon BGA614 [179] high-frequency germanium amplifier. This increases the SiPM

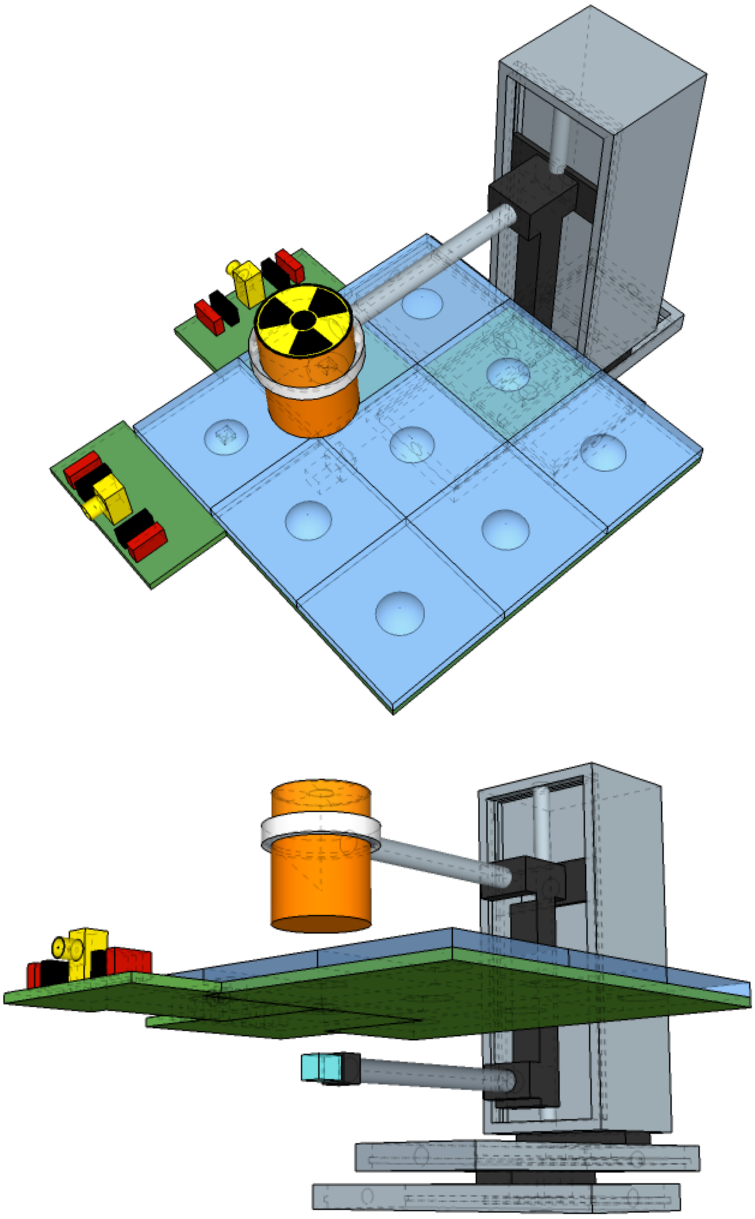

Figure 8.10.: Schematic view of the tile scan setup. A radioactive ^{90}Sr source is mounted, collinear to a trigger detector, on a XY traslation unit via a "U" bracket. Between the source and the trigger is the tile under investigation, in this case a $90 \times 90\,\mathrm{mm}^2$ 9-channel laser-engraved tile with two connected readout channels. The source is then moved over the tile and the response of the two readout channels is measured over 1000 triggers for each spatial position.

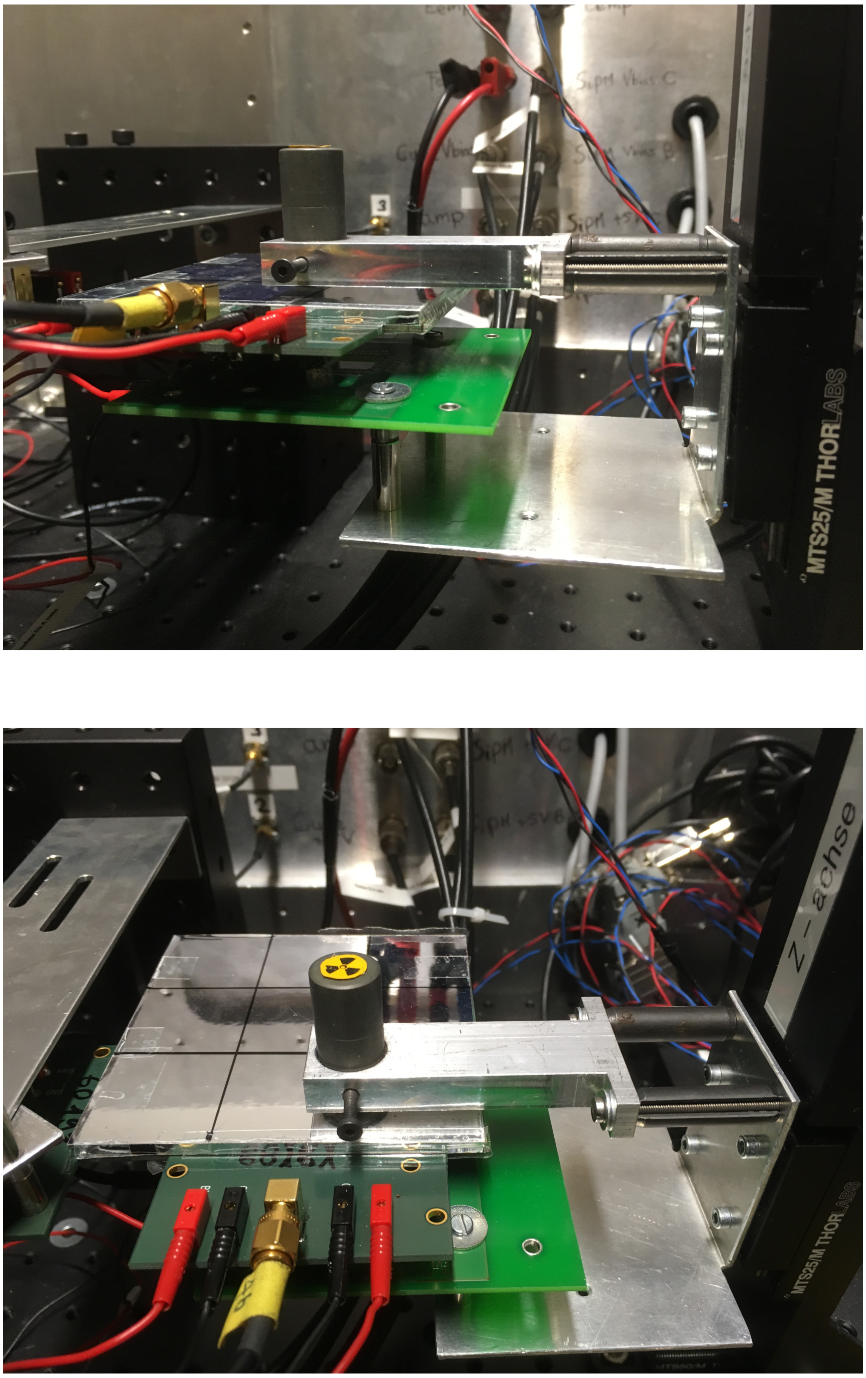

Figure 8.11.: The ^{90}Sr position-sensitive scanner, after the installation of the $90 \times 90\,\mathrm{mm}^2$ megatile prototype.

output signal by one order of magnitude. Before the output coaxial connector, a passive high-pass filter is present to filter the DC component from the signal line. The boosted signal can then be fed to an external oscilloscope via a coaxial cable.

For this setup, the oscilloscope of choice was a Picoscope 6404D [180], a 4-input device with a sampling rate of 1.25 GHz and an 8-bit per channel ADC converter. The oscilloscope is set to trigger on a dedicated input channel connected to the trigger device. This consists of a $5 \times 5 \times 5\,\mathrm{mm}^3$ scintillating cube coupled to a SiPM, that is readout via an electronic board identical to that just introduced for the signal channels.

For each scanning position, a total of 1000 trigger events is collected. On top of that, since the SiPM technology exhibit random single micro-cell discharges with rates in the order of tens of kHz, it is possible to exploit such behavior to implement a continuous gain calibration strategy. The procedure works as follows:

- for each position, after the physics trigger have been collected, each readout channel is set in auto-trigger mode with a trigger threshold approximately half of the width of the typical one-photon (in short 1 p.e.) dark noise signal. Figure 8.12 shows the signal amplitude associated to one of these 1 p.e. events, as a function of time, for a SiPM preamplified with a gain of 19 dB.

- 1000 of such auto-trigger events are then collected for each channel.

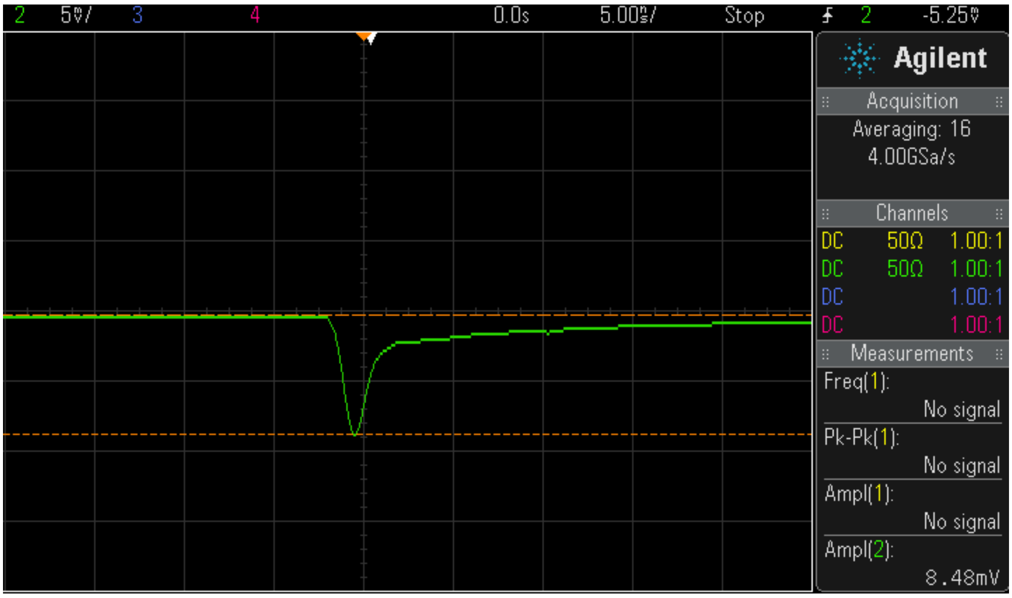

Figure 8.12.: Typical SiPM response for a one-photon equivalent (1 p.e.) signal ($5\,\mathrm{mV/div}$ vertical and $5\,\mathrm{ns/div}$ horizontal resolution). The signal, preamplified by a BGA614 amplifier, is generated by a single microcell discharging. The exponential decay rate is determined by the relation between the cell capacitance and the value of the quenching resistor. Image courtesy of Daniel Heuchel.

- after a pedestal-subtraction step, the integral of the average 1 p.e. response is calculated to obtain a gain-corrected calibration coefficient for each scanning position.
- each signal waveform is then normalized with this coefficient to compensate for eventual gain-shifts over the scanning procedure

This step is particularly useful for finely spaced tile scans over large surfaces. In fact the scanning of a tile with this procedure lasts several days of uninterrupted acquisition and the continuous gain corrections help compensating for external factors such as day/night temperature cycles, a parameter to which the SiPM's gain is particularly sensitive.

8.4. Results from SSLE Tiles

The first step in the process of producing laser-engraved optical trenches in plastic scintillators is to find a suitable material that can withstand the thermal stresses of the exposure to the pulsed laser beam without softening.

Several candidates were investigated among the organic scintillators used in the CALICE collaboration: two from Saint-Gobain, i.e. Bicron BC-408 and BC-420, polystyrene (PS), and EJ-200 from Eljen Technology [181].

Most of these scintillators, with the exclusion of PS, are based on PVT (or proprietary slight variations thereof), whose chemical composition can be seen in figure 8.13.

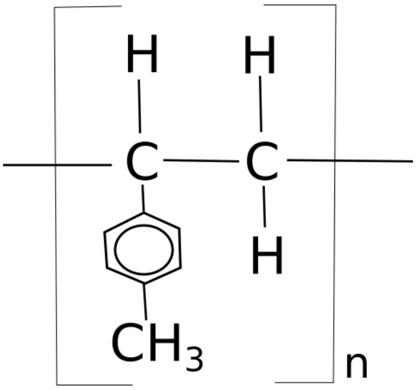

Figure 8.13.: Chemical structure of polyvinyl-toluene plastic (PVT). Image from [182].

It is worth noting the high carbon content per polymer unit, especially in the aromatic group. This property explains why, when exposed to the intense energy of a pulsed laser beam, *charring* can occur. Charring is the process in which, in an oxygen-poor atmosphere, the carbon-hydrogen bonds in a material are broken under high heat, without the further carbon oxidation step present in normal combustion. This results in a cloud of carbon atoms that quickly combines into amorphous carbon or partially crystallized graphite. The consequence of such a process is that the surface of the material turns to a deep black color. As one can see in figure 8.14, laser-engraved plastic is an ideal material for such a mechanism to occur since the carbon chains, in the low-oxygen environment inside the plastic, are combined with the intense heat from the laser sour ce. This is potentially a problem, since it results in light absorption rather than diffused reflection that can lower the amount of light collected by a SiPM.

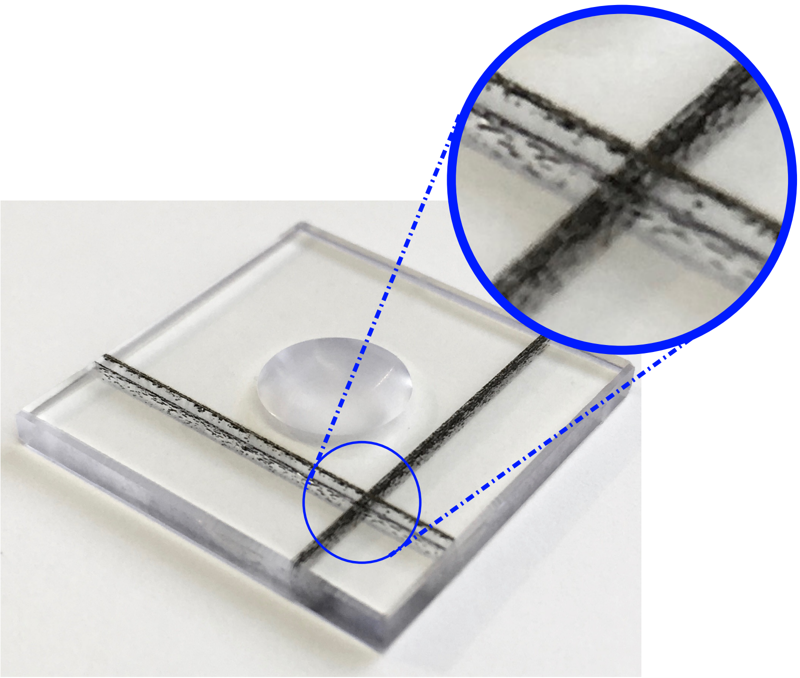

Figure 8.14.: Charring in a laser-engraved BC-408 AHCAL tile prototype. During the intense heat exposure from the laser beam, the hydrogen-carbon chemical bonds breaks allowing the carbon to produce an amorphous or partially crystallized graphite layer on the internal surface of the ablated material. This exhibits the characteristic deep black coloration.

Since each material is slightly different, the SSLE company needed a learning phase in which the main parameters for the laser, such as intensity, pulse duration and focusing, could be optimized. This resulted in a few test samples that exhibit intense structural damages. These have been investigated using a Keyence VHX-5000 [183] digital scanning microscope, whose results are presented, for EJ-200, in figure 8.17 and 8.18.

From these it is possible to observe two kind of damage: surface and bulk. Surface damage is related to the laser beam focusing parameter and the quality of the surface finishing, while bulk damage seems to be more sensitive to the laser intensity and pulse duration.

It is interesting to note that, despite the fact that the producers state that EJ-200 and BC-408 are commercially equivalent, the latter presented more intense surface damage. This was noticed also by the SSLE company that reported that the BC-408 samples were prone to partial melting and surface smoking. It is unclear if such behavior is connected to any difference in the chemical composition of the material (since these are proprietary compounds for which no exact composition is available for public access), or if the phenomenon is related to a difference in the quality of the surface polishing and cleanliness.

Using the 3D scanning function of the microscope, it was possible to assess the depth of the surface fractures in BC-408 generated in the engraving process, as shown in figure 8.15. For EJ-200 the fracture depth was negligible.

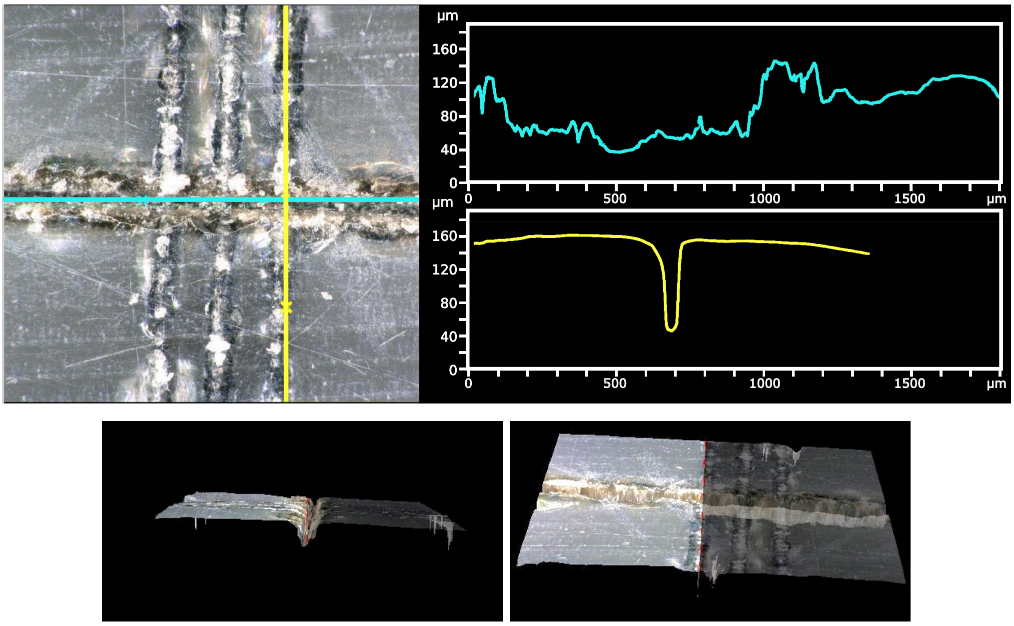

Figure 8.15.: Measurement of the depth of a surface defect in BC-408 generated by SSLE. The trench has a maximal depth of ≈ 120 µm and a total width of ≈ 50 µm. The three vertical stripes, also laser-engraved in the bulk of the material, exhibit a very exiguous degree of surface damage.

Test where also performed on PS and, again, on EJ200, to assess the minimum distance at which multiple lines could be engraved to increase the optical insulation in the material. Figure 8.16 shows the results on both materials with optimized laser settings that produce minimal damage on the surface and the bulk of the material, other than the controlled engraving of the optical trenches.

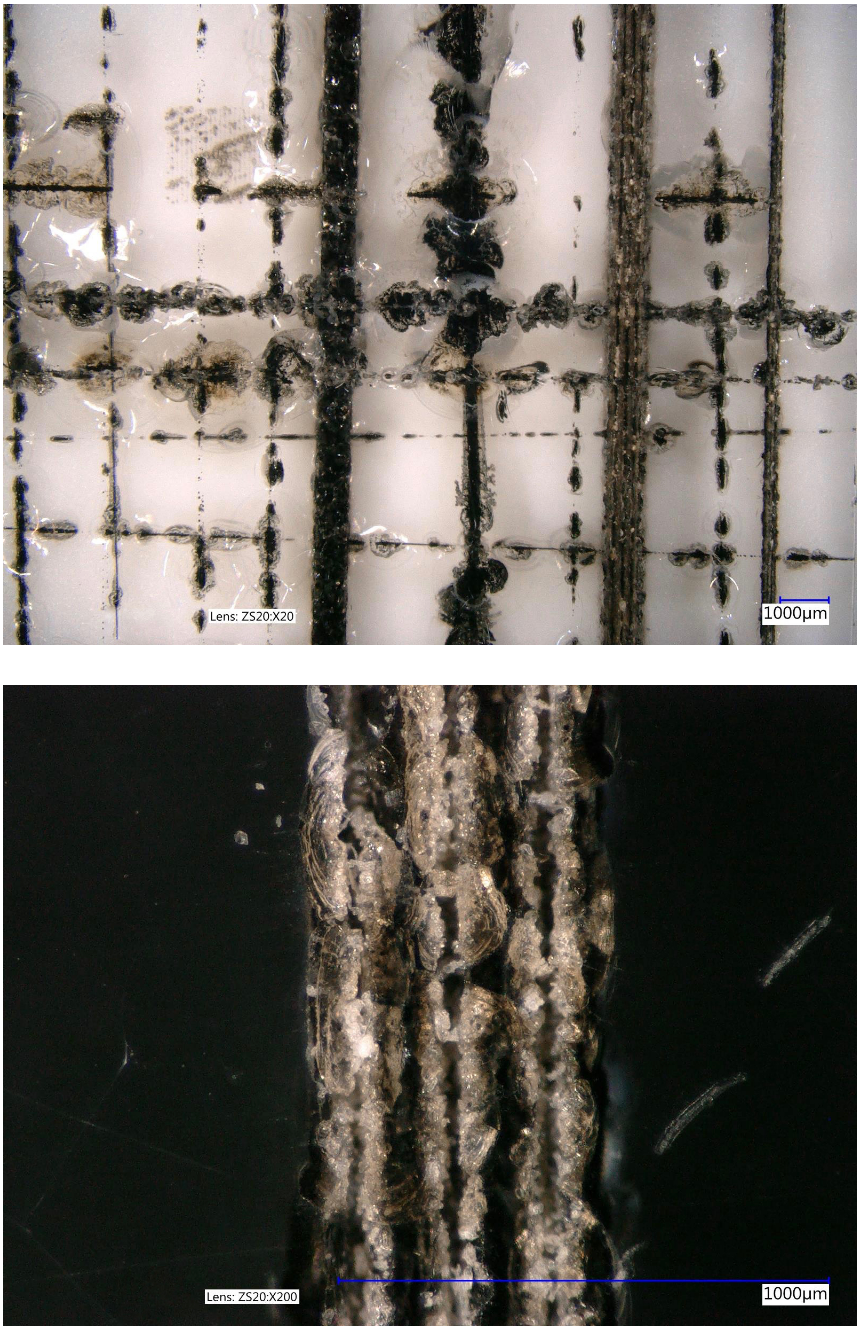

Figure 8.17.: Surface damage on EJ-200 generated during the testing phase of the laser settings for SSLE.

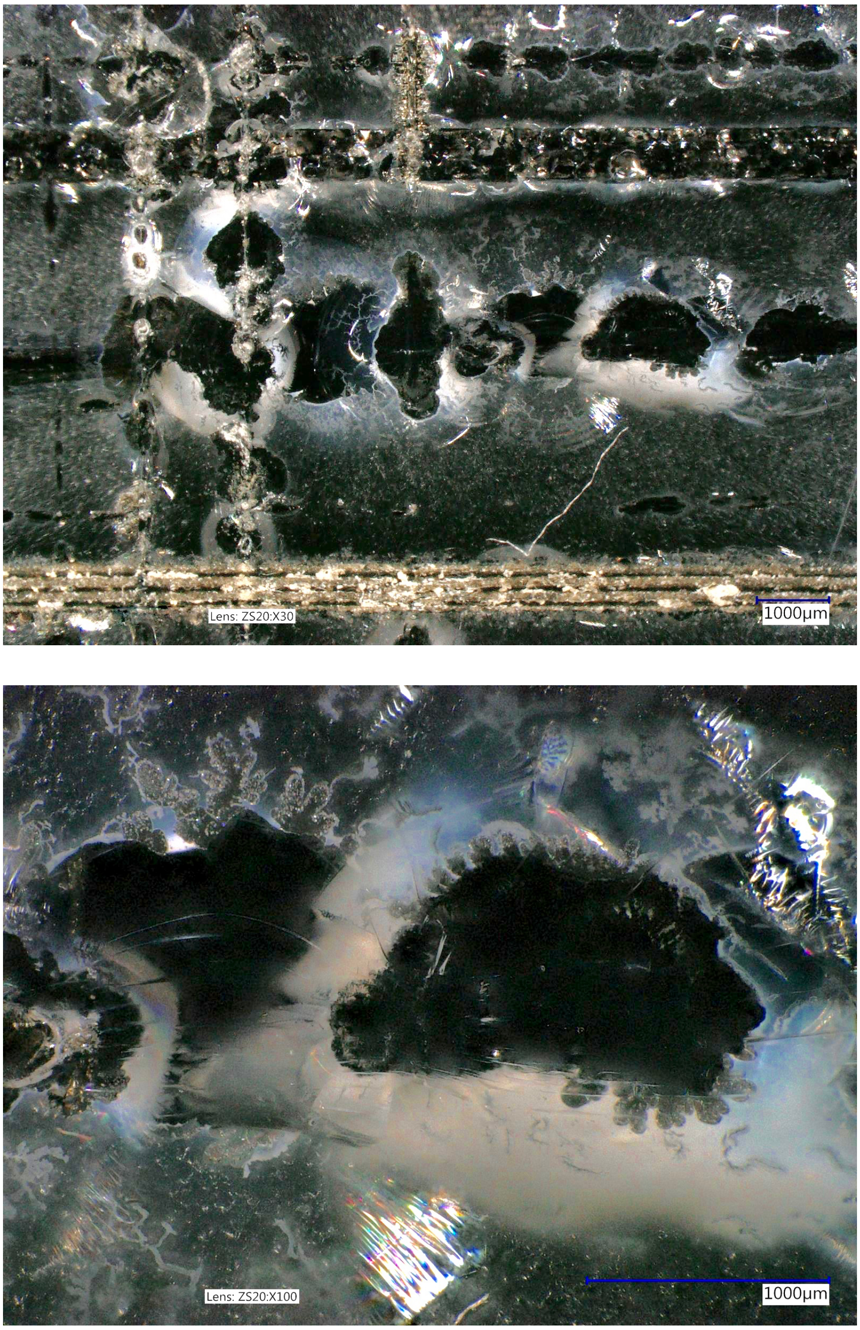

Figure 8.18.: Mechanical damages to the plastic core of EJ-200 during the testing phase of the laser settings for SSLE. In the top figure it is possible to see the cracks resulting from intense ablation, caused by a too-intense laser beam setting. In the magnification below it is possible to see seeds of carbon crystallization at the edges of the ablation bubble.

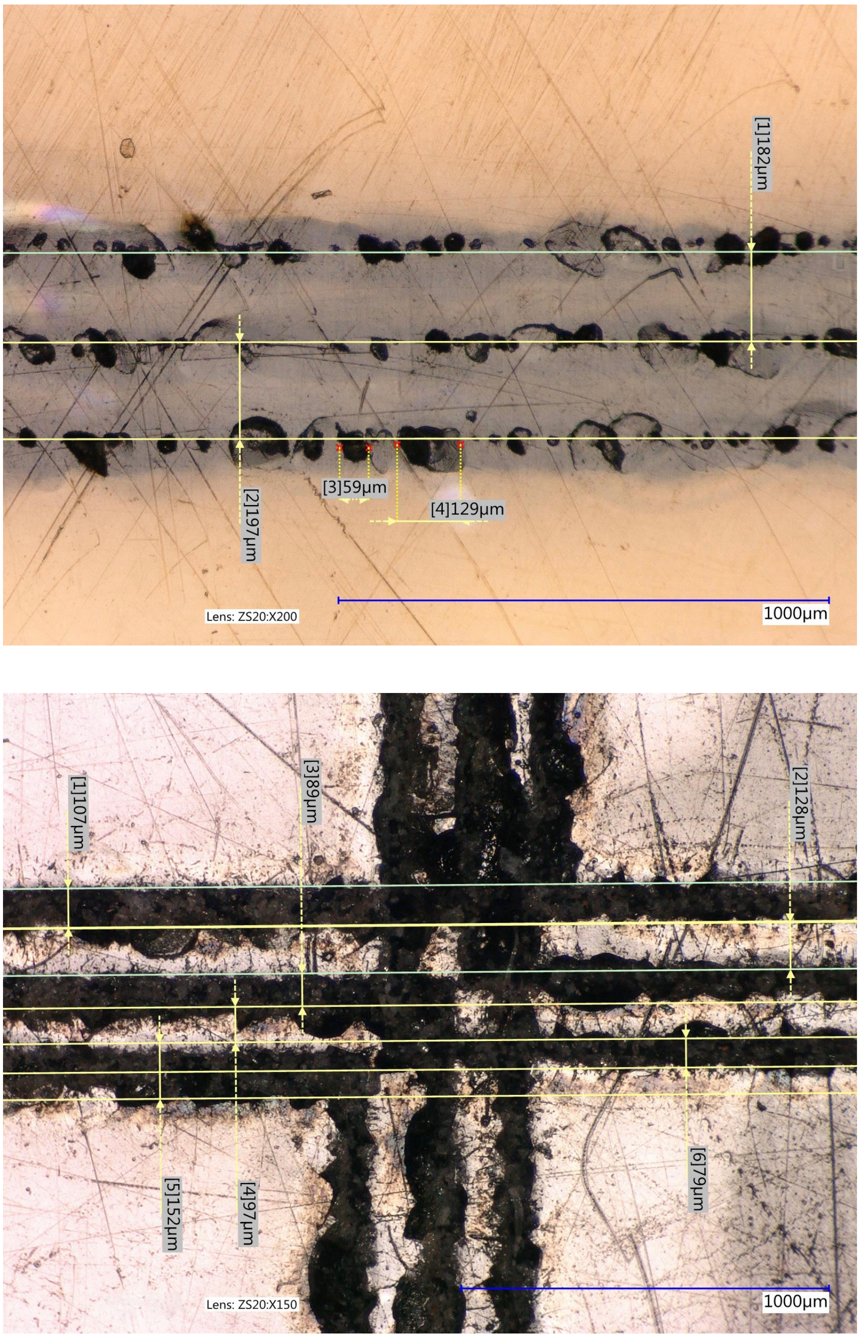

Figure 8.16.: Multiple laser engravings on PS (top) and EJ200 (bottom), to assess the thickness of the optical barriers and the minimum separation achievable between them in optimized laser setting conditions. The surface and bulk damage with such settings is negligible for both materials.

Polystyrene proved to be a very friendly material from the get-go for SSLE, but acceptable results were obtained with EJ200 once the laser settings were optimized. The typical thickness for the optical barriers is in both cases of the order of 100 µm with a comparable minimum distance between them. The total thickness of a triple engraving amounts to ≈ 500 µm, a gap thickness that is still very competitive with that produced by wrapping two neighboring tiles in reflective foil or in other megatile approaches.

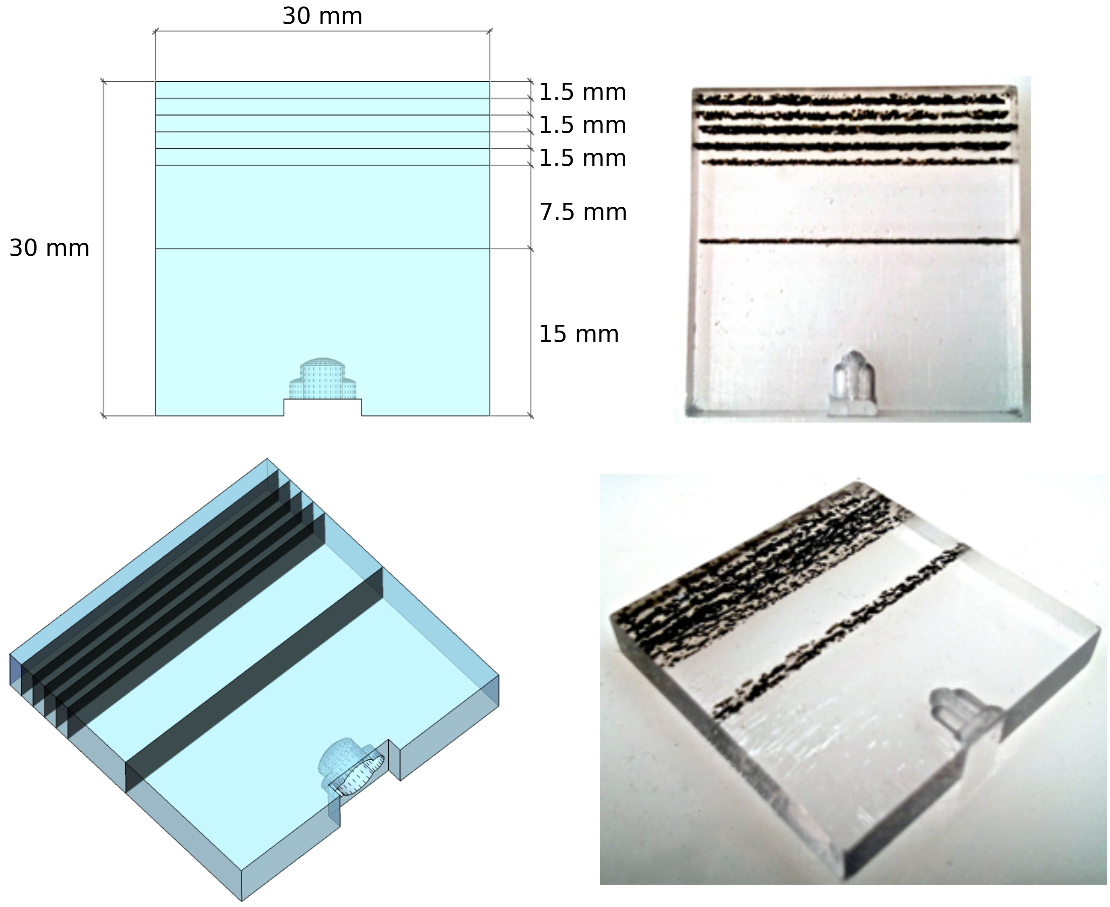

Figure 8.19.: Schematic design of the first BC-420 tile sample processed with the SSLE technique to be scanned with ionizing radiation. The dome-shaped dimple at the bottom couples to a side-mounted SiPM.

The first tile to be measured with the scanning setup introduced in the previous section, after being exposed to the subsurface laser engraving technique, served as a proof of principle of the viability of such a method. This prototype tile is a spare from an older AHCAL design, in which the SiPM is mounted laterally on a custom milled dimple that has the dual task of collecting the light on the SiPM active area and to uniform the tile response to ionizing particles over its surface. The material used is Bicron BC-420 with a thickness of 5 mm, with six optical barriers, engraved at various distances perpendicular to the SiPM active face, as shown in figure 8.19.

After placing the SiPM in the designated cavity, the tile was wrapped in 3M DF 2000

MA [184], an aluminium-based multicoated reflective foil particularly well suited for the soft-UV 391 nm emission peak of BC-420. The tile was then placed in the scanning setup to undergo a 1 mm pitched scan, the result of which is reported in figure 8.20.

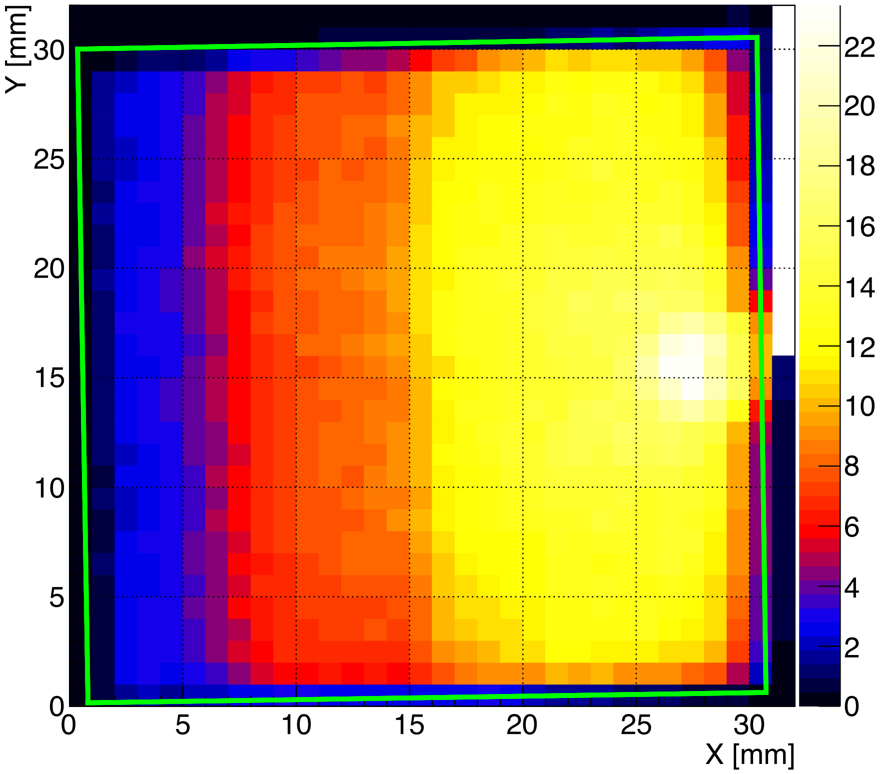

Figure 8.20.: Position-sensitive response of a 30 × 30 mm^2 BC-420 scintillating tile (green box) to ionizing radiation. 0.546 MeV β^- trigger a coincidence cube placed underneath the sample and the response of a SiPM (coupled on the right hand side) to the light produced in the tile is measured. Two SSLE optical barriers (at ≈ 15 mm and ≈ 7.5 mm) are clearly visible and account for a light reduction of approximately 40-50% each.

From the figure, the optical separation of the SSLE barriers is clearly visible and accounts for a factor two reduction in the transmitted light. Although this level of cross-talk is probably not acceptable for calorimetry, it must be noted that this result is achieved with a single stripe of laser engraving. This gave us confidence that, using the multi-line separations investigated in PS and EJ200, a satisfactory attenuation would have been achievable. For this reason a larger prototype tile was produced from a 3 mm sheet of EJ200, this time using triple-line engraving and the same bottom dimples geometry foreseen in the AHCAL active layer design. EJ200 was preferred over PS because of its higher light yield and the PVT base, common to many of the scintillator candidates for the final detector.

To simulate the real-size geometry of the AHCAL readout channels, optical barriers were engraved on a $90 \times 90\,\mathrm{mm}^2$ plastic sample in order to produce a total of 9 readout tiles, as shown in figure 8.21.

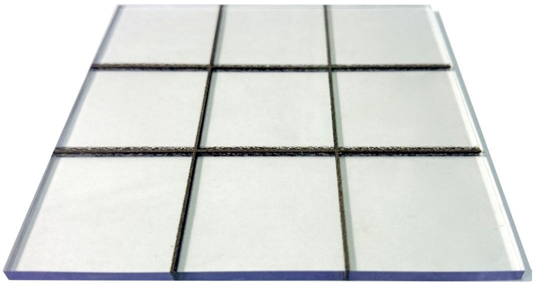

Figure 8.21.: EJ-200 laser-engraved 9-channel megatile prior to dimple milling and wrapping in reflective foil.

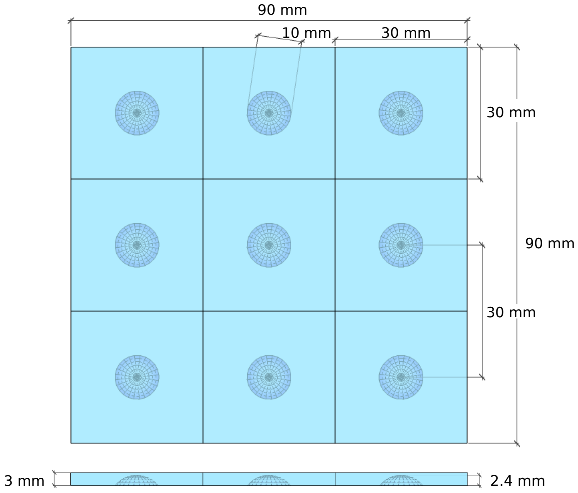

Figure 8.22.: Technical drawing of the surface dimples in the megatile prototype.

After SSLE, the megatile prototype was further processed with surface dimples to accommodate the SiPMs, as per figure 8.22 and wrapped in 3M DF 2000 MA. To perform a measurement of the inter-channel cross-talk, two SiPMs were installed on neighboring channels, one at one edge and one at the corner of the megatile, as shown in figure 8.23.

To ensure more sensitivity to the low light signals reaching the SiPM active area from behind the optical barriers, larger than usual Hamamatsu MPPC S13600 SiPMs with an active area of $3 \times 3\,\mathrm{mm}^2$ were installed on the underlying PCB board for this measurement. Just from geometrical considerations the collected light is enhanced by almost one order of magnitude compared to the standard SiPM used before.

Since the travel of the motorized stage that performs the scanning is limited to $48 \times 48\,\mathrm{mm}^2$, the scanning area was picked to overlap as many SSLE lines as possible, while covering one of the tiles equipped with a SiPM readout to assess its uniformity and light yield, as shown in figure 8.23.

A first 2 mm pitched scan was performed to assess the response of the megatile, the results are shown in figure 8.24.

From these it is possible to see that the triple laser-engraved optical barriers are quite effective in attenuating the transmitted photons to the neighboring parts of the megatile. The downsides, compared to non-engraved tiles that are fully wrapped in reflective foil, are in the loss of response uniformity inside a tile and the diminished light yield of this solution. While the former can be partially justified by the fact that the shape of the dimples, that collect the blue/UV-photons to the SiPMs, have been optimized for

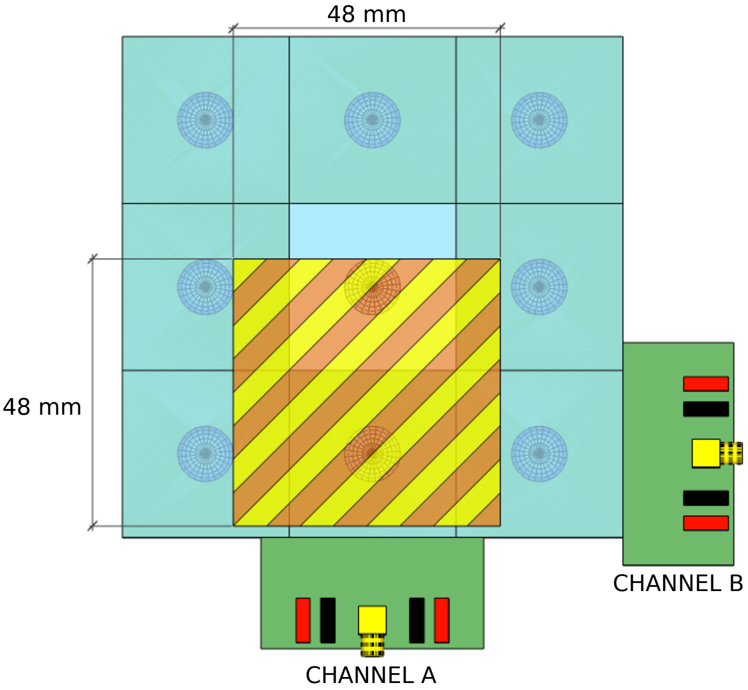

Figure 8.23.: Schematic drawing of the instrumented megatile prototype. Two SiPMs are place at the bottom center (channel A) and bottom right (channel B) positions. The scanning area is defined by the striped area.

reflective walls and could probably be redesigned to account for absorbing barriers, the latter issue is particularly concerning.

In fact not only was the material tested among those with higher light yield, but the bigger SiPMs adopted for the measurement collect, in first approximation, almost ten times more light than the reference $1.3 \times 1.3\,\mathrm{mm}^2$ SiPMs. We know that at least some of the 0.546 MeV β^- of the ^{90}Sr decay are fully penetrating the scintillator tile, since they have to reach the underlying cube to trigger the readout. From previous measurements, we also know that the calibration factor between the energy deposited by one of these flying-through electrons and a MIP is 1.2 [185]. This would resolve in an average MIP response of the scintillating tiles of 5 p.e. or less, too low to be of use. Possible solutions to overcome this issue are:

- Replace the scintillator material with one with higher light yield
- Increase the thickness of the scintillator layer
- increase the active area of the SiPMs

Unfortunately all the options above are not compatible, either because of costs or for geometrical constrains, with the current AHCAL designs, which suggests that the SSLE technology is not a viable option for this project.

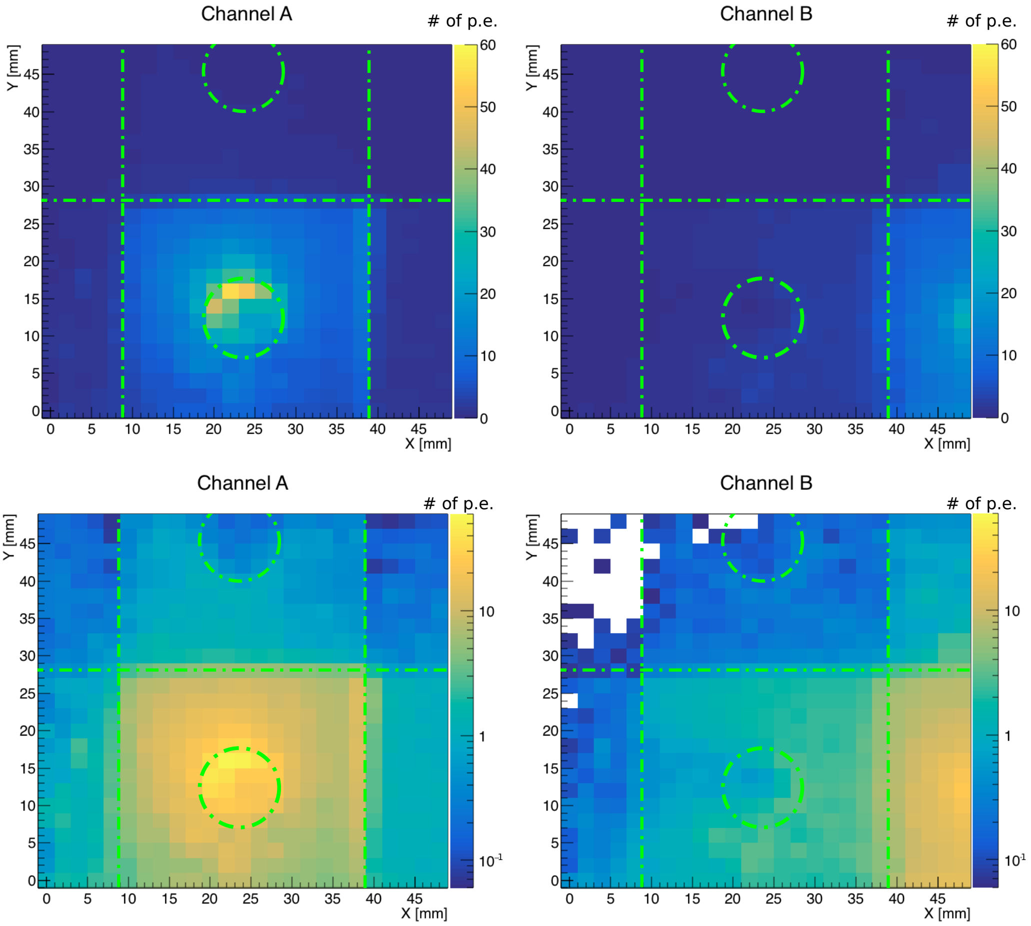

Figure 8.24.: Results of the scan of the triple SSLE EJ-200 megatile prototype with a ^{90}Sr source. The left column refers to the response of the SiPM situated under the bottom center channel of the megatile, while the right column to the one under the bottom right channel. The x and y axes represents the scanning position in mm, while the z axis shows the tile response (calibrated in p.e.) on linear (top row) and logarithmic (bottom row) scales. While the linear scale helps assess the uniformity of the response, the logarithmic one improves on the details of cross-talk.

For completeness, to have a better quantitatively estimate of the cross-talk magnitude, another finer scanning was performed perpendicularly to the optical separation. This was a single line, with a scanning pitch of 1 mm and a span of 10 mm in both directions from the laser-engraved line. The results of the scan was then normalized, for each channel, to the average response of the SiPM readout for scanning positions inside that channel, that is scanning position only on the side of the optical barrier closer to the SiPM. This was done to equalize the response of both channels, so that the cross-talk magnitude could be compared. Figure 8.25 shows the results of such scanning.

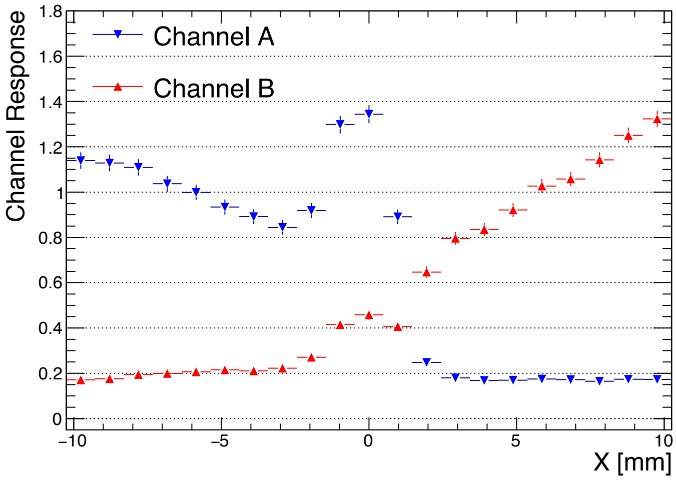

Figure 8.25.: Response of the laser-engraved megatile prototype to a single-line scan across the SSLE optical barrier. The results are normalized, for each channel, to the average response of the SiPM readout for that channel's scintillator.

The first thing that can be noticed is that, right at the optical barrier, there seems to be a higher response to the ionizing radiation. The reasons for this increase are unclear, but it seem to be consistent across multiple measurements of triple-engraved optical separations at different positions on several tiles. One possible explanation could reside in the interaction of the ionizing radiation with the products of ablation on the engraving surfaces. The fact that it affects measurements taken up to 1 mm away from the interface is consistent with the spatial resolution of the radioactive source.

To minimize the bias of this artifact in the quantification of the inter-channel cross-talk, the three central data points, around the optical barrier, have been removed from the calculation. We can, then, define the cross-talk as the ratio of the average responses of the scintillator on each side of the barrier. This results in a total cross-talk of 18% and 21% for channel A and B respectively.

Overall, the results of the test of this engraving technique are not yet compatible with the specifications required for the active layer of the AHCAL. Although the uniformity could potentially be improved, by an effort in redesigning the geometry of the bottom dimple where the SiPM is locates, the main source of concern at the moment, is the overall drop in the light yield of this readout, when compared with tiles with reflective sides. The use of a SiPM with a larger active area can certainly mitigate the problem, as the be the increase of the plastic layer thickness. Switching to inorganic scintillators could certainly mitigate the drawbacks of charring, but most inorganic crystals are much more expensive than their plastic counterparts, thus diminishing the appeal of this technique.

9. Conclusions

The CLIC and ILC colliders, which are being discussed as future global facilities in particle physics, provide the possibility for precision measurements going substantially beyond the capabilities of the LHC. One of the main topic of research of such linear e^+e^- accelerators will be an accurate characterization of the Higgs sector, for which the R&D teams of both accelerator concepts are performing extensive benchmark analyses based on realistic full-detector simulations. This thesis contributes to this effort, with an analysis on the achievable precision for the hadronic decay modes of the Higgs boson in a 350 GeV center-of-mass energy stage 1 scenario for CLIC. Studying the Higgs boson at this energy is of particular interest, since, unlike at other energies, the Higgs boson is produced via two different mechanisms with comparable cross-sections. These are Higgs-Strahlung, where a Z boson emits a Higgs, and Vector-Boson-Fusion, in which the Higgs boson is generated in the fusion of two W bosons. Being able to access these simultaneously allows to perform multiple $\sigma \times BR$ measurements of the same decays of the Higgs that, when combined with a recoil-mass measurement of the total cross-section $\sigma(ZH)$, allows to extract the Higgs width Γ_H with minimal model assumptions. This will be a key factor when combining all the Higgs-related measurements performed at all energy stages foreseen for these e^+e^- colliders.

Of all the possible Higgs decays, the fraction of where it decays into either a $b\bar{b}$ or a $c\bar{c}$ quark-antiquark pair or into two gluons (i.e. the hadronic decay modes) accounts for almost 70% of all decay modes. Despite this being a large fraction of the total number of Higgs produced, it must not be forgotten that Higgs events are relatively rare, when compared to the Standard Model background. At 350 GeV, ZH and VBF account for a total cross-section of less than 150 fb, while the $e^+e^- \rightarrow q\bar{q}$ background alone shadows this quantity by more than 200 times. In order to investigate the properties of the Higgs boson, the first step of the analysis consists in the development of a multivariate method to extract Higgs events candidates from the large background of other Standard Model processes, using *boosted decision trees*. This algorithm has the distinct advantage over many other machine learning methods to be particularly robust to overtraining and correlations of the input variables, providing the user with a good compromise between classification performance and efficiency. Two BDTs are trained, to account for the different signals final state signatures. One is dedicated to classify hadronic Higgs decays produced in VBF and in ZH, Z→neutrinos events, while the other specializes on ZH events where both bosons decay hadronically. The training set of each classifier consists of a representative sample of all the signal and background processes, using observables computed from Monte Carlo-generated events, processed by members of the CLICdp collaboration with a full-detector reconstruction based on particle flow. Among these are the properties of particle jets in the final state, that are identified applying the Durham clustering algorithm to the reconstructed particles in the final state. The large quantity of observables at disposal is trimmed down in an iterative process that discards the least significant input variables, until a target number of observables is reached.

The rather good background rejection capabilities of these classifiers, as low as 10^{-5} for some backgrounds, and a signals efficiencies of up to 58%, are alone not sufficient to isolate low-statistics signal channels like $\sigma(VBF) \times BR(H \to c\bar{c})$, that has a total cross-section of less than 1 fb.

For this reason, and to be able to split the signal candidates into the three distinct hadronic decay species, an additional multidimensional binned *Likelihood* template fit is developed, using flavor information of the jets previously tagged by a neural-network-based classifier, provided by the lcfiplus software library, and trained with $Z\nu\bar{\nu}, Z \to q\bar{q}$ final states. In addition, to be sensitive to the different production mechanism of the Higgs, the fit considers transverse momentum as well. The resulting fit is then applied to simulated data sets in a toy Monte Carlo procedure that estimates the uncertainties of a total of six parameters: $\sigma \times BR(H \to b\bar{b}, c\bar{c}, gg)$ in both ZH and in VBF production channels. The final statistical uncertainties for this six observables are, for a total integrated luminosity of $500\,\text{fb}^{-1}$, 0.86% and 1.9% for $H \to b\bar{b}$, 14.4% and 25.8% for $H \to c\bar{c}$, and 6.1% and 10.2% for $H \to gg$ in ZH and VBF productions, respectively. The simultaneous extraction of the uncertainties of multiple observables gives access to their correlation matrix. This has been used by members of the CLICdp collaboration to ameliorate the results of the model-independent global fit of the Higgs sector, that now projects resolutions of 3.0%, 6.2% and 3.7% in the couplings of the Higgs to b-quarks, c-quarks and gluons, respectively, for the first stage of CLIC.

Several possible sources of systematic errors are investigated. Among these, the impact of the estimated systematic shifts of the signals and backgrounds templates is in most cases very low, with the only noticeable changes being in the $\sigma(ZH) \to b\bar{b}$ and $\sigma(ZH) \to gg$, that move to 0.9% and 6.8%, respectively.

The amount of MC events available at the moment, despite consisting of a sample of almost 15 million entries, is for some of the measured observables potentially at the lower limit of what can be used to perform a robust, unbiased, binned-template fit analysis. Fortunately, the ever-increasing availability of cheap computational power, will allow, in the future, to perform similar analyses with much larger simulated samples in a reasonable amount of time.

The systematic uncertainties associated with the input variables of the BDT classifiers are not investigated. Should a similar analysis be performed in the future with real experimental data, it will be necessary to carefully consider the systematic errors associated with each of them. This task is, at present, difficult to perform, because these systematics are associated to possible inaccuracies of the detector and the physics models that can be properly estimated only with control channels populated with real data.

As a side note to this analysis, it must be noted that the current proposal for the first energy stage of the CLIC baseline has been shifted from a 350 GeV to a 380 GeV. The analysis presented here still uses the 350 GeV design option for several reasons: (1) the decision to increase the energy is quite recent and the analysis was already under development at that point, (2) a good fraction of the total simulated statistics had already been generated and it would have been impossible to obtain an equally-sized event sample in a reasonable time-scale, and (3) the 350 GeV center-of-mass energy was adopted by several other Higgs-related analyses that, together with this study and the benchmarks for the higher 1.4 and 3 TeV CLIC energy stages, have been summarized in a comprehensive paper that reviews the potential of CLIC in the investigation of the Higgs sector. The paper is, at present, at the peer-review stage. Nevertheless, to have an impression of the sensitivity achievable by a 380 GeV CLIC experiment, the fit is applied to a set of 350 GeV templates, rescaled to account for the different process cross-sections at 380 GeV. Beam polarization scenarios, up to +80/-30 at 350 GeV, are also considered. For the 380 GeV scenario, the resolution achievable on the Higgs-strahlung channels is reduced on average by 10%, while that of VBF channels enhanced, by roughly 25% on average. This is to be expected, since with the energy increase the *t-channel* processes are enhanced, while *s-channel* processes drop. The asymmetry between the gain in the first and the loss in the second, is explained by the reduced cross-section of $e^+e^- \to q\bar{q}$, the most abundant of the background channels. For polarized beams, the -80/+30 configuration seems to be, overall, the most beneficial one. It must be stressed, though, that these studies are by no means replacements of proper full-detector studies, and should only be used as an estimation of the tendencies of the uncertainties.

In the second part of this thesis, we investigate an innovative idea to perform the spatial segmentation of large organic scintillators for highly granular calorimeters by means of an industrial 3D engraving process known as sub-surface laser engraving. This is done, in the framework of the CALICE collaboration, in an effort to find a possible alternative method for the production of scintillating tiles for a highly segmented analog hadronic calorimeter (AHCAL). The scope is for this method to be more cost effective and less time consuming than those investigated so far. After selecting a few plastic scintillator materials as potential candidates, an external company has been commissioned to produce optical barriers in the plastic medium by means of the SSLE technique. This process, used in glass for a few decades now, has the advantage, in principle, of minimizing the change in the mechanical properties of the target material and to leave the external surfaces unmodified. After a few prototype iterations, the company found an acceptable set of parameters to operate on PVT-based plastics. Contrary to inorganic scintillators, the laser-induced ablations in plastics produces a carbonization process known in materials science as charring. This results in a set of black spots, where the carbon-hydrogen bonds have been broken by the thermal shocks from the laser pulsed beam. After performing detailed optical inspections of several tile prototypes based on different base polymers, we used a scanning setup developed at the Max Planck Institute for Physics to characterize the spatial response of a larger $9 \times 9\,\mathrm{cm}^2$ tile, segmented in nine $3 \times 3\,\mathrm{cm}^2$ sectors with laser-engraved optical barriers.

The tile uniformity and the cross-talk between neighboring channels has been quantified with a SiPM-based readout, using a ^{90}Sr radioactive isotope as a source of penetrating β^- radiation to measure the response of the scintillator to ionizing radiation. The total cross-talk of an sub-surface engraved optical barrier was estimated to be at the 20% level. The more concerning characteristic of the laser-engraved tiles, compared to the typical response of a other CALICE-developed readout tiles, was the large drop in total light yield, that can be at least partially justified by the fact that the charred barriers absorb incoming photons rather than diffusing them in the direction of the SiPM readout. Based on these measurements, this technology does not yet meet the requirements for the AHCAL development, but could potentially be of use in scenarios with less stringent constrains, where a thicker scintillator material or SiPMs with a larger active area can be adopted.

A. Input Variables for the BDT Classifiers

Input Variables for the $H\nu\bar{\nu}$ BDT Classifier

Observable	Rank	Importance	Observable	Rank	Importance
evt.Pt	1	5.572e-02	*evt.thrustMin*	26	1.838e-02
evt.energy	2	3.995e-02	*evt.Pz*	27	1.819e-02
evt.nunu.Higgs.Mass	3	3.391e-02	*evt.chi2*	28	1.805e-02
hnunuboost	4	2.783e-02	*p1p2nunu*	29	1.771e-02
evt.Pmax	5	2.676e-02	*evt.jets.Hd2.theta*	30	1.743e-02
evt.thrust	6	2.564e-02	*evt.jets.Hd2.Energy*	31	1.694e-02
evt.nunu.Higgs.Pt	7	2.483e-02	*evt.jets.H_jets_angle*	32	1.688e-02
evt.jets.Hd2.Pt	8	2.429e-02	*evt.thrX*	33	1.676e-02
evt.jets.Hd2.n_trk	9	2.329e-02	*evt.nunu.Hd2.Mass*	34	1.673e-02
evt.jets.Higgs.Mass	10	2.288e-02	*evt.thrustMaj*	35	1.654e-02
evt.nunu.ynn[2]	11	2.283e-02	*evt.jets.Zd2.n_trk*	36	1.620e-02
evt.n_trk	12	2.268e-02	*evt.jets.Hd1.phi*	37	1.580e-02
evt.nunu.Hd2.Pt	13	2.197e-02	*evt.jets.Zd2.phi*	38	1.566e-02
hjetsboost	14	2.163e-02	*evt.tth_sphericity*	39	1.537e-02
evt.jets.H_jets_cos_angle	15	2.151e-02	*evt.nunu.H_jets_angle*	40	1.510e-02
evt.jets.Hd1.n_trk	16	2.066e-02	*evt.nunu.ynn*[3]	41	1.500e-02
evt.nunu.H_jets_cos_angle	17	2.058e-02	*evt.nunu.Higgs.theta*	42	1.492e-02
evt.thrust_cos_theta	18	2.022e-02	*evt.jets.Hd1.theta*	43	1.472e-02
evt.jets.Zd2.theta	19	2.019e-02	*hnunuth2*	44	1.435e-02
zjetsboost	20	1.943e-02	*evt.nunu.Hd1.phi*	45	1.407e-02
evt.nunu.H_jet_max_M	21	1.928e-02	*evt.jets.Higgs.Energy*	46	1.393e-02
evt.nunu.Hd2.n_trk	22	1.910e-02	*evt.jets.Higgs.Pt*	47	1.311e-02
evt.jets.Zd1.n_trk	23	1.909e-02	*evt.jets.Higgs.theta*	48	1.255e-02
evt.jets.Zd1.Ctag	24	1.877e-02	*evt.jets.Hd1.n_chrg_trk*	49	1.196e-02
evt.nunu.Hd1.n_chrg_trk	25	1.867e-02	*evt.n_photons*	50	1.193e-02

Table A.1.: TMVA method-specific rank and importance for the input obervables of the $H\nu\bar{\nu}$ BDT classifier.

Variables for the $Hq\bar{q}$ BDT Classifier

Observable	Rank	Importance	Observable	Rank	Importance
evt.chi2	1	4.262e-02	*evt.jets.Higgs.Mass*	26	1.852e-02
evt.nunu.H_jet_max_M	2	4.090e-02	*evt.nunu.ynn[1]*	27	1.846e-02
evt.thrust	3	3.577e-02	*evt.nunu.Higgs.theta*	28	1.814e-02
evt.n_trk	4	3.273e-02	*evt.jets.Hd1.n_trk*	29	1.792e-02
hnunuboost	5	3.208e-02	*evt.nunu.ynn[4]*	30	1.750e-02
evt.nunu.Higgs.Mass	6	3.150e-02	*evt.jets.Hd2.n_trk*	31	1.688e-02
evt.tth_sphericity	7	2.877e-02	*evt.thrZ*	32	1.667e-02
evt.nunu.Hd2.Mass	8	2.659e-02	*evt.jets.Hd1.Px*	33	1.658e-02
evt.nunu.ynn[3]	9	2.361e-02	*evt.nunu.Hd1.Energy*	34	1.658e-02
evt.thrustMaj	10	2.321e-02	*evt.jets.Zd2.Pt*	35	1.657e-02
evt.energy	11	2.296e-02	*evt.jets.Zd1.n_trk*	36	1.599e-02
zjetsboost	12	2.252e-02	*evt.jets.H_jets_angle*	37	1.594e-02
hjetsboost	13	2.173e-02	*evt.nunu.Hd2.Energy*	38	1.583e-02
evt.nunu.Hd1.Pt	14	2.098e-02	*evt.jets.Zboson.Mass*	39	1.539e-02
evt.jets.H_jets_cos_angle	15	2.025e-02	*evt.jets.Zd2.n_trk*	40	1.466e-02
evt.jets.Hd2.Energy	16	2.008e-02	*evt.jets.Hd2.Mass*	41	1.443e-02
evt.nunu.Hd1.Pz	17	1.999e-02	*evt.jets.Zboson.Py*	42	1.422e-02
evt.nunu.Hd2.n_trk	18	1.962e-02	*evt.jets.Hd1.Py*	43	1.419e-02
evt.nunu.Hd1.Mass	19	1.955e-02	*evt.jets.Hd2.Pt*	44	1.396e-02
evt.thrust_cos_theta	20	1.949e-02	*evt.nunu.H_jets_angle*	45	1.377e-02
evt.thrustMin	21	1.931e-02	*evt.tth_aplanarity*	46	1.336e-02
evt.jets.Zd2.Energy	22	1.895e-02	*evt.jets.Zd2.Pz*	47	1.336e-02
evt.Pmax	23	1.879e-02	*evt.jets.Zd2.Py*	48	1.333e-02
evt.nunu.ynn[2]	24	1.859e-02	*evt.jets.Hd2.n_chrg_trk*	49	1.061e-02
evt.jets.Higgs.theta	25	1.855e-02			

Table A.2.: TMVA method-specific rank and importance for the input obervables of the $Hq\bar{q}$ BDT classifier.

B. H$\nu\nu$ Templates for the Likelihood Fit

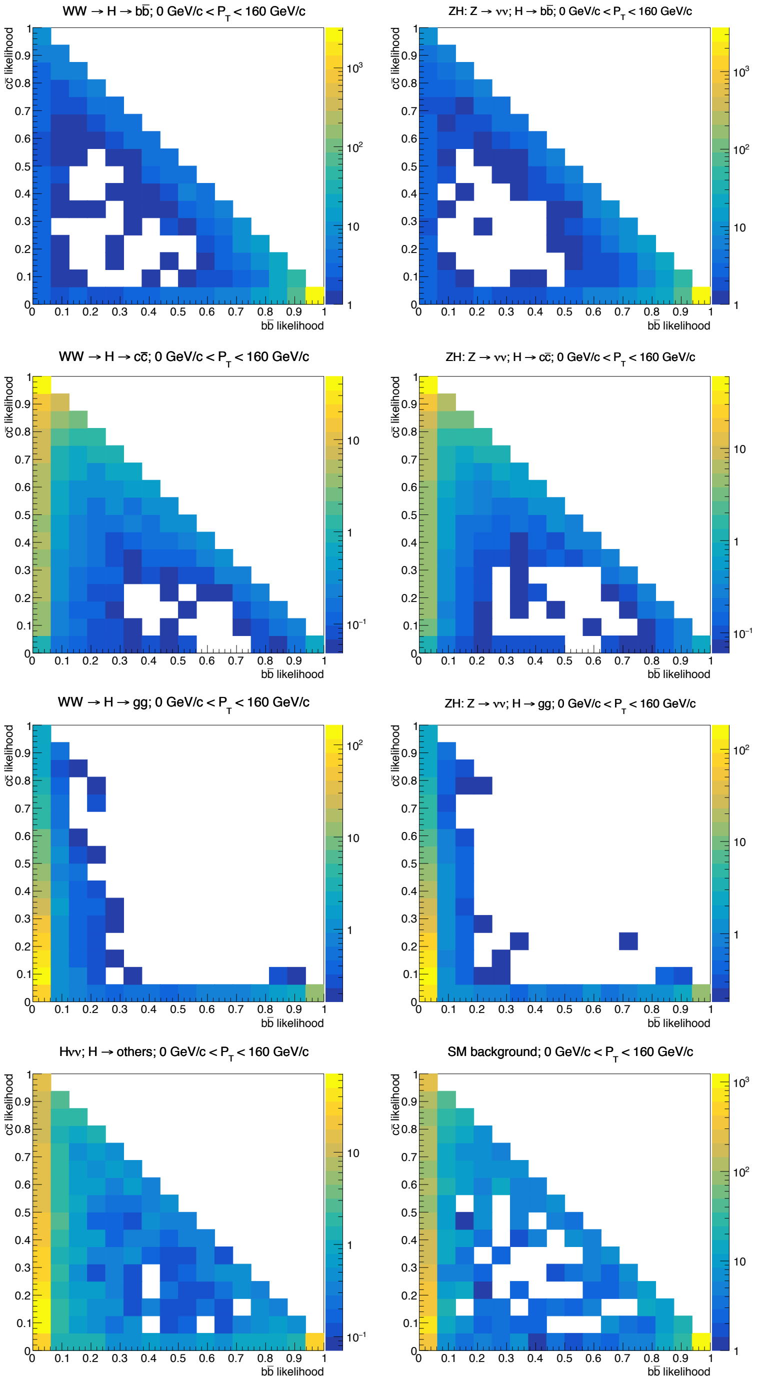

Figure B.1.: Projection of the eight signal and background 3D templates, to the $bb-$like and $cc-$like space.

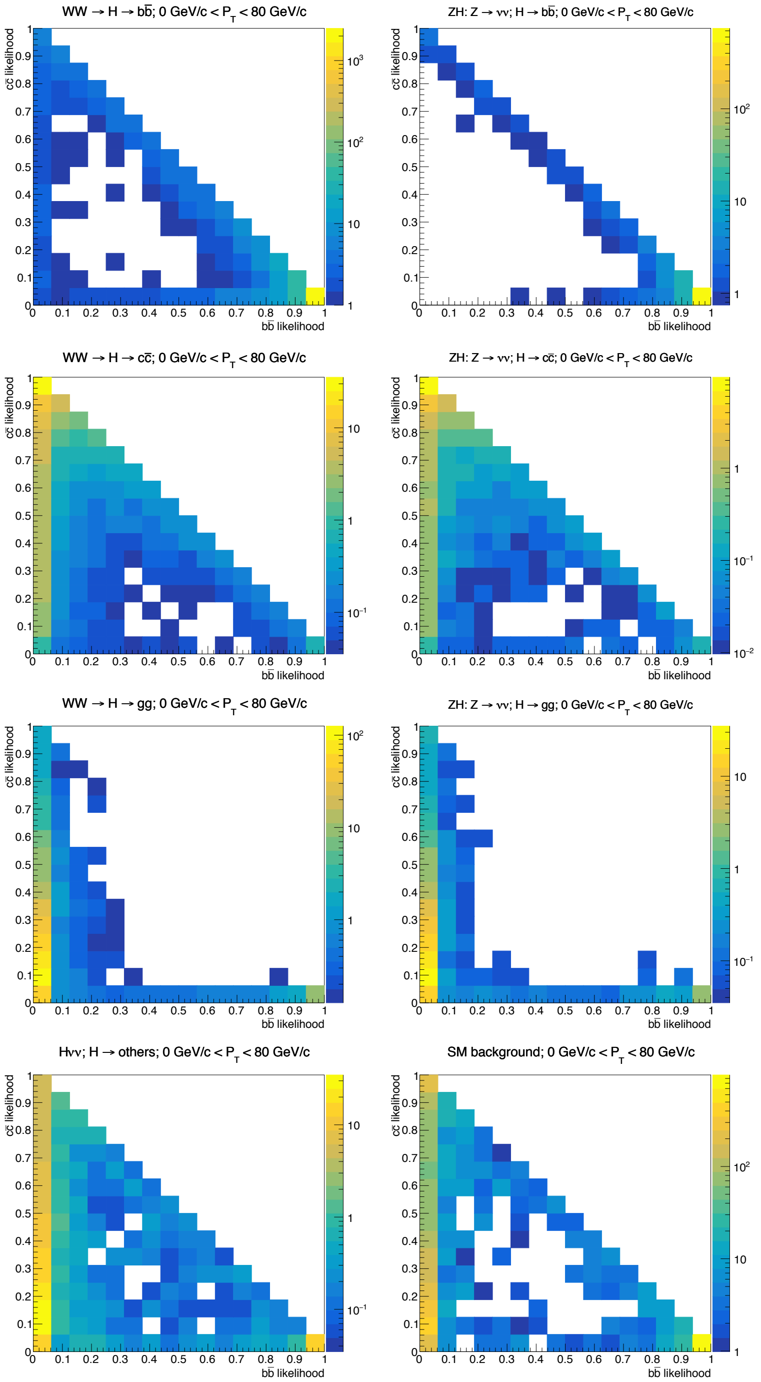

Figure B.2.: Projection of the eight signal and background 3D templates, to the $bb-$like and $cc-$like space, with a cut $P_T < 80 GeV/c$.

List of Figures

List of Tables

Bibliography

[1] J. McIntyre et al. “Does the brain model Newton’s laws?” In: *Nature neuroscience* 4.7 (2001), pp. 693–694.

[2] W. N. Cottingham and D. A. Greenwood. *An introduction to the standard model of particle physics*. Cambridge university press, 2007.

[3] A. Einstein. “Über einen die Erzeugung und Verwandlung des Lichtes betreffenden heuristischen Gesichtspunkt.” In: *Annalen der physik* 322.6 (1905), pp. 132–148.

[4] A. Einstein. “Zur Elektrodynamik bewegter Körper.” In: *Annalen der physik* 322.10 (1905), pp. 891–921.

[5] W. Pauli. “Open letter to the group of radioactive people at the Gauverein meeting in Tübingen.” In: *Translation by Kurt Riesselmann),(December, 4, 1930)* (1930).

[6] E. Fermi. “An attempt of a theory of beta radiation. 1.” In: *Z. phys* 88.161 (1934), p. 19.

[7] S. Weinberg, A. Salam, and S. Glashow. “Elementary particle theory.” In: *Phys. Rev. Lett* 19 (1967), p. 1264.

[8] G. Arnison et al. “Experimental observation of lepton pairs of invariant mass around 95 GeV/c^2 at the CERN SPS collider.” In: *Physics Letters B* 126.5 (1983), pp. 398–410.

[9] C. Rubbia. “Experimental observation of the intermediate vector bosons W^+, W^-, and Z^0.” In: *Reviews of Modern Physics* 57.3 (1985), p. 699.

[10] B. R. Stella and H.-J. Meyer. “Y (9.46 GeV) and the gluon discovery (a critical recollection of PLUTO results).” In: *The European Physical Journal H* 36.2 (2011), pp. 203–243.

[11] L. Whitlow et al. “A precise extraction of R= σL/σT from a global analysis of the SLAC deep inelastic ep and ed scattering cross sections.” In: *Physics Letters B* 250.1-2 (1990), pp. 193–198.

[12] S. Chatrchyan et al. “Observation of a new boson at a mass of 125 GeV with the CMS experiment at the LHC.” In: *Physics Letters B* 716.1 (2012), pp. 30–61.

[13] G. Aad et al. “Observation of a new particle in the search for the Standard Model Higgs boson with the ATLAS detector at the LHC.” In: *Physics Letters B* 716.1 (2012), pp. 1–29.

[14] B. P. Abbott et al. "Observation of gravitational waves from a binary black hole merger." In: *Physical review letters* 116.6 (2016), p. 061102.

[15] LHC Study Group and European Organization for Nuclear Research. *Design study of the large hadron collider (LHC): a multiparticle collider in the LEP tunnel*. 3. 1991.

[16] M. Aicheler et al. *A Multi-TeV linear collider based on CLIC technology: CLIC Conceptual Design Report*. CERN Geneva, Switzerland, 2012.

[17] N. Phinney, N. Toge, and N. Walker. "ILC reference design report volume 3-accelerator." In: *arXiv preprint arXiv:0712.2361* (2007).

[18] `https://www.nlm.nih.gov/dreamanatomy/da_g_Z-1.html`.

[19] W. Crookes. *Improvement in apparatus for indicating the intensity of radiation*. US Patent 182,172. 1876.

[20] H. Geiger and E. Marsden. "On a Diffuse Reflection of the α -Particles." In: *Proceedings of the Royal Society of London Series A* 82 (July 1909), pp. 495–500.

[21] J. J. Thomson. "On the Structure of the Atom: an Investigation of the Stability and Periods of Oscillation of a number of Corpuscles arranged at equal intervals around the Circumference of a Circle; with Application of the Results to the Theory of Atomic Structure." In: *Philosophical Magazine Series 6* 7.39 (1904).

[22] E. Rutherford. "The Scattering of α and β Particles by Matter and the Structure of the Atom." In: *Philosophical Magazine Series 6* 21 (1911).

[23] J. N. Bahcall. *Neutrino astrophysics*. Cambridge University Press, 1989.

[24] R. Bernabei et al. "New limits on particle dark matter search with a liquid Xenon target-scintillator." In: *Physics Letters B* 436.3 (1998), pp. 379–388.

[25] P. Bryant. "A brief history and review of accelerators." In: *RESEARCH-REPORTS-CERN* (1994), pp. 1–1.

[26] R. Wideröe. "On a new principle for the production of higher voltages." In: *Archiv für Elektrotechnik* 21 (1928), pp. 387–391.

[27] R. J. Van De Graaff. "A 1,500,000 volt electrostatic generator." In: *Phys. Rev* 38 (1931), p. 1919.

[28] J. Cockcroft and E. Walton. "Artificial production of fast protons." In: *nature* 129 (1932), p. 242.

[29] J. D. Cockcroft and E. T. S. Walton. "Disintegration of lithium by swift protons." In: *Nature* 129.3261 (1932), pp. 649–649.

[30] E. O. Lawrence and M. S. Livingston. "The production of high speed light ions without the use of high voltages." In: *Physical Review* 40.1 (1932), p. 19.

[31] E. O. Lawrence and M. S. Livingston. "The multiple acceleration of ions to very high speeds." In: *Physical Review* 45.9 (1934), p. 608.

[32] P. C. Aebersold. “The Cyclotron: A Nuclear Transformer 1.” In: *Radiology* 39.5 (1942), pp. 513–540.

[33] A. W. Chao et al. *Handbook of accelerator physics and engineering*. World scientific, 2013.

[34] D. W. Kerst. “The acceleration of electrons by magnetic induction.” In: *Physical Review* 60.1 (1941), p. 47.

[35] D. A. Edwards and M. J. Syphers. *An introduction to the physics of high energy accelerators*. John Wiley & Sons, 2008.

[36] A. E. Harrison. *Klystron tubes*. McGraw-Hill Book Company, 1947.

[37] A. Chao and W. Chou. *Reviews of accelerator science and technology*. Vol. 1. World Scientific, 2008.

[38] V. I. Veksler. “A new method of acceleration of relativistic particles.” In: *J. Phys.* 9 (1945), pp. 153–158.

[39] E. M. McMillan. “The relation between phase stability and first-order focusing in linear accelerators.” In: *Physical Review* 80.3 (1950), p. 493.

[40] E. M. McMillan. “The synchrotron—a proposed high energy particle accelerator.” In: *Physical Review* 68.5-6 (1945), p. 143.

[41] M. H. Blewett. “The Cosmotron—A Review.” In: *Review of Scientific Instruments* 24.9 (1953), pp. 725–737.

[42] E. Wilson. “Fifty years of synchrotrons.” In: *Proceedings of the 1996 European Particle Accelerator Conference (EPAC’96)*. 1996, pp. 135–139.

[43] N. Christofilos. *Focussing system for ions and electrons*. US Patent 2,736,799. 1956.

[44] E. D. Courant, M. S. Livingston, and H. S. Snyder. “The strong-focusing synchroton—A new high energy accelerator.” In: *Physical Review* 88.5 (1952), p. 1190.

[45] J. P. Blewett. “Radial focusing in the linear accelerator.” In: *Physical Review* 88.5 (1952), p. 1197.

[46] V. Veksler. “Principles of acceleration of charged particles.” In: *The Soviet Journal of Atomic Energy* 1.1 (1956), pp. 77–83.

[47] E. Regenstreif. *The CERN Proton Synchrotron, pt. 1*. Tech. rep. CERN, 1959.

[48] F. Close, M. Marten, and C. Sutton. *The Particle Odyssey: A Journey to the Heart of the Matter: A Journey to the Heart of the Matter*. Oxford University Press, USA, 2002.

[49] E. Keil. *The Intersecting Storage Rings*. Tech. rep. Cern, 1972.

[50] C. Bernardini et al. “Progress report on AdA (Frascati storage ring).” In: *Il Nuovo Cimento (1955-1965)* 23.1 (1962), pp. 202–207.

[51] F. Amman et al. “Anello di Accumulazione per elettroni e positroni (ADONE), Frascati National Laboratories.” In: *Nota Interna* 68 (1961).

[52] UA2 Collaboration et al. "A precise determination of the W and Z masses at the CERN pp collider." In: *Physics Letters B* 241.1 (1990), pp. 150–164.

[53] J.-E. Augustin et al. "Discovery of a Narrow Resonance in e+ e- Annihilation." In: *Physical Review Letters* 33.23 (1974), p. 1406.

[54] J. D. Bjorken and E. A. Paschos. "Inelastic electron-proton and γ-proton scattering and the structure of the nucleon." In: *Physical Review* 185.5 (1969), p. 1975.

[55] M. Gell-Mann. "Quarks." In: *Elementary Particle Physics*. Springer, 1972, pp. 733–761.

[56] D. Möhl et al. "Physics and technique of stochastic cooling." In: *Physics Reports* 58.2 (1980), pp. 73–102.

[57] J. R. Rees. "The Stanford linear collider." In: *Scientific American;(USA)* 261.4 (1989).

[58] G. Dugan. "Tevatron status." In: *Particle Accelerator Conference, 1989. Accelerator Science and Technology., Proceedings of the 1989 IEEE*. IEEE. 1989, pp. 426–430.

[59] S. Myers. *The LEP collider, from design to approval and commissioning*. Tech. rep. European Organization for Nuclear Research, 1991.

[60] Atlas Collaboration et al. "ATLAS detector and physics performance Technical Design Report." In: *CERN/LHCC* 99.14 (1999), pp. 99–15.

[61] CMS collaboration et al. "CMS physics technical design report, volume II: physics performance." In: *Journal of Physics G: Nuclear and Particle Physics* 34.6 (2007), p. 995.

[62] CMS collaboration et al. "Observation of a new boson at a mass of 125 GeV with the CMS experiment at the LHC." In: *arXiv preprint arXiv:1207.7235* (2012).

[63] C. M. Ankenbrandt et al. "Status of muon collider research and development and future plans." In: *Physical Review Special Topics-Accelerators and Beams* 2.8 (1999), p. 081001.

[64] M. Alsharoa. "Status of Neutrino Factory and Muon Collider Research and Development and Future Plans." In: *Phys. Rev. Spec. Top. Accel. Beams* 6.hep-ex/0207031 (2002), p. 081001.

[65] M. Ruan. "Higgs measurement at e^+e^- circular colliders." In: *Nuclear and Particle Physics Proceedings* 273 (2016), pp. 857–862.

[66] M. Benedikt et al. *Challenges for highest energy circular colliders*. Tech. rep. 2014.

[67] T. Behnke et al. "The International Linear Collider Technical Design Report-Volume 1: Executive Summary." In: *arXiv preprint arXiv:1306.6327* (2013).

[68] L. Linssen et al. "Physics and detectors at CLIC: CLIC conceptual design report." In: *arXiv preprint arXiv:1202.5940* (2012).

[69] `http://www.physi.uni-heidelberg.de/_schoning`.

[70] `http://flc.desy.de`.

[71] `http://research-instrument.de`.

[72] K. Tiedtke et al. “The soft x-ray free-electron laser FLASH at DESY: beamlines, diagnostics and end-stations.” In: *New journal of physics* 11.2 (2009), p. 023029.

[73] T. Barklow et al. “ILC Operating Scenarios.” In: *arXiv preprint arXiv:1506.07830* (2015).

[74] `clicdp.web.cern.ch`.

[75] J. G. Navarro et al. “High-gradient structure performances: ongoing tests and summary.” In: *Proc. of CLIC Workshop*. 2016.

[76] G. Geschonke and A. Ghigo. *CTF3 design report*. Tech. rep. 2002.

[77] T. Ekelöf et al. “The Two-beam Test-stand in CTF3.” In: *proc. EPAC*. Vol. 6. 20. 2006, p. 2445.

[78] M. Boland et al. *Updated baseline for a staged Compact Linear Collider*. Tech. rep. CERN, 2016.

[79] T. CLIC et al. “Updated baseline for a staged Compact Linear Collider.” In: *arXiv preprint arXiv:1608.07537* (2016).

[80] B. Dalena et al. *The CLIC BDS TOWARDS the Conceptual Design Report*.

[81] F. Zimmermann et al. *Final-Focus System for CLIC at 3 TeV*. Tech. rep. 2000.

[82] T. Antičić, K. Kadija, and T. Šuša. “Alice: Physics performance report, volume ii.” In: (2006).

[83] A. A. Alves Jr et al. “The LHCb detector at the LHC.” In: *Journal of instrumentation* 3.08 (2008), S08005.

[84] F. Simon. “Detector Systems at CLIC.” In: *Physics Procedia* 37 (2012), pp. 63–71.

[85] S. Schael et al. “Precision electroweak measurements on the Z resonance.” In: *Physics Reports* 427.5-6 (2006), pp. 257–454.

[86] `http://www.hep.phy.cam.ac.uk/linearcollider/physics/`.

[87] G. Aad et al. “Measurement of the inclusive isolated prompt photon cross section in p p collisions at s= 7 TeV with the ATLAS detector.” In: *Physical Review D* 83.5 (2011), p. 052005.

[88] M. Thomson. “Particle flow calorimetry.” In: *Journal of Physics: Conference Series*. Vol. 110. 9. IOP Publishing. 2008, p. 092032.

[89] S. Heinemeyer et al. “Handbook of LHC Higgs cross sections: 3. Higgs properties.” In: *arXiv preprint arXiv:1307.1347* (2013).

[90] N. A. Tehrani. “Optimisation studies for the CLIC vertex-detector geometry.” In: *Journal of Instrumentation* 10.07 (2015), p. C07001.

[91] C. Patrignani, P. D. Group, et al. “Review of particle physics.” In: *Chinese physics C* 40.10 (2016), p. 100001.

[92] R. Wigmans. *Calorimetry: Energy measurement in particle physics*. Vol. 107. Oxford University Press, 2000.

[93] P. Valerio et al. "65nm technology for HEP: status et perspective." In: *23rd International Workshop on Vertex Detectors (VERTEX 2014)*. 2014, p. 043.

[94] P. Valerio, M. Campbell, and R. Ballabriga. *Design of the 65 nm CLICpix demonstrator chip*. Tech. rep. 2012.

[95] D. Dannheim. "Vertex-detector R&D for CLIC." In: *Journal of Instrumentation* 9.03 (2014), p. C03026.

[96] C. Garabatos. "The Alice TPC." In: *Nuclear Instruments and Methods in Physics Research Section A: Accelerators, Spectrometers, Detectors and Associated Equipment* 535.1 (2004), pp. 197–200.

[97] K. Ahmet, M. Akrawy, and G. Alexander. "The OPAL detector at LEP." In: *Nuclear Instruments and Methods in Physics Research, Section A* 305.2 (1991), pp. 275–319.

[98] B. Aubert et al. "The BABAR detector." In: *Nuclear Instruments and Methods in Physics Research Section A: Accelerators, Spectrometers, Detectors and Associated Equipment* 479.1 (2002), pp. 1–116.

[99] I. Belle. "Technical design report." In: *KEK report* 1 (2010), p. 2010.

[100] M. M. Angarano, CMS Tracker Collaboration, et al. "The silicon strip tracker for CMS." In: *Nuclear Instruments and Methods in Physics Research Section A: Accelerators, Spectrometers, Detectors and Associated Equipment* 501.1 (2003), pp. 93–99.

[101] M. Battaglia. "The Vertex Tracker at future e+ e- linear colliders." In: *Nuclear Instruments and Methods in Physics Research Section A: Accelerators, Spectrometers, Detectors and Associated Equipment* 530.1 (2004), pp. 33–37.

[102] B. Aubert et al. "Performance of the ATLAS electromagnetic calorimeter barrel module 0." In: *Nuclear Instruments and Methods in Physics Research Section A: Accelerators, Spectrometers, Detectors and Associated Equipment* 500.1 (2003), pp. 202–231.

[103] A. Caldwell et al. "Design and implementation of a high precision readout system for the ZEUS calorimeter." In: *Nuclear Instruments and Methods in Physics Research Section A: Accelerators, Spectrometers, Detectors and Associated Equipment* 321.1-2 (1992), pp. 356–364.

[104] ZEUS Calorimeter Group et al. "Construction and beam test of the ZEUS forward and rear calorimeter." In: *Nuclear Instruments and Methods in Physics Research Section A: Accelerators, Spectrometers, Detectors and Associated Equipment* 309.1-2 (1991), pp. 101–142.

[105] I.-M. Gregor. "The zeus uranium calorimeter-15 Years of successful operation." In: *Nuclear Science Symposium Conference Record, 2007. NSS'07. IEEE*. Vol. 1. IEEE. 2007, pp. 249–253.

[106] I. G. Knowles and G. D. Lafferty. "Hadronization in Z^0 decay." In: *Journal of Physics G: Nuclear and Particle Physics* 23.7 (1997), p. 731.

[107] M. Thomson. "Particle flow calorimetry and the PandoraPFA algorithm." In: *Nuclear Instruments and Methods in Physics Research Section A: Accelerators, Spectrometers, Detectors and Associated Equipment* 611.1 (2009), pp. 25–40.

[108] `https://en.wikipedia.org`.

[109] M. Gell-Mann. "Symmetries of baryons and mesons." In: *Physical Review* 125.3 (1962), p. 1067.

[110] K. J. Barnes. *Group theory for the standard model of particle physics and beyond*. Taylor & Francis, 2010.

[111] C.-N. Yang and R. L. Mills. "Conservation of isotopic spin and isotopic gauge invariance." In: *Physical review* 96.1 (1954), p. 191.

[112] J. Goldstone, A. Salam, and S. Weinberg. "Broken symmetries." In: *Physical Review* 127.3 (1962), p. 965.

[113] Y. Nambu. "Nobel Lecture: Spontaneous symmetry breaking in particle physics: A case of cross fertilization." In: *Reviews of Modern Physics* 81.3 (2009), p. 1015.

[114] A. Salam and J. C. Ward. "Electromagnetic and weak interactions." In: *Physics Letters* 13.2 (1964), pp. 168–171.

[115] S. Dawson. "Introduction to the Physics of Higgs Bosons." In: *CP Violation and the Limits of the Standard Model*. 1995, p. 445.

[116] R. Häußling and E. Kraus. "Gauge parameter dependence and gauge invariance in the Abelian Higgs model." In: *Zeitschrift für Physik C Particles and Fields* 75.4 (1997), pp. 739–750.

[117] H. Abramowicz et al. "Higgs Physics at the CLIC Electron-Positron Linear Collider." In: *arXiv preprint arXiv:1608.07538* (2016).

[118] C. Amsler, P. D. Group, et al. "partial update for the 2010 edition." In: *Cut-off date for this update was January* 15 (2009), p. 2009.

[119] H. Li. "Higgs recoil mass and cross-section analysis at ILC and calibration of the CALICE SiW ECAL prototype." PhD thesis. Université Paris Sud-Paris XI, 2009.

[120] M. A. Thomson. "Model-independent measurement of the e^{{+}} e^{-}\ rightarrow HZ cross section at a future e^{{+}} e^{-} linear collider using hadronic Z decays." In: *The European Physical Journal C* 76.2 (2016), pp. 1–14.

[121] H. Baer et al. "The International linear collider technical design report-volume 2: physics." In: *arXiv preprint arXiv:1306.6352* (2013).

[122] T. I. C. Group. "The international large detector: Letter of intent." In: *arXiv preprint arXiv:1006.3396* (2010).

[123] S. Dittmaier et al. "Handbook of LHC Higgs cross sections: 1. Inclusive observables." In: *arXiv preprint arXiv:1101.0593* (2011).

[124] `http://articles.sae.org/13996/`.

[125] E. De Schutter. *Computational Neuroscience: Trends in Research 2003*. Elsevier, 2003.

[126] R. Hecht-Nielsen et al. "Theory of the backpropagation neural network." In: *Neural Networks* 1.Supplement-1 (1988), pp. 445–448.

[127] A. Hoecker et al. "TMVA-Toolkit for multivariate data analysis." In: *arXiv preprint physics/0703039* (2007).

[128] Y. Freund and R. Schapire. "The strength of weak learnability." In: *Journal of Computer and System Sciences* 55 (1997), pp. 119–139.

[129] S. Dittmaier et al. "Handbook of LHC Higgs cross sections: 2. Differential distributions." In: *arXiv preprint arXiv:1201.3084* (2012).

[130] T. Ohl, A. Para, and H. Fisk. "O'mega & whizard: Monte carlo event generator generation for future colliders." In: *AIP Conference Proceedings*. Vol. 578. 1. AIP. 2001, pp. 638–641.

[131] W. Kilian, T. Ohl, and J. Reuter. "WHIZARD—simulating multi-particle processes at LHC and ILC." In: *The European Physical Journal C-Particles and Fields* 71.9 (2011), pp. 1–29.

[132] F. Simon. *Top Quark Precision Physics at Linear Colliders*. Tech. rep. 2014.

[133] T. Sjöstrand, S. Mrenna, and P. Skands. "PYTHIA 6.4 physics and manual." In: *Journal of High Energy Physics* 2006.05 (2006), p. 026.

[134] S. Agostinelli et al. "GEANT4—a simulation toolkit." In: *Nuclear instruments and methods in physics research section A: Accelerators, Spectrometers, Detectors and Associated Equipment* 506.3 (2003), pp. 250–303.

[135] P. M. De Freitas and H. Videau. "Detector simulation with MOKKA/GEANT4: Present and future." In: *International Workshop on Linear Colliders (LCWS 2002), Jeju Island, Korea*. 2002, pp. 26–30.

[136] A. Münnich and A. Sailer. *The CLIC ILD CDR geometry for the CDR Monte Carlo mass production*. Tech. rep. 2012.

[137] G. Mavromanolakis and D. Ward. "Comparisons of hadronic shower packages." In: *arXiv preprint physics/0409040* (2004).

[138] F. Gaede. "Marlin and LCCD—Software tools for the ILC." In: *Nuclear Instruments and Methods in Physics Research Section A: Accelerators, Spectrometers, Detectors and Associated Equipment* 559.1 (2006), pp. 177–180.

[139] T. Tanabe and T. Suehara. *LCFIPlus*.

[140] G. P. Salam. "Towards jetography." In: *The European Physical Journal C* 67.3-4 (2010), pp. 637–686.

[141] S. Moretti, L. Lönnblad, and T. Sjöstrand. "New and old jet clustering algorithms for electron-positron events." In: *Journal of High Energy Physics* 1998.08 (1998), p. 001.

[142] S. Catani et al. "New clustering algorithm for multijet cross sections in e+ e- annihilation." In: *Physics Letters B* 269.3-4 (1991), pp. 432–438.

[143] B. Naroska. "e+ e- Physics with the JADE detector at PETRA." In: *Physics Reports* 148.2-3 (1987), pp. 67–215.

[144] W. Bartel et al. "Experimental studies on multijet production ine+ e- annihilation at PETRA energies." In: *Zeitschrift für Physik C Particles and Fields* 33.1 (1986), pp. 23–31.

[145] S. M. RAL, L. Lönnblad, and T. Sjöstrand. "New and Old Jet Clustering Algorithms for Electron-Positron Events." In: ().

[146] `https://confluence.slac.stanford.edu/display/ilc/LCFIPlus+Variables`.

[147] `http://home.thep.lu.se/{~}torbjorn/ppp2011/lec8.pdf`.

[148] J. Marshall and M. Thomson. *Higgs Mass and Cross-Section Measurements at a 500 GeV CLIC Machine, Operating at sqrt (s)= 350 GeV and 500 GeV*. Tech. rep. 2012.

[149] F. James and M. Roos. "Minuit-a system for function minimization and analysis of the parameter errors and correlations." In: *Computer Physics Communications* 10.6 (1975), pp. 343–367.

[150] B. Segal et al. "Grid computing: The European data grid project." In: *IEEE Nuclear Science Symposium and Medical Imaging Conference*. Vol. 1. 2. 2000.

[151] M. L. Swartz. "Physics with polarized electron beams." In: *SLAC Pub* 4656 (1988).

[152] V. Barger, M. Ishida, and W.-Y. Keung. "Total width of 125 GeV Higgs boson." In: *Physical review letters* 108.26 (2012), p. 261801.

[153] F. Simon. *Personal Comunication*. 2017.

[154] C. Adloff et al. "Construction and commissioning of the CALICE analog hadron calorimeter prototype." In: *Journal of Instrumentation* 5.05 (2010), P05004.

[155] T. Abe et al. *The international large detector: Letter of intent*. Tech. rep. 2010.

[156] N. Dinu et al. "Development of the first prototypes of Silicon PhotoMultiplier (SiPM) at ITC-irst." In: *Nuclear Instruments and Methods in Physics Research Section A: Accelerators, Spectrometers, Detectors and Associated Equipment* 572.1 (2007), pp. 422–426.

[157] D. R. Schaart et al. "A novel, SiPM-array-based, monolithic scintillator detector for PET." In: *Physics in medicine and biology* 54.11 (2009), p. 3501.

[158] M. Bedjidian et al. "Performance of Glass Resistive Plate Chambers for a high-granularity semi-digital calorimeter." In: *Journal of Instrumentation* 6.02 (2011), P02001.

[159] CALICE collaboration et al. "First results of the CALICE SDHCAL technological prototype." In: *Journal of Instrumentation* 11.04 (2016), P04001.

[160] CALICE collaboration et al. "Electron data with the CALICE tile AHCAL prototype at the CERN test-beam." In: *CAN-011* (2007).

[161] R. Fabbri. "CALICE Second Generation AHCAL Developments." In: *arXiv preprint arXiv:1007.2358* (2010).

[162] D. Dannheim, E van der Kraaij, and W Klempt. *Beam tests with the CALICE tungsten analog hadronic calorimeter prototype*. Tech. rep. 2012.

[163] `http://www.ilcild.org/`.

[164] K. Seidel, Calice Collaboration, et al. "Particle showers in a highly granular hadron calorimeter." In: *Nuclear Instruments and Methods in Physics Research Section A: Accelerators, Spectrometers, Detectors and Associated Equipment* 628.1 (2011), pp. 343–346.

[165] `http://www.crystals.saint-gobain.com/sites/imdf.crystals.com/files/documents/organics-brochure.pdf`.

[166] G. Barbarino et al. "High gain hybrid photomultipliers based on solid state pn junctions in Geiger mode and their use in astroparticle physics." In: *Physics Procedia* 37 (2012), pp. 703–708.

[167] `http://www.hamamatsu.com/eu/en/product/category/3100/4004/4113/S13360-3025PE/index.html`.

[168] `https://www.liverpool.ac.uk/quasar/research/eu-projects/sipm/`.

[169] F. Simon and C. Soldner. "Uniformity studies of scintillator tiles directly coupled to SiPMs for imaging calorimetry." In: *Nuclear Instruments and Methods in Physics Research Section A: Accelerators, Spectrometers, Detectors and Associated Equipment* 620.2 (2010), pp. 196–201.

[170] M. Tesař et al. "Study of detection efficiency distribution and areal homogeneity of SiPMs." In: *arXiv preprint arXiv:1211.6330* (2012).

[171] H. J. LeFevre. "Analysis of an integrated readout layer for use in a highly granular analog hadron calorimeter." PhD thesis. NORTHERN ILLINOIS UNIVERSITY, 2016.

[172] O. Hartbrich. *Status of the CALICE Scintillator HCAL Engineering Prototype*. Tech. rep. 2013.

[173] R. M. Clement, N. R. Ledger, and R. P. Sunman. *Sub-surface marking*. US Patent 5,206,496. 1993.

[174] `http://ippog.web.cern.ch/`.

[175] T. Moriya et al. “Development of PET detectors using monolithic scintillation crystals processed with sub-surface laser engraving technique.” In: *Nuclear Science Symposium Conference Record (NSS/MIC), 2009 IEEE*. IEEE. 2009, pp. 3560–3564.

[176] T. Moriya et al. “Fabrication of Finely Pitched LYSO Arrays Using Subsurface Laser Engraving Technique with Picosecond and Nanosecond Pulse Lasers.” In: *IEEE Transactions on Nuclear Science* 61.2 (2014), pp. 1032–1038.

[177] `http://www.laser-gruener.de/`.

[178] S. El Yacoubi. *AIDA-2020 Kick-off meeting*. Tech. rep. 2015.

[179] `http://www.infineon.com/`.

[180] `https://www.picotech.com/oscilloscope/6000/picoscope-6000-overview`.

[181] `http://www.eljentechnology.com/products/plastic-scintillators/ej-200-ej-204-ej-208-ej-212`.

[182] `https://en.wikipedia.org/wiki/Polyvinyl_toluene$`.

[183] `http://www.keyence.com/ss/products/microscope/vhx5000/`.

[184] `http://multimedia.3m.com/mws/media/9824490/3mtm-specular-film-df2000ma-technical-data-sheet.pdf`.

[185] C. Soldner. “The time development of hadronic showers and the T3B experiment.” PhD thesis. lmu, 2013.